

Composite Materials

Lauge Fuglsang Nielsen

Composite Materials

Properties as Influenced by Phase Geometry

With 241 Figures

 Springer

Lauge Fuglsang Nielsen

Technical University of Denmark
Dept. Civil Engineering, Bld. 118
2800 Lyngby, Denmark
e-mail: lfn@byg.dtu.dk

Library of Congress Control Number: 2005920510

ISBN -10 3-540-24385-2 Springer Berlin Heidelberg New York
ISBN -13 978-3-540-24385-4 Springer Berlin Heidelberg New York

This work is subject to copyright. All rights are reserved, whether the whole or part of the material is concerned, specifically the rights of translation, reprinting, reuse of illustrations, recitation, broadcasting, reproduction on microfilm or in any other way, and storage in data banks. Duplication of this publication or parts thereof is permitted only under the provisions of the German Copyright Law of September 9, 1965, in its current version, and permission for use must always be obtained from Springer. Violations are liable for prosecution under the German Copyright Law.

Springer is a part of Springer Science+Business Media
springeronline.com

© Springer-Verlag Berlin Heidelberg 2005
Printed in The Netherlands

The use of general descriptive names, registered names, trademarks, etc. in this publication does not imply, even in the absence of a specific statement, that such names are exempt from the relevant protective laws and regulations and therefore free for general use.

Typesetting: by the authors and TechBooks using a Springer L^AT_EX macro package
Cover design: deblik, Berlin

Printed on acid-free paper SPIN: 11002154 89/3141/jl 5 4 3 2 1 0

To my family and friends

Overview

The subject dealt with in this book is the mechanical and physical behavior of composites as influenced by composite geometry. This subject has a high priority in the general study of composite materials. A better understanding of the behavior of natural composites, improvement of such materials, and design of new materials with prescribed properties are just three examples in modern materials research where more knowledge on geometry versus materials property is absolutely necessary.

An analysis of various composite properties versus composite geometries is presented in this book as the result of integrating the results of two sub-studies:

One study is made on composite properties as these can be related to composite geometry in general by so-called geometry functions. The second study is made on geometry functions as these are related to the geometry of specific composites, such as particulate composites, impregnated materials, laminated composites, and composites made by compaction of powders.

In other words, global solutions for composite properties are developed in the first study, which apply for any composite. Final solutions for composites with specific geometries are then obtained from the global solutions introducing specific geometry functions developed in the second study.

Special composite properties considered are stiffness, shrinkage, hygro-thermal behavior, viscoelastic behavior, and internal stress states. Other physical properties considered are thermal and electrical conductivities, diffusion coefficients, dielectric constants and magnetic permeability. Special attention is given to the effect of pore shape on the mechanical and physical behavior of porous materials.

The theories and the methods developed are verified by results obtained from a FEM-analysis presented, and by experimental and theoretical data from the composite literature. A number of examples are presented which illustrate the very decisive influence of the internal geometry on the mechanical and physical properties of composites.

As a spin-off result the composite theory developed is re-organized to become a “diagnostic tool” with respect to quality control of empirical or semi-theoretical prediction methods suggested in the field of composite materials. Aspects of materials design are also considered.

It is emphasized that strength is not considered as a genuine materials property in this book. It is a phenomenon where discontinuities in the materials structure suddenly occur as the result of violating local potentials to carry stress and/or strain for example. As such strength is a “materials property” that can be calculated from stress/strain results obtained in this book. Examples of such strength predictions for composite materials are presented.

Readers Guidance

Roughly speaking the book is divided into two parts. A theoretical part, and a more applicative part, starting at Chap. 10 where the theories developed are simplified, adapted, and generalized for most practice. Readers, who are interested primarily in applications, may start at this chapter. Any problem considered in Chap. 10 and subsequent chapters can be solved using the software package COM-APPL developed for easy composite analysis¹.

Lists of notations and references used are presented at the end of the book. The former list should be consulted frequently. Symbols and notations used in the book are generally explained only at their first appearance in the text.

The following superior concept of notations is emphasized: Whenever needed to distinguish single component properties from composite properties, subscripts P and S refer to property of component P and property of component S respectively while composite property is not subscripted. Usually the subscripts g and k are used to indicate quantities obtained from – or used in deviatoric analysis and in volumetric analysis respectively. Formally these analyses are very often identical. In such cases only the volumetric analysis is presented with deviatoric results referred to by analogy. Alternatively both subscripts k and g are dropped when the feature discussed applies in principles for both volumetric and deviatoric behavior.

A special subscript, Q, is used in conductivity studies to distinguish results obtained in these studies from similar quantities obtained in the analysis of elastic behavior.

A number of auxiliary expressions are presented in appendix sections at the end of the book: Basic information is given on isotropic elasticity and cubical elasticity in Appendix A. A method is presented in Appendix B for the numerical determination of stresses in ellipsoidal particles in isotropic dilute

¹ COM-APPL can be downloaded from [http:// www.mat-mek.dk](http://www.mat-mek.dk)

suspensions. A generalized version of the so-called SCS-analysis (Self Consistency Scheme) of composite materials is presented in Appendix C. General viscoelastic models are presented in Appendix D. And finally, models are presented in Appendix E for volume compositions of hardening Portland cement paste and concrete.

Contents

1	Introduction	1
1.1	Objectives of This Work	4
1.1.1	Summary of Composites Considered	5
2	Classification of Composites	7
2.1	Volume Concentrations	7
2.2	Geometry at Fixed Phase Concentrations	8
2.2.1	Geometrical Classification	9
2.3	Composites with Variable Geometry	10
2.3.1	Geometrical Classification	10
2.3.2	Some Composite Examples	14
3	Preliminaries on Stress/Strain	17
3.1	Stiffness	17
3.1.1	Dilute Suspension	19
3.2	Stress	20
3.3	Composite Stiffness Estimated by SCS	20
4	Composite Stress and Geometry	23
4.1	Volumetric Stress	23
4.1.1	CSA-Composites	23
4.1.2	Any Composite – Geometry Function	24
4.1.3	Geometry Function and Shape Function	25
4.1.4	Shape Functions – A Closer Look	27
4.1.5	Summary	30
4.2	Deviatoric Stress	31
4.2.1	Stress and Geometry	31
4.3	Summary on Stress and Geometry	32
4.3.1	Stress	32
4.3.2	Geo-Function	32

5	Composite Stiffness and Geometry	35
5.1	Bulk Modulus and Shear Modulus	35
5.1.1	Porous Materials and Stiff Pore Systems	35
5.2	Young's Modulus and Poisson's Ratio	36
5.3	Special Composites and Observations	36
5.3.1	CSA-Composites	37
5.3.2	Composites with Special Shear Moduli	37
5.3.3	Paul/Hansen versus Geo-Functions	38
6	Composite Eigenstrain/Stress	39
6.1	Basics	39
6.1.1	Simple Composites	40
6.2	General Geometry	40
6.2.1	Eigenstrain and Eigenstress	40
6.2.2	Pore Pressure in Porous Materials	41
7	Quantification of Geometry	43
7.1	Shape Factors	47
7.1.1	DC-Composites	47
7.1.2	CD-Composites	53
7.1.3	MM-Composites	54
7.2	Shape Functions and Geo-Path	57
7.2.1	Default	57
7.2.2	Alternative I	60
7.2.3	Alternative II	61
7.3	Geo-Paths	62
8	Composite Theory – Elasticity	65
8.1	Illustrative Examples	65
8.1.1	DC-CD Composite	65
8.1.2	Crumbled Foils Composite	67
8.1.3	Particulate (DC-DC) Composite	69
8.2	Other Examples	71
8.2.1	Cracks	71
8.2.2	Special DC-CD Composites	75
8.3	FEM-Analysis versus Theory	78
8.3.1	FEM-Analysis	78
8.3.2	Particulate Composite	80
8.3.3	Defective Particulate Composite	82
8.3.4	Pearls on a String Composite	87
8.3.5	Grid Composite	91
8.3.6	Cracked Material	94
8.3.7	Discussion of FEM-Analysis	95
8.4	Conclusion	98

9	Composite Theory – Conductivity	99
9.1	Theory	99
9.2	Illustrative Examples	100
9.2.1	Porous Materials and Stiff Pore Systems	100
9.2.2	Dilute Porous Materials and Stiff Pore Systems	102
9.2.3	Cracked Materials (Soft and Stiff Cracks)	102
9.2.4	Crumbled Foils Composite	104
9.3	Theory versus Experiments	104
9.3.1	Chloride Diffusion in HCP and HCP with Silica Fume	104
9.3.2	Thermal Conductivity of Plane-Isotropic Fiber Composite	107
9.4	Theory versus SCS-Estimates	109
9.5	Conclusion	109
10	Simplified Composite Theory – Elasticity	113
10.1	Basis of Analysis	115
10.1.1	Geometry	115
10.1.2	Quantification of Composite Geometry	117
10.1.3	Preparation of Composite Analysis	121
10.2	Analysis	122
10.2.1	Bounds and Other Accurate Stiffness Expressions	123
10.2.2	Test of Theory	123
10.3	Illustrative Examples	125
10.3.1	Composites with Spherical Particles (CSA_P)	126
10.3.2	Nearly CSA_P Composites	126
10.3.3	Phase Symmetric Composites	127
10.3.4	Eigenstrain/Stress versus Geometry	132
10.3.5	Porous Materials	132
10.4	Theory and Experiments	137
10.4.1	Some Irregular Geometries	137
10.4.2	Various Porous Materials	140
10.4.3	Sulphur Impregnated Cement/Silicate System	144
10.4.4	Salt Infected Bricks	146
10.4.5	Non-Flexible Particles in Particulate Composite	147
10.4.6	Defective Phase Contact in Concrete	149
10.4.7	Hydrating Cement Paste and Concrete	151
10.5	Conclusion	154
11	Simplified Composite Theory – Conductivity	155
11.1	Illustrative Example	155
11.1.1	On the Accuracy of Simplification	156
11.2	Applications	156
11.2.1	Thermal Conductivity of Fire-Brick	156
11.2.2	Electrical Conductivity of Binary Metallic Mixtures	156

11.2.3 Chloride Diffusion in Cement Paste System	158
11.3 Conclusion	161
12 Diagnostic Aspects of Theory	163
12.1 Stiffness	165
12.1.1 Examination of Stiffness Expressions	165
12.2 Conductivity	171
12.2.1 Examination of SCS-Expressions	171
12.3 Discussion	174
13 Aspects of Materials Design	177
13.1 Geometries versus Properties	177
13.2 Design	178
13.3 Illustrative Examples	178
13.3.1 Stiffness	178
13.3.2 Conductivity	180
13.4 Discussion	182
14 Viscoelasticity	183
14.1 Stress-Strain Relations	184
14.1.1 Analogy Young's Modulus	185
14.1.2 Vibrations	187
14.2 Models of Viscoelastic Materials	189
14.2.1 Simple Models	190
14.2.2 Less Simple Models	190
14.3 Summary, Analysis, and Approximate Analysis	195
14.3.1 Approximate Analysis	196
15 Viscoelastic Composites	199
15.1 Composite Analysis	200
15.1.1 Accurate Analysis	200
15.1.2 Approximate Analysis	200
15.2 Applications	202
15.2.1 Porous Materials and Stiff Pore Systems	203
15.2.2 Particulate Composite	203
15.2.3 Mature Cement Concrete	204
15.2.4 Young Concrete	210
15.2.5 Influence of Geometry on Viscoelastic Composite Behavior	210
15.2.6 Monomer Impregnated HCP and Porous Glass	215
15.2.7 Damping of Wood	218
15.3 Discussion	220
16 Final Remarks	221

A	Elasticity	223
A.1	Isotropy	223
A.1.1	Composite Aspects	223
A.1.2	Stress-Strain	223
A.2	Cubic Elasticity	224
A.2.1	Poly-Cubic Elasticity	225
A.2.2	Composite Aspects	226
B	Dilute Particulate Composites	227
B.1	Cubic Stiffness, Shape Parameters, and Stress	227
B.1.1	Particle Stress	228
B.1.2	Isotropic Stiffness, Shape Coefficients, and Stress	230
B.1.3	Particle Stress	230
C	SCS-Analysis	231
C.1	Stiffness	231
C.1.1	Spherical Particles	232
C.1.2	Various Particle Shapes and Cracks	233
C.1.3	Multi-Shaped Particles	234
C.2	Other Physical Properties	235
C.2.1	Spherical Particles	236
C.2.2	Particles of Various Shapes and Cracks	236
C.2.3	Multi-Shaped Particles	238
D	General Viscoelastic Models	239
E	HCP and Concrete	241
E.1	Volume Models	241
E.2	Porosity of Hardening Cement Paste	242
	Notations	245
	References	249

Introduction

In the past five decades considerable attention has been devoted to composite materials. A number of expressions have been suggested by which macroscopic properties can be predicted when the properties, geometry, and volume concentrations of the constituent components are known. Many expressions are purely empirical or semi-theoretical. Others, however, are theoretically well founded such as the exact results from the following classical boundary studies:

Bounds for the elastic moduli of composites made of perfectly coherent homogeneous, isotropic linear elastic phases have been developed by Paul [1] and Hansen [2] for unrestricted phase geometry and by Hashin and Shtrikman [3] for phase geometries, which cause macroscopic homogeneity and isotropy.

The composites dealt with in this book are of the latter type. For two specific situations (later referred to), Hashin [4] and Hill [5] derived exact solutions for the bulk modulus of such materials. Hashin considered the so-called Composite Spheres Assemblage (CSA) consisting of tightly packed congruent composite elements made of spherical particles embedded in concentric matrix shells. Hill considered materials in which both phases have identical shear moduli.

In the field of predicting the elastic moduli of homogeneous isotropic composite materials in general the exact Hashin and Hill solutions are of theoretical interest mainly. Only a few real composites have the geometry defined by Hashin or the stiffness distribution assumed by Hill. The enormous significance, however, of the Hashin/Hill solutions is that they represent bounds which must not be violated by stiffness predicted by any new theory claiming to consider geometries in general.

For a variety of other composites (than Hashin/Shtrikman/Hill) other theoretically well-founded analytical methods have been developed for strictly defined specific phase geometries. Examples are: Ellipsoidal particles in a continuous matrix are examined by Christoffersen [6] and Levin [7]. Other particulate composites are considered in [8–12]. A special particulate composite with compacted spherical particles is examined by Budiansky in [13].

Special fiber reinforced materials are examined by Stang [14], and so-called graded composite materials are considered in [15,16].

Early composite theories based on statistically defined phase geometries are reviewed in [17]. Such approach, using statistical continuum theories, has been further developed by Torquato in [18,19].

If real geometry and theoretically assumed geometry agree with each other excellent results can very often be obtained by the methods just mentioned. Many real composites, however, have geometries, which are substantially different from any of the geometries considered in prediction methods known to day. Composites geometry will change – not only from type of composite to another type – but also in composites individually. First of all, it is very likely that the geometry of material components will vary with phase concentration. This means, for example, that a method for stiffness prediction applying at one concentration is not necessarily the right one to use at another concentration.

This feature is illustrated in Fig. 1.1 showing the influence of porosity on the stiffness of real porous systems such as tile and hardened cement paste. Very often a final critical porosity of 55–75% is approached where stiffness becomes zero. Obviously the critical porosity indicates the extreme state of a continuous process of geometry transformation where the solid phase is increasingly separated and surrounded by an increasing amount of pores. No model with fixed geometry can be used to predict stiffness of porous material. For this reason most relations to day between stiffness of porous materials and porosity are still the empirical expressions developed in [20–22] for

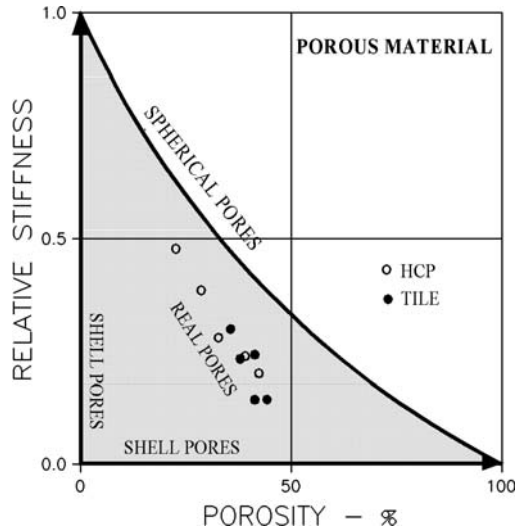


Fig. 1.1. Stiffness of isotropic porous materials as related to pore shapes. Dots are various experimental data reproduced from Chap. 10

example. Only empirical relations are qualified which do not violate the shaded area in Fig. 1.1 bounded by the theory of Hashin [4] previously referred to.

In itself the large number of completely different empirical stiffness expressions suggested for porous materials clearly indicates a need for a more rational research on composite properties versus composite geometry such as reported by the present author in a study [23] on porous materials and impregnated materials.

Change of geometry will influence any mechanical/physical behavior of composites. Stiffness and viscoelasticity (creep and relaxation) will change. Shrinkage and eigenstress-strain (such as hygro-thermal) properties, and heat conductivity are other examples of materials behavior, which will change with geometry.

In order to cope rationally with such changes in composite analysis we must increase our freedom to choose other analytical models than the specific, non-variable ones most often used to day. Valuable progress in materials science can then be achieved in areas, such as a better understanding of the behavior of natural composites, a more rational improvement of such composites, and a rational design of new materials.

Some ideas on how to obtain such freedom are presented by the author in [24] where it is shown that “global” property relations for composites can be established with geometry considered by independent variables, so-called shape functions, which can be studied separately with respect to specific geometries (discrete, continuous, etc).

Aspects of the same problem, how to construct a composite geometry such that prescribed properties can be obtained, have been studied by Milton [25] who introduced the term “inverse homogenization problem” for such composite analysis. Sigmund [26, 27] approaches the problem of inverse homogenization numerically looking at basic porous material structures made by trusses and plates. Milton and Cherkaev [28] provide a basis for studying the problem through analytical studies and construction of so-called extreme materials.

Modern numerical solution techniques such as Finite Element Methods (FEM) have had a tremendous impact on the research on composite materials. These techniques introduced into composite analysis in the 1970es [29, 30] have proved themselves to be very efficient tools in handling composite problems of a complexity (e.g. [31–36]) far beyond what can be treated by analytical means. Recently, numerical methods have also proved their potentials with respect to optimization between shape and properties of structures [37, 38] and between geometry and properties of some special orthotropic composites [39]. Such studies are very useful in the research of optimizing composite geometry in general with respect to composite properties. This feature has been recognized in the works of Sigmund [26, 27] previously referred to.

1.1 Objectives of This Work

In summary, the main objectives of this book are to increase our general understanding of the influence of composite geometry on composite behavior. Some good reasons for increasing our knowledge on geometry versus behavior of composite materials have already been mentioned. Examples are: A better understanding is obtained on the mechanical/physical behavior of natural composites, and a more rational basis is achieved for improving such materials. Geometrical potentials are revealed for the benefit of new materials design with respect to prescribed properties.

As can be noticed from the literature previously cited, other composite researchers agree, that research is necessary on the significance of composite geometry. A number of ways have been applied to approach the problem. Important works have been reported which are based on very strict descriptions and studies (analytical or FEM) of composite geometries, statistically defined (as in [18]), or arranged from basic microstructures (as in [26, 28]). Fine results can be expected from such studies using continuum mechanics on microstructures the geometries of which are basically fixed.

The author's approach presented in this book has another point of departure with respect to "real" composite geometry: It is recognized that varying phase geometries produced by nature or by man can not in general be described (or defined) very precisely. A description must reflect deductions made from experimental studies primarily, including such, which consider technologies used to produce composites.

Basically the methods presented are further developments of the ideas presented in [23, 24, 40] of predicting the properties of any composite material from global expressions with general composite geometries considered by so-called geometry functions. Such functions are presented with specific composite geometries reflected by so-called shape functions. Geometries quantified by these functions are shown to be consistent with the overall composite assumptions previously made with respect to macroscopical homogeneity and isotropy.

Shape functions are developed for a variety of composites including such with geometries previously considered in the literature. Also considered are the somewhat self-defining geometries, which appear in so-called SCS-analysis of composites (Self-Consistency-Scheme).

Special composite problems/properties considered are stiffness, shrinkage, hygro-thermal behavior, viscoelastic behavior, and internal stress states – as well as other physical properties of composites such as thermal and electrical conductivities, diffusion coefficients, dielectric constants and magnetic permeabilities.

The theoretical results obtained are verified by a FEM-analysis made by the author and by theoretical results obtained by other authors. The principal success criteria, however, for the methods developed are that the results

predicted comply with data obtained from experiments on real composites as these data are reproduced from the composite literature.

As a spin-off result the composite theory developed is re-organized to become a “diagnostic tool”, useful in materials design and in quality control of empirical or semi-theoretical prediction methods suggested in the field of composite materials (are such methods consistent with “promises” made with respect to geometry and isotropy).

1.1.1 Summary of Composites Considered

We re-call that the composites primarily considered in this book are perfectly coherent two-phase materials with phase geometries causing macroscopic homogeneity and isotropy. Both phases are isotropically linear-elastic (or -viscoelastic).

Flexible phase geometries primarily are considered which can adjust themselves to form a tight composite. The adjustment can be natural (as in suspensions) or organic (as in bone structures) or it can be the result of compaction (as in sintered powder composites).

As in most literature on composite materials the terms composite, composite material, and two-phase material are used synonymously – unless otherwise indicated as in minor sections of this book where composites in practice do not behave “theoretically”:

When phase geometries are not flexible (such as in composites made of stiff particles in a solidifying matrix as concrete for example) air voids are inevitable at certain concentrations. The two-phase material originally considered becomes a porous two-phase material. In practice such a material can be considered as a normal two-phase composite with a porous matrix. This feature is explained in further details in Sect. 10.4 together with some other composite “defects” (such as incomplete impregnation and incomplete phase contact), which can also be considered introducing some simple phase modifications.

Classification of Composites

A systematic classification of composites is a necessity in any discussion and analysis of, how the mechanical and physical properties of composites are influenced by their internal geometries. A model is suggested in this book by which basic isotropic composite geometries can be classified continuously as stages in a process of geometry transformation where one phase changes from spheres to spherical shells (“anti-spheres”) – while the other phase in a complementary way transforms from spherical shells to spheres.

Spherical shapes and spherical shell shapes are the most extreme geometries when isotropic composites are considered. Arguments for accepting this geometrical concept can be found in the work of Hashin and Shtrikman [3] on bulk stiffness bounds for isotropic composites. One H/S-bound is the exact solution to stiffness of a composite where one phase has the geometry of spheres. The other H/S-bound is the exact solution to stiffness of a composite where the other phase has the geometry of spheres.

2.1 Volume Concentrations

The most elementary information needed to quantify a composite is its content of constituent phases. In the analysis of composites with respect to mechanical and physical behavior it is very appropriate to quantify the content of a certain phase by its volume fraction relative to the composite volume. It is implicitly understood in this book that concentration c means volume fraction of phase P as defined in (2.1) where volumes are indicated by V . Phase S concentration is then $1 - c$.

$$c = \frac{V_P}{V_P + V_S}(\text{phase P}) ; \quad 1 - c = \frac{V_S}{V_P + V_S}(\text{phase S}) \quad (2.1)$$

On the basis of phase concentrations, material property bounds can be developed assuming that phase geometries take their most extreme, opposite

shapes: Parallel lamella for anisotropic composites – and sphere/shell geometries for isotropic composites. No more information can be achieved on the behavior of composites unless additional information is given on internal geometry.

Information on phase geometry is just as essential as concentration is. In some cases it is even more important. A very simple example will demonstrate this statement: A cracked material is a porous material with pores (phase P) having an extremely flat geometry of no volume, meaning $c = 0$. Stiffness (and strength) of this material is not at all equal to stiffness and strength of the original un-cracked material which, of course, also has a porosity of $c = 0$. From an elastic point of view it is more appropriate to compare the cracked material with a material with spherical pores of diameters equal to crack diameters in the original material. Thus a real porous material can easily be a “better” material than a material that is thought to be non-porous.

2.2 Geometry at Fixed Phase Concentrations

At fixed phase concentrations composites can be classified according to their internal geometry as stylized in Fig. 2.1. A phase with continuous geometry (C) is a phase in which the total composite can be traversed without crossing

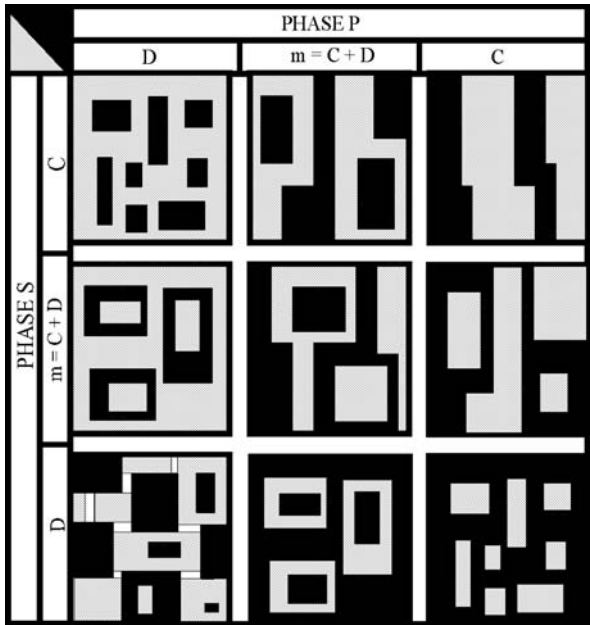


Fig. 2.1. Phase geometries in two-phase materials. C , D and $m(= C + D)$ denote continuous geometry, discrete geometry, and mixed geometry respectively

the other phase. This is not possible in a phase with discrete geometry (D). A mixed geometry (m) is a continuous geometry with some discrete elements. It is noticed that there are only eight possibilities of mixing phase P and phase S. A mixture where both phases are discrete is not possible.

2.2.1 Geometrical Classification

Figure 2.2 is used in this work as a simplified classification scheme for composite geometries at fixed volume concentrations c . The former and the latter letter used in combinations indicate phase P and phase S geometry respectively.

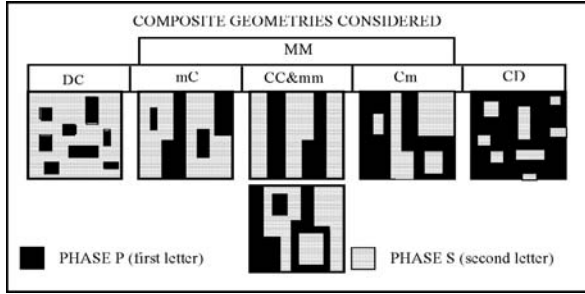


Fig. 2.2. Simplified scheme of geometry classification

- DC means that phase P appears as discrete elements in a continuous phase S.
- MM is a common descriptor for geometries mC, CC, mm, and Cm defined in Fig. 2.1. Continuous elements are always present in MM. Especially is observed that CC geometries (mixtures of two fully continuous phases) subsequently will be grouped, operationally, as composites with MM geometries¹.
- CD means that phase P appears as continuous elements in a discrete phase S.

Combinations Dm and mD are not considered in this classification scheme. They are anticipated to appear in very narrow transition geometries, which are very rare relative to other combinations, found in practice (just think of a concrete made with aggregates which are both surrounded and filled with mortar).

¹ Occasionally the signature CC will be used subsequently instead of MM. Only, however, if MM in fact stands for a mixture of two fully continuous phases.

2.3 Composites with Variable Geometry

Any of the geometry combinations considered in Sect. 2.2 can be thought of as stages in a process of geometry transformation, where phase P transforms organically from having a compact discrete geometry to having a continuous geometry. In a complementary way phase S transforms simultaneously from having a continuous geometry to having a compact discrete geometry.

The variable composite geometry just outlined can be illustrated as shown in Fig. 2.3 where the critical concentrations c_P and c_S indicate geometrical transitions between MM geometries and the geometry of phase P being fully continuous with fully discrete phase S particles (CD geometry) at c_P – and the geometry of phase S being fully continuous with fully discrete phase P particles (DC geometry) at c_S . The critical concentrations illustrated in Fig. 2.3 are real (inside $c = 0 - 1$). Formally, however, they can also be non-real (outside $c = 0 - 1$). This feature is demonstrated shifting the movable geo-cylinders outlined in Fig. 2.4. Examples: If $c_S < 0$ then a MM-composite is described at low concentrations. If $c_P > 1$ then a MM-composite is described at high concentrations. If $c_S < 0$ and $c_P > 1$, then a composite is described which has a MM-geometry at any concentration.

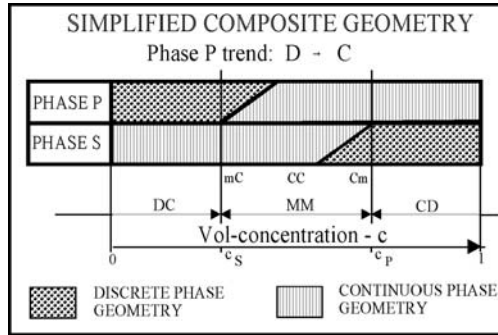


Fig. 2.3. Composite geometry when phase P goes from D to C

2.3.1 Geometrical Classification

Various geometrical compositions can be illustrated by the model illustrated in Fig. 2.4 where the movable “geometry cylinders” help us to classify composites as shown in (2.2).

$$\begin{array}{ll}
 \text{DC-DC} & \text{MM-MM} \\
 \text{DC-MM} & \text{MM-CD} \\
 \text{DC-CD} & \text{CD-CD}
 \end{array}
 \quad \left(\begin{array}{l} \text{first two letters : geometry at } c = 0 \\ \text{last two letters : geometry at } c = 1 \end{array} \right) \quad (2.2)$$

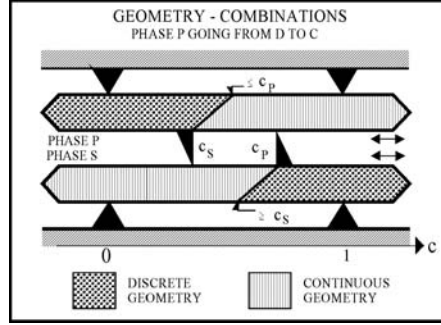


Fig. 2.4. Change of geometry. Various composites are defined by different positions of the movable geo-cylinders

Equation (2.2) is the main scheme of composite classification used in this book. It defines a composite by its geometries at $c = 0$ and $c = 1$. Critical concentrations required to “realize” these geometries are explained in Fig. 2.5. We re-call from Sect. 2.2.1 that CC geometries operationally are included in MM geometries.

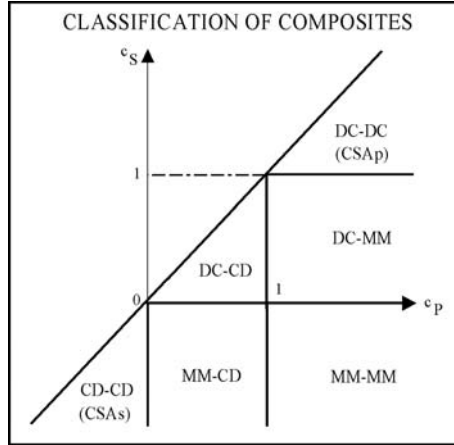


Fig. 2.5. Composite geometries as related to critical concentrations (CSA-geometries are explained in Sect. 2.3.2)

In principles the process of geometry-change proceeds as previously indicated in this chapter. For both natural and man-made composites, geometries change as the result of increasing the concentration of one phase on the expense of the other.

Remark: It is re-called at this point that it is assumed implicitly in this book that geometries change such that phase P varies on a path from discrete

geometry to continuous geometry (as in Figs. 2.3 and 2.4) unless otherwise indicated. The choice of phase numbering (P, S) in practice can always be chosen to agree with this assumption involving critical concentrations $c_P \geq c_S$.

Critical Concentrations

It is obvious that the critical concentrations previously defined are very important classification parameters. They are key-concentrations defining what concentrations are used to change phase P from discrete particles in a continuous S-matrix to the inverse of this geometry, namely discrete phase S particles in a continuous P-matrix. Real critical concentrations (in $c = 0 - 1$) are decided by technology (including appearance and size distribution of raw materials) used to produce composite materials.

To illustrate the latter statement: In a DC-CD composite such as a porous material the critical concentration c_S is that void concentration at which discrete voids start to interfere forming continuous geometries. Single sized voids will produce lower c_S than will aggregates (voids) with a smooth and continuous size distribution. At increasing void concentration the interference becomes so pronounced that the porous material loses its coherence (no stiffness, no strength) at a critical void concentration of c_P . The original porous material has become a composite with solid particles dissolved in a “void matrix”.

Remark: It has been mentioned that critical concentrations can be real (inside $0 - 1$) or they can be non-real (outside $0 - 1$). It is emphasized that the latter concentrations are fictitious having no physical meanings others than indicating directions of geometrical trends.

Percolation, Permeability, Impregnability

The discussion of composites geometry is closely related to the study of percolation in composites. Percolation theory considers the connectivity of a phase across a microstructure [41, 42]. A minor study on connectivity as related to the geometrical classification of composites has been made by the author in [43]. Transport properties of composite materials were considered such as permeability and impregnability of porous materials.

The relation between geometrical classification and connectivity is outlined in Fig. 2.6 with so-called percolation graphs. When the material considered in the figure has an empty phase P (pores) we notice that the material is not impregnable in $c = 0 - c_S$. It is partly impregnable in $c = c_S - 0.4$, and it is fully impregnable in $c = 0.4 - 1$. In $c = c_P - 1$, however, the porous material breaks down because of no coherence. As noticed from Fig. 2.7 the percolation graphs can easily be converted to volume concentrations of continuous phases.

The concept of connectivity has recently been used by Bentz in [44] to relate the microstructure of cement paste to the amount of cement hydrated.

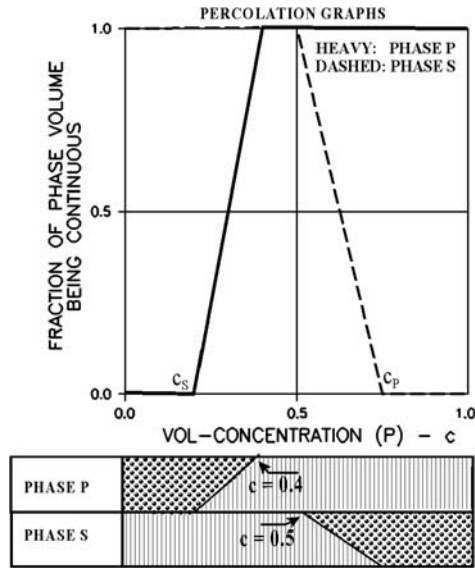


Fig. 2.6. An example of Percolation graphs for phase P and phase S respectively

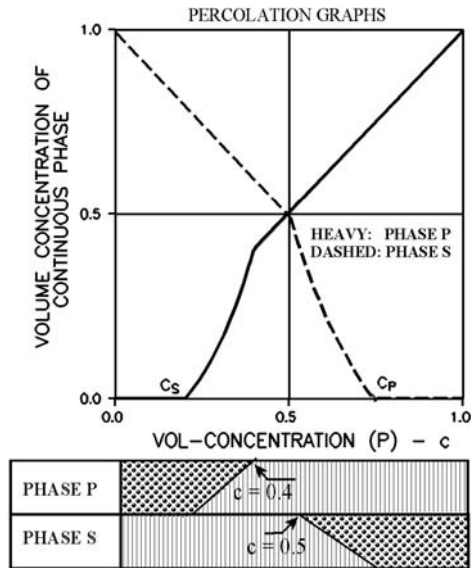


Fig. 2.7. Concentration of continuous parts of phase P and phase S respectively. Example from Fig. 2.6

2.3.2 Some Composite Examples

Some composites may keep their geometrical type independently of volume concentrations. Normally, however, composites change their geometry with volume concentrations. Some examples of both types are considered in this section.

Composite Spheres Assemblage (CSA)

The Composite Spheres Assemblage shown in Fig. 2.8 is a theoretical model of a two-phase material introduced by Hashin [4]: Tightly packed congruent composite elements made of spherical particles embedded in concentric matrix shells. Two types of CSA-materials are subsequently referred to: A CSA_P -material has phase P particles and a phase S matrix at any concentration, which makes it a type DC-DC composite. A CSA_S -material, see subsequent Fig. 4.1, has phase S particles and a phase P matrix at any concentration which makes it a type CD-CD composite.

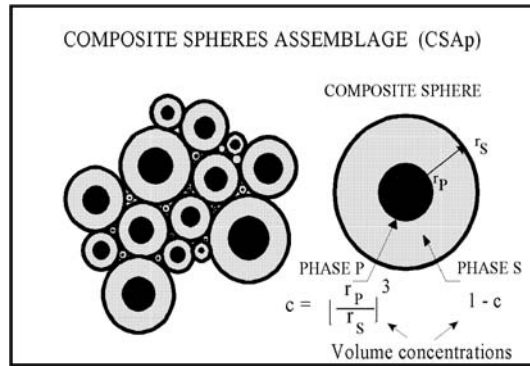


Fig. 2.8. Composite Spheres Assemblage with phase P particles (CSA_P)

Particulate Composites

At low concentrations a particulate composite is a mixture of discrete phase P particles in a continuous phase S (so-called matrix). An ideal particulate composite has a DC geometry at any concentration. This does not necessarily mean that the geometry at $c = 1$ is exactly the same as at $c = 0$ (such as in the CSA-composites previously considered).

Shapes may change considerably within a certain type classification. New shapes may be formed, for example, by particle agglomeration. Ideal particulate composites are classified as DC-DC composites. Very often the term, particulate composite, is kept even if phase P particles grow together at higher

concentrations such that MM and CD geometries are formed. Thus, the term particulate composite is frequently used as a somewhat inaccurate common descriptor for any DC-DC, DC-MM, and DC-CD composite.

Special particulate composites are fiber-reinforced materials. The fibers can be straight or shaped like pearls on a string (rugged fibers). Other particulate composites considered in this book are disc-reinforced materials. The discs can be plain (pennies) or shaped like a jelly-fish (frayed discs), or shaped like fried eggs (rugged discs).

Lamella Composites (Incl. Crumbled Foils)

A lamella composite is the result of mixing two phases the geometries of which are continuous at any concentration. Lamella composites (ribbons, long fibers, sheets, and foils included) can be the results of mixing lamella shaped phase P elements into a continuous phase S. They can also be the results of compacting a mixture made of phase P lamella and phase S lamella. Lamella composites are type CC composites at any concentration, which make them of the CC-CC type. When equal types of phase P and phase S geometries are used lamella composites are likely to become phase-symmetric as explained below.

A special lamella material considered in this book is a so-called “Pearls on a string” composite with lamella geometries like interconnected compact particles. Both pearls on a thin string and pearls on a thick string are considered. Also considered is a special lamella composite, the “Crumbled foils” composite with both phases having the shapes of crumbled foils (or sheets).

Powder Composites

A powder composite is the result of compacting a mixture of two powders. At low concentrations (of phase P) such a composite appear as a type DC composite. At high concentrations it is a type CD composite. When equally shaped powders are used, powder composites are likely to become phase-symmetric as explained below. In general powder composites are of type DC-CD. In the terminology used in this book powder composites are special particulate composites.

Phase-Symmetric Composites

Phase-symmetric composites have geometries which are symmetric with respect to $c = 0.5$: The type of composite geometry at $c = 0.5 - \Delta c$ (fx DC) equals the symmetric type of composite geometry at $c = 0.5 + \Delta c$ (CD). Composites qualifying to be phase-symmetric are types DC-CD and MM-MM (including CC-CC).

Porous Material and Impregnable Material

The geometry of pores in a porous material changes with porosity (c). Pores are not impregnable at $c < c_S$, see Figs. 2.6 and 2.7. Pores start being impregnable at $c = c_S$ and become increasingly impregnable as $c = c_P$ is approached. A 100% impregnability is guaranteed beyond $c = c_P$. Then, however, the porous material is not coherent as in bricks which cannot in general be produced with porosities higher than $c = c_P \approx 70\%$ without losing their strength and stiffness. A pore system with pearls on a string geometry is a transition system between a discrete pore system and a continuous pore system. The strings are so-called bottlenecks.

Preliminaries on Stress/Strain

Some basic expressions are presented in this chapter, which are subsequently used to predict composites behavior as influenced by variable geometry. A consistent composite analysis is ensured when these basic expressions are used properly. In the present context consistency means that predicted stiffness, for example, does not violate the Hashin/Shtrikman bounds [3] (H/S) presented in (3.1) and illustrated by solid lines in Figs. 3.1 and 3.2. Prediction methods are no good which involve violation of these bounds, even if they predict stiffness which do not violate the Poul/Hansen bounds [1,2] (P/H) presented in (3.2) and illustrated by dashed lines in Figs. 3.1 and 3.2. (In the presentation of bounds just made both Poisson's ratios $\nu_P = \nu_S = 0.2$ have been assumed).

$$\frac{n+1+c(n-1)}{n+1-c(n-1)} \leq e \leq n \frac{2+c(n-1)}{2n-c(n-1)} \begin{cases} \text{Isotropic bounds for } n \geq 1 \\ \text{reverse } \leq \text{ when } n < 1 \end{cases} \quad (3.1)$$

$$1 + (n-1)c \geq e \geq \frac{n}{n - (n-1)c} \quad \text{Anisotropic bounds} \quad (3.2)$$

The symbols used have the following meanings: Stiffness ratio is $n = E_P/E_S$. Relative Young's modulus of composite is $e = E/E_S$. Young's modulus of phase P, phase S, and composite are E_P , E_S , and E respectively.

3.1 Stiffness

Hill [5] has shown that the remarkably simple relations presented in (3.3) exist between averages (by volume) of stresses, strains, and stiffness of homogeneous (not necessarily isotropic) composite materials consisting of homogeneous and isotropically elastic components.

$$\begin{aligned} \sigma_{kk} &= (1-c)\sigma_{Skk} + c\sigma_{Pkk} & s_{ij} &= (1-c)s_{Sij} + cs_{Pij} \\ \varepsilon_{kk} &= (1-c)\varepsilon_{Skk} + c\varepsilon_{Pkk} & e_{ij} &= (1-c)e_{Sij} + ce_{Pij} \\ \varepsilon_{Pkk} &= \frac{\sigma_{Pkk}}{3K_P} & \varepsilon_{Skk} &= \frac{\sigma_{Skk}}{3K_S} & e_{Pij} &= \frac{s_{Pij}}{2G_P} & e_{Sij} &= \frac{s_{Sij}}{2G_S} \end{aligned} \quad (3.3)$$

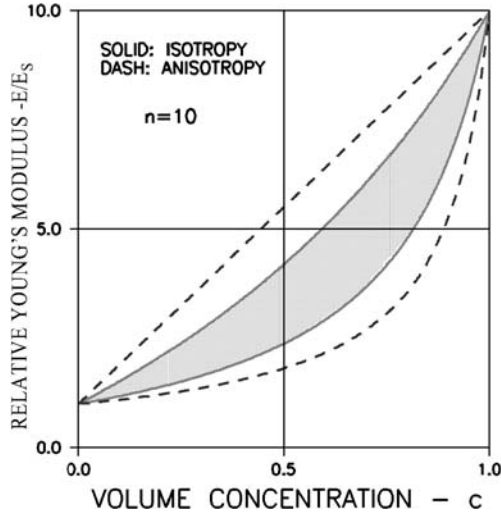


Fig. 3.1. Shaded area is range of stiffness for isotropic composites

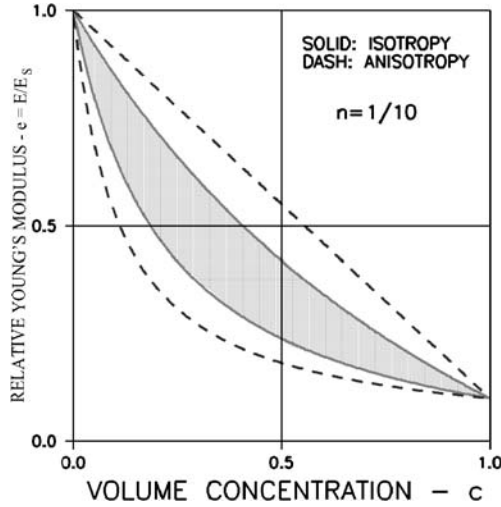


Fig. 3.2. Shaded area is range of stiffness for isotropic composites

The symbols used have the following meanings: σ_{kk} is volumetric stress, s_{ij} is deviatoric stress, ε_{kk} is volumetric strain, e_{ij} is deviatoric strain. K is bulk modulus, and G is shear modulus. As before, subscripts P and S indicate phase of composite. No subscripts P and S indicate overall (average) stresses and strains of composite.

The expressions in (3.3) form the basis of the author's stiffness analysis of composites made in this book. They can be organized as follows,

$$\varepsilon_{kk} = \frac{\sigma_{kk}}{3K_S} + c \sigma_{Pkk} \left(\frac{1}{3K_P} - \frac{1}{3K_S} \right); \quad e_{ij} = \frac{s_{ij}}{2G_S} + cs_{Pij} \left(\frac{1}{2G_P} - \frac{1}{2G_S} \right) \quad (3.4)$$

from which the stiffness of isotropic composites can be obtained introducing the overall isotropic stress-strain relations,

$$\varepsilon_{kk} = \frac{\sigma_{kk}}{3K}; \quad e_{ij} = \frac{s_{ij}}{2G} \quad (3.5)$$

The results are the following simple expressions, which tell that composite stiffness can be predicted from knowing the average stress (or strain) in phase P.

$$\begin{aligned} k &= \frac{K}{K_S} = \left[1 + c \frac{1 - n_k}{n_k} \frac{\sigma_{Pkk}}{\sigma_{kk}} \right]^{-1} = 1 + c(n_k - 1) \frac{\varepsilon_{Pkk}}{\varepsilon_{kk}} \\ g &= \frac{G}{G_S} = \left[1 + c \frac{1 - n_g}{n_g} \frac{s_{Pij}}{s_{ij}} \right]^{-1} = 1 + c(n_g - 1) \frac{e_{Pij}}{e_{ij}} \end{aligned} \quad (3.6)$$

The symbols used, $k = K/K_S$ and $g = G/G_S$, are relative bulk modulus and relative shear modulus respectively. Bulk stiffness ratio is $n_k = K_P/K_S$. Shear stiffness ratio is $n_g = G_P/G_S$.

Remarks: It is emphasized that any expression mentioned above and subsequent expressions derived from them are exact, meaning for example, that exact stiffness is predicted if the exact phase P stress is known. It is furthermore noticed that stiffness (K_C, G_C) of cubical composites, with stress/strain planes coinciding with planes of elastic symmetry are also described by (3.6). We only have to replace (k, g) with $(k_C = K_C/K_S, g_C = G_C/G_S)$. Cubic elasticity is considered in Appendix A at the end of this book.

It is noticed that the simple anisotropic P/H bounds are described by (3.6) introducing a homogeneous stress condition ($\sigma_P/\sigma = 1$) and a homogeneous strain condition ($\varepsilon_P/\varepsilon = 1$) respectively.

Curiosum: With Poisson's ratios ν_P and ν_S the following expression (to be used in Appendix B) can also be derived from (3.3). It applies also for both isotropic composites and cubical composites.

$$\begin{aligned} e &= \frac{E}{E_S} = \left[1 + c \frac{1 - n}{n} \frac{S_{Pii}}{\sigma_{ii}} \right]^{-1} \quad \text{when } n = \frac{E_P}{E_S} \quad \text{and} \\ S_{Pii} &= \frac{1 + \nu_P - n(1 + \nu_S)}{1 - n} \sigma_{Pii} - \frac{\nu_P - n\nu_S}{1 - n} \sigma_{Pkk} \quad (ii = 11, 12, 33) \end{aligned} \quad (3.7)$$

3.1.1 Dilute Suspension

At very low phase P concentration (dilute suspension) where there is no interaction between phase elements (3.6) can be written as follows where superscript 0 indicates stress at vanishing concentration c .

$$\frac{1}{k} = 1 + c \frac{1 - n_k}{n_k} \frac{\sigma_{Pkk}^0}{\sigma_{kk}}; \quad \frac{1}{g} = 1 + c \frac{1 - n_g}{n_g} \frac{s_{Pij}^0}{s_{ij}} \quad (3.8)$$

Example: From the Goodier's and Dewey's analysis [45, 46] of a spherical particle in an infinite matrix we have

$$\begin{aligned} \frac{\sigma_{Pkk}^0}{\sigma_{kk}} &= \frac{n_k(1 + \kappa_S)}{n_k + \kappa_S} (= f_k(E_P, E_S, \nu_P, \nu_S)) \\ \frac{s_{Pij}^0}{s_{ij}} &= \frac{n_g(1 + \gamma_S)}{n_g + \gamma_S} (= f_g(E_P, E_S, \nu_P, \nu_S)) \end{aligned} \quad (3.9)$$

where κ_S, γ_S are Poisson parameters defined in Appendix A and f_k, f_g are so-called stress functions. The stiffness of a dilute suspension with spherical particles is now predicted as follows from (3.8).

$$\frac{1}{k} = 1 + \frac{(1 + \kappa_S)(1 - n_k)}{n_k + \kappa_S} c; \quad \frac{1}{g} = 1 + \frac{(1 + \gamma_S)(1 - n_g)}{n_g + \gamma_S} c \quad (3.10)$$

3.2 Stress

Equation (3.6) can be used as follows for stress prediction when stiffness is known.

$$\frac{\sigma_{Pkk}}{\sigma_{kk}} = \frac{1/k - 1}{c(1/n_k - 1)}; \quad \frac{\sigma_{Skk}}{\sigma_{kk}} = \frac{1/n_k - 1/k}{(1 - c)(1/n_k - 1)} \quad (3.11)$$

$$\frac{s_{Pij}}{s_{ij}} = \frac{1/g - 1}{c(1/n_g - 1)}; \quad \frac{s_{Sij}}{s_{ij}} = \frac{1/n_g - 1/g}{(1 - c)(1/n_g - 1)} \quad (3.12)$$

Stresses in general (σ_{ij}) are determined from Appendix A combining these expressions. Stress prediction is exact if exact stiffness properties are known.

3.3 Composite Stiffness Estimated by SCS

The stress functions, f_k and f_g , defined in (3.9) can be used to estimate phase P stress in general if the phase S properties are replaced with the composite properties (not yet known). This method of generalizing a dilute suspension stress to apply at any phase P concentration is the basis of so-called SCS-estimates (Self Consistency Scheme), which can be made for the behavior of composite materials.

A numerical SCS-analysis is developed in Appendix C at the end of this book. It is based on (3.6) with phase P stresses introduced by numerically determined SCS-estimates. Composites are considered with mixtures of ellipsoidal particles of arbitrary shapes. Results of applying the SCS-analysis on stiffness of porous materials with voids of various shapes are presented in Fig. 3.3.

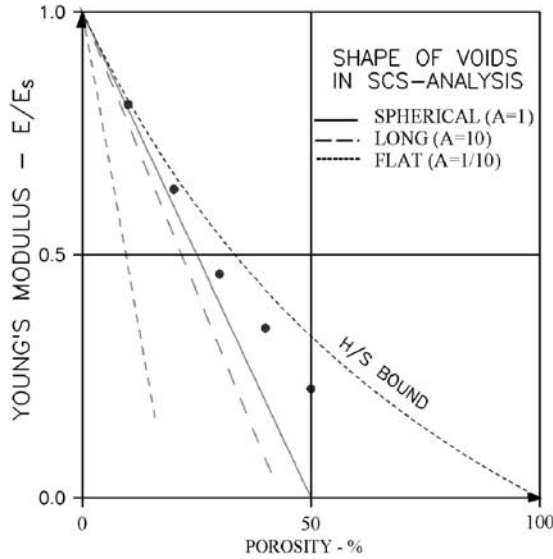


Fig. 3.3. Stiffness of porous materials predicted by SCS. The pores are ellipsoidal of various shapes (aspect ratio A is length of void relative to its diameter). Experimental data are from tests on porous sintered Aluminum [22]

Closed analytical SCS-solutions for various aspects of the mechanical/physical behavior of composites with special uni-shaped particles have previously been presented in the literature: Spherical particles were considered by Landauer, Böttcher, and Budiansky in [13,47,48], extremely thin discs were considered by Bruggeman in [49], and extremely long fibers were considered by Van Beek in [50].

Obviously a SCS-solution is accurate at low phase P concentrations (dilute suspensions). In Fig. 3.3 this feature is observed by noticing that the SCS-solution for a spherical pore system coincides with the H/S bound at low concentrations, (it is subsequently shown in this book that the stiffness of porous CSA_P composites is very well predicted with the upper H/S-bound).

The approximate nature of stiffness estimates by SCS at higher phase P concentrations must be emphasized. In general the SCS-analysis works on self-defined geometries the real shapes of which can, at the present time, only be guessed upon. It is demonstrated in Appendix C (as indicated in Fig. 3.3 that any deviation from spherical pores will cause lower SCS stiffness predictions than the prediction obtained with spherical pores. Thus, the experimental data [22] in Fig. 3.3 cannot be better described by SCS than by assuming that the pores are spherical voids.

Remarks: It is obvious that the success of the SCS-method to predict stiffness of composites in practice depends on how much the geometry in practice resembles the self-defined geometry made by the SCS-analysis. Obviously the

real pore system of the porous aluminum considered in Fig. 3.3 has a geometry, which disagrees with the SCS-geometry at higher porosities. Thus, SCS-methods cannot in general be used as a “tool” in the research on composite materials behavior versus composite geometry. This statement applies also for modified SCS-methods where “new particles” are defined as the original ones surrounded by some matrix (e.g. [51]).

Composite Stress and Geometry

It has been shown in Chap. 3, (3.6), that any stiffness modulus of isotropic composite materials can be predicted if stress is known for one of the constituent phases. Therefore, the analysis of stiffness versus phase geometry is basically an analysis of internal stresses as a function of phase geometry.

In this chapter a method is developed by which consistent estimates can be given on stress versus geometry as classified in Chap. 2 for various types of composites. The term, consistent, means that the stress estimates presented agree with exact quantities whenever such are known from the literature on composite materials – and that the stiffness predictions subsequently made in Chap. 5 do not violate the H/S bounds previously referred to.

4.1 Volumetric Stress

As previously stated, the most extreme, opposite phase geometries to think of when isotropic composites are considered, are defined by the CSA_P geometry illustrated in Fig. 2.8 and the CSA_S geometry illustrated in Fig. 4.1. This feature forms the basis in this chapter to establish consistent stress solutions for any isotropic composite.

4.1.1 CSA-Composites

The phase P stress in a CSA_P -material can easily be derived from Hashin [4], Goodier [45], or Sokolnikoff [52]. The result can be written as shown in the first expression of (4.1). The second expression is the phase S stress derived by the equilibrium expression in (3.3). The Poisson parameter κ_S is a function of the Poisson's ratio ν_S as explained in Appendix A.

$$\left. \begin{aligned} \frac{\sigma_{Pkk}}{\sigma_{kk}} &= \frac{n_k(1 + \kappa_S)}{n_k + \kappa_S[1 + (n_k - 1)c]} \\ \frac{\sigma_{Skk}}{\sigma_{kk}} &= \frac{n_k + \kappa_S}{n_k + \kappa_S[1 + (n_k - 1)c]} \end{aligned} \right) CSA_P \text{ geometry} \quad (4.1)$$

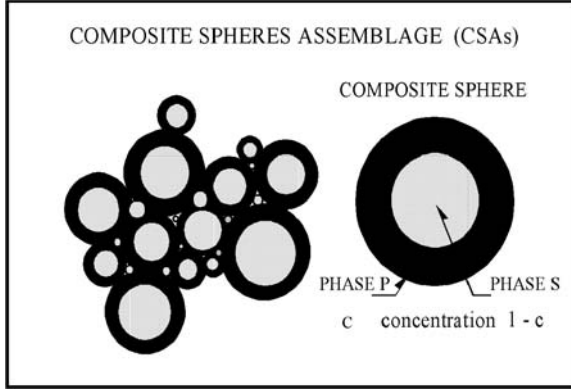


Fig. 4.1. Composite Spheres Assemblage with phase S particles of concentration $1 - c$ (CSA_S)

The stress state of a CSA_S material can be obtained from the CSA_P stresses in (4.1) by subscript interchange, $(S, c, n_k, \kappa_S) \Leftrightarrow (P, 1 - c, 1/n_k, \kappa_P)$. The results are presented in (4.2).

$$\left. \begin{aligned} \frac{\sigma_{Pkk}}{\sigma_{kk}} &= \frac{1 + n_k \kappa_P}{1 + \kappa_P[1 + (n_k - 1)c]} \\ \frac{\sigma_{Skk}}{\sigma_{kk}} &= \frac{1 + \kappa_P}{1 + \kappa_P[1 + (n_k - 1)c]} \end{aligned} \right\} \text{CSA}_S \text{ geometry} \quad (4.2)$$

It is observed, see [24], that (4.1) and (4.2) can be given a common formulation as shown in (4.3) where the parameter $\theta_k = \kappa_S$ when phase P has the geometry of spheres and $\theta_k = N_k \kappa_S$ when the phase P geometry is that of spherical shells. The modified stiffness ratio N_k introduced has the meaning given in (4.4) with Poisson parameters (κ) introduced from Appendix A.

$$\frac{\sigma_{Pkk}}{\sigma_{kk}} = \frac{n_k(1 + \theta_k)}{n_k + \theta_k[1 + c(n_k - 1)]} ; \quad \frac{\sigma_{Skk}}{\sigma_{kk}} = \frac{n_k + \theta_k}{n_k + \theta_k[1 + c(n_k - 1)]} \quad (4.3)$$

$$N_k = n_k \frac{\kappa_P}{\kappa_S} = n_g \quad \text{Modified stiffness ratio} \quad (4.4)$$

4.1.2 Any Composite – Geometry Function

The quantities $\theta_k = \kappa_S$ and $\theta_k = N_k \kappa_S$ express the boundaries of an area, described in (4.5) and illustrated in Fig. 4.2, where general geometry functions θ_k are found which generalize (4.3) to predict stresses in composites with any isotropic geometry following the arrows in Fig. 4.2 between the geometries of CSA_P and CSA_S .

$$N_k \leq \frac{\theta_k}{\kappa_S} \leq 1 \text{ when } N_k \leq 1 \text{ and } N_k \geq \frac{\theta_k}{\kappa_S} \geq 1 \text{ when } N_k > 1 \quad (4.5)$$

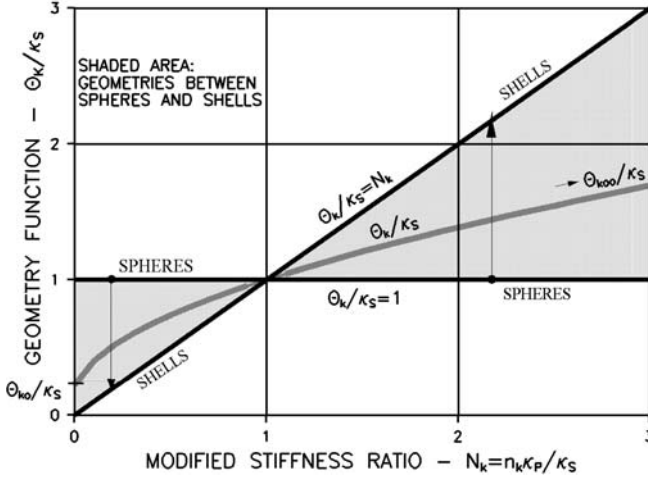


Fig. 4.2. Influence of phase P geometry on the geometry function θ_k (geo-function)

Any isotropic composite geometry is represented in Fig. 4.2 by its own geometry function θ_k . Because composites in general change geometry with volume concentrations, this statement is similar to saying that any volume concentration will have its own geo-function. Exceptions are geometry types, which are independent of concentrations such as in CSA composites. In these cases all volume concentrations have the same geo-function.

Remark: It follows from (4.3) and Fig. 4.2 that the volumetric stresses are independent of geometry when $n_k = 1$ and when $N_k = 1$ respectively. The latter observation is of special interest: It tells (because $N_k = n_g$) that volumetric stresses are independent of geometry when shear moduli of the constituent phases are the same. The consequence on bulk stiffness of this observation is discussed in Sect. 5.3.2.

4.1.3 Geometry Function and Shape Function

The stress solutions predicted by (4.3) with θ_k from (4.5) and Fig. 4.2 are consistent with the concept of composite materials being isotropic. At this time we do not know more about stress. Stress prediction still has to be related to type of composite as classified in Chap. 2.

As a first step to establish such relationship we observe that θ_k obviously is a function of not only n_k, v_P, v_S , but also of the more detailed geometry of phase P and phase S. We consider these geometries by so-called shape functions $\mu_{Pk} = \mu_{Pk}(c)$ and $\mu_{Sk} = \mu_{Sk}(c)$ respectively such that a geometry function (geo-function) can be described by the former expression in (4.6).

$$\theta_k = \theta_k(n_k, \nu_P, \nu_S, \mu_{Pk}, \mu_{Sk}) = n_k \theta_k(1/n_k, \nu_S, \nu_P, \mu_{Sk}, \mu_{Pk}) \quad (4.6)$$

Invariance with respect to phase numbering is ensured by the latter expression in (4.6), which is obtained from (4.3) claiming that the first expression (σ_P) must equal the latter expression (σ_S) when subscripts P and S are interchanged (including $c \Leftrightarrow 1 - c$).

The geometry function just defined is further restricted when specific composites are considered as they are classified in Chap. 2 according to their critical concentrations c_P and c_S . The influence of composite type on the geometry function is subsequently determined by looking at a composite where phase P can be extremely stiff ($n_k = \infty$) or it can be extremely soft ($n_k = 0$). The following expressions, derived from (4.3) (with some help from (3.3) with $K_P = n_k K_S$), tell about stress and strain in these two cases. θ_{k0} and $\theta_{k\infty}$ are limiting values of θ_k for $n_k \rightarrow 0$ and $n_k \rightarrow \infty$ respectively. $M = \lim(\theta_k/n_k)$ for $n_k \rightarrow \infty$ has a finite value between 0 and κ_P , see (4.5) with N_k from (4.4).

$$\begin{aligned} \text{Very soft P : } n_k = 0 &\Rightarrow \varepsilon_{Pkk} = \frac{\sigma_{kk}}{3 K_S} \frac{1 + \theta_{k0}}{\theta_{k0}(1 - c)} \\ \text{Very stiff P : } n_k = \infty &\Rightarrow \sigma_{Skk} = \sigma_{kk} \frac{1 + M}{1 + M(1 - c) + c \theta_{k\infty}} \end{aligned} \quad (4.7)$$

Equation (4.7) can be used to “calibrate” the geometry function to become consistent with the classification of composites made in Chap. 2. We simply compare this expression with the following general deductions, which can be made from considering the two types of composites defined above ($n_k \rightarrow 0$ and $n_k \rightarrow \infty$):

- Phase S is completely dissolved by phase P in $c \geq c_P$. This means that strain of a very soft phase P becomes infinite in $c \geq c_P$. The strain is finite in $c < c_P$.
- Phase P starts becoming continuous at $c = c_S$. This means that phase S stress becomes 0 in $c \geq c_S$ where phase P has become an extremely stiff skeleton. Stress is finite in $c < c_S$.

Equation (4.7) complies with these deductions only if θ_{k0} and $\theta_{k\infty}$ vary in principles as described in (4.8) and illustrated in Fig. 4.3. Also shown in Fig. 4.3 is $\theta_{k1} \equiv \kappa_S$ which is θ_k from Fig. 4.2 at $N_k = 1$.

$$\theta_{k0} = \begin{cases} \text{finite} ; c < c_P \\ \equiv 0 ; c \geq c_P \end{cases} ; \quad \frac{1}{\theta_{k\infty}} = \begin{cases} \text{finite} ; c < c_S \\ \equiv 0 ; c \geq c_S \end{cases} \quad (4.8)$$

A number of θ_k -expressions yield the conditions required in (4.5), (4.6), and (4.8). The relatively simple expression presented in (4.9) is a slightly modified version of an expression suggested in [24],

$$\theta_k = \frac{\kappa_S}{2} \left[\mu_{Pk} + \mu_{Sk} N_k + \sqrt{(\mu_{Pk} + \mu_{Sk} N_k)^2 + 4 N_k (1 - \mu_{Pk} - \mu_{Sk})} \right] \quad (4.9)$$

where the influence of geometry is decided by the shape functions $\mu_{Pk}(c)$ and $\mu_{Sk}(c)$ varying with phase geometry as outlined in (4.10) and Fig. 4.4.

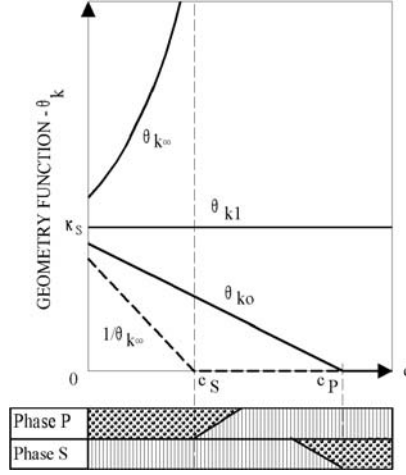


Fig. 4.3. The variation in principles of θ for two-phase materials with gradually changing phase geometry

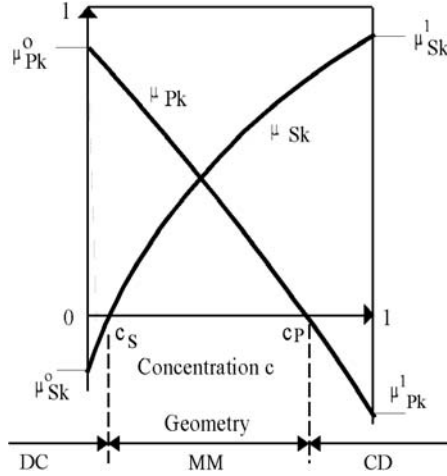


Fig. 4.4. Shape functions μ_{Pk} and μ_{Sk} are both ≤ 1

$$\begin{aligned} 1 \geq \mu_{Pk} \geq 0 & \quad \text{at } c \leq c_P ; \quad \mu_{Pk} < 0 \quad \text{at } c > c_P \\ 1 \geq \mu_{Sk} \geq 0 & \quad \text{at } c \geq c_S ; \quad \mu_{Sk} < 0 \quad \text{at } c < c_S \end{aligned} \quad (4.10)$$

4.1.4 Shape Functions – A Closer Look

It is noticed from (4.10) and Fig. 4.4 that DC, MM, and CD composite geometries are described by shape functions of magnitudes $(\mu_{Pk}, \mu_{Sk}) = (+, -)$, $(\mu_{Pk}, \mu_{Sk}) = (+, +)$, and $(\mu_{Pk}, \mu_{Sk}) = (-, +)$ respectively. These

properties of shape functions represent the basic geometrical “signals” sent to (4.3), through (4.9), that a special composite is considered.

Shape Factors

Shape function values of special interest are the so-called shape factors, $\mu_{Pk}^0, \mu_{Sk}^0 = \mu_{Pk}(0), \mu_{Sk}(0)$ quantifying the composite geometry of a P-S mixture with a dilute (vanishing) amount of phase P. In the subsequent text the term “shape factor” is also used for $\mu_{Pk}^1, \mu_{Sk}^1 = \mu_{Pk}(1), \mu_{Sk}(1)$. An important principal difference between the two set of shape factors is emphasized by sharpening (re-phrasing) the terms of definition: A composite geometry is quantified by μ_{Pk}^0, μ_{Sk}^0 at vanishing amounts of phase P, while it is quantified by μ_{Pk}^1, μ_{Sk}^1 at overwhelming amounts of phase P.

Special Shape Functions

CSA-geometries: It is immediately observed that the special DC and CD shape functions presented in (4.11) apply for the CSA_P and CSA_S composites.

$$\begin{aligned} \mu_{Pk} &\equiv 1 \text{ and } \mu_{Sk} \leq 0 \Rightarrow \theta_k = \kappa_S & (\text{CSA}_P \text{ geometry}) \\ \mu_{Sk} &\equiv 1 \text{ and } \mu_{Pk} \leq 0 \Rightarrow \theta_k = \kappa_S N_K & (\text{CSA}_S \text{ geometry}) \end{aligned} \quad (4.11)$$

Crumbled foils: The crumbled foils geometry, outlined in Fig. 4.5, is thought to present a plausible “mid-way” transition geometry of phase P changing organically from being spheres in CSA_P to being spherical shells in CSA_S .

The following hypothesis, stated in (4.12), is suggested for a crumbled foils composite: The shape functions are identically 0 such that the geo-function

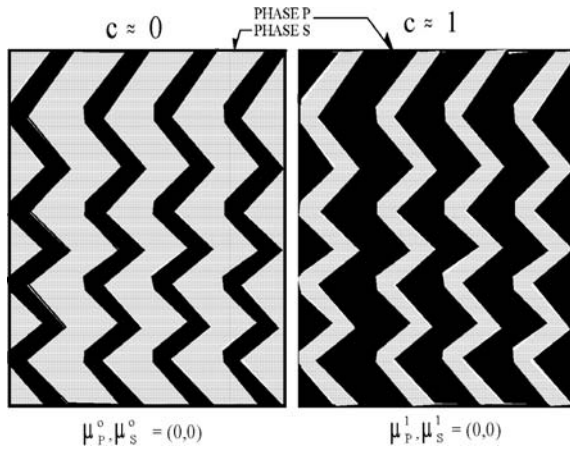


Fig. 4.5. Crude model of a crumbled foils composite. $\mu_p = \mu_s \equiv 0$ at any c

becomes the square mean of the geo-functions applying for the CSA composites presented in (4.11).

$$\mu_{Pk} = 0 \text{ and } \mu_{Sk} = 0 \Rightarrow \theta_k = \kappa_S \sqrt{N_k} \left(\begin{array}{l} \text{Crumbled foils geometry} \\ = \sqrt{\text{CSA}_P * \text{CSA}_S} \end{array} \right) \quad (4.12)$$

At several occasions the crumbled foils geometry is discussed in more details in subsequent sections of this book.

Outline of Shape Function Graphs

It has been explained in Chap. 2 that composites considered in this book have geometries changing along “stations” between the geometries of a CSA_P material and a CSA_S material. Possible shape functions are outlined in Fig. 4.6 for a composite, which starts up as a CSA_P material at low concentrations and ends as a CSA_S material at high concentrations. We will think of a processing technique, which can keep a CSA_P structure up to the first “dashed concentration” and then a less ideal DC structure up to the critical concentration c_S . In a similar way the technique used can keep a CSA_S structure after the second “dashed concentration” with a less ideal CD structure between this concentration and the critical concentration c_P . In the concentration area between the critical concentrations c_S and c_P both phases P and S appear with mixed geometries.

The principles of the above description of shape functions are the ones subsequently used in Chap. 7 to describe composite geometries in general. Obviously the simplified scheme of geometry classification used in this book

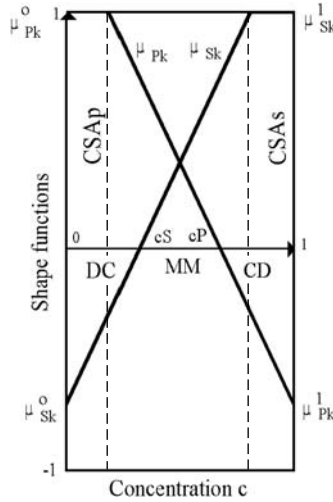


Fig. 4.6. Shape functions for an ideal DC-CD composite

(Fig. 2.2) requires that the concentration at which μ_S becomes 1 is greater than c_P – and that the concentration at which μ_P becomes 1 is smaller than c_S .

Interaction

In composite theory the term “no interaction between phase elements” means that a stress-strain analysis of a phase element can be made disregarding the presence of “neighboring” elements. The CSA_P material subjected to volumetric load is a well-known example of composites with no interaction between particles.

Geometries involving no interaction between phase elements are described by constant shape functions in the geo-function (4.9). The geometrical influence on stress is absent when shape functions are constants.

The presence of interaction (variable shape functions) cannot be clearly demonstrated as it is mixed up with the effect of geometrical changes. It can, however, be shown by FEM-analysis that interaction also depends on loading mode, see Fig. 8.22 in Chap. 8. A volumetric analysis and a deviatoric analysis were made on exactly the same particulate composite (TROC). The first analysis was clearly not influenced very much by interaction. The second analysis was. A similar effect was observed from a FEM-analysis of a grid-reinforced composite (CROSS), see Fig. 8.44.

In the present study the term “interaction” is used quite practically: The influence of geometry in general is considered as the joint influence of load induced interaction and geometrically induced interaction. “Complete” interaction is obtained at real critical concentrations (in $c = 0 - 1$) where geometries change from particulate to mixed. Geometrically induced interaction is anticipated to be overriding when critical concentrations are real, while load induced interaction is anticipated to be overriding when critical concentrations are non-real (outside $c = 0 - 1$) – as they are in the TROC and CROSS composites mentioned above.

4.1.5 Summary

Equation (4.3) predicts volumetric stresses for any isotropic composite geometry. The overall influence of geometry is reflected by the so-called geometry function (geo-function) presented in (4.9) where specific geometries and the variations of such with respect to volume concentration c are considered by so-called shape functions outlined in Fig. 4.4 and subsequently quantified in Chap. 7.

Implicitly, volume concentrations appear in the geo-function only to tell about geometry at these concentrations. In a composite with variable geometry this means that each volume concentration has its own geometry function. When the class of composite geometry considered (DC, MM, or CD) does not change with c , then geo-functions are expected to keep relatively close in

Fig. 4.2. They are extremely close (coinciding) when composites with no interaction between phase elements are considered such as in CSA_P and CSA_S materials with $\theta_k \equiv 1$ and $\theta_k \equiv n$ respectively ($v_P = v_S = 0.2$).

4.2 Deviatoric Stress

The phase P deviatoric stress in a CSA_P composite is postulated to be the following modified copy of the former expression in (4.1).

$$\frac{s_{Pij}}{s_{ij}} = \frac{n_g(1 + \gamma_S)}{n_g + \gamma_S[1 + (n_g - 1)c]} \quad (4.13)$$

Equation (4.1) is exact. Equation (4.13), however, is an approximation. No such simple, exact, and closed form relation is known from the literature. The approximation, however, is very good. This has been justified in a FEM stiffness analysis of particulate composites presented in [24]. The approximation becomes exact at low phase P concentrations ($c \rightarrow 0$) where the following solution has been presented [45, 46, 53].

$$\frac{s_{Pij}}{s_{ij}} = \frac{n_g(1 + \gamma_S)}{n_g + \gamma_S} \quad (4.14)$$

Remark: We emphasize that (4.13) is considered exact in subsequent deductions with respect to the behavior of composite materials. Such procedure is strongly supported by some results obtained by Christoffersen [6] and Levin [7] in their analysis of materials reinforced with randomly distributed spherical particles. Predicted shear moduli in these references are the same as can be predicted by the present theory (Chap. 5) with (4.13) considered exact.

4.2.1 Stress and Geometry

Thanks to (4.13) the deviatoric stresses in an isotropic composite can be considered just as volumetric stresses were considered in Sect. 4.1. In fact, the results subsequently presented in the following summary, Sect. 4.3, are complete duplicates of results obtained in Sect. 4.1 except that bulk properties are replaced with shear properties. This means that the bulk stiffness ratio n_k is replaced with the shear stiffness ratio $n_g = G_P/G_S$, the bulk Poisson parameters κ_S, κ_P are replaced with the shear Poisson parameters γ_S, γ_P (see Appendix A), and the bulk geo-function θ_k is replaced with the shear geo-function θ_g . The modified bulk stiffness ratio N_k is at the same time replaced with the modified shear stiffness ratio $N_g = n_g\gamma_P/\gamma_S$.

The shape functions μ_{Pk} and μ_{Sk} are replaced with their deviatoric counterparts μ_{Pg} and μ_{Sg} to be determined just as μ_{Pk}, μ_{Sk} in the subsequent Chap. 7. Deviatoric shape factors are $\mu_{Pg}^0 = \mu_{Pg}(0), \mu_{Pg}^1 = \mu_{Pg}(1), \mu_{Sg}^0 = \mu_{Sg}(0)$, and $\mu_{Sg}^1 = \mu_{Sg}(1)$.

Deviatoric interaction is considered in a similar way as volumetric interaction has been considered in Sect. 4.1.4.

4.3 Summary on Stress and Geometry

A brief summary of the main results obtained in this chapter is presented below. Expressions are added which apply especially for porous materials ($n = 0$) and for composites with extremely stiff pore systems ($n = \infty$). We emphasize, once again, that the stress expressions are *global*. They apply for any geometry encountered. Geometrical information on specific composites is “hidden” in the shape functions μ_{Pk} , μ_{Sk} , μ_{Pg} , and μ_{Sg} considered in details in Chap. 7.

4.3.1 Stress

$$\begin{aligned} \frac{\sigma_{Pkk}}{\sigma_{kk}} &= \frac{n_k(1 + \theta_k)}{n_k + \theta_k[1 + c(n_k - 1)]} ; & \frac{\sigma_{Skk}}{\sigma_{kk}} &= \frac{n_k + \theta_k}{n_k + \theta_k[1 + c(n_k - 1)]} \\ \frac{s_{Pij}}{s_{ij}} &= \frac{n_g(1 + \theta_g)}{n_g + \theta_g[1 + c(n_g - 1)]} ; & \frac{s_{Sij}}{s_{ij}} &= \frac{n_g + \theta_g}{n_g + \theta_g[1 + c(n_g - 1)]} \end{aligned} \quad (4.15)$$

4.3.2 Geo-Function

$$\begin{aligned} \theta_k &= \frac{\kappa_S}{2} \left[\mu_{Pk} + \mu_{Sk} N_k + \sqrt{(\mu_{Pk} + \mu_{Sk} N_k)^2 + 4 N_k(1 - \mu_{Pk} - \mu_{Sk})} \right] \\ \text{with } N_K &= n_k \frac{\kappa_P}{\kappa_S} = n_g \\ \theta_g &= \frac{\gamma_S}{2} \left[\mu_{Pg} + \mu_{Sg} N_g + \sqrt{(\mu_{Pg} + \mu_{Sg} N_g)^2 + 4 N_g(1 - \mu_{Pg} - \mu_{Sg})} \right] \\ \text{with } N_g &= n_g \frac{\gamma_P}{\gamma_S} \end{aligned} \quad (4.16)$$

Table 4.1. Geo-functions for porous materials and stiff pore systems

Porous Material		Stiff Pore System	
$\theta_{k0} = \kappa_S \mu_{Pk}$	$c \leq c_P$	$\theta_{k\infty} = \kappa_S \frac{\mu_{Pk} + \mu_{Sk} - 1}{\mu_{Sk}}$	$c < c_S$
$\theta_{k0} \equiv 0$	$c > c_P$	$\theta_{k\infty} \equiv \infty$	$c > c_S$
$\theta_{g0} = \gamma_S \mu_{Pg}$	$c \leq c_P$	$\theta_{g\infty} = \gamma_S \frac{\mu_{Pg} + \mu_{Sg} - 1}{\mu_{Sg}}$	$c < c_S$
$\theta_{g0} \equiv \infty$	$c > c_P$	$\theta_{g\infty} \equiv \infty$	$c > c_S$
Dilute Porous		Dilute Stiff	
$\theta_{k0}^0 = \kappa_S \mu_{Pk}^0$	$c \ll 1$	$\theta_{k\infty}^0 = \kappa_S \frac{\mu_{Pk}^0 + \mu_{Sk}^0 - 1}{\mu_{Sk}^0}$	$c \ll 1$
$\theta_{g0}^0 = \gamma_S \mu_{Pg}^0$		$\theta_{g\infty}^0 = \gamma_S \frac{\mu_{Pg}^0 + \mu_{Sg}^0 - 1}{\mu_{Sg}^0}$	

Porous Materials and Stiff Pore Systems

The geo-functions have the values presented in Table 4.1 when porous materials ($n = 0$) and stiff pore systems ($n = \infty$) are considered. Also presented in this table are the geo-functions for such systems if they are dilute ($c \ll 1$).

Composite Stiffness and Geometry

It has been stated in Chap. 4, that the analysis of stiffness versus phase geometry is basically an analysis of internal stresses versus phase geometry. This statement is made very concrete in this chapter: Composite stiffness is predicted by (3.6) introducing stresses as they have been determined in Chap. 4 (summary in Sect. 4.3). The results of this straightforward procedure are subsequently presented with only a few comments.

The stiffness expressions presented are *global* just as are the stress expressions introduced. Specific geometrical information is hidden in the shape functions μ to be considered in more details in Chap. 7.

5.1 Bulk Modulus and Shear Modulus

In general bulk modulus and shear modulus are predicted as follows with geo-functions introduced from (4.16).

$$k = \frac{n_k + \theta_k[1 + c(n_k - 1)]}{n_k + \theta_k - c(n_k - 1)} \quad ; \quad g = \frac{n_g + \theta_g[1 + c(n_g - 1)]}{n_g + \theta_g - c(n_g - 1)} \quad (5.1)$$

5.1.1 Porous Materials and Stiff Pore Systems

When porous materials ($n = 0$) and very stiff pore systems ($n = \infty$) are considered (5.1) reduces as follows with geo-functions introduced from Table 4.1. It is noticed that $k_0 = g_0 \equiv 0$ are predicted when $c > c_P$, and that $1/k_\infty = 1/g_\infty \equiv 0$ are predicted at $c > c_S$.

$$\left. \begin{aligned} k_0 &= \frac{1 - c}{1 + c/\theta_{k0}} \quad ; \quad \frac{1}{k_\infty} = \frac{1 - c}{1 + c\theta_{k\infty}} \\ g_0 &= \frac{1 - c}{1 + c/\theta_{g0}} \quad ; \quad \frac{1}{g_\infty} = \frac{1 - c}{1 + c\theta_{g\infty}} \end{aligned} \right\} \begin{array}{l} \text{porous material and} \\ \text{stiff pore system} \end{array} \quad (5.2)$$

$$\left. \begin{aligned} k_0 &= 1 - \left(1 + \frac{1}{\theta_{k0}^0}\right) c ; \quad \frac{1}{k_\infty} = 1 - (1 + \theta_{k\infty}^0) c \\ g_0 &= 1 - \left(1 + \frac{1}{\theta_{g0}^0}\right) c ; \quad \frac{1}{g_\infty} = 1 - (1 + \theta_{g\infty}^0) c \end{aligned} \right\} \begin{array}{l} \text{dilute porous} \\ \text{material and} \\ \text{dilute stiff} \\ \text{pore system} \end{array} \quad (5.3)$$

5.2 Young's Modulus and Poisson's Ratio

The Young's modulus and Poisson's ratio are determined as follows (Appendix A) with bulk modulus and shear modulus introduced as just predicted by (5.1).

$$e = \frac{3kg}{2(1 + \nu_S)k + (1 - 2\nu_S)g} ; \quad \nu = \frac{(1 + \nu_S)k - (1 - 2\nu_S)g}{2(1 + \nu_S)k + (1 - 2\nu_S)g} \quad (5.4)$$

5.3 Special Composites and Observations

We re-call that (5.1) and (5.4) apply in general for composite stiffness. As previously mentioned, specific composites are considered introducing shape functions, which specify and quantify the special type of composite geometry considered. At this point of the analysis our knowledge to shape functions versus type of composite is limited to what is outlined in Fig. 5.1, which is a summary of information presented in Chaps. 2 and 4. Conclusive information on shape functions in general is presented in Chap. 7 for various types of composites. Important observations, however, on some special composites can be made already now.

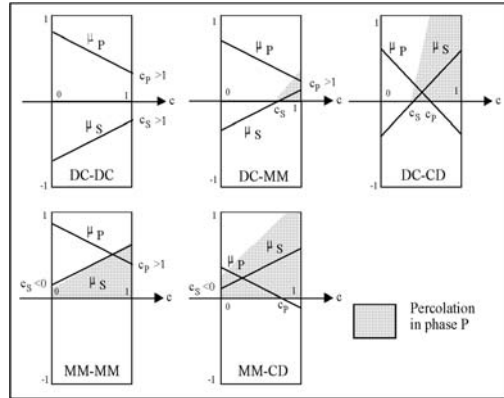


Fig. 5.1. Composite types as related to critical concentrations. First two letters denote geometry at $c = 0$. Latter two letters denote geometry at $c = 1$

5.3.1 CSA-Composites

For two special composites we do not have to calculate the geo-functions. The CSA_P -composite and the CSA_S -composite have $(\theta_k, \theta_g) \equiv (\kappa_S, \gamma_S)$ and $(\theta_k, \theta_g) \equiv (N_k \kappa_S, N_g \gamma_S)$ respectively (see Fig. 4.2). The stiffness moduli of the CSA-composites are then immediately obtained from (5.1). We get

$$k = \frac{n_k + \kappa_S[1 + c(n_k - 1)]}{n_k + \kappa_S - c(n_k - 1)} ; \quad g = \frac{n_g + \gamma_S[1 + c(n_g - 1)]}{n_g + \gamma_S - c(n_g - 1)} \quad \text{CSA}_P \quad (5.5)$$

$$k = n_k \frac{1 + \kappa_P[1 + c(n_k - 1)]}{n_k(1 + \kappa_P) - c(n_k - 1)} ; \quad g = n_g \frac{1 + \gamma_P[1 + c(n_g - 1)]}{n_g(1 + \gamma_P) - c(n_g - 1)} \quad \text{CSA}_S \quad (5.6)$$

Hashin/Shtrikman's Bounds

We re-call that these relations express the Hashin/Shtrikman's lower and upper bounds [3] respectively for isotropic composites with $n_{k,g} \geq 1$. When $n_{k,g} < 1$ the stiffness of CSA_P and CSA_S change their roles with respect to bounds.

5.3.2 Composites with Special Shear Moduli

Geo-Independent Bulk Moduli

It has previously been observed in Sect. 4.1.2 that the volumetric stress in a composite is independent of geometry when $N_k = n_g = 1$. With (3.6) in mind this observation leads directly to the finding of Hill [5] previously referred to that the volumetric stiffness of a composite does not depend on geometry when shear moduli of the constituent phases are the same. This exact result can also be deduced from [54, 55] where exact solutions are studied in the theory of composite materials.

Geo-Independent Shear Moduli

It comes from the particles deviatoric stress in (4.15)¹ and the deviatoric counterpart to Fig. 4.2 that deviatoric stresses are independent of geometry when $n_g \equiv 1$ and $N_g = (n_g \gamma_P / \gamma_S) \equiv 1$ respectively. Referring to (3.6) the latter identity means that shear moduli of composite materials are independent of geometry when $n_g \equiv (4-5v_P)^*(7-5v_S)/((4-5v_S)^*(7-5v_P))$.

¹ Still assuming, see Sect. 4.2, that the stress expression in (4.13) is exact.

5.3.3 Paul/Hansen versus Geo-Functions

It is interesting to notice that the homogeneous stress analysis made by Paul [1] and Hansen [2] to determine lower stiffness bounds for anisotropic composites is exactly reflected by the present theory introducing $\theta_k = \theta_g \equiv 0$ into the stiffness expressions (5.1). In a similar way the homogeneous strain analysis made by Paul and Hansen to determine upper stiffness bounds for anisotropic composites is exactly reflected by the present theory introducing $\theta_k = \theta_g \equiv \infty$.

It might be worthwhile exploring the possibility of generalizing the concept of geo-functions to more general geometries. Apparently θ is, in a way, proportional to a “phase aspect ratio”, $\underline{\theta}$, defined by phase “length” parallel to load divided by phase “thickness” perpendicular to load. The material models (parallel laminates) such defined by $\underline{\theta} = 0$ and $\underline{\theta} = \infty$ are exactly those used by Hansen [2] to establish the lower and upper bound respectively for stiffness of composites with unrestricted (un-known) phase geometries.

Composite Eigenstrain/Stress

An analysis is made in this chapter on composites subjected to eigenstress (self-equilibrated residual stresses) caused by different eigenstrains of the constituent components. Typical eigenstrains are hygro-thermal strains like shrinkage, swelling and thermal expansion that develop in solids without external forces and surface restraint. Another example of eigenstrain is strain developed during phase transformation such as in solidification of a liquid impregnant. The analysis is a modified version of similar analysis made by the author in [56–58].

6.1 Basics

The following expressions describe the volumetric stress-strain state in an isotropic composite subjected to eigenstrains just as (3.3) describes the stress-strain state in a composite subjected to external load. Stresses and strains are volume averages (leaving no averages of deviatoric stress and deviatoric strain). Volumetric eigenstrains are denoted by $\lambda_{kk} = 3\lambda$ where λ is linear eigenstrain.

$$\begin{aligned}
 0 &= c\sigma_{Pkk} + (1-c)\sigma_{Skk} && \text{Equilibrium condition} \\
 \lambda_{kk} &= c\varepsilon_{Pkk} + (1-c)\varepsilon_{Skk} && \text{Compatibility condition} \\
 \left. \begin{aligned} \sigma_{Pkk} &= 3K_P(\varepsilon_{Pkk} - \lambda_{Pkk}) \\ \sigma_{Skk} &= 3K_S(\varepsilon_{Skk} - \lambda_{Skk}) \end{aligned} \right\} && \text{Physical conditions}
 \end{aligned} \tag{6.1}$$

The expressions in (6.1) can be arranged as shown in (6.2) to predict composite strain from a known phase P stress,

$$\lambda_{kk} = \lambda_{Skk} + c \left[\Delta\lambda_{kk} + \frac{\sigma_{Pkk}}{3K_P} (1 - n_k) \right] ; \quad \Delta\lambda_{kk} = \lambda_{Pkk} - \lambda_{Skk} \tag{6.2}$$

6.1.1 Simple Composites

The eigenstrain of a CSA_P composite is predicted by (6.2) introducing the phase P stress presented in (6.3) which is a re-written version of an expression developed by the author [59] in a stress analysis of CSA_P composites subjected to eigenstrain. The phase S stress also presented in (6.3) is obtained from the equilibrium expression in (6.1)

$$\left. \begin{aligned} \frac{\sigma_{Pkk}}{3K_P} &= -\Delta\lambda_{kk} \frac{\kappa_S(1-c)}{n_k + \kappa_S[1 + (n_k - 1)c]} \\ \frac{\sigma_{Skk}}{3K_P} &= \Delta\lambda_{kk} \frac{\kappa_S c}{n_k + \kappa_S[1 + (n_k - 1)c]} \end{aligned} \right\} \text{(CSA}_P \text{ geometry)} \quad (6.3)$$

The eigenstrain of a CSA_S composite is predicted by (6.2) introducing the phase P stress as it develops in a CSA_S composite. With a constant volume concentration this stress is expressed by (6.4) obtained from (6.3) interchanging the subscripts and replacing c with $1 - c$.

$$\left. \begin{aligned} \frac{\sigma_{Pkk}}{3K_P} &= -\Delta\lambda_{kk} \frac{\kappa_P(1-c)}{1 + \kappa_P[1 + (n_k - 1)c]} \\ \frac{\sigma_{Skk}}{3K_P} &= \Delta\lambda_{kk} \frac{\kappa_P c}{1 + \kappa_P[1 + (n_k - 1)c]} \end{aligned} \right\} \text{(CSA}_S \text{ geometry)} \quad (6.4)$$

6.2 General Geometry

It is noticed that (6.3) and (6.4) can be given a common description as shown in the following (6.5) where the parameter $\theta_k = \kappa_S$ when CSA_P composites are considered and where $\theta_k = N_k \kappa_S$ when CSA_S composites are considered. The quantities $\theta_k = \kappa_S$ and $\theta_k = N_k \kappa_S$ introduced express the boundaries of the area illustrated in Fig. 4.2, where general geometry functions θ_k can be defined which generalize (6.5) to predict eigenstress in composites with any geometry (following the arrows in Fig. 4.2 between the geometries of CSA_P and CSA_S). Consistency with other volumetric stress predictions presented in this book is obtained introducing the geo-function as it is expressed by the former expression in (4.16).

$$\left. \begin{aligned} \frac{\sigma_{Pkk}}{3K_P} &= -\Delta\lambda_{kk} \frac{\theta_k(1-c)}{n_k + \theta_k[1 + (n_k - 1)c]} \\ \frac{\sigma_{Skk}}{3K_P} &= \Delta\lambda_{kk} \frac{\theta_k c}{n_k + \theta_k[1 + (n_k - 1)c]} \end{aligned} \right\} \text{general geometry} \quad (6.5)$$

6.2.1 Eigenstrain and Eigenstress

Now, the eigenstrain/stress problem of a composite can be predicted in general by (6.2) with phase P stress introduced from (6.5). Doing so, and eliminating

the geo-function by the former expression in (5.1), the remarkably simple results presented in (6.6) and (6.7) are obtained between linear eigenstrain ($\lambda = \lambda_{kk}/3$) and hydrostatic stress ($\rho = \sigma_{kk}/3$).

$$\lambda = \lambda_S + \Delta\lambda \frac{1/k - 1}{1/n_k - 1} ; \quad (\Delta\lambda = \lambda_P - \lambda_S) \quad (6.6)$$

$$\rho_P = -3K_S\Delta\lambda \frac{c(1/n_k - 1) - (1/k - 1)}{c(1/n_k - 1)^2} ; \quad \rho_S = -\frac{c}{1-c}\rho_P \quad (6.7)$$

Equation (6.6) reduces as shown in (6.8) when eigenstrain is only experienced by phase S,

$$\frac{\lambda}{\lambda_S} = \frac{1/n_k - 1/k}{1/n_k - 1} ; \quad (\lambda_P = 0) \quad (6.8)$$

Remark: The eigenstrain/stress phenomenon of composites has also been considered by other authors [9, 60–63]. Relative to these works the present study of the eigenstrain/stress problem has the advantage of reflecting the influence of any phase geometry – and at the same time predict the internal composite stresses.

6.2.2 Pore Pressure in Porous Materials

The linear composite strain $\varepsilon (= \varepsilon_{kk}/3)$ of a porous material with a hydrostatic pore pressure $p (= -\sigma_{Pkk})$ is developed as shown in (6.9), first line, expressing that composite strain can be considered as the difference between strains obtained by considering the composite loaded (1) both externally and internally, and (2) only externally with the pore pressure p . (K and K_S denote bulk moduli of porous material and solid phase respectively).

The linear pore strain (ε_P) relation presented in (6.9) is obtained combining the composite strain just developed with the compatibility condition also shown in (6.9) for the problem considered.

$$\left. \begin{aligned} \varepsilon_{kk} &= \frac{\sigma_{kk}}{3} \left(\frac{1}{K_S} - \frac{1}{K} \right) \\ \varepsilon_{kk} &= c\varepsilon_{Pkk} + (1-c)\varepsilon_{Skk} \end{aligned} \right\} \Rightarrow \left\{ \begin{aligned} \varepsilon &= \frac{p}{3} \left(\frac{1}{K} - \frac{1}{K_S} \right) \text{ composit strain} \\ \varepsilon_P &= \frac{p}{3c} \left(\frac{1}{K} - \frac{1+c}{K_S} \right) \text{ pore strain} \end{aligned} \right. \quad (6.9)$$

These expressions have been used by the present author in [57] and in [64] to study the frost resistance and the phenomenon of drying shrinkage respectively in porous materials. Recently the drying shrinkage phenomenon in porous glass has been studied in [65] using a method similar to the one developed by the present author in [64].

Quantification of Geometry

We re-call from Chap. 5 that phase P and phase S shape functions $\mu_{Pj} = \mu_{Pj}(c)$ and $\mu_{Sj} = \mu_{Sj}(c)$ ($j = k, g$) consider the influence of phase geometries on internal composite stresses – and therefore also on composite stiffness. Thus, shape functions are the prime information needed in any analysis of composites. The behavior of natural composites cannot be explained – and design of new materials cannot be made without knowing these functions.

In general it is not possible to determine shape functions analytically. The complexity of most real composite geometries is much too high and too un-predictable. As demonstrated in this chapter it is, however, possible to estimate, in a relatively simple way, shape functions of relevance for studies of the composites considered in this book, see Fig. 7.1.

We will construct shape functions from knowing about shape factors, which can be calculated or accurately estimated, and knowing about critical concentrations at which, shape function values are zero. It is recognized that the

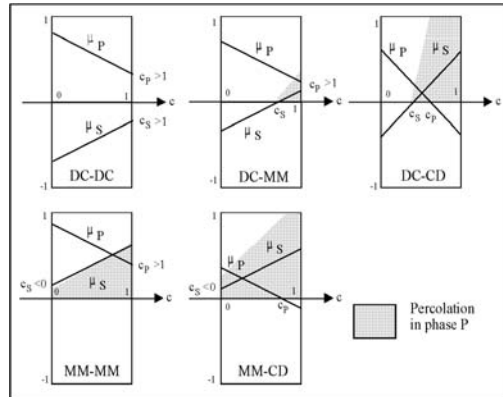


Fig. 7.1. Composite types as related to critical concentrations. First two letters denote geometry at $c = 0$. Latter two letters denote geometry at $c = 1$

latter statement is an approximation when non-real critical concentrations (outside $0 - 1$) are considered. This feature is further discussed in Sect. 7.2 where the final determination of shape functions is considered.

The basic geometrical models used for shape factor determination are outlined in the following.

DC (and CD) Composite: The basic materials model to be used extensively in the shape function analysis of DC and CD composites is the following: A dilute particulate composite with isotropically distributed particles of regular shapes as defined in Fig. 7.2. Fiber length is l , cross-section is $d * d$, and aspect ratio is $A = l/d$. With particles of compact shapes, flat shapes, and long shapes this model can be considered as a reasonable working model with $A = 1$, $A < 1$, and $A > 1$ respectively.

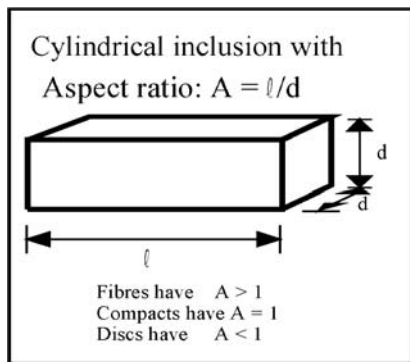


Fig. 7.2. Cylindrical inclusions are fibers, compacts, and discs of ellipsoidal shapes enveloped as shown

MM (or CC) Composite: The particulate composites model presented in Fig. 7.2 cannot be used for the analysis of shape factors of MM composites. Results from FEM analysis have to be used. One of the FEM models applied for this purpose is an isotropic mixture of cubic grid-composites as illustrated in Fig. 7.3.

Transition DC to MM to CD: The two models just defined are unable to handle the “organic” particle shapes considered in this book. They cannot model transition shapes between particles and continuous geometries. Mathematically, however, this difficulty is overcome by the geo-functions previously introduced. These functions act as a transition model which adjust particles to become continuous shapes and vice versa.

Basically the transition model is used with shape factors based on the strict particles model with aspect ratios, A , defined as explained in Fig. 7.2. The meaning of shapes, however, are re-interpreted according to the following: Flat phase P particles with low aspect ratios are understood as organic particles preparing to serve as an enveloping matrix for flat phase S particles. Long

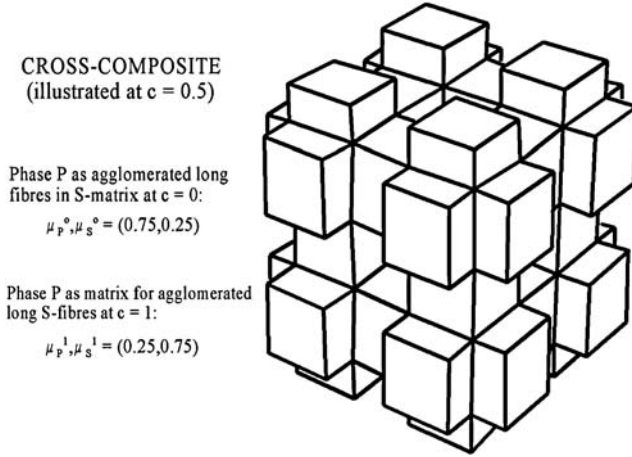


Fig. 7.3. FEM-model used for shape factor analysis of MM-composites. Shape factors indicated are deduced from a volumetric analysis (k)

phase P particles with high aspect ratios are understood as organic particles preparing to serve as an enveloping matrix for long phase S shapes.

Examples of stress predictions by the transition model are shown in Figs. 7.4–7.6: A dilute solution is considered with flat organic phase P particles changing their shapes in a DC-CD transition. Also shown in the figures are

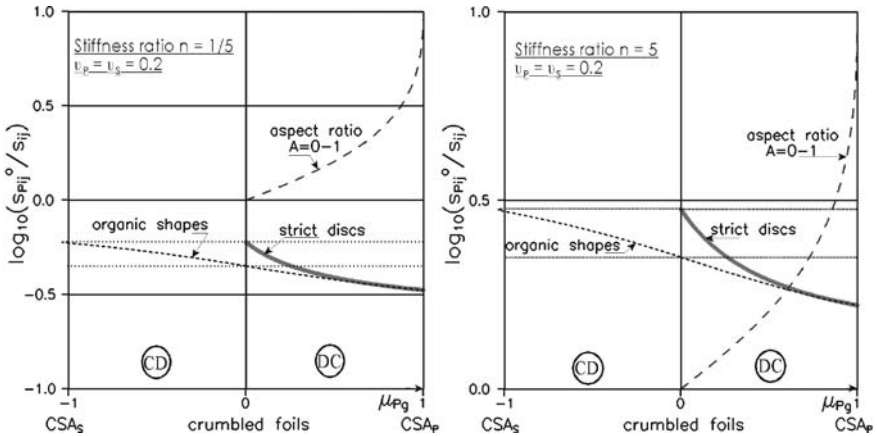


Fig. 7.4. Phase P stress in a dilute solution as influenced by shapes changing from spheres (CSA_P) to shells (CSA_S)

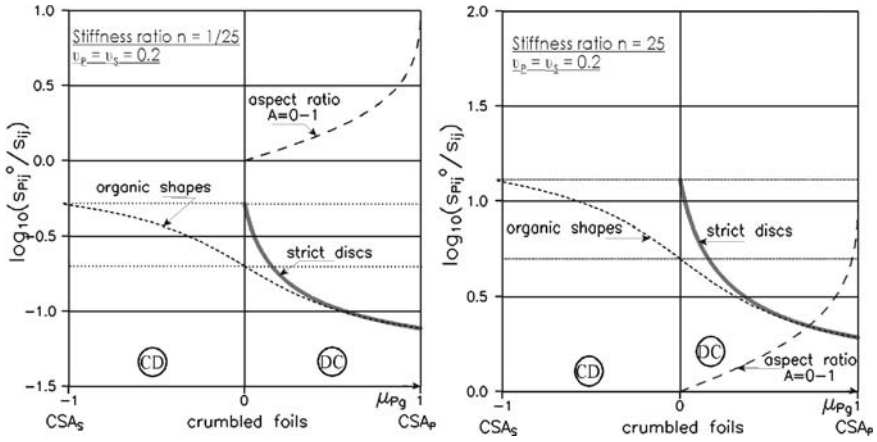


Fig. 7.5. Phase P stress in a dilute solution as influenced by shapes changing from spheres (CSA_P) to shells (CSA_S)

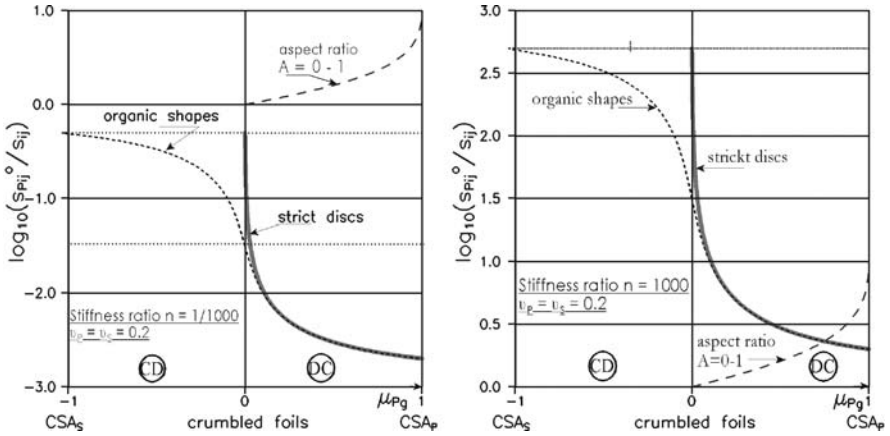


Fig. 7.6. Phase P stress in a dilute solution as influenced by shapes changing from spheres (CSA_P) to shells (CSA_S)

stresses, as they would develop in a counterpart solution with flat traditional strict shapes¹.

Discussion: We notice that the “organic” and the “strict” stresses approach each other for all aspect ratios as the stiffness ratio approaches extreme values (0 and ∞). At the same time is observed that the area of aspect ratios where the two stresses coincide becomes broader. At $n = \infty$ and at $n = 0$ the stresses

¹ For reader checks: For strict particles the analysis associated is performed by Appendix B. For organic particles the analysis is made by (4.15) with shape factors developed in Chap. 7.

coincide for any aspect ratio. Similar results are obtained when long particles (fibers) are considered.

Conclusions: Looking at the overall results of the analysis the following “working conclusion” can be made: Organic particles behave like strict particles when extreme stiffness ratios ($n \rightarrow 0$, $n \rightarrow \infty$) are approached and/or aspect ratios $\approx 1/4 < A < \approx 4$ are considered.

The determination of shape factors and shape functions can proceed on the basis of the two geometrical models explained above. Geometry transition is automatically taken care of just by shape re-interpretation as explained above.

Remark: We notice that “preparing to become continuous” shapes are probably more relevant in practice than strict shapes. It is very likely that interference between long and thin particles will form these particles to appear organically.

7.1 Shape Factors

7.1.1 DC-Composites

The stiffness expression in (3.8) for dilute suspensions is the basis of the present analysis. At extreme stiffness ratios ($n = 0$ and ∞) this equation can be written as presented in (7.1) with so-called *shape parameters* determined by (7.2).

$$\left. \begin{aligned} k_0 &= 1 - \left(1 + \frac{1}{m_{k0}}\right) c \\ g_0 &= 1 - \left(1 + \frac{1}{m_{g0}}\right) c \end{aligned} \right\} n = 0 ; \quad \left. \begin{aligned} \frac{1}{k_\infty} &= 1 - \left(1 + \frac{1}{m_{k\infty}}\right) c \\ \frac{1}{g_\infty} &= 1 - \left(1 + \frac{1}{m_{g\infty}}\right) c \end{aligned} \right\} n = \infty \quad (7.1)$$

$$\begin{aligned} \frac{1}{m_{k0}} &= \lim_{n_k \rightarrow 0} \left(\frac{1 - n_k}{n_k} \frac{\sigma_{Pkk}^0}{\sigma_{kk}} - 1 \right) ; \quad \frac{1}{m_{k\infty}} = - \lim_{n_k \rightarrow \infty} \left(\frac{1 - n_k}{n_k} \frac{\sigma_{Pkk}^0}{\sigma_{kk}} + 1 \right) \\ \frac{1}{m_{g0}} &= \lim_{n_g \rightarrow 0} \left(\frac{1 - n_g}{n_g} \frac{s_{Pij}^0}{s_{ij}} - 1 \right) ; \quad \frac{1}{m_{g\infty}} = - \lim_{n_g \rightarrow \infty} \left(\frac{1 - n_g}{n_g} \frac{s_{Pij}^0}{s_{ij}} + 1 \right) \end{aligned} \quad (7.2)$$

Accurate shape parameters, $(m_{k0}, m_{g0}) = (\kappa_S, \gamma_S)$ and $(m_{k\infty}, m_{g\infty}) = (1/\kappa_S, 1/\gamma_S)$, for spherical particles ($A = 1$) are easily obtained from (7.2) introducing the exact phase P stress solutions presented in (3.9). In general, however, numerical methods have to be used to calculate shape parameters for arbitrary fiber aspect ratios A .

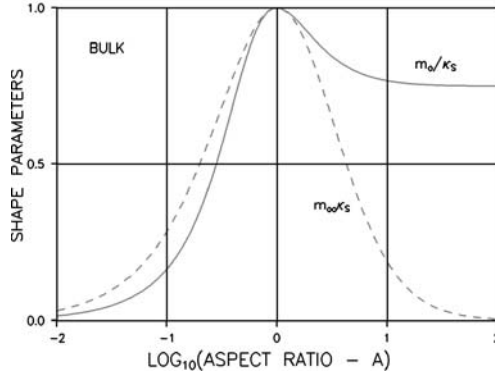


Fig. 7.7. Bulk shape parameters for isotropic composite with $v_S = 0.2$

For this purpose such a method has been developed in Appendix B by which particles stress in isotropic dilute composites (with ellipsoidal inclusions) can be calculated for any stiffness ratio (n). Shape parameters for any aspect ratio can then be determined numerically with stiffness ratios n approaching 0 and ∞ in (7.2) simulated by $n = 10^{-30}$ and 10^{30} respectively. Examples of shape parameters determined in this way are shown in Figs. 7.7 and 7.8. Shape parameters do not depend very much on the phase P Poisson's ratio v_P . When spherical inclusions ($A = 1$) are considered they do not depend at all.

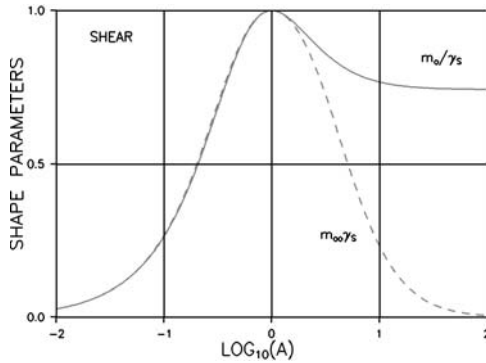


Fig. 7.8. Shear shape parameters for isotropic composite, $v_S = 0.2$

For the sake of curiosity: Young's modulus related shape parameters defined in (7.3) are obtained from their bulk and shear counterparts by (7.4) which is developed from (7.1) and (A.2) in Appendix A with $c \rightarrow 0$. Examples of shape parameters related to Young's modulus are illustrated in Fig. 7.9.

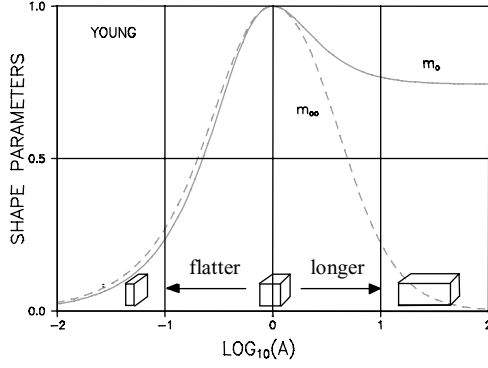


Fig. 7.9. Uniaxial shape parameters for isotropic composite with $v_S = 0.2$

$$e_0 = 1 - \left(1 + \frac{1}{m_{e0}}\right) c ; \quad \frac{1}{e_\infty} = 1 - \left(1 + \frac{1}{m_{e\infty}}\right) c \quad (7.3)$$

$$\frac{1}{m_{ei}} = \frac{1}{3} \left[\frac{1 - 2\nu_S}{m_{ki}} + \frac{2(1 + \nu_S)}{m_{gi}} \right] \quad (i = 0, \infty) \quad (7.4)$$

Shape Factors (Accurate)

Shape parameters are related to “dilute” geo-functions comparing (7.1) with (5.3). We get $(m_0, 1/m_\infty)_{k,g} = (\theta_0^0, \theta_\infty^0)_{k,g}$ which, by using Table 4.1, can be re-written as shown in (7.5) to relate shape parameters and shape factors. Overlined m means shape parameter normalized as indicated in (7.5). This equation can be solved explicitly with respect to shape factors as shown in (7.6). Like shape parameters, shape factors can be considered practically independent of v_P .

So-called shape factor graphs can now be established as shown in Figs. 7.10–7.12 which relate shape factors μ_P^0 of a discrete phase P to the complementary shape factors μ_S^0 of the continuous phase S.

$$\overline{m}_{k0} = \frac{m_{k0}}{\kappa_S} = \mu_{Pk}^0 ; \quad \overline{m}_{k\infty} = m_{k\infty} \kappa_S = \frac{\mu_{Sk}^0}{\mu_{Pk}^0 + \mu_{Sk}^0 - 1} \quad (7.5)$$

$$\overline{m}_{g0} = \frac{m_{g0}}{\gamma_S} = \mu_{Pg}^0 ; \quad \overline{m}_{g\infty} = m_{g\infty} \gamma_S = \frac{\mu_{Sg}^0}{\mu_{Pg}^0 + \mu_{Sg}^0 - 1}$$

$$\mu_{Pj}^0 = \overline{m}_{j0} ; \quad \mu_{Sj}^0 = -\overline{m}_{j\infty} \frac{1 - \overline{m}_{j0}}{1 - \overline{m}_{j\infty}} ; \quad (j = k, g) \quad (7.6)$$

Remarks: We notice that the shape factors for a CSA_P composite are $\mu_P^0 = 1$ and $\mu_S^0 \approx -1$ at any Poisson’s ratio around 0.2. As the exact quantities are not needed very often we keep $(\mu_P^0, \mu_S^0) = (1, -1)$ as reference quantities for CSA_P composites whenever shape factors in general are subsequently discussed in this book.

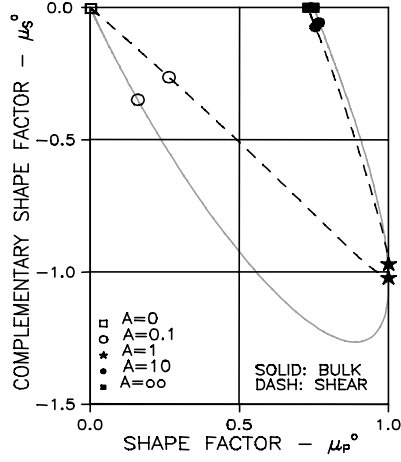


Fig. 7.10. Shape factor graphs. $v_s = 0.15$

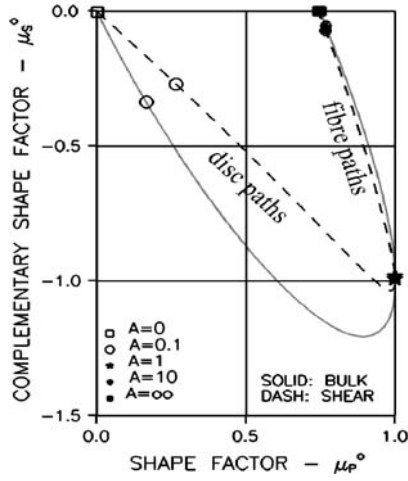


Fig. 7.11. Shape factor graphs. $v_s = 0.2$

Shape Factors (Approximate)

The somewhat cumbersome accurate determination of shape factors for uni-shaped particles, represented by (7.6), can be well approximated as follows for Poisson's ratios $0 < v_s < 0.5$.

$$\mu_{Pj}^0 = \bar{m}_{j0} ; \mu_{Sj}^0 = -\bar{m}_{j\infty} \frac{1 - \bar{m}_{j0}}{1 - \bar{m}_{j\infty}} (= -X_0^2 \text{ at } \mu_{Pj}^0 = 1) ; (j = k, g) \quad (7.7)$$

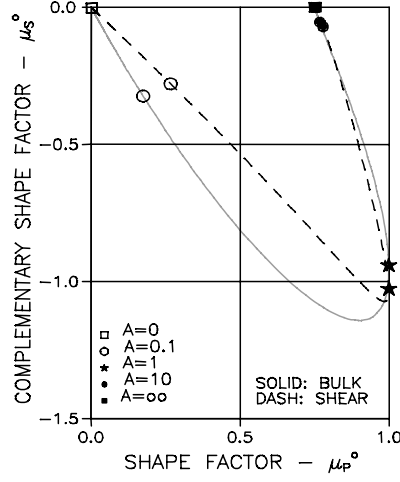


Fig. 7.12. Shape factor graphs. $v_S = 0.25$

$$\begin{aligned} \bar{m}_{j\infty} &= \frac{3A}{A^2 + A + 1} ; \quad \bar{m}_{j0} = \frac{3A^Z}{A^{2Z} + A^Z + 1} ; \quad (j = k, g) \text{ when } A \leq 1 \\ \bar{m}_{j\infty} &= \frac{3A^Z}{A^{2Z} + A^Z + 1} ; \quad \bar{m}_{j0} = \frac{3X_0^2(1 - \bar{m}_{j\infty}) + \bar{m}_{j\infty}}{4X_0^2(1 - \bar{m}_{j\infty}) + \bar{m}_{j\infty}} \quad \text{when } A > 1 \end{aligned} \quad (7.8)$$

Power $Z = X + (X_0 - X)A^{-3 \log(A)}$

$$\begin{aligned} \text{Bulk } (k) &\begin{cases} X_0 = 0.84 + 0.21\kappa_S - 0.05\kappa_S^2 \\ X = 1.3(0.73 + 0.38\kappa_S - 0.11\kappa_S^2) \end{cases} \\ \text{Shear } (g) &\begin{cases} X_0 = 1.78 - 1.88\gamma_S + 1.10\gamma_S^2 \\ X = 0.6 + 0.4\gamma_S \end{cases} \end{aligned} \quad (7.9)$$

Remark: Accurately determined shape factors are normally used in this book. Approximate shape factors are used only if explicitly noticed as in the simplified theory presented in Chap. 10 where the shear version of the above approximation is used with $v_S = 0.2$. The very simple expressions obtained in this way can be seen in Table 10.2.

Multi-Shaped Particles

Composite geometries hitherto considered in this chapter are based on uni-shaped regular fibers and discs. More realistic models of composite geometries can be made introducing shape distributed particles as shown in this section.

The average volumetric stress $\langle \sigma_{Pkk}^0 \rangle$ in particles of mixed shapes in a dilute suspension is expressed by (7.10) where $\sigma_{Pkk,i}^0$ is volumetric stress in a volume fraction α_i of phase P.

$$\frac{\langle \sigma_{Pkk}^0 \rangle}{\sigma_{kk}} = \sum_{i=1}^{\infty} \alpha_i \frac{\sigma_{Pkk,i}^0}{\sigma_{kk}} \text{ is average stress in phase P ; } \left(\sum_{i=1}^{\infty} \alpha_i = 1 \right) \quad (7.10)$$

Average deviatoric particle stress is expressed in a similar way. It comes from (7.2) that the average shape parameters of the mixture considered with discrete shape distributions can be determined by (7.11). The resulting average shape factors are presented in (7.12), which is a modified copy of (7.6).

$$\frac{1}{\langle \bar{m}_{mj} \rangle} = \sum_{i=1}^{\infty} \frac{\alpha_i}{\bar{m}_{mj,i}} ; \quad (m = k, g, j = 0, \infty) \quad (7.11)$$

$$\begin{aligned} \langle \mu_{Pm}^0 \rangle &= \langle \bar{m}_{m0} \rangle ; \\ \langle \mu_{Sm}^0 \rangle &= -\langle \bar{m}_{m\infty} \rangle \frac{1 - \langle \bar{m}_{m0} \rangle}{1 - \langle \bar{m}_{m\infty} \rangle} ; \quad (m = k, g) \end{aligned} \quad (7.12)$$

Continuous shape distributions $\Phi = \Phi(A)$ can be used as shown in (7.13). An example is presented in (7.14) with a linear log-A shape distribution. Average aspect ratio and standard deviation are denoted by A_{AV} and s respectively.

$$\frac{1}{\langle \bar{m}_{mj} \rangle} = \int_0^{\infty} \frac{1}{\bar{m}_{mj}(A)} d\Phi(A) ; \quad (\text{subscripts } m = k, g, j = 0, \infty) \quad (7.13)$$

$$\begin{aligned} \Phi &= \frac{1}{2} \left(1 + \frac{\log_{10}(A/A_{AV})}{s} \right) \equiv \begin{cases} 0 & \text{when } \log_{10}(A/A_{AV}) < -s \\ 1 & \text{when } \log_{10}(A/A_{AV}) > s \end{cases} \Rightarrow \\ \frac{1}{\langle \bar{m}_{mj} \rangle} &= \frac{1}{2s} \int_{\bar{X}-s}^{\bar{X}+s} \frac{dX}{\bar{m}_{mj}(X)} ; \quad (X, \bar{X} = \log_{10} A, \log_{10} A_{AV}) \end{aligned} \quad (7.14)$$

Rugged Fibres, Frayed Discs, and Rugged Discs

Three examples of special dilute suspensions made with double shaped particles are shown in Fig. 7.13:

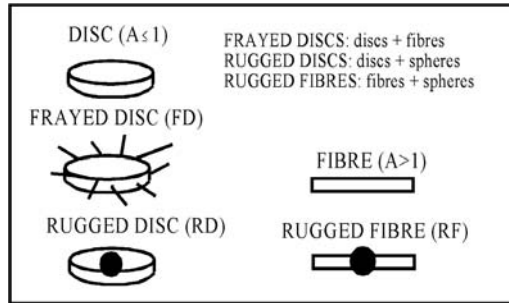


Fig. 7.13. Special multi-shaped particles. Stylized

- *Rugged fibers* (RF) are fibers ($A > 1$) mixed with spheres ($A = 1$). Rugged fibers are subsequently also referred to as “Pearls on a string” fibers, thinking of spheres interconnected by fibers (strings). Pearls on a thick/thin string are referred to when the volume fraction of fibers is larger/smaller than the volume fraction of spheres.
- *Frayed discs* (jelly-fish) (FD) are discs ($A < 1$) mixed with fibers ($A > 1$).
- *Rugged discs* (fried eggs) (RD), are discs ($A < 1$) mixed with spheres ($A = 1$).

Shape factors for Rugged fibers, Frayed discs, and Rugged discs have orders of magnitudes as outlined in Fig. 7.14.

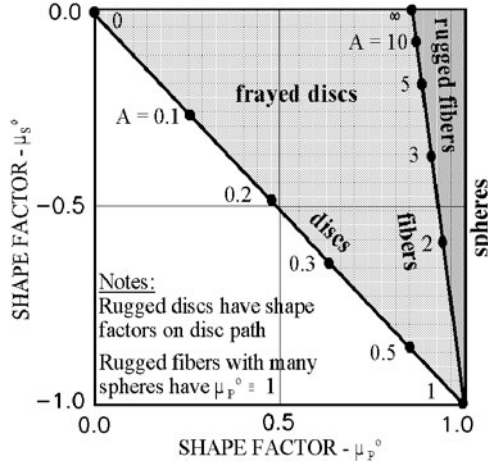


Fig. 7.14. Shear shape factors for multi-shaped particles. $v_P = v_S = 0.2$

7.1.2 CD-Composites

The shape factors hitherto considered (μ_P^0, μ_S^0) are those which quantify the geometry of a DC-composite with a very small amount of phase P ($c \approx 0$). A similar quantification can be made with respect to the shape factors (μ_P^1, μ_S^1), which quantify the geometry of a CD-composite with a very small amount of phase S ($c \approx 1$).

CD shape factors can be determined copying the DC-analysis with phase properties interchanged: Let us say that the DC shape factors are calculated by the algorithm FAC. Then CD shape factors are determined as explained in (7.15).

$$\begin{aligned} \text{If DC - shape factors are obtained by } \text{FAC}(\nu_P, \nu_S, A_P, \mu_P^0, \mu_S^0) \\ \text{then CD - shape factors are obtained by } \text{FAC}(\nu_S, \nu_P, A_S, \mu_S^1, \mu_P^1) \end{aligned} \quad (7.15)$$

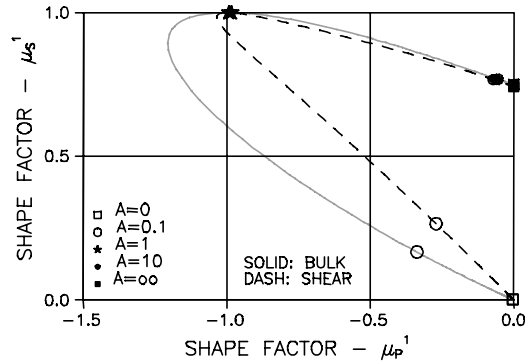


Fig. 7.15. Shape factors in CD-composite. $v_P = 0.2$. Aspect ratios indicated apply for phase S fibers

NAME	$c = 0$	$c = 1$	TYPE	SHAPE FACTORS
CSA_P			DC-DC	$\mu_P^0, \mu_S^0 = 1, -1$ $\mu_P^1, \mu_S^1 = 1, -1$
CSA_S			CD-CD	$\mu_P^0, \mu_S^0 = -1, 1$ $\mu_P^1, \mu_S^1 = -1, 1$
BUDIANSKY			DC-CD	$\mu_P^0, \mu_S^0 = 1, -1$ $\mu_P^1, \mu_S^1 = -1, 1$
LANDAUER			CD-DC	$\mu_P^0, \mu_S^0 = -1, 1$ $\mu_P^1, \mu_S^1 = 1, -1$

Fig. 7.16. Bulk shape factors for CSA composites. $v_P = v_S (= 0.2)$

Remark: We re-call from Sect. 4.1.4 that μ_P^1, μ_S^1 in Fig. 7.15 quantify the geometry of a composite material where phase P is the enveloping phase for a small concentration of discrete S particles of aspect ratios as indicated in the figure.

Theoretically, the above observations agree with Fig. 7.16 where results are shown from deductions of various theoretical/experimental data subsequently considered in this book.

7.1.3 MM-Composites

To get a full picture of how shape factors vary with phase geometries we need information with respect to MM-composites, which are transition materials where geometries change from being DC to CD. Such information cannot be obtained that easily. In this book we will establish some coarse rules based on deductions from stiffness results obtained in the FEM analysis presented in Sect. 8.3:

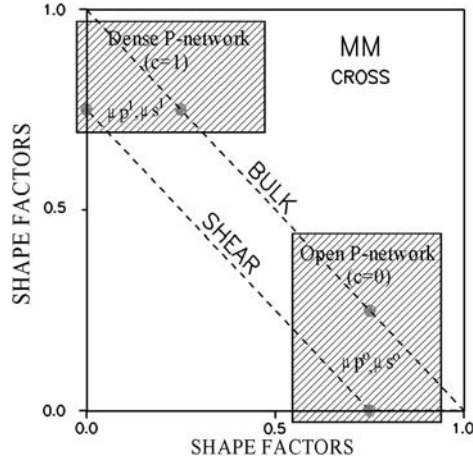


Fig. 7.17. Shape factors for a 3-D grid reinforced material (CROSS) ($v_P = v_S = 0.2$). Deduced from FEM-analysis

The CROSS-composite is a phase-symmetric material reinforced by three-dimensional grids. The pearl on a string composite is a material reinforced by continuous fibers grown together with compacts (rugged fibers). The shape factor results for these composites are presented in Figs. 7.17 and 7.18 with data reproduced from Table 8.1.

The geometry of a dilute CROSS-system is that of a matrix reinforced with a 3-D fiber work of very long agglomerated fibers. It is therefore not surprising that the magnitudes of shape factors for this system are close to

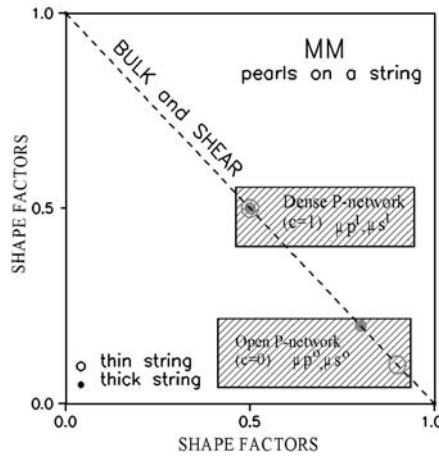


Fig. 7.18. Shape factors for a rugged fiber reinforced material ($v_P = v_S = 0.2$). Deduced from FEM-analysis

the theoretical result $(\mu_P^0, \mu_S^0 = 0.75, 0)$ previously obtained in Fig. 7.11 for particulate composites with very long cylindrical inclusions ($A \rightarrow \infty$). The geometrical symmetry of the CROSS-system is reflected by $(\mu_P^1, \mu_S^1 = \mu_S^0, \mu_P^0)$. We will use these observations to suggest that shape factors for *agglomerating fibers* develop with $\mu_P^{0,1} + \mu_S^{0,1} \approx \text{constant}$ between 0.75 and 1, see Fig. 7.17.

The pearl on a string path previously considered has $\mu_P^0 \equiv 1$ in the DC-section, see Fig. 7.14. From this observation and Fig. 7.18 is suggested that the shape factors for *pearls on a string* geometry proceed in MM such that $\mu_P^{0,1} + \mu_S^{0,1} \approx 1$.

The *crumbled foils* composite previously defined in Sect. 4.1.4 as a mixture of crumbled flat discs can be represented in Figs. 7.17 and 7.18 with $\mu_P^{0,1} + \mu_S^{0,1} = 0$.

Summarizing the observations made above we suggest that shape factors for MM-composites can be estimated as suggested in (7.16) for both μ_P^0, μ_S^0 and μ_P^1, μ_S^1 . Graphical representations of (7.16) are presented in Fig. 7.19.

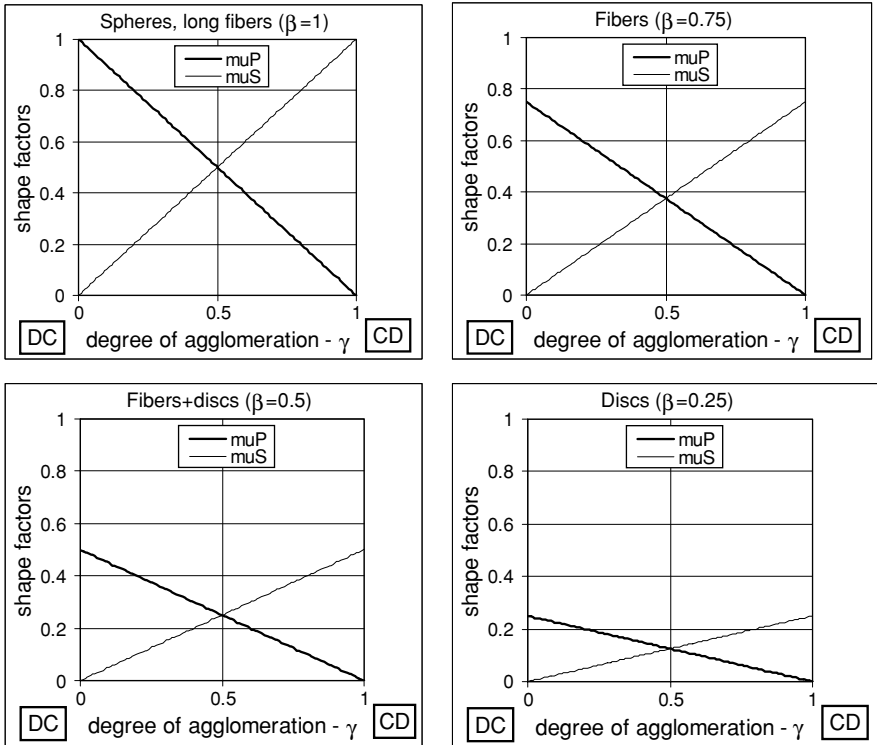


Fig. 7.19. Shape factors for MM-composites. Estimated by (7.16)

$$\mu_P^i \approx \beta (1 - \gamma^i); \quad \mu_S^i \approx \beta \gamma^i \quad (i = 0, 1)$$

where β quantifies basic shapes agglomerating:

$$\begin{aligned} &\text{Long fibers and rugged} \\ &\text{fibers have } \beta = 3/4 - 1 \\ &\text{Discs-fiber mixture has } \beta \approx 0 - 3/4 \\ &\text{Discs have } \beta \approx 0 \end{aligned} \quad (7.16)$$

and γ^i quantifies degree of agglomeration:

$$\begin{aligned} &\text{from a DC geometry with } \gamma^0 = 0 \\ &\text{to a CD geometry with } \gamma^1 = 1 \end{aligned}$$

Remarks: We re-call that (7.16) is a coarse estimate. As such it considers no influence on shape factors of Poisson ratios.

From Fig. 7.17 is noticed that $(\mu_P^0 - \mu_P^1)_k < (\mu_P^0 - \mu_P^1)_g$ and $(\mu_S^1 - \mu_S^0)_k < (\mu_S^1 - \mu_S^0)_g$, confirming the statement previously made that shear interaction and bulk interaction are not necessarily the same. For pearls on a string, however, Fig. 7.18 indicates that the two interactions are the same.

7.2 Shape Functions and Geo-Path

Shape functions are difficult to determine accurately. A few attempts have been made such as in [40] where shape function descriptions such as $\mu_P \approx \mu_P^0(1 - c/c_P)^{0.42}$ for $c \leq c_P$ were determined and successfully applied in research on self-compacting concrete [66, 67]. Numerically determined shape function descriptions are established by FEM in this book, Sect. 8.3.1.

Approximate shape function descriptions applied in this book are presented in the following sections: Default descriptions are presented in Sect. 7.2.1, which are based on the concept of non-real critical concentrations. For other composites more appropriate shape function descriptions are suggested in Sect. 7.2.2 and Sect. 7.2.3.

Remark: It is important to notice that *any* shape function description complying with the conditions explained in Sect. 4.1.3 can be used theoretically. The suggestions made in this chapter are presented exclusively to facilitate calculations on the basis of a minimum of relevant geometrical information.

7.2.1 Default

Estimates have to be made, the quality of which depends on the level of geometrical knowledge one has to the composite considered. Unless otherwise indicated the approximate description of shape functions presented in this section will be used as a *default description* in this book. It is based on a so-called “fairly high level of geometrical knowledge” from which shape factors and critical concentrations can be determined/estimated.

Shape functions are constructed by simple straight line interpolations between known shape function data sets: At $c = 0$ and $c = 1$ with shape factors

(μ_P^0, μ_S^0) and (μ_P^1, μ_S^1) determined from Sect. 7.1 – and at critical concentrations c_P and c_S where shape function values are zero. The results are simple broken lines with “knees” at the critical concentrations – and unknown geometries approximated to vary linearly. This shape function construction technique is applied (exercised) in the following Fig. 7.20 where a DC-CD composite is considered.

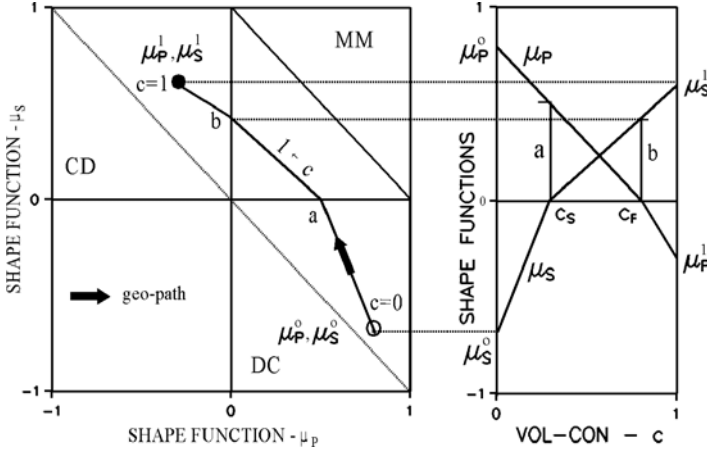


Fig. 7.20. DC-CD: Shape factors $(\mu_P^0, \mu_S^0, \mu_P^1, \mu_S^1)$ determined from Sect. 7.1. Critical concentrations $(1 > c_P > c_S > 0)$ determined from processing/experiments/experience

In principles shape functions for both bulk and deviatoric behavior are established in the same way. Subscripts, k and g , are therefore omitted.

- Determine $\mu_P^0, \mu_S^0, \mu_P^1, \mu_S^1$ as explained in Sect. 7.1 with known specific shape distributions of particles at $c \approx 0$ and $c \approx 1$.
- Mark these data as $(0, \mu_P^0)$, $(0, \mu_S^0)$ and $(1, \mu_P^1)$, $(1, \mu_S^1)$ in a shape function coordinate system (c, μ) together with the critical concentration data $(c_P, 0)$ and $(c_S, 0)$. Also mark (μ_P^0, μ_S^0) and (μ_P^1, μ_S^1) into a (μ_P, μ_S) coordinate system (a so-called *geo-path* system).
- In the shape function system, connect with straight lines $(0, \mu_P^0)$ to $(c_P, 0)$ to $(1, \mu_P^1)$, and $(0, \mu_S^0)$ to $(c_S, 0)$ to $(1, \mu_S^1)$. The shape functions are now described.
- Read $a = \mu_P(c_S)$ and $b = \mu_S(c_P)$ in the shape function system and mark these data as $(a, 0)$ and $(0, b)$ into the *geo-path* system – and connect (μ_P^0, μ_S^0) to $(a, 0)$ to $(0, b)$ to (μ_P^1, μ_S^1) . The graph such obtained is the so-called *geo-path*, which describes type of composite geometry traversed as c proceeds from 0 to 1.

Mathematically the construction of shape functions for DC-CD composites can be put into the 6-parameter representations shown in (7.17). In principle

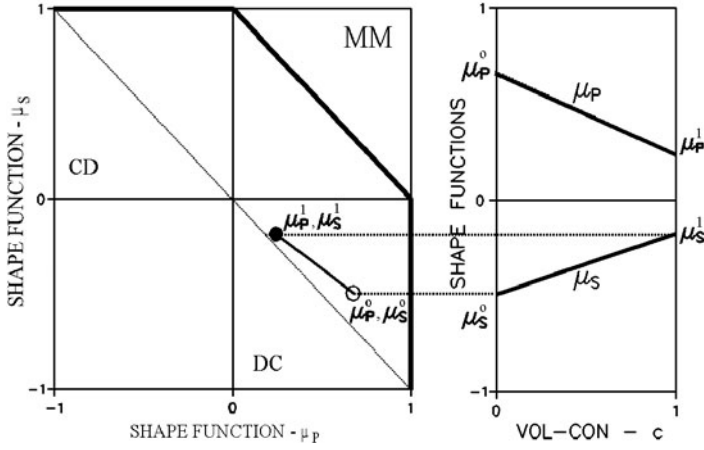


Fig. 7.21. DC-DC: Shape functions determined by (7.17) with geo-parameters from (7.18)

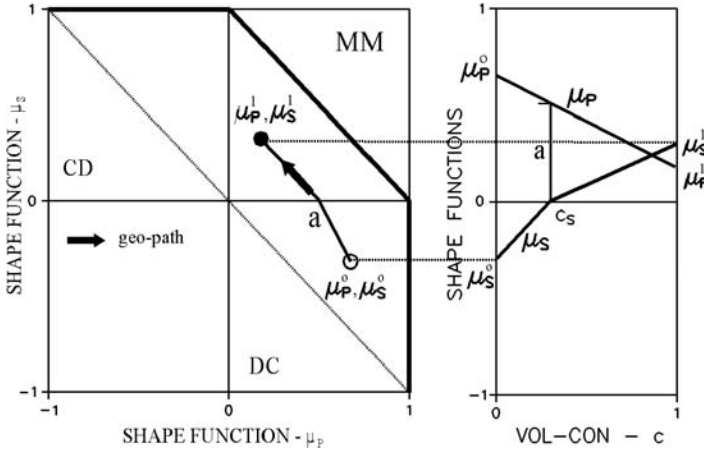


Fig. 7.22. DC-MM: Shape functions determined by (7.17) with geo-parameters from (7.19)

shape functions for other composites, DC-DC, DC-MM, and MM-MM are “constructed” as for the DC-CD composite. However, geo-parameters others than μ_P^0, μ_S^0 have to be derived as shown in the following expressions. Then (7.17) can be kept to describe shape functions analytically, see Figs. 7.21–7.23.

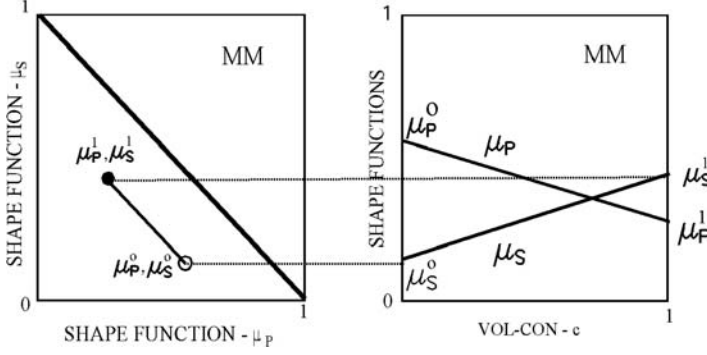


Fig. 7.23. MM-MM: Shape functions determined by (7.17) with geo-parameters from (7.20)

DC-CD

$$\begin{aligned}
 &\text{calculate/estimate } \begin{cases} \text{shape factors: } \mu_P^0, \mu_S^0, \mu_P^1, \mu_S^1 \\ \text{crit. concentr.: } 0 \leq c_S \leq c_P \leq 1 \end{cases} \\
 &\text{default description } \mu_P = \begin{cases} \mu_P^0 \frac{c_P - c}{c_P} & \text{at } c \leq c_P \\ \mu_P^1 \frac{c - c_P}{1 - c_P} & \text{at } c > c_P \end{cases}; \quad \mu_S = \begin{cases} \mu_S^0 \frac{c_S - c}{c_S} & \text{at } c \leq c_S \\ \mu_S^1 \frac{c - c_S}{1 - c_S} & \text{at } c > c_S \end{cases} \quad (7.17)
 \end{aligned}$$

DC-DC

$$\begin{aligned}
 &\text{calculate/estimate } \begin{cases} \text{shape factors } \mu_P^0, \mu_S^0 \\ \text{critical concentrations } c_P \geq c_S \geq 1 \end{cases} \quad (7.18) \\
 &\text{derive shape factors } \mu_P^1 = \mu_P^0 (1 - 1/c_P); \quad \mu_S^1 = \mu_S^0 (1 - c/c_S)
 \end{aligned}$$

DC-MM

$$\begin{aligned}
 &\text{calc./estim. } \begin{cases} \text{shape factors } \mu_P^0, \mu_S^0 \\ \text{shape factors } \mu_P^1, \mu_S^1 \text{ ((7.16) with } 1 > \beta > 0 \text{ and } \gamma^1 > 0) \\ \text{critical concentration } 0 < c_S < 1 \end{cases} \quad (7.19) \\
 &\text{derive critical concentration } c_P = 1/(1 - \mu_P^1/\mu_P^0)
 \end{aligned}$$

MM-MM

$$\begin{aligned}
 &\text{calc./estim. } \begin{cases} \text{shape factors } \mu_P^0, \mu_S^0 \text{ ((7.16) with } 0 < \beta < 1 \text{ and } \gamma^0 > 0) \\ \text{shape factors } \mu_P^1, \mu_S^1 \text{ ((7.16) with } \beta = \beta \text{ and } \gamma^1 > \gamma^0) \end{cases} \quad (7.20) \\
 &\text{derive crit. concentr. } c_P = 1/(1 - \mu_P^1/\mu_P^0); \quad c_S = 1/(1 - \mu_S^1/\mu_S^0)
 \end{aligned}$$

7.2.2 Alternative I

As previously mentioned *non-real critical concentrations* are fictitious having no physical meanings others than indicating directions of geometrical trends – and orders of magnitudes for average interactions. The latter statement means

that c_P and c_S are not necessarily the same in bulk and shear analysis of DC-DC, DC-MM, and MM-MM composites – which has been assumed in the default description. An improved default description of shape functions for these composites can be made with (7.21). As indicated in the introductory remarks to this section, more geometrical knowledge is needed to establish more accurate shape function descriptions. In this case the shape factors (μ_P^1, μ_S^1) have to be known. The stiffness predictions made in Sect. 8.3 of so-called TROC- and CROSS-composites are examples where improved shape functions have been applied.

DC-DC and MM-MM

$$\begin{aligned} \text{known shape factors } \mu_P^0, \mu_S^0, \mu_P^1, \mu_S^1 & \quad (7.21) \\ \text{alternative I description } \mu_P &= (1-c)\mu_P^0 + c\mu_P^1; \mu_S = (1-c)\mu_S^0 + c\mu_S^1 \end{aligned}$$

7.2.3 Alternative II

When enough geometrical information is at hand, shape function descriptions can be improved as demonstrated in the following example:

A special fabrication technique has been developed such that the following DC-CD composite can be produced: Up to a concentration of $c = 0.47$ the geometry is that of discrete phase P spheres in a continuous phase S. From a concentration of $c = 0.68$ the geometry is that of discrete phase S spheres in a continuous phase P. The agglomeration of P-spheres starts creating continuous phase P elements at $c = 0.52$. “De-agglomeration” of phase S into discrete spheres starts at $c = 0.63$. A skeletal microstructure defines the composite geometry in the transition area $c = 0.52 - 0.63$ where there is no clearly defined matrix and reinforcement phase.

These observations are enough to suggest shape functions to follow graphs defined by Table 7.1 and Fig. 7.24.

Table 7.1. The symbols used are explained in Fig. 7.24. Shape factors $\mu_P^0, \mu_S^0, \mu_P^1, \mu_S^1$ are from Sect. 7.1

Alternative (II) Shape Function Description	
$\mu_P = \mu_P^0$ $\mu_S = \mu_S^0$	$0 \leq c < c_{SS}$
$\mu_P = \mu_P^0(c_S - c)/(c_S - c_{SS}) + \mu_{PS}(c - c_{SS})/(c_S - c_{SS})$ $\mu_S = \mu_S^0(c_S - c)/(c_S - c_{SS})$	$c_{SS} \leq c < c_S$
$\mu_P = \mu_{PS}(c_P - c)/(c_P - c_S)$ $\mu_S = \mu_{SP}(c - c_S)/(c_P - c_S)$	$c_S \leq c < c_P$
$\mu_P = \mu_P^1(c - c_P)/(c_{PP} - c_P)$ $\mu_S = \mu_{SP}(c_{PP} - c)/(c_{PP} - c_P) + \mu_S^1(c - c_P)/(c_{PP} - c_P)$	$c_P \leq c < c_{PP}$
$\mu_P = \mu_P^1$ $\mu_S = \mu_S^1$	$c_{PP} \leq c < 1$

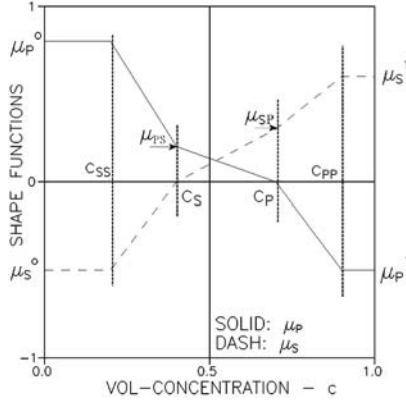


Fig. 7.24. Shape functions as defined in Table 7.1

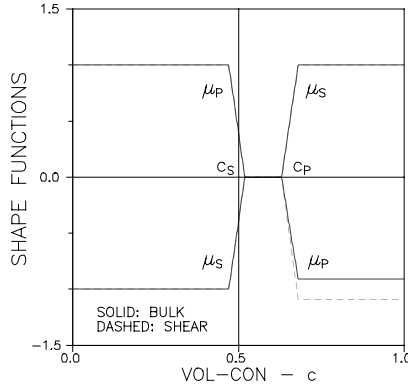


Fig. 7.25. Shape functions for a special DC-CD composite defined in the text

In the present example we have $(\mu_{PS}, \mu_{SP}) = (0, 0)$ and $(c_{SS}, c_S, c_P, c_{PP}) = (0.47, 0.52, 0.63, 0.68)$. An example with $(v_P, v_S) = (0.3, 0.2)$ is presented in Fig. 7.25.

7.3 Geo-Paths

Any of the shape functions considered in this chapter can be represented by a geo-path as outlined in Fig. 7.26.

Numbers are aspect ratios, A , of strict discs/fibers. A shape function value in DC quantifies the geometry of discrete phase P in a continuous phase S. A shape function value in CD quantifies the geometry of discrete phase S fibers in a continuous phase P. Very rugged fibers are fibers mixed with a large amount of spheres. Fiberworks are agglomerating crumbled P and S fibers. Fiber/disc

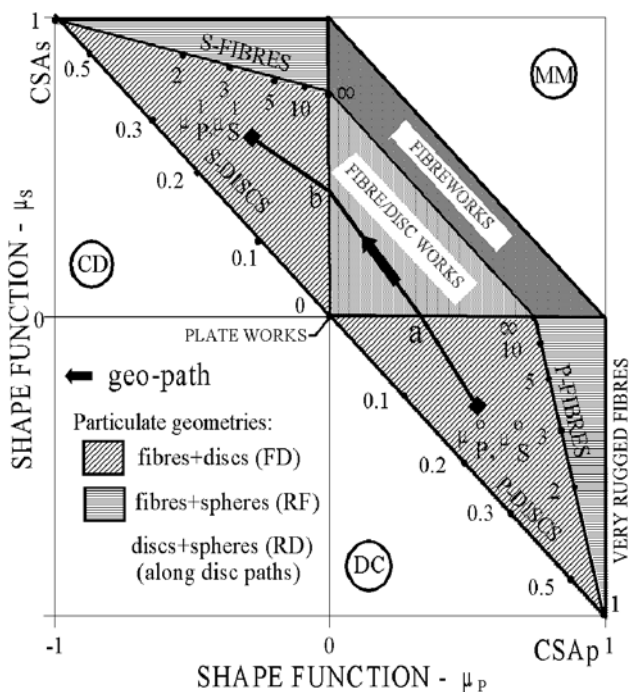


Fig. 7.26. Stylized shape function graph and geo-path (in shear). Numbers are aspect ratios, A , of strict discs/fibers. A shape function value in DC quantifies the geometry of discrete phase P in a continuous phase S. A shape function value in CD quantifies the geometry of discrete phase S fibers in a continuous phase P. Very rugged fibers are fibers mixed with a large amount of spheres. Fiberworks are agglomerating crumbled P and S fibers. Fiber/disc works are agglomerating crumbled P and S fibers and discs. Plateworks are agglomerating crumbled discs

works are agglomerating crumbled P and S fibers and discs. Plateworks are agglomerating crumbled discs.

Following the geo-path, we re-call from the introduction to this chapter that the area just below the “ x -axis” ($\mu_S = 0$) operationally should be understood as phase P particles preparing to become continuous. In the area just above the x -axis phase P particles start becoming continuous as demonstrated in Fig. 2.3. In a reversed order, similar shape transitions (now with phase S) appear around the “ y -axis” ($\mu_P = 0$).

Composite Theory – Elasticity

A composite analysis proceeds as follows for any type of composite considered. Default shape function descriptions from Sects. 7.2.1 and improved defaults descriptions from Sect. 7.2.1 as well as alternative expressions from Sects. 7.2.2 and 7.2.3 are applied. Which description is used depend on the level of geometrical knowledge present.

- Geo-functions are determined as shown in (4.16) (Chap. 4).
- Composite stresses are calculated by (4.15) (Chap. 4).
- Bulk modulus, shear modulus, Young’s modulus, and Poisson’s ratio are calculated by (5.1) and (5.4) (Chap. 5) respectively.
- Eigenstrain/stress behavior and pore-pressure/strain relations are determined by (6.6)–(6.8)(Chap. 6).

For a rational computer programming it is worth recognizing that the general stress/stiffness analysis is in fact a combination of two almost identical analyses. A volumetric analysis where geometry is considered by volumetric shape functions and a deviatoric analysis where geometry is considered by deviatoric shape functions. Formally the eigenstrain/stress analysis is a volumetric analysis.

It is anticipated that modern technologies (in the near future) can produce any composite geometry. Examples are presented which show that that the geo-path/geometry concept discussed is realistic enough to pursue experimentally.

8.1 Illustrative Examples

8.1.1 DC-CD Composite

The DC-CD composite geometry presented in Fig. 8.1 can be thought of as produced by the following process: Phase P and phase S powders are made as indicated in the capture of Fig. 8.1 The powders are mixed and compacted

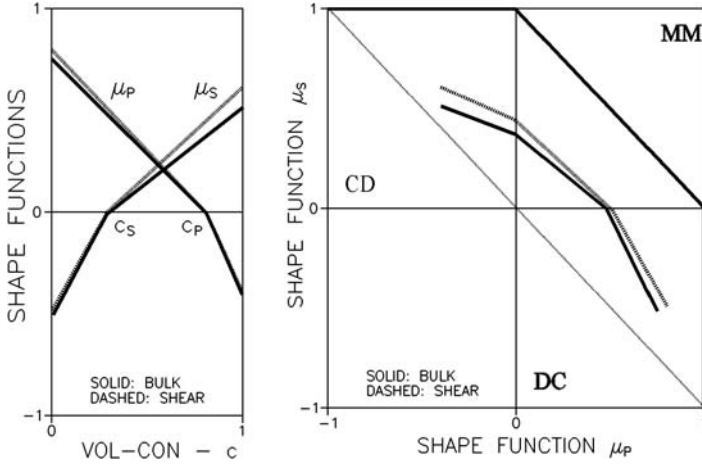


Fig. 8.1. Shape functions and geo-paths for a DC-CD composite, $(v_P, v_S) = (0.3, 0.1)$. Critical concentrations $(c_P, c_S) = (0.8, 0.3)$. Particulate mixture at $c = 0$: P -particles with 80% ($A = 3$) + 20% ($A = 0.3$). At $c = 1$: S -particles with 50% ($A = 5$) + 50% ($A = 0.2$)

(voids squeezed out) such that the phase P concentration is c – and such that the first sign of P -continuity appears at $c = c_S = 0.3$ – and that full S -discontinuity appears at $c = c_P = 0.8$. Results from a composite analysis are presented in Figs. 8.2–8.5.

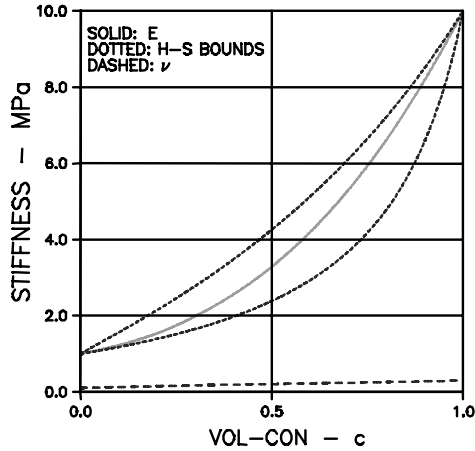


Fig. 8.2. Stiffness and Poisson's ratio of a DC-CD composite with geometry and Poisson ratios defined in Fig. 8.1. $(E_P, E_S) = (10, 1)$ MPa

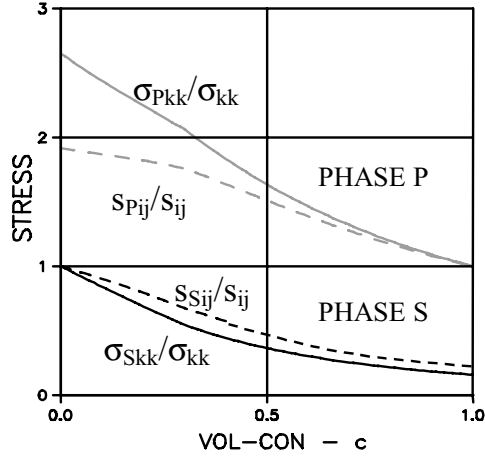


Fig. 8.3. Stresses in a DC-CD composite with geometry and Poisson ratios defined in Fig. 8.1. $(E_P, E_S) = (10, 1)$ MPa

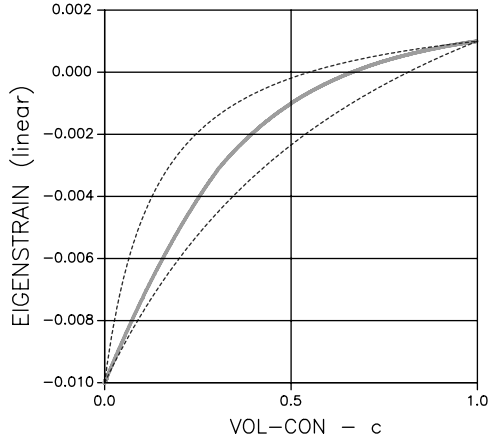


Fig. 8.4. Eigenstrain in a DC-CD composite with geometry defined in Fig. 8.1. $(\lambda_P, \lambda_S) = (0.001, -0.010)$. $(E_P, E_S) = (10, 1)$ MPa

Average geometries met at increasing concentrations of phase P can be estimated by placing the geo-path graph in Fig. 8.1 on top of Fig. 7.26.

8.1.2 Crumbled Foils Composite

The results presented in (8.1), Fig. 8.6, and Fig. 8.7 are from a composite bulk analysis of a crumbled foils composite with $(E_P, E_S) = (10, 1)$ and $v_P = v_S = 0.2$. We re-call from Sect. 4.1.4 that the composite considered is made of crumbled P -foils mixed with crumbled S -foils, producing a 3-dimensional Plywood geometry, with geo-functions determined from (4.12), (or from (7.20))

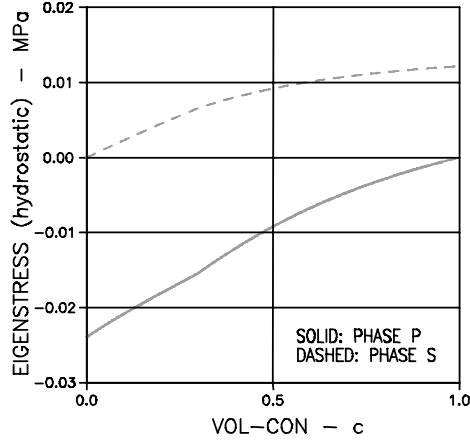


Fig. 8.5. Eigenstress a DC-CD composite with geometry defined in Fig. 8.1. $(\lambda_P, \lambda_S) = (0.001, -0.010)$. $(E_P, E_S) = (10, 1)$ MPa

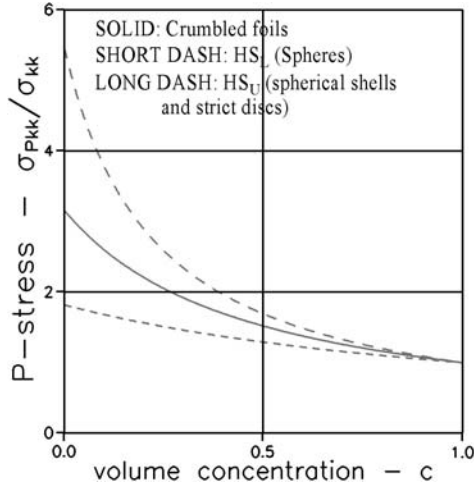


Fig. 8.6. Phase P stress in a crumbled foils composite

assuming a MM-MM geometry with a very low β).

$$\frac{\sigma_{Pkk}}{\sigma_{kk}} = \frac{\sqrt{n}}{1 + c(\sqrt{n} - 1)} ; \quad \frac{\sigma_{Skk}}{\sigma_{kk}} = \frac{1}{1 + c(\sqrt{n} - 1)} ;$$

$$k = \frac{n + \sqrt{n}[1 + c(n - 1)]}{n + \sqrt{n} - c(n - 1)} \quad (\theta_k \equiv \sqrt{n}) \quad (8.1)$$

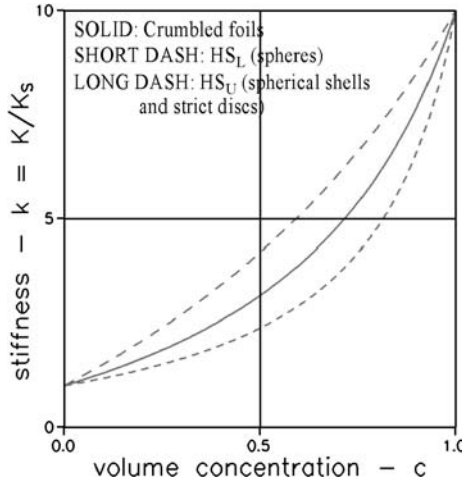


Fig. 8.7. Bulk modulus of a crumbled foils composite

8.1.3 Particulate (DC-DC) Composite

The DC-DC geometry presented in Fig. 8.8 can be thought of as being the result of mixing extremely well graded phase P particles into a solidifying phase S. An estimate of critical concentrations $c_P = c_S > 1$ is used as suggested in [24] for particulate composites.

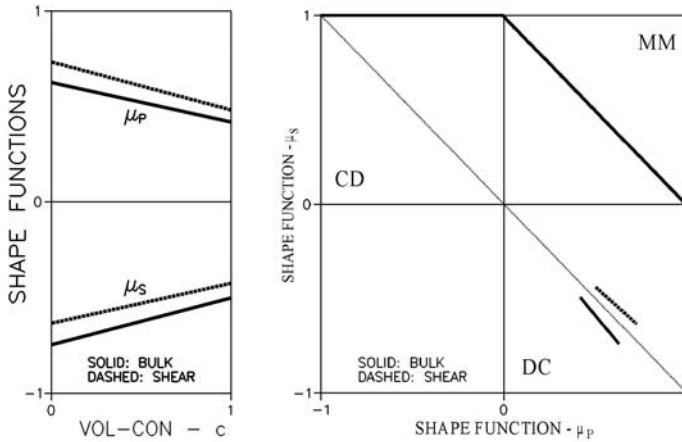


Fig. 8.8. Shape functions and geo-paths for a DC-DC composite $(v_P, v_S) = (0.2, 0.2)$. Particulate mixture at $c = 0$: P -particles: 60% ($A = 0.3$) + 40% ($A = 3$). Estimated non-real critical concentrations: $c_P = c_S = 3$

The results of a stiffness and stress analysis of the composite considered are presented in Figs. 8.9 and 8.10 respectively.

Average geometries met at increasing concentrations of phase P can be estimated by placing the geo-path graph in Fig. 8.8 on top of Fig. 7.26. Results from an eigenstrain/stress analysis are shown in Figs. 8.11 and 8.12.

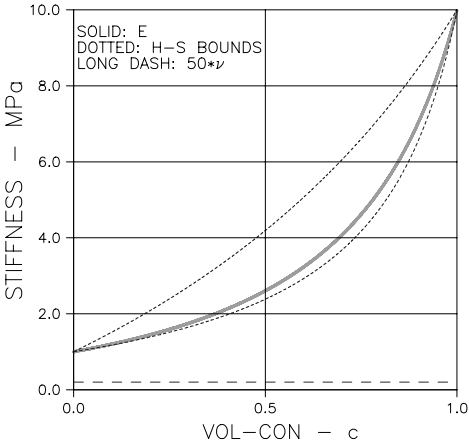


Fig. 8.9. Stiffness and Poisson's ratio of a DC-DC composite with geometry and Poisson ratios defined in Fig. 8.8. $(E_P, E_S) = (10, 1)$ MPa

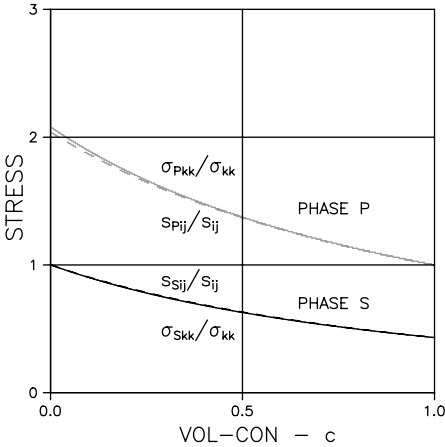


Fig. 8.10. Stresses in a DC-DC composite with geometry and Poisson ratios defined in Fig. 8.8. $(E_P, E_S) = (10, 1)$ MPa

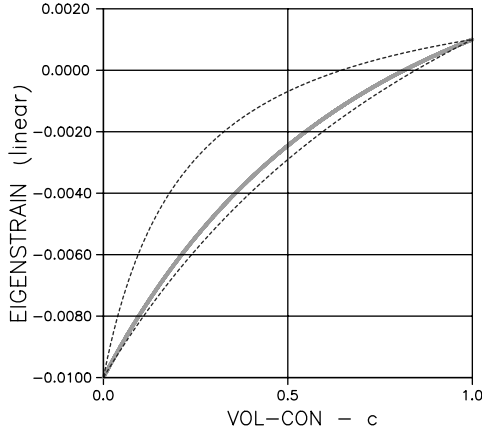


Fig. 8.11. Eigenstrain of a DC-DC composite with geometry defined in Fig. 8.8. $(\lambda_P, \lambda_S) = (0.001, -0.010)$. $(E_P, E_S) = (10, 1)$ MPa

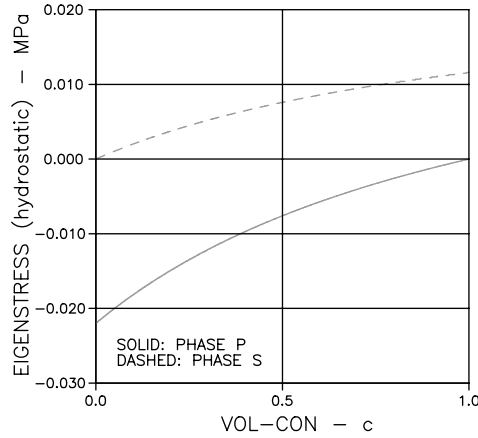


Fig. 8.12. Eigenstress in a DC-DC composite with geometry defined in Fig. 8.8. $(\lambda_P, \lambda_S) = (0.001, -0.010)$. $(E_P, E_S) = (10, 1)$ MPa

8.2 Other Examples

8.2.1 Cracks

In this section results from a crack analysis based on the present theory are compared with results analytically determined by Levin [7]. Also considered are results, which can be deduced from the FEM-analysis of defective particulate composites presented in Sects. 8.3.3 and 8.3.6. Any crack considered is strict as defined by the cylinder model in the introduction to Chap. 7 with an aspect ratio of $A \approx 0$. Also from the introduction to Chap. 7: As extremely low (or high) stiffness ratios are considered, no re-definition of flat shapes is

required. This means that a composite analysis with organic particle shapes in the present theory produce the same results as a composite analysis with strict particle shapes.

Soft Cracks

Stiffness of dilute porous materials with isotropically distributed fiber shaped voids can be written as presented in (8.2) and (8.3) derived from (5.3) and (5.4) with geo-functions from Table 4.1, and porosity of ellipsoidal voids $c = (\pi/6)pd^3$ where p is void density (number of voids per vol-unit). As usual d and A denote diameter and aspect ratio respectively of a fiber.

$$k_0 = 1 - h_k pd^3 = 1 - \frac{6h_k}{\pi A} c; \quad h_k = \frac{\pi}{6} A \left(1 + \frac{1}{\kappa_S \mu_{P_k}^0} \right) \quad (8.2)$$

$$g_0 = 1 - h_g pd^3 = 1 - \frac{6h_g}{\pi A} c; \quad h_g = \frac{\pi}{6} A \left(1 + \frac{1}{\gamma_S \mu_{P_g}^0} \right) \Rightarrow$$

$$e_0 = 1 - h_e pd^3 = 1 - \frac{6h_e}{\pi A} c; \quad h_e = \frac{h_k + 4h_g}{5} \quad (8.3)$$

Examples of the h_k and h_g factors from (8.2) are shown in Figs. 8.13 and 8.14 with shape factors (μ_P^0) calculated as explained Chap. 7. The situation of a cracked material is approached with aspect ratio $A \rightarrow 0$.

It is noticed from Figs. 8.13 and 8.14 that the crack results ($A = 0$) of the present analysis agree with results presented in (8.4) which are deduced from Levin's theoretical work [7] on materials with isotropically distributed cracks. Similar expressions can also be obtained from other works [14, 23, 68] in the field of cracked materials.

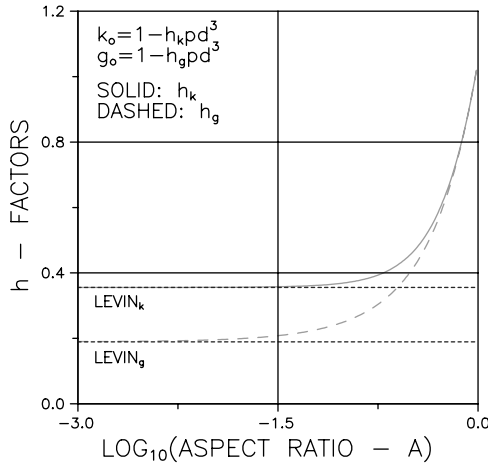


Fig. 8.13. h -factors for soft disc mixture. $v_S = 0.2$. Dotted lines, see text

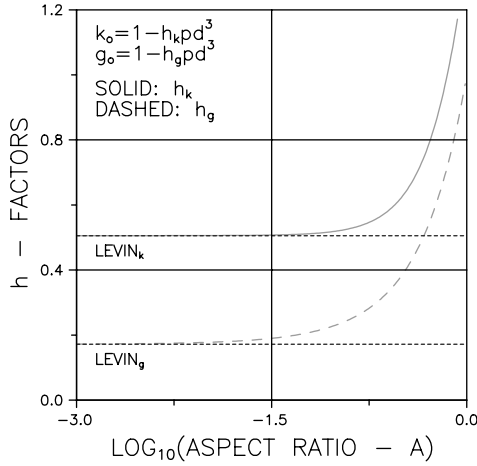


Fig. 8.14. h -factors for soft disc mixture. $\nu_S = 0.3$. Dotted lines, see text

$$h_k = \frac{2}{9} \frac{1 - \nu_S^2}{1 - 2\nu_S} ; \quad h_g = \frac{4}{45} \frac{(1 - \nu_S)(5 - \nu_S)}{2 - \nu_S} ; \quad \text{Levin } (A = 0) \quad (8.4)$$

Remarks: It is noticed from comparing the results from the present analysis with the Levin results that “thick” cracks can be considered as real cracks as long as $A < 0.01$. This feature is illustrated in Figs. 8.15 and 8.16 (with a porosity of $c = (\pi/6)pAd^3$).

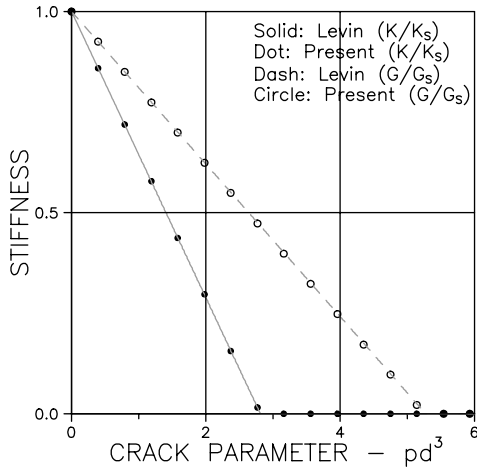


Fig. 8.15. Stiffness of material with *thick* “cracks”. $(A, \nu_S) = (0.001, 0.2)$

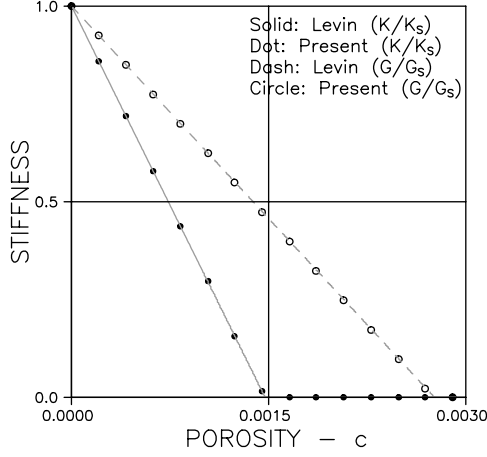


Fig. 8.16. Stiffness of material with *thick* “cracks”. $(A, \nu_S) = (0.001, 0.2)$

It is worth noticing that the results in Figs. 8.15 and 8.16 are accurately predicted also by the SCS-method presented in Appendix C with $(E_P, E_S) = (0^+, 1)$, $(\nu_P, \nu_S) = (\text{arbitrary}, 0.2)$, $A < 0.01$, and $pd^3 = 6c/(\pi A)$. The statement previously made that SCS-solutions can be considered accurate when composites considered are dilute is clearly supported by this observation where very small crack “volumes” are involved.

Stiff “Cracks”

The problem of very stiff discs in a material can be solved in a very similar way as the “soft crack” problem was solved. The results are presented in (8.5) with the h -factors illustrated in Fig. 8.17. As for soft cracks the stiff crack solutions apply also for thick cracks of finite thickness $A < 0.01$.

$$\begin{aligned} \frac{1}{k_\infty} &= 1 - h_k pd^3 = 1 - \frac{6h_k}{\pi A} c; \quad h_k = \frac{\pi A}{6} \left(1 + \kappa_S \frac{\mu_{Pk}^0 + \mu_{Sk}^0 - 1}{\mu_{Sk}^0} \right) \\ \frac{1}{g_\infty} &= 1 - h_g pd^3 = 1 - \frac{6h_g}{\pi A} c; \quad h_g = \frac{\pi A}{6} \left(1 + \gamma_S \frac{\mu_{Pg}^0 + \mu_{Sg}^0 - 1}{\mu_{Sg}^0} \right) \end{aligned} \quad (8.5)$$

Discussion

A very satisfying agreement is observed in this section between stiffness of materials with isotropically distributed cracks predicted by the present theory and results presented in [7]. It is furthermore concluded that “thick” cracks with $A < 0.01$ can be considered as real cracks.

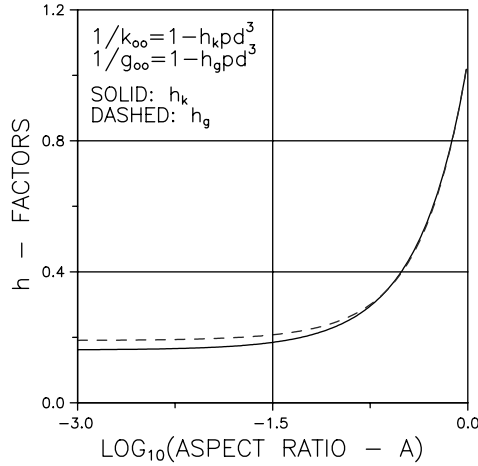


Fig. 8.17. h -factors for stiff disc mixture. $\nu_S = 0.2$

8.2.2 Special DC-CD Composites

Isotropy

The results presented in Fig. 8.19 are from an analysis of an isotropic DC-CD composite. Phase P is Silicon carbide (SiC) with $E_P = 320$ GPa and $\nu_P = 0.3$. Phase S is Carbon (C) with $E_S = 28$ GPa and $\nu_S = 0.3$. These phase properties are adopted from [15, 16] where a FEM-analysis, further discussed in the subsequent section, was made on a plane-isotropic SiC-C composite.

The composite geometry is as described in Sect. 7.2.3 for a special DC-CD composite. The alternative shape function description suggested in Sect. 7.2.3 is therefore adopted for the present analysis, see Fig. 8.18.

Remark: It is noticed that predicted stiffness and SCS-determined stiffness are very close in the geometrical transition area. It is obvious, however, that such simple procedure for stiffness estimation can only be used when the transition area is small with a “center” around $c = 0.5$.

The author is aware of no results from experimental analysis or FEM-analysis of isotropic particulate DC-CD composites to which the results predicted in this section can be compared. Implicitly, however, justifications of the theory can be found studying the results from the following FEM-analysis.

Plane-Isotropy

A FEM-analysis was made in [15, 16] on various mechanical/physical properties of a parallel-layered composite. With gradually increasing amount of phase P each layer can be considered as a plane-isotropic version of the isotropic DC-CD composite just considered: Up to a volume concentration of $c = 0.47$ the

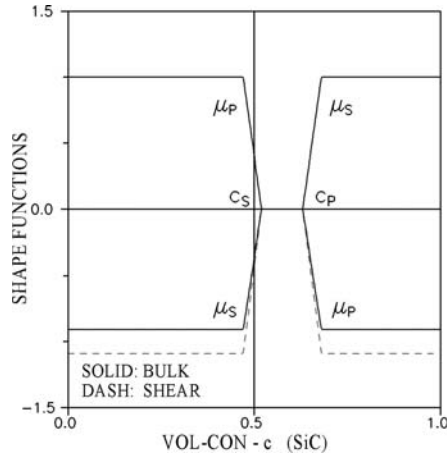


Fig. 8.18. Shape functions for a special isotropic SiC/C composite. $v_P = v_S = 0.3$

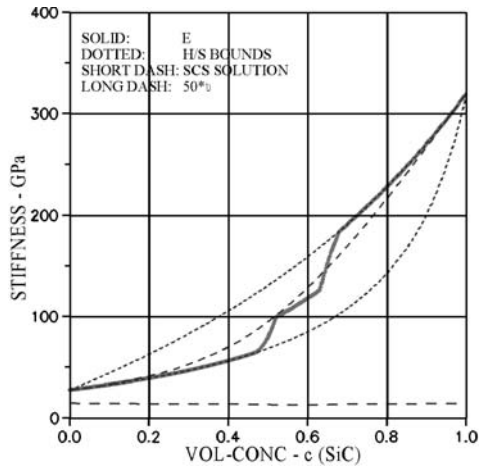


Fig. 8.19. Stiffness of a special isotropic DC-CD SiC/C composite

composite geometry is FEM-modeled by discrete phase P fibers of hexagonal cross-sections in a continuous phase S. From a concentration of $c = 0.68$ the geometry is modeled by discrete phase S fibers with hexagonal cross-sections in a continuous phase P. The agglomeration of P-fibers starts creating continuous phase P elements at $c = 0.52$. “De-agglomeration” of phase S into discrete fibers starts at $c = 0.63$.

It is observed in [16] that the numerical FEM-results obtained are very close to results which can be obtained in an analysis of the layered composite considered with each layer homogenized as follows with properties predicted by known analytical plane-isotropic composite expressions: By the Mori-Tanaka theory [11] at lower and higher concentrations (discrete cylinders

in a continuum), and by the Davies SCS-expression [69] at medium concentrations (skeletal microstructure). The “gaps” between the two estimates (at $c \approx 0.49$ and $c \approx 0.65$) were considered in [16] by some empirical “transition functions”.

The observation made in [15,16] with respect to plane-isotropic, transverse composite Young’s moduli versus phase P concentrations are presented graphically in Fig. 5 of the latter reference which is extremely well reproduced by Fig. 8.20 presenting the results of a composite analysis made using the plane-isotropic version [24, Appendix C], of the isotropic theory presented in this book.

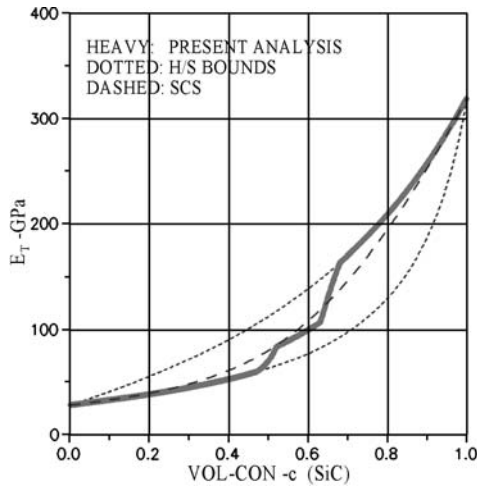


Fig. 8.20. Stiffness of plane-isotropic composite with parallel circular fibers. $(E_P, E_S) = (320, 28)$ GPa, $v_P = v_S = 0.25$

With Poisson’s ratios $v_P = v_S = 0.25$ the plane-isotropic analysis simplifies as summarized in (8.6). The difference between the actual Poisson’s ratios, $v_P = v_S = 0.3$, and values of $v_P = v_S = 0.25$ is considered small enough to use this expression as a reliable basis for numerical evaluations. Shape functions are assumed to be similar to those used in the isotropic analysis just considered in the previous section.

Plane-Isotropic Stiffness

For DC-CD composites with fibers of circular cross-sections and $v_P = v_S = 0.25$ the plane-isotropic theory referred to can be summarized as presented in (8.6) where $k_t = K_t/K_S$, $g_t = G_t/G_S$, and $e_t = E_t/E_S$, are transverse plane strain bulk modulus, transverse shear modulus, and transverse Young’s modulus normalized with respect to their respective phase S moduli. The

transverse Poisson's ratio is denoted by v_t . The stiffness ratio is $n = E_P/E_S$. SCS-solutions are very close to solutions obtained with shape functions $\mu_P = -\mu_S = 1 - 2c$.

$$\begin{aligned}
 k_t = g_t &= \frac{n + \theta[1 + c(n-1)]}{n + \theta - c(n-1)} = x \\
 e_t &= \frac{16x}{15 + x/[1 + c(n-1)]}; \quad \nu_t = 1.25 \frac{e_t}{g_t} - 1 \\
 \theta &= \frac{1}{4} \left[\mu_P + n\mu_S + \sqrt{(\mu_P + n\mu_S)^2 + 4n(1 - \mu_P - \mu_S)} \right]; \\
 \text{H/S: bounds with } \theta &\equiv \begin{cases} 1/2 \\ n/2 \end{cases}
 \end{aligned} \tag{8.6}$$

Discussion

We may conclude from this section that theoretically predicted Young's moduli of a plane-isotropic DC-CD composite agree well with results obtained by FEM-analysis. The suggestion made in [15,16] of estimating stiffness by SCS and "transition functions" in areas of geometrical transition is acceptable only in small transition areas around $c = 0.5$. The present theoretical approach of considering the transition geometry as a platework (crumbled foils) geometry is better, and more logical. This approach also provides a more continuous analysis, well qualified for computer analysis.

8.3 FEM-Analysis versus Theory

The "experimental" data presented in this section are the results of a FEM-analysis of some composite materials reported by the author in [70]. The objectives of the analysis are further explained in the subsequent Sect. 8.3.1.

Only stiffness data (including Poisson ratios) are presented. These data, however, are representatives also for composite stresses; meaning that a justification of the theory with respect to stiffness prediction automatically is a justification also with respect to stress prediction, see Chap. 3.

8.3.1 FEM-Analysis

The composite theory presented in this book is based on the concept introduced in Chap. 2 and quantified in Chap. 7 that the geometry of any isotropic composite can be thought of as stages in a process of one phase transforming its geometry from spherical to anti-spherical (spherical shell), while the geometry of the other phase in a complementary way transforms from spherical shells to spheres.

The following three composites have been chosen to test the stiffness prediction method presented and the underlying geometrical concept. The four-letter classification used refers to the path of geometrical changes explained in Chap. 2¹. “Shortcut classifications” are indicated in Italian.

- DC-DC composite: Compact particles in continuous matrix at any volume concentration (“*Particulate composite*”).
- CC-CC composite: Interconnected compact particles in continuous matrix (“*pearls on a string composite*”).
- CC-CC composite: Three-dimensional grids of one phase in complementary grids of the other phase (“*Grid composite*”). The composite considered is phase symmetric.

A special analysis of the influence of *defective phase-contacts* on composite stiffness has been made as part of the analysis of particulate composites.

Parts of the FEM-analysis have previously been reported in [24, 71]. The complete report with data compilation is presented in [70]. All FEM-results obtained are presented graphically in this chapter and discussed together with results theoretically predicted.

Data Presentation

The FEM-results presented apply to isotropic composites as converted from isotropic mixtures of cubic composites. This means that shear moduli, Young’s moduli, and Poisson’s ratios are determined as simple averages of bounds presented in [70]. This procedure is well justified, as these bounds are very close. FEM-data are shown by dots in the figures. Theoretical (predicted) data are shown by graphs. The two data sets are very close. Whenever there might be any doubt, which FEM-result “belongs” to which theoretical graph, it is always the closest graph.

Shape Factors and Shape Functions

For any of the composites considered predicted data are calculated with shape functions described by (8.7), which is the alternative shape function description suggested in Sect. 7.2.2 for the composites considered. The shape factors (μ^0, μ^1) associated are calibrated as summarized in Table 8.1.

$$\begin{aligned}\mu_P &= (1 - c)\mu_P^0 + c\mu_P^1 \\ \mu_S &= (1 - c)\mu_S^0 + c\mu_S^1\end{aligned}\tag{8.7}$$

¹ We re-call from Chap. 2 that CC-CC is classified as part of MM-MM.

Table 8.1. Summary of shape factors for DC-DC composites and CC-CC composites deduced from the FEM-analysis presented in this section with $v_P = v_S = 0.2$

Composite Type	Mode	μ_P^0	μ_S^0	μ_P^1	μ_S^1
Troc-Particulate (DC-DC)	bulk (k)	1.0	−1.0	0.95	−0.95
	shear (g)			0.5	−0.5
Pearls on a Thin String ($\alpha = 76\%$) (CC-CC)	bulk (k)	0.9	0.1	0.5	0.5
	shear (g)				
Pearls on a Thick String ($\alpha = 60\%$) (CC-CC)	bulk (k)	0.8	0.2	0.5	0.5
	shear (g)				
Cross-Grid (CC-CC)	bulk (k)	0.75	0.25	0.25	0.75
	shear (g)	0.75	0.0	0.0	0.75

8.3.2 Particulate Composite

The TROC-composite shown in Fig. 8.21 is the material model used in the FEM-analysis of particulate composites (DC-DC) with compact particles. It is a tight composition of identical composite elements each of which has the shape of a TRuncated OCtahedron with edges of equal lengths. The composite element is reinforced by a centrally placed particle the shape and orientation of which are similar to the composite element itself. Basically the TROC-material is cubic. From a modeling point of view this is no problem. Isotropic composites can be considered as isotropic mixtures of parts from cubic model sources. These sources may have different sizes of composite elements such that the final composite modeled by TROC elements can be thought of as

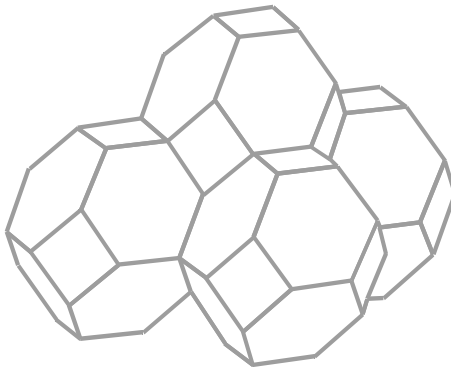


Fig. 8.21. TROC-composite. Stacked TROC composite elements

a material made by filling smaller and smaller composite elements into holes left in a stack of larger composite elements.

The FEM-data presented in Figs. 8.24–8.33 are reproduced from [70, Table 3]. The theoretical stiffness data presented are predicted with the shape functions and geo-paths illustrated in Figs. 8.22 and 8.23.

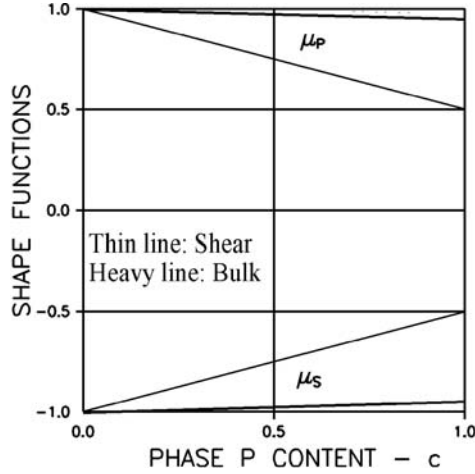


Fig. 8.22. Shape functions of DC-DC composite considered (TROC)

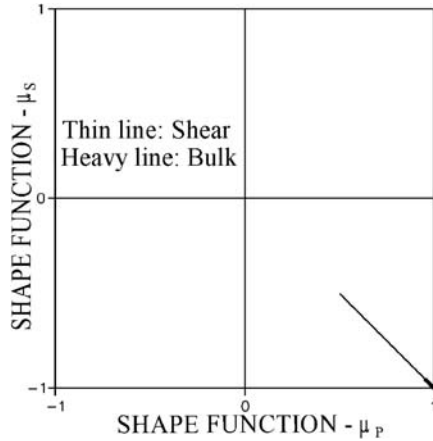


Fig. 8.23. Geo-paths for DC-DC composite considered (TROC)

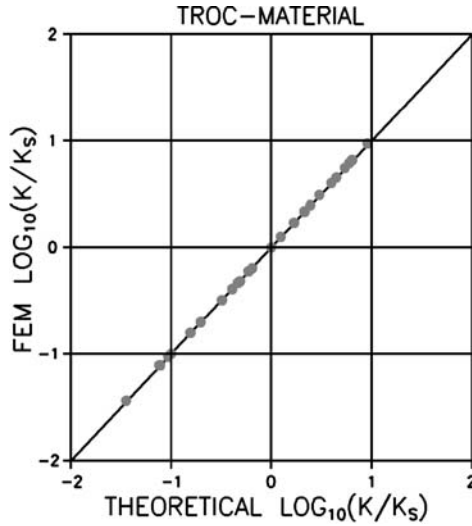


Fig. 8.24. TROC-composite with various ν -combinations: All bulk modulus data

Discussion

An excellent agreement is observed between FEM-results and results predicted theoretically with the shape functions illustrated in Fig. 8.22. We recall that these are described according to the alternative expression suggested in Sect. 7.2.2 with more detailed information on composite geometry (here μ_P^1, μ_S^1). The bulk modulus shape functions are close to $(\mu_P, \mu_S)_k \equiv (1, -1)$ which indicate that the TROC-composite behaves almost like the theoretical CSA_P -composite in volumetric compression with no interaction between phase P elements. In shear the TROC-composite behaves strictly as a CSA_P -composite only at low phase P concentrations where there is no interaction. Increasing deviations of $(\mu_P, \mu_S)_g$ from $(1, -1)$ indicate increasing interaction between phase elements.

We recall that any TROC-analysis made in this section are based on shape factors (Table 8.1) calibrated from FEM-tests where $\nu_S = 0.2$. Thus, the results with ν_S different from 0.2, presented in Figs. 8.24, 8.25, and 8.30–8.33 indicate that shape functions are not very sensitive to ν_S variations in the area 0–0.4. It has previously been indicated that the influence of ν_P on DC-DC shape factors is insignificant. Thus, DC-DC shape functions can practically be considered to be independent of Poisson's ratios.

8.3.3 Defective Particulate Composite

A special FEM-analysis was made on TROC-composites with thin layers of “voids” (or zones of missing phase contact) spread over the surface of the particle phase. Such zones were introduced by simple joint cutting and by finite

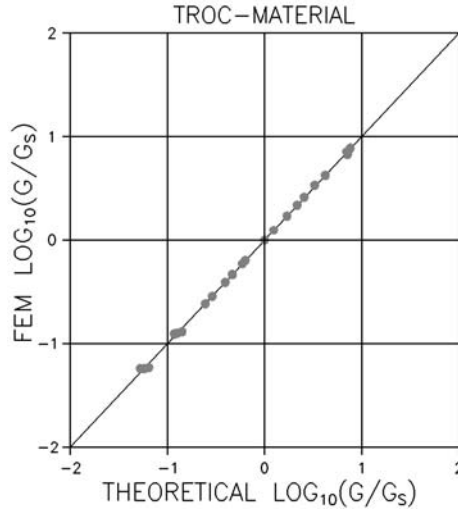


Fig. 8.25. TROC-composite with various ν -combinations. All shear modulus data (bounds)

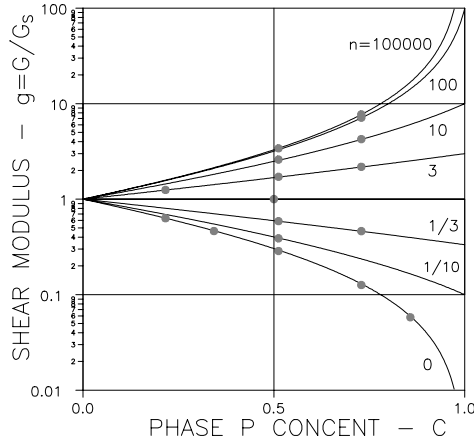


Fig. 8.26. TROC-composite with $v_S = v_P = 0.2$. Shear modulus

elements of no stiffness. Sufficient openings are assumed between opposite zone faces such that load does not produce closure effects. The degree of missing phase contact χ is defined in (8.8) together with concentration c_a of associated void volume, relative to composite volume. Particle surface is denoted by S . Thickness of void, relative to mean radius vector of particle, is denoted by Δ .

$$\begin{aligned} \chi &= S_{\text{INACTIVE}}/S_{\text{TOTAL}} \text{ degree of missing phase contact} \\ c_a &= \chi c[(1 + \Delta)^3 - 1] \text{ associated void volume} \end{aligned} \quad (8.8)$$

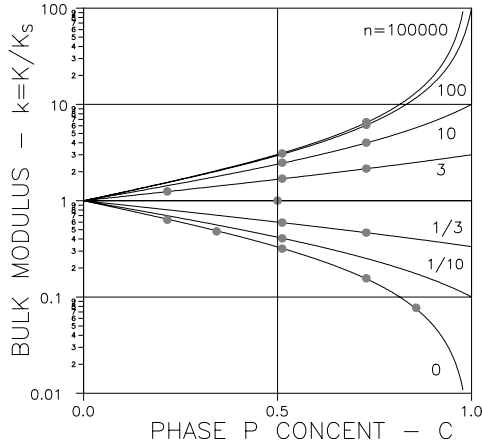


Fig. 8.27. TROC-composite with $v_S = v_P = 0.2$. Bulk modulus

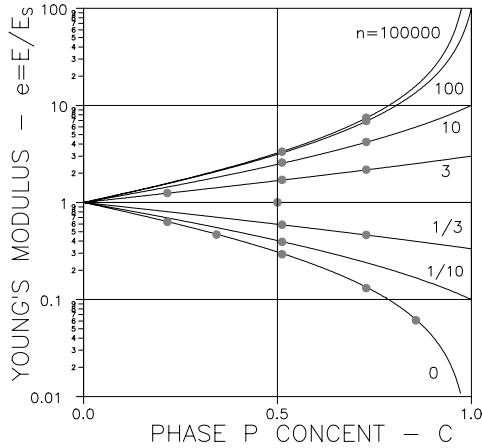


Fig. 8.28. TROC-composite with $v_S = v_P = 0.2$. Young's modulus

The FEM-data presented in Figs. 8.34–8.36 are reproduced from [70, Table 6]. These data cannot be used for verification of the theory presented in this book where perfect phase contact is assumed in general. They can, however, be used to suggest an approximate method by which the Young's modulus of defective particulate composites with compact particles can be predicted. This feature is discussed just below.

Discussion

The hypothesis is suggested that Young's modulus of defective particulate composites can be approximated with the Young's modulus of a CSA_P -composite with a defect-dependent phase P stiffness, $E_{P, \text{EFF}}$. At the same

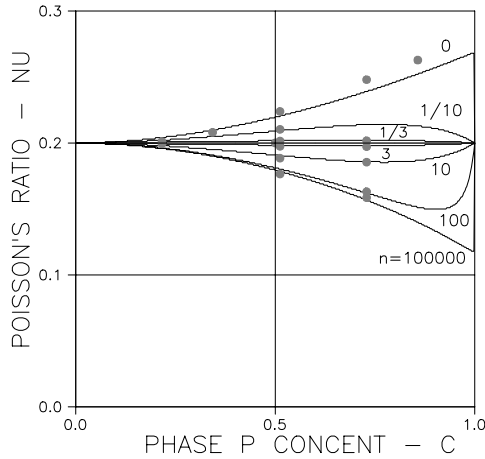


Fig. 8.29. TROC-composite with $\nu_S = \nu_P = 0.2$. Poisson's ratio

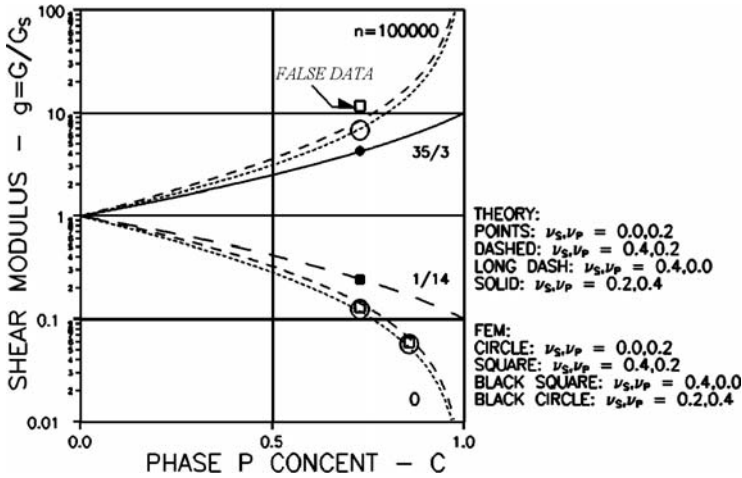


Fig. 8.30. TROC-composite with $\nu_S \neq \nu_P$. Shear modulus

time voids associated with defective areas can be considered by a simple reduction factor, f . The resulting stiffness expression (8.9), comes from (5.4) and (5.5) with $\nu_P = \nu_S = 0.2 \Rightarrow \kappa_S = \gamma_S = 1$.

The effective stiffness, $E_{P, \text{EFF}}$, and the reduction factor, f , are determined by (8.10), calibrating the hypothesis (8.9) to FEM-results. Few larger defective areas are considered with the lower distribution parameter b . Many smaller defective areas are considered with a higher b .

“Theoretical” data calculated by (8.9) are presented in Figs. 8.34–8.36 with solid lines. The hypothesis considered seems well justified by these figures. This conclusion is consistent with results obtained in a work reported in [71]

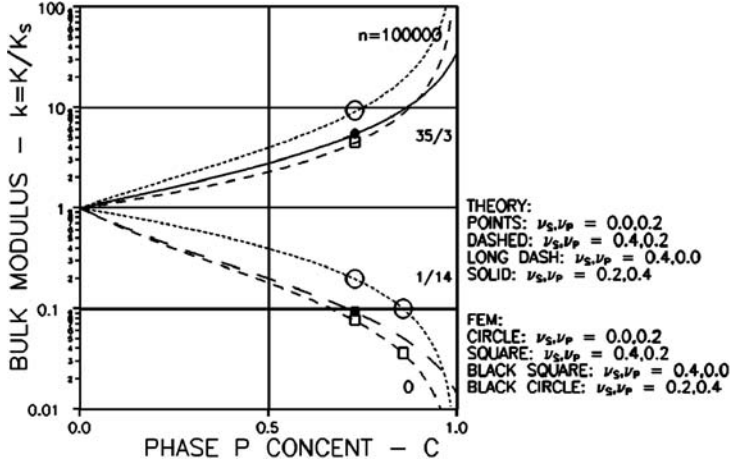


Fig. 8.31. TROC-composite with $\nu_s \neq \nu_p$. Bulk modulus

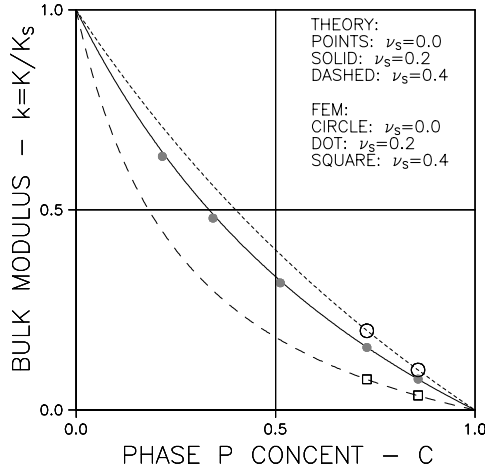


Fig. 8.32. Porous TROC-composite with different Poisson's ratios ν_s . Bulk modulus

on particulate composites with defective phase contacts. Only Young's moduli have been considered in this section. The FEM-results in [70, Table 6] indicate, however, that the influence of defective phase contacts on Young's moduli, bulk moduli, and shear moduli can be estimated in similar ways.

$$e \approx \frac{n_{\text{EFF}} + 1 + c(n_{\text{EFF}} - 1)}{n_{\text{EFF}} + 1 - c(n_{\text{EFF}} - 1)} * f; \quad n_{\text{EFF}} = \frac{E_{P, \text{EFF}}}{E_S} \quad \text{with} \quad (8.9)$$

$$E_{P, \text{EFF}} \approx E_P(1 - \chi^a) \quad \text{with} \quad a = \max\left(1, \frac{b}{5+n}\right); \quad b = 7 - 15; \quad n = \frac{E_P}{E_S} \quad (8.10)$$

$$f = 1 - zc_a \quad \text{with} \quad z \approx 1.5$$

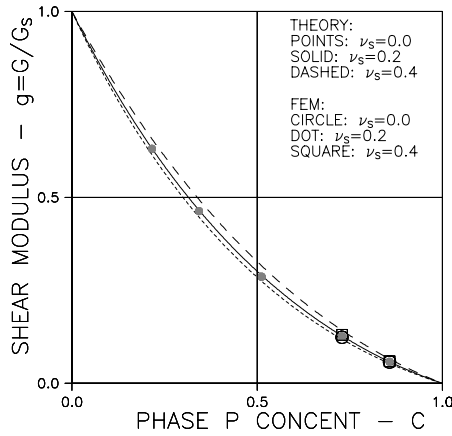


Fig. 8.33. Porous TROC-composite with different Poisson's ratios ν_s . Shear modulus

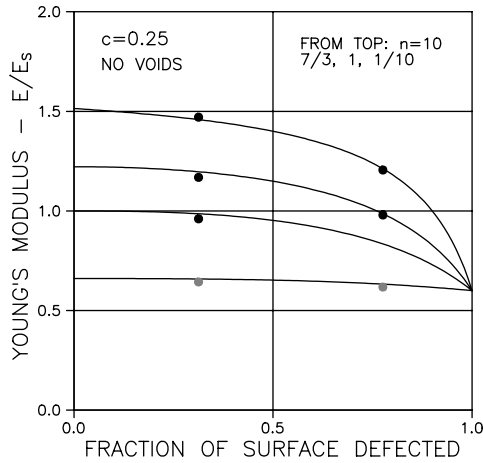


Fig. 8.34. Defective TROC with both $\nu = 0.2$. Prediction with $b = 15$

8.3.4 Pearls on a String Composite

A special FEM-analysis was made on TROC-materials where particles grow together changing phase P from being discrete to being continuous like pearls on a string – or in other words, from being a *closed “pore” system* to being an *open “pore” system*. The growing together zones were introduced by letting phase S FEM-elements between TROC-particles take the phase P elastic properties. The term “open” is used because the composite may be thought of as an impregnated porous material with a fully continuous pore systems.

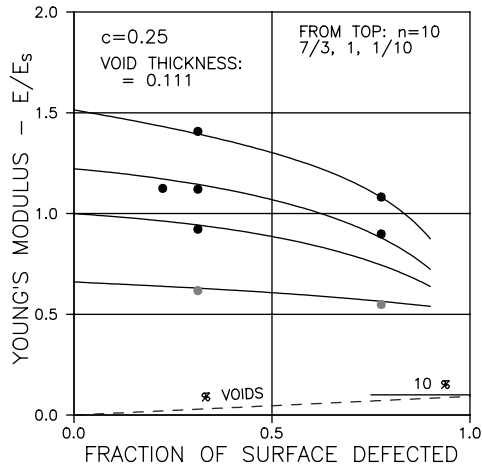


Fig. 8.35. Defective TROC with $v_P = v_S = 0.2$. ($b = 15$ and $z = 1.5$)

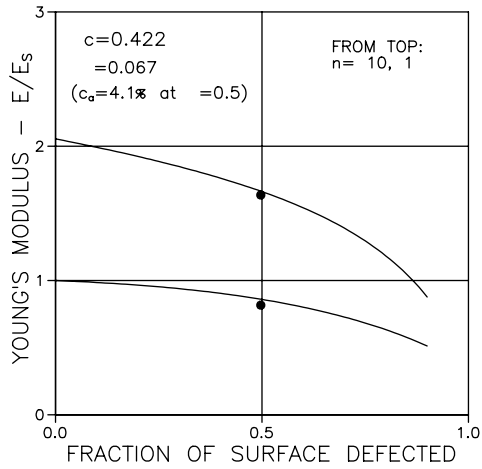


Fig. 8.36. Defective TROC with both $v = 0.2$. Prediction with $b = 15$

The phase P volume occupied by TROC-particles is quantified by the volume fraction α of the total phase P volume. α is large for *pearls on a thin string* and small for *pearls on a thick string* geometry.

The FEM-data presented in Figs. 8.41 and 8.42 are reproduced from [70, Table 9]. The theoretical data presented are predicted with CC-CC shape functions presented in Figs. 8.37 and 8.38 for $\alpha = 0.76$, and in Figs. 8.39 and 8.40 for $\alpha = 0.60$ with shape factors as summarized in Table 8.1. “Closed system” data presented in Figs. 8.41 and 8.42 are added from the analysis of TROC-composites in Sect. 8.3.2.

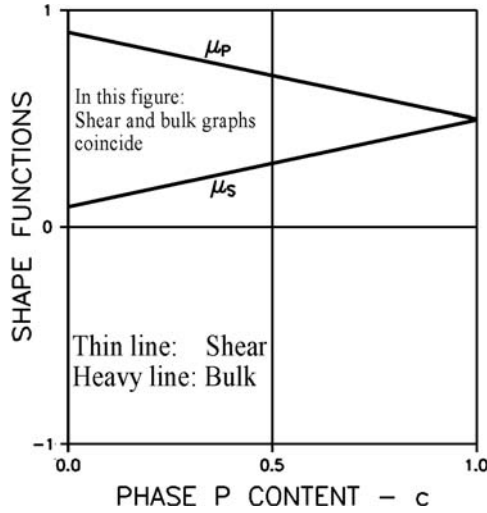


Fig. 8.37. Shape functions for a pearls on a thin string composite ($\alpha = 76\%$)

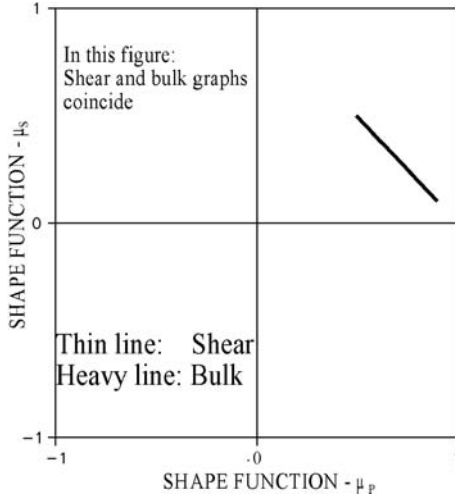


Fig. 8.38. Geo-paths for a pearls on a thin string composite ($\alpha = 76\%$)

Discussion

A very fine agreement is observed between FEM-results and results predicted theoretically with the shape functions represented by Figs. 8.37–8.40. It is noticed that $\mu_P + \mu_S = 1$ applies for both the bulk modulus shape functions and the shear modulus shape functions independently of thickness (α) of strings.

Shape factors $\mu_P^0 > 0.75$ are expected because the phase P geometry at low phase P concentrations can be considered as a frame work formed by

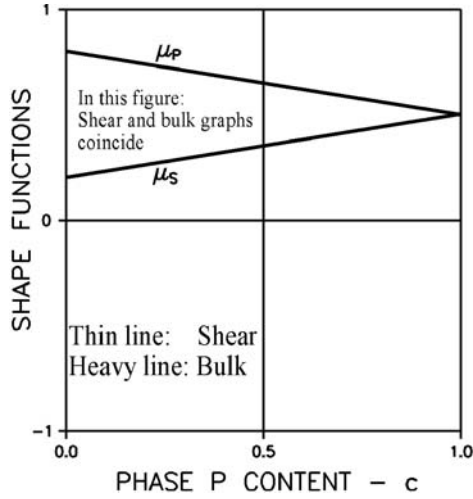


Fig. 8.39. Shape functions for a pearls on a thick string composite, ($\alpha = 60\%$)

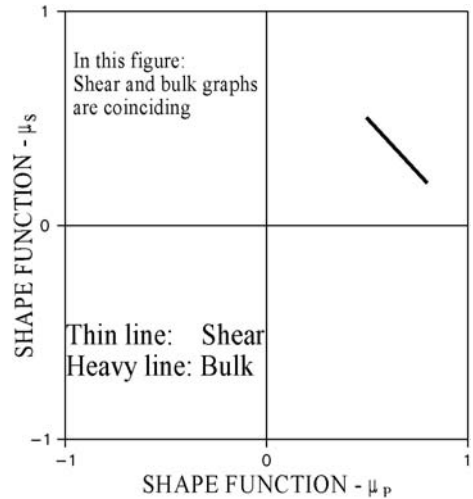


Fig. 8.40. Geo-paths for a pearls on a thick string composite, ($\alpha = 60\%$)

an agglomeration of long rugged fibers, see Fig. 7.14. Individually such fibers have shape factors >0.75 increasing with increasing degree of ruggedness (increasing fraction of spherical shapes). In the present context of pearls on a string this means that the higher shape factors, μ_P^0 , should apply at $\alpha = 76\%$, which is also the case, see Fig. 8.38 versus Fig. 8.40.

The influence of pore geometry on the stiffness of porous materials impregnated with a stiff impregnant ($n > 1$) is clearly demonstrated in Figs. 8.41 and

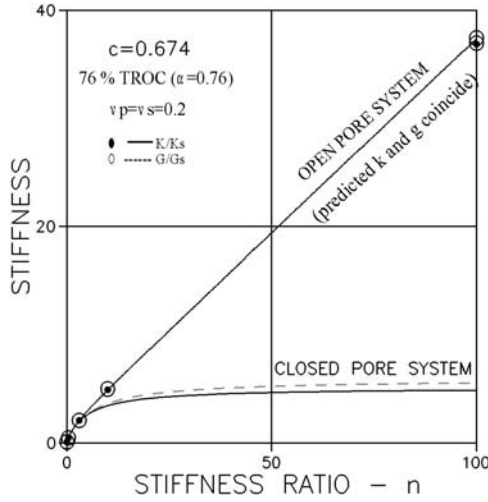


Fig. 8.41. Pearls on a thin string, $v_S = v_P = 0.2$, 76% of phase P is TROC

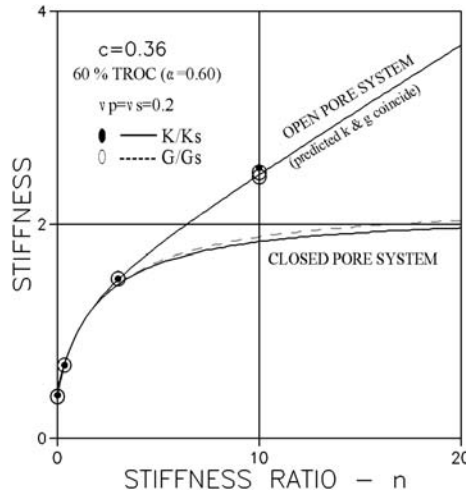


Fig. 8.42. Pearls on a thick string, $v_S = v_P = 0.2$, 60% of phase P is TROC

8.42: Composite stiffness increases considerably when pores transform from discrete (closed) pores to continuous (open) pores.

8.3.5 Grid Composite

The CROSS-composite shown in Fig. 8.43 is the material model used in the FEM-analysis of grid composites (CC-CC). It is a phase symmetric cubic framework of phase P embedded in a complementary cubic framework of phase S. Basically the CROSS-material is cubic. From a modeling point of view this

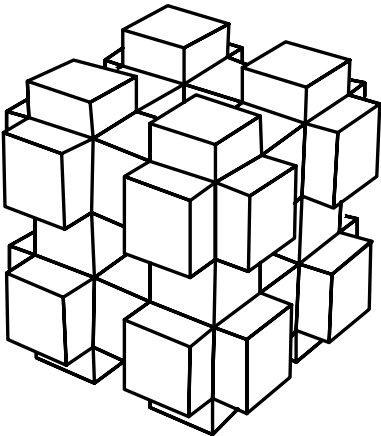


Fig. 8.43. CROSS composite. As illustrated, $c = 0.5$

is no problem as previously indicated. Isotropic composites can be considered as isotropic mixtures of parts from cubic model sources. These sources may have different sizes of composite elements.

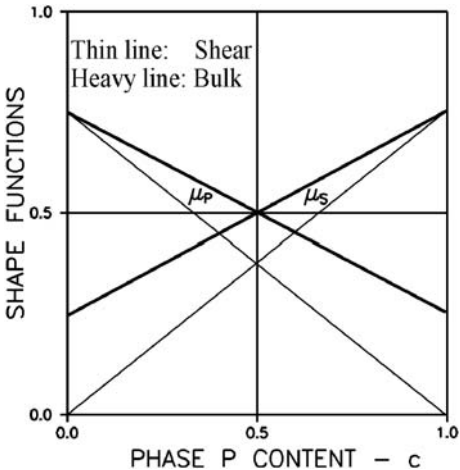


Fig. 8.44. CROSS-composite: Shape functions

The FEM-data presented in Figs. 8.46–8.53 are reproduced from [70, Table 12]. The theoretical data presented are based on the phase symmetric CC-CC shape functions illustrated in Figs. 8.44 and 8.45 with shape factors summarized in Table 8.1.

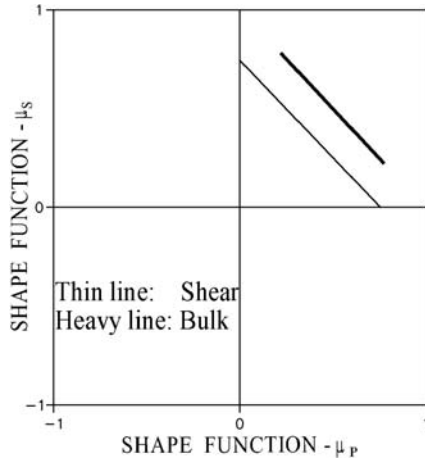


Fig. 8.45. CROSS-composite: Shape function graph

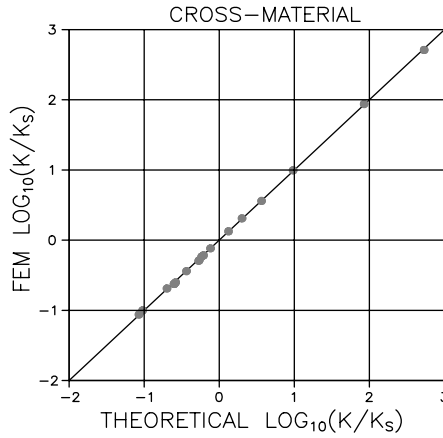


Fig. 8.46. CROSS-composite with $v_s = v_p = 0.2$: All bulk modulus data

Discussion

A very fine agreement is observed between FEM-results and predicted results. It is observed that $(\mu_P + \mu_S)_g = 0.75$ and $(\mu_P + \mu_S)_k = 1$. Shape factors $\mu_{Pk}^0 \approx \mu_{Pg}^0 \approx 0.75$ were expected because the CROSS-model at low phase P concentrations can be considered as a framework formed by agglomeration of long fibers, see Fig. 7.14. The shape function μ_{Pg} decreases more rapidly than μ_{Pk} , indicating that shear interaction is greater than bulk interaction – just as was observed in the TROC analysis.

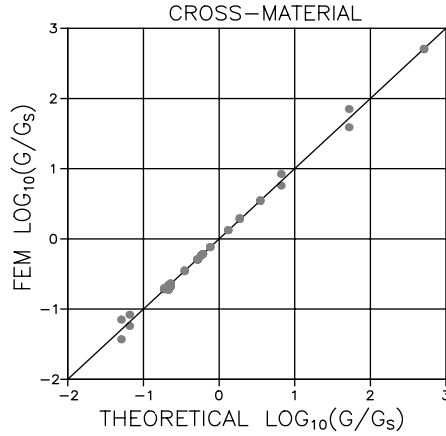


Fig. 8.47. CROSS-composite with $v_S = v_P = 0.2$: All shear data (bounds)

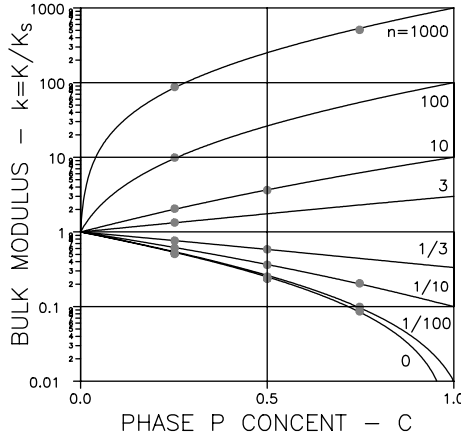


Fig. 8.48. CROSS-composite with $v_S = v_P = 0.2$: Bulk modulus

8.3.6 Cracked Material

Some results were presented in Sect. 8.3.3 from a FEM-analysis on defective “composites” with $(n, \nu_P = \nu_S) = (1, 0.2)$. This composite is in fact a cracked material with cracks placed on hypothetical TROC particles. These cracks, however, are not isotropically distributed. They form a certain pattern by which the original material in the end will transform to a porous material of finite stiffness with TROC shaped pores. We do not, therefore, expect the results of the FEM-analysis to be accurately predicted by (8.2) and (8.3).

It is, however, of some interest to compare the two data sets. This is done in Fig. 8.54 with crack parameters (pd^3) and aspect ratios (A) calculated in [70, Sect. “Defective particulate composite”]. The comparison is satisfying. As can be seen from Fig. 8.54, the FEM-results are somewhat underestimated

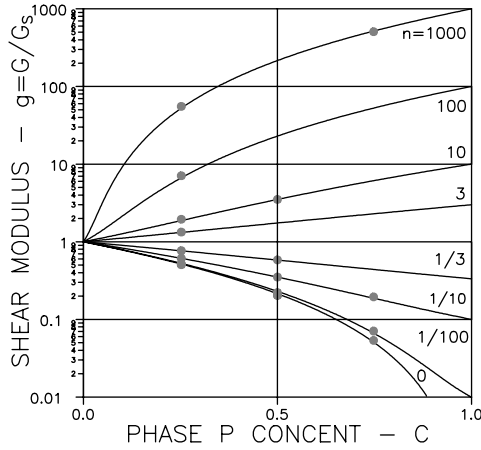


Fig. 8.49. CROSS-composite with $v_S = v_P = 0.2$: Shear modulus

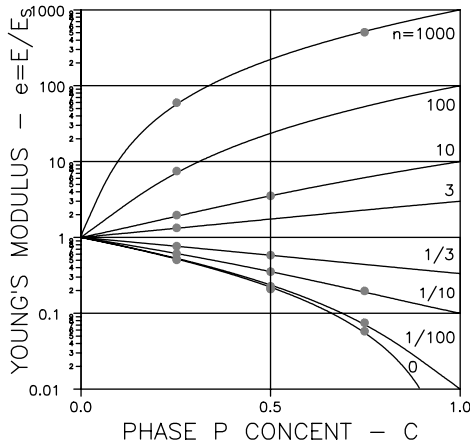


Fig. 8.50. CROSS-composite with $v_S = v_P = 0.2$: Young's modulus

by the theory because the cracks are defined to follow paths on imaginary TROC-particles ($n = 1$), creating, at the end, a porous material of finite stiffness.

8.3.7 Discussion of FEM-Analysis

The influence on composite stiffness of two very different types of composite geometries have been FEM-analyzed in this section: The TROC-composite with a DC geometry at any concentration – and the CROSS-composite with a CC geometry at any concentration.

A very satisfying agreement is observed between stiffness results obtained by FEM-analysis of these composites and results obtained by the theory

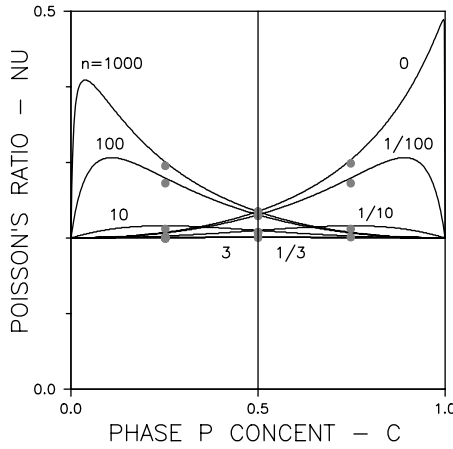


Fig. 8.51. CROSS-composite with $\nu_S = \nu_P = 0.2$: Poisson's ratio

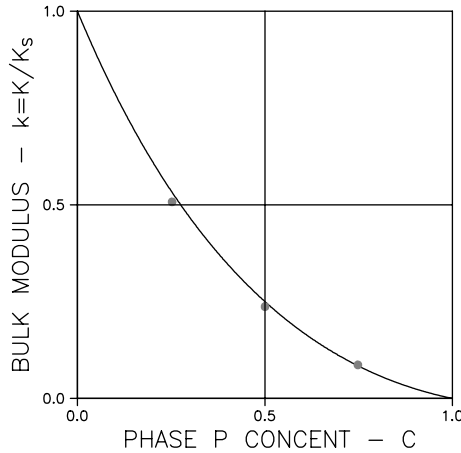


Fig. 8.52. Porous CROSS-composite with $\nu_S = 0.2$: Bulk modulus

developed in this book. Shape functions used in the theory are fully compatible with such expected from the analysis in Chap. 7 on shape quantification.

The composite geometries considered represent important “stations” on the path of geometrical changes, $DC \rightarrow CC \rightarrow CD$. The TROC geometry is the start of this path. The CROSS geometry is the middle of the path – and a $TROC_S$ geometry (phase S particles) is the end of the path. It is expected that other composites along the path just indicated can also be considered by the theory developed. For example: DC-MM and DC-CD composites. Support to this expectation is obtained from the very satisfying agreement observed in Sect. 8.3.4 between stiffness results of “Pearls on a string” composites obtained

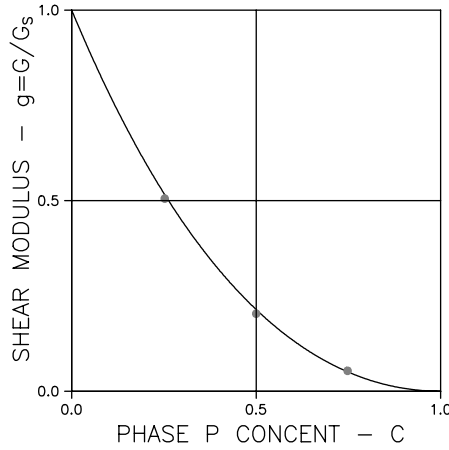


Fig. 8.53. Porous CROSS-composite with $v_s = 0.2$: Shear modulus

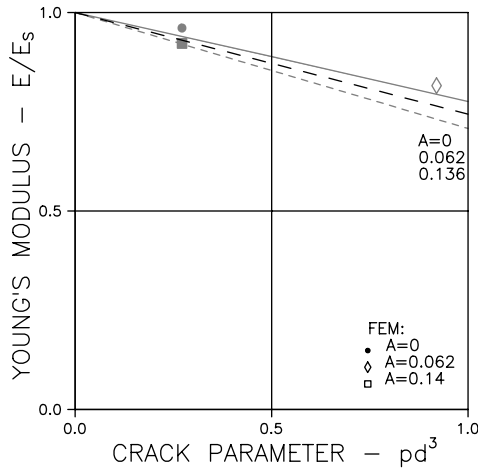


Fig. 8.54. Lines: Isotropically cracked material. FEM-data: Cracks placed on hypothetical TROC-particles. $v = 0.2$ all over

by FEM-analysis and by theoretical predictions. The phase P geometry of this composite can be seen as a framework made of long rugged fibers, see Fig. 7.14.

An important conclusion can be made from the analysis of Pearls on a string composites: Stiffness of porous materials impregnated with a stiff impregnant will increase considerably when pores transform from discrete (closed) pores to continuous (open) pores.

Finally, from the FEM-analysis of TROC-composites: A semi-theoretical method is suggested in Sect. 8.3.3 on, how defective phase contacts can be considered in stiffness predictions of particulate composites. The method is subsequently justified by experimental results presented in Sect. 10.4.6.

8.4 Conclusion

A general analysis of stiffness and eigenstrain/stress behavior has been presented in this chapter. Important aspects of this analysis, including the underlying geometrical concepts, have been checked successfully:

- Stiffness predictions of various composites, DC-DC, MM-MM, and DC-CD, compare positively with results obtained by FEM-analysis.
- Stiffness predictions of cracked materials compare positively with results obtained by FEM-analysis and theoretical results obtained by other authors.
- From the CROSS analysis presented in Sect. 8.3.5 is noticed that shape functions reverse from (μ_P^0, μ_S^0) at $c = 0$ to $(\mu_P^1, \mu_S^1) = (\mu_S^0, \mu_P^0)$ at $c = 1$ where composite geometries have reversed. The same observation can be made from looking at the special DC-CD composite analysis presented in Sect. 8.2.2.
- From the latter analysis is also observed that composite geometry changes from DC to CD through a transition area with shape functions $(\mu_P, \mu_S) \equiv (0, 0)$. These observations speak in favor of the concept, introduced in Chap. 4, of considering transition geometries as the result of discrete shapes agglomerating into crumbled continuous shapes.

It seems now justified to suggest that the theory developed in this book can be used in a complete analysis of isotropic composite materials with arbitrary geometries. Results from real experiments reported in subsequent chapters support this statement. We re-call that positive conclusions with respect to stiffness predictions automatically imply positive conclusions with respect to stress and eigenstrain/stress predictions.

Composite Theory – Conductivity

Many physical properties are proportionality constants between fluxes and potential gradients (just as Young's modulus is proportionality constant between stress and strain), e.g. thermal and electrical conductivities, and diffusion coefficients. Other physical properties are proportionality constants between inductions and force field strengths, e.g. dielectric constants and magnetic permeabilities. A composite materials analysis with respect to any of these properties will, by analogy, follow the same pattern and produce similar solutions. For example, expressions developed to predict the bulk stiffness of composites can also be used to predict thermal conductivity of composites. Of course appropriate substitutions of notations have to be introduced (including proper transformation of vector field phenomenon (stiffness) to scalar field phenomenon (like thermal conductivity)). The existence of an analogy is clearly observed comparing the works on dielectric properties by Hashin [72] and Hashin and Shtrikman [73] on CSA materials with the same authors analysis [3, 4] previously referred to on stiffness of such materials.

The bulk stiffness expressions presented in this book for composites of arbitrary geometry are generalized by the author [24] to include other physical properties only by introducing $v_S = v_P = 0$ into the geometry function θ_k , which means $\kappa_S = \kappa_P = 2$ and bulk shape factors determined for $v_S = v_P = 0$.

Note: The term conductivity is subsequently used as a synonym for any of the scalar field properties previously considered. This means, for example that the solutions subsequently presented apply to both thermal conductivity and electrical conductivity as well as to dielectricity and magnetic permeability.

9.1 Theory

The results of the analogy presented above are summarized in (9.1)–(9.3). The bounds presented in the latter expression are the exact conductivities for CSA_P and CSA_S composites respectively. They correspond to $\theta_Q \equiv 2$ and $\theta_Q \equiv 2n_Q$ respectively, see Fig. 9.1.

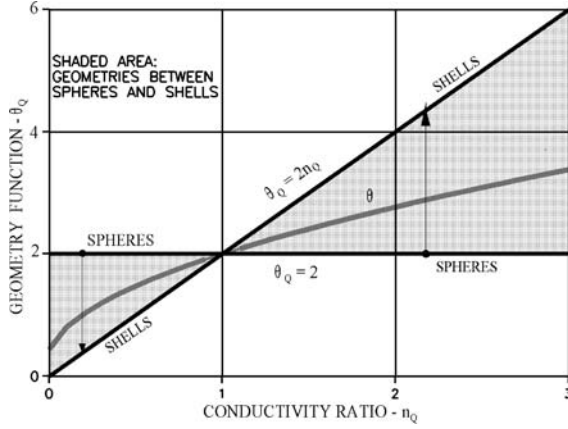


Fig. 9.1. Influence of phase P geometry on geometry function

$$q = \frac{Q}{Q_s} = \frac{n_Q + \theta_Q[1 + c(n_Q - 1)]}{n_Q + \theta_Q - c(n_Q - 1)} ; \quad \left(n_Q = \frac{Q_P}{Q_S} \right) \quad (9.1)$$

$$\theta_Q = \mu_P + n_Q \mu_S + \sqrt{(\mu_P + n_Q \mu_S)^2 + 4n_Q(1 - \mu_P - \mu_S)} \quad (9.2)$$

$$\frac{n_Q + 2[1 + c(n_Q - 1)]}{n_Q + 2 - c(n_Q - 1)} \leq q \leq n_Q \frac{3 + 2c(n_Q - 1)}{3n_Q - c(n_Q - 1)} ; \quad n_Q \geq 1 \text{ (reverse “<” when } n_Q < 1) \quad (9.3)$$

We notice that the left side expression in (9.3) equals the well-known Maxwell relation for electrical and magnetic permeability [118] of particulate composites with spherical particles.

It is emphasized that composite geometry is considered in conductivity analysis just as in stiffness analysis, meaning that shape functions to introduce into (9.2) are the bulk shape functions determined in Chap. 7 (with $v_P = v_S = 0$). Then the basic shape factor graph becomes the one shown Fig. 9.2.

9.2 Illustrative Examples

Results from a conductivity analysis of the DC-CD composite defined in Fig. 9.3 are presented in Fig. 9.4. The composite considered has previously been subjected to a stiffness analysis in this book; see Sect. 8.1.1, Figs. 8.1 and 8.2.

9.2.1 Porous Materials and Stiff Pore Systems

It comes immediately from (9.2) and the analogy previously explained ($\kappa = 2$) that the conductivity of particulate composites with very “soft” ($n_Q = 0$)

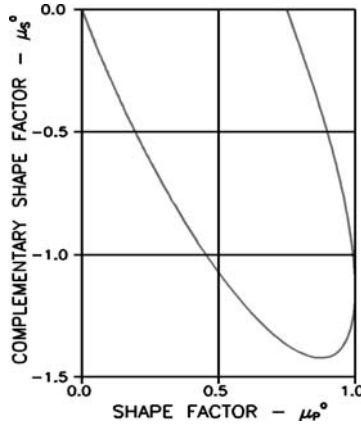


Fig. 9.2. Shape factor graph for conductivity analysis

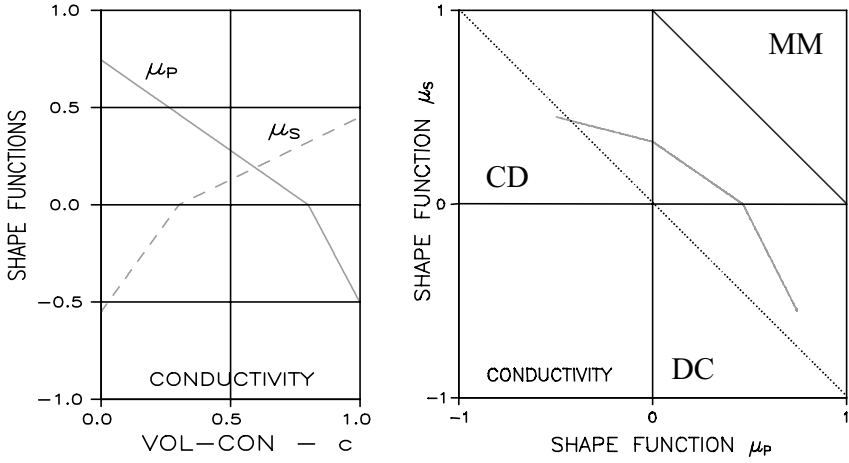


Fig. 9.3. Shape functions and geo-path for a DC-CD composite with $(c_P, c_S) = (0.8, 0.3)$. At $c = 0$: P -particles: 80% ($A = 3$) + 20% ($A = 0.3$). At $c = 1$: S -particles 50% ($A = 5$) + 50% ($A = 0.2$)

particles and very “stiff” particles ($n_Q = \infty$) can be written as presented in (9.4).

$$q_0 = \frac{Q_0}{Q_S} = \frac{1-c}{1+c/\theta_0} \quad \text{with } \theta_0 = \begin{cases} 2\mu_P & \text{when } c < c_P \\ 0 & \text{when } c > c_P \end{cases}$$

$$q_\infty = \frac{Q_\infty}{Q_S} = \frac{1+\theta_\infty c}{1-c} \quad \text{with } \theta_\infty = \begin{cases} 2\frac{\mu_P + \mu_S - 1}{\mu_S} & \text{when } c < c_S \\ \infty & \text{when } c > c_S \end{cases} \quad (9.4)$$

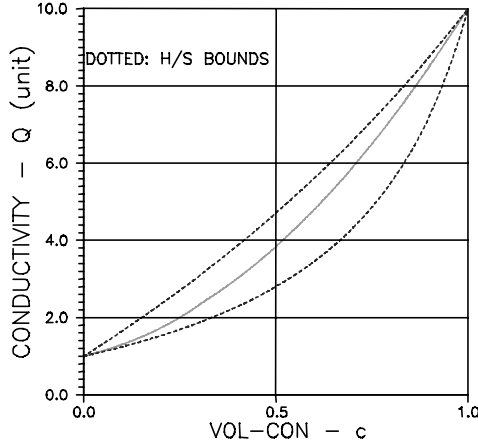


Fig. 9.4. Conductivity of composite as defined in Fig. 9.3. $(Q_P, Q_S) = (10, 1)$, same units

9.2.2 Dilute Porous Materials and Stiff Pore Systems

The conductivities of dilute systems are obtained introducing $c \rightarrow 0$ into (9.4). The results are presented in (9.5).

$$q_0 = 1 - \left(1 + \frac{1}{2\mu_P^0}\right)c; \quad q_\infty = 1 + \left(1 + 2\frac{\mu_P^0 + \mu_S^0 - 1}{\mu_S^0}\right)c \quad (9.5)$$

Notes: Special solutions obtained by (9.5) are presented in (9.6). They agree with results obtained in [47, 48] for spheres and in [50] for fibers. The disc (crack) result is presented only for the sake of completeness. Cracks have no volume.

$$\begin{aligned} \text{Spheres } (A = 1) : \quad & q_0 = 1 - 1.5c; \quad q_\infty = 1 + 3c \\ \text{Fibres } (A = \infty) : \quad & q_0 = 1 - \frac{5}{3}c; \quad q_\infty = 1 + \infty c \\ \text{Discs (cracks) } (A = 0) : \quad & q_0 = 1 - \infty c; \quad q_\infty = 1 + \infty c \end{aligned} \quad (9.6)$$

9.2.3 Cracked Materials (Soft and Stiff Cracks)

The conductivity of materials with cracks (soft cracks, $n_Q = 0$) or stiff “cracks” ($n_Q = \infty$) can be considered by (9.5). We introduce $c = (\pi/6)pAd^3$ where p is crack density (number of cracks per vol-unit), A is aspect ratio of (ellipsoidal) fiber considered (with $A \rightarrow 0$), and d is crack (fiber) diameter. We get

$$\begin{aligned} q &= 1 - h_q pd^3 \text{ with } h_q = \frac{\pi A}{6} \left(1 + \frac{1}{2\mu_P^0}\right) \quad \text{cracks (soft)} \\ \frac{1}{q} &= 1 - h_q pd^3 \text{ with } h_q = \frac{\pi A}{6} \left(1 + 2\frac{\mu_P^0 + \mu_S^0 - 1}{\mu_S^0}\right) \quad \text{stiff cracks} \end{aligned} \quad (9.7)$$

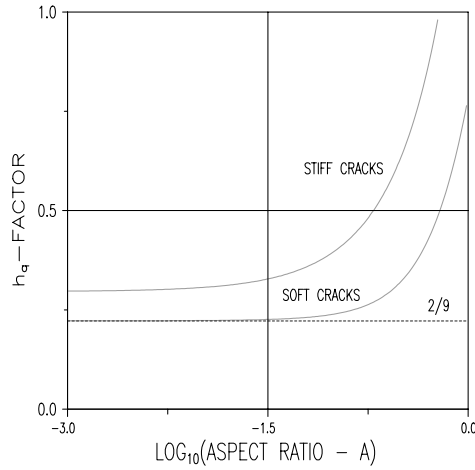


Fig. 9.5. h_q factor for conductivity of “cracked” composite

The h_q -factors are shown in Fig. 9.5 with shape factors determined numerically as explained in Chap. 7. It is noticed that discs practically can be considered to be cracks for any $A < 0.01$. This means that the influence of discs with $A < 0.01$ on composite conductivity can be considered as if the discs were real cracks ($A = 0$).

The crack results predicted by the present theory are successfully compared in Fig. 9.6 with exact results, $q = 1 - (2/9)pd^3$, as they can be deduced from the Levin’s bulk modulus analysis [7] considered in Sect. 8.2.1 with

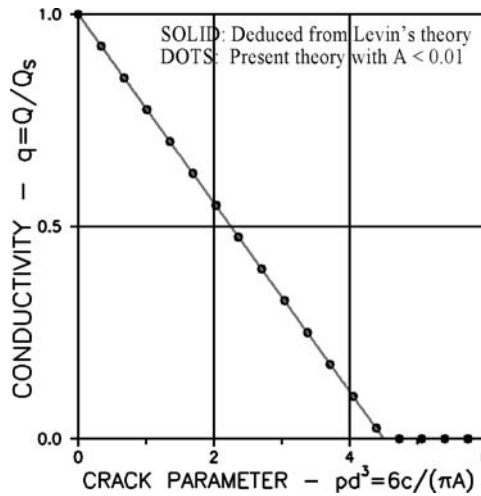


Fig. 9.6. Present crack theory versus results deduced from Levin’s crack theory

$v_S = 0$. In a similar way the conductivity of a material with stiff cracks is developed numerically from the latter expression in (9.7). The result is very close to $q = 1 + 0.3pd^3$.

Remark: It has been checked that the results in Fig. 9.5 can be predicted accurately also by the SCS-method presented in Appendix C with $(Q_P, Q_S) = (0^+, 1)$ and $A < 0.01$. The statement previously made that SCS-solutions can be considered accurate when composites considered are dilute is clearly supported by this observation where very little crack “volume” is involved.

9.2.4 Crumbled Foils Composite

In a crumbled foils composite, see Sect. 4.1.4, both phases have continuous flat geometries, meaning that both shape functions $(\mu_P, \mu_S) \equiv 0$. The conductivity of such composites is easily derived from (9.1) with a geo function $\theta_Q = 2\sqrt{n_Q}$ introduced from (9.2).

$$q = \frac{Q}{Q_S} = \frac{n_Q + 2\sqrt{n_Q}[1 + c(n_Q - 1)]}{n_Q + 2\sqrt{n_Q} - c(n_Q - 1)} \quad (9.8)$$

9.3 Theory versus Experiments

9.3.1 Chloride Diffusion in HCP and HCP with Silica Fume

The data shown in Figs. 9.7 and 9.8 are from a study reported in Bentz et al. [74] on the influence of silica fume on the chloride diffusion in cement based materials. The materials considered were computer-simulated applying a cement paste model, which has previously been developed by

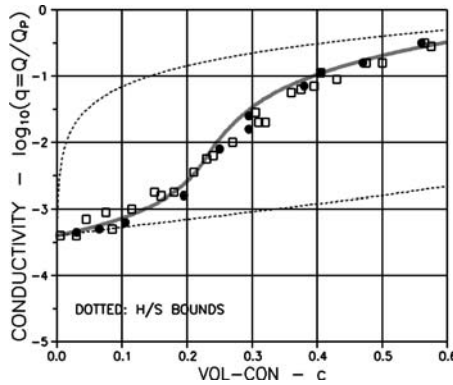


Fig. 9.7. $(c_P, c_S) = (0.78, 0.24)$. $(Q_P, Q_S) = (1, 0.0004)$. $(A_P, A_S) = (4, 0.3)$. Silica fume: $(\square, \blacksquare) = (0, 3)\%$

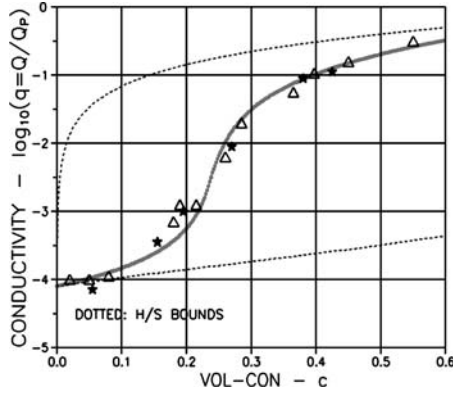


Fig. 9.8. $(c_P, c_S) = (0.78, 0.24)$. $(Q_P, Q_S) = (1, 0.00008)$. $(A_P, A_S) = (4, 0.3)$. Silica fume: $(\Delta, *) = (6, 20)\%$

Bentz in [34]. Bentz et al. [74] verify their (model-)results comparing them with experimental data reported in [75] and re-evaluated experimental data ($W/C = 0.3$, $c \approx 0.043$) reported in [76]. (Leaching systems used in [76] versus un-leaching systems in [74]).

The diffusion coefficients presented in Figs. 9.7 and 9.8 are normalized with respect to the chloride diffusion coefficient of free water, $Q_P \approx 2 \cdot 10^9 \text{m}^2/\text{sec}$, suggested in [77]. Volume concentrations of capillary pores (obtained using W/C ranging from 0.2 to 0.7) are denoted by c .

Percolation model-results presented in [74] show that phase P (capillary pores) starts being continuous at $c \approx 0.2$. In the terminology of the present book this corresponds to a critical concentration of $c_S \approx 0.2$. Adding an estimate of $c_P \approx 0.78$ for the other critical concentration (beyond which 0-stiffness of HCP is normally expected [78] the solid lines presented in Figs. 9.7 and 9.8 are predicted by the conductivity analysis presented in this book with shape functions illustrated in Fig. 9.9. A_P and A_S denote aspect ratios of phase P at $c = 0$ (discrete ellipsoidal cap-pores) and of phase S at $c = 1$ (discrete ellipsoidal solid particles dissolved in a continuous cap-pore system) respectively.

Curiosum: It has been mentioned that the model-results of Bentz et al. [74] were verified by re-evaluated experimental data ($W/C = 0.3$, $c \approx 0.043$) reported by Mejlhede in [76]. The data shown in Fig. 9.10 are the original chloride diffusion data for leaching systems reported in [76]. The following discussion will show that these data can, on their own, be given a micro structural explanation: Apparently the capillary pores of Mejlhede's system are permeable already from $c = 0$, meaning that $c_S \leq 0$. The diffusivities shown in Fig. 9.10 with a solid line are predicted with shape functions as presented in Fig. 9.11, meaning that the capillary pore system always has a

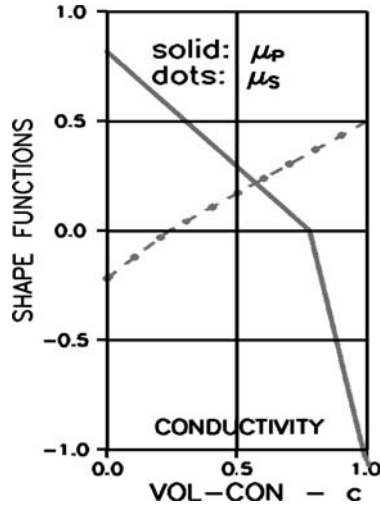


Fig. 9.9. Shape functions: $(c_P, c_S) = (0.78, 0.24)$, $(A_P, A_S) = (4, 0.3)$

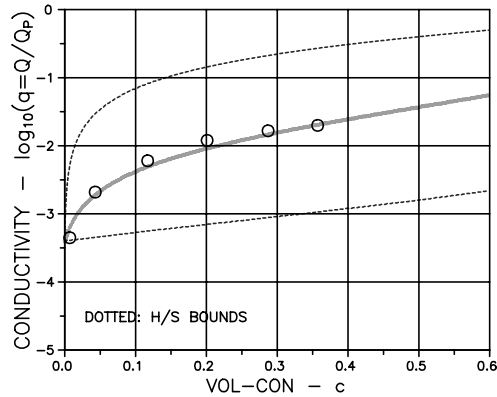


Fig. 9.10. $(c_P, c_S) = (0.6, < 0)$. $(Q_P, Q_S) = (1, 0.0004)$. $\mu_P^0 = 0.3$, $\mu_S \equiv 0$. No silica fume

MM-geometry, starting at $c = 0$ with a pore geometry of long shapes mixed with flat shapes, and ending at $c = 1$ with a shape of crumbled foils.

Discussion: Apparently two different capillary pore systems are revealed by the studies on leaching systems [76] and on un-leaching systems [74]. An explanation is that the pore system changes as the results of leaching. The pore system opens up decreasing the critical concentration c_S and transforming the capillary pore system to be crumbled foils.

It is interesting to notice that the experimental chloride diffusion data obtained by Mejlhede [76] (including HCP with silica fume) under leaching conditions were fitted excellently by (9.8). This expression applies for pores

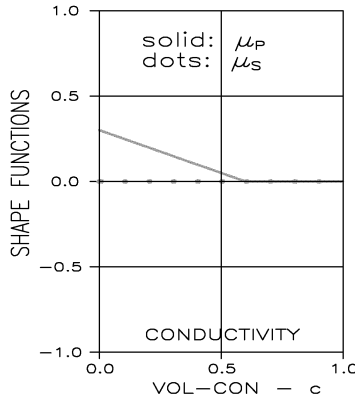


Fig. 9.11. Shape functions: $(c_P, c_S) = (0.6, < 0)$, $\mu_P^0 = 0.3$, $\mu_S \equiv 0$

with crumbled foil geometries at any pore concentration. The hypothesis can be made that stiffness (and strength) of HCP reduces as the result of leaching chloride exposure.

Future research on chloride diffusivity of HCP will show that this problem can be solved only by considering also the mechanical behavior of this material: Measured stiffness before, and after chloride exposure.

The theory developed in this book for the prediction of conductivity of composite materials is well justified by the results of this section. The justification is even more pronounced by the observation made in [74] that the general trends of chloride diffusivity of leaching HCP systems are in good agreement with experimental data obtained by Christensen [79] with respect to the electrical conductivity of such systems: $W/C = 0.4$ with 0% and 20% silica fumes.

9.3.2 Thermal Conductivity of Plane-Isotropic Fiber Composite

The results presented in Figs. 9.12 and 9.13 are from an analysis of the plane-isotropic fiber composite previously considered in Sect. 8.2.2. From the FEM-analysis [15, 16] is known that phase P is Silicon carbide (SiC) with $Q_P = 135 \text{ Wm}^{-1}/^\circ\text{C}$. Phase S is Carbon (C) with $Q_S = 9.5 \text{ Wm}^{-1}/^\circ\text{C}$.

The conductivity (perpendicular to fibers) of this composite can be predicted from (9.9) developed from a plane-isotropic version [24, Appendix C] of the isotropic composite theory presented in this book. We approximate the fibers to be of circular cross-sections. Then the shape function shown in Fig. 9.12, can be described according to Sect. 7.2.3 with shape factors very close to $(\mu_P^0, \mu_S^0) = -(\mu_P^1, \mu_S^1) = (1, -1)$.

The predicted results, shown in Fig. 9.13, agree very positively with results [16, Fig. 7] deduced from the FEM-analysis [15, 16] previously referred to.

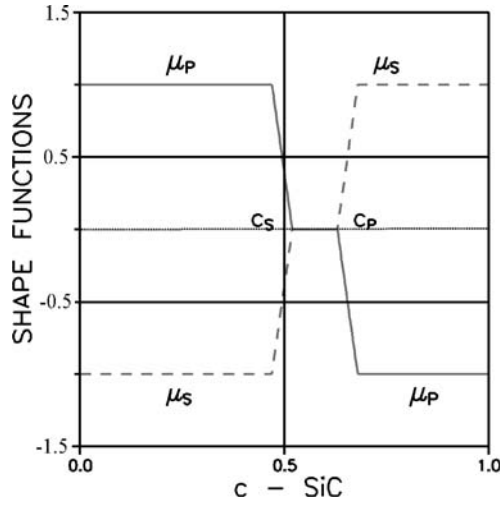


Fig. 9.12. Shape functions for plane isotropic composite considered

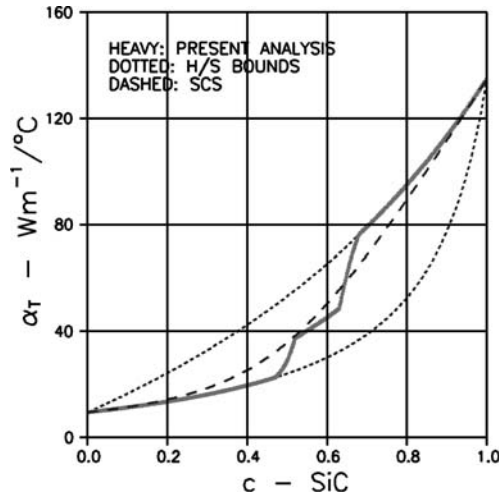


Fig. 9.13. Perpendicular to fiber thermal conductivity of plane-isotropic composite with parallel circular fibers. $(Q_P, Q_S) = (135, 9.5) \text{ Wm}^{-1}/^{\circ}\text{C}$

$$q_T = \frac{Q_T}{Q_S} = \frac{n_Q + \theta_Q[1 + c(n_Q - 1)]}{n_Q + \theta_Q - c(n_Q - 1)} \quad (\text{perpendicular to fibers}) \quad (9.9)$$

$$\text{with } \theta_Q = \frac{1}{2} \left[\mu_P + n_Q \mu_S + \sqrt{(\mu_P + n_Q \mu_S)^2 + 4n_Q(1 - \mu_P - \mu_S)} \right]$$

H/S bounds: $\theta_Q \equiv 1$ and $\theta_Q \equiv n_Q$

Remark: In principles, the discussion made in Sect. 8.2.2 on the description of geometry transitions around $c = 0.5$ applies also when conductivity predictions are considered.

9.4 Theory versus SCS-Estimates

The numerical SCS-method previously referred to in Chap. 3 to estimate composite stiffness has also been generalized in this book to consider composite conductivity. The results are presented in Appendix C where composites are considered with a larger range of particle shapes than what is considered in analytical SCS-methods presented in the literature:

Electrical conductivity and dielectricity of two-phase materials was studied by Landauer [47] and Böttcher [48] respectively using a SCS-model with spheres as the basic element. Their theoretical results can, after some re-writing, be expressed as shown in Table 9.1, first row. It is interesting to observe that this expression can be obtained from (9.1) introducing $\theta_Q = 2q$.

Table 9.1. Some SCS solutions for the conductivity of composite materials. Strict ellipsoidal particles

Author	Basic Element	Conductivity, $q = Q/Q_S$
Böttcher [48] Landauer [47]	Sphere ($A = 1$)	$q = \frac{1}{4} \left[B + \sqrt{B^2 + 8n_Q} \right]$ with $B = 2 - 3c - n_Q(1 - 3c)$
Beek [50]	Long fiber ($A = \infty$)	$q = \frac{1}{2} \left[B + \sqrt{B^2 + 4n_Q \left[1 + \frac{c}{3}(n_Q - 1) \right]} \right]$ with $B = (1 - n_Q) \left(1 - \frac{5}{3}c \right)$
Bruggeman [49]	Thin disc ($A = 0$)	$q = n_Q \frac{3 + 2c(n_Q - 1)}{3n_Q - c(n_Q - 1)}$

Other conductivity expressions were developed for a composite with extremely long fibres by Van Beek [50], and for a composite with extremely thin discs by Bruggeman [49]. After some re-writing the results obtained by these authors can be formulated as shown in Table 9.1, second and third row respectively. All three SCS solutions presented in Table 9.1 are illustrated in Figs. 9.14 and 9.15 which compare very accurately with the numerical SCS-results obtained in Appendix C.

9.5 Conclusion

A method has been developed in this chapter by which the stiffness theory for composite materials presented in Chap. 8 can be used in the analysis of other

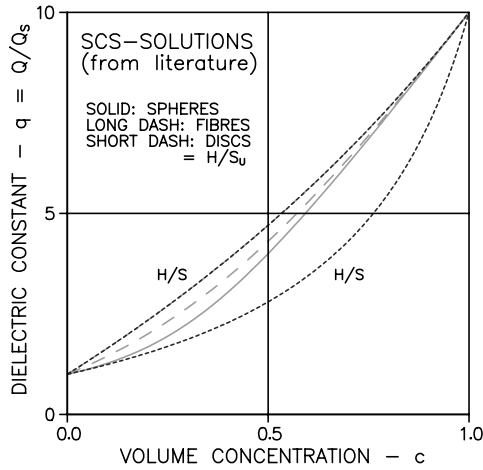


Fig. 9.14. Composite dielectricity. Fibers ($A = \infty$), spheres ($A = 1$), discs (H-S upper bound) ($A = 0$). ($n_Q = 10$)

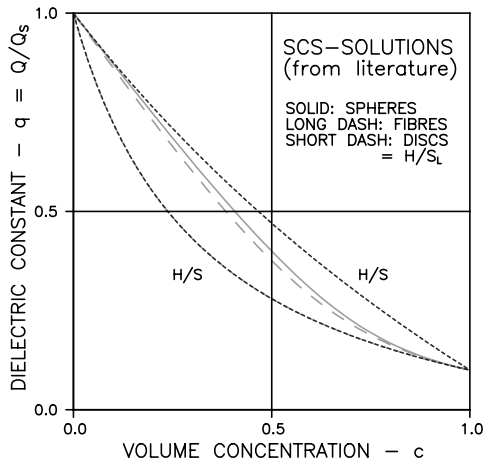


Fig. 9.15. Composite dielectricity. Fibers ($A = \infty$), spheres ($A = 1$), discs (H-S lower bound) ($A = 0$). ($n_Q = 0.1$)

physical properties of composites with arbitrary geometry. Examples of properties considered are thermal conductivity, electrical conductivity, dielectric constant, and magnetic permeability.

The method presented is based on a very simple modification of the bulk modulus expression from the general stiffness theory. It is emphasized that the influence of composite geometry on other physical properties considered is the same as on stiffness. The analysis has been verified by comparison of predicted

results with theoretically and experimentally obtained data – including SCS-estimates (Self-Consistent-Scheme) known from the literature.

A generalized, numerical SCS-method has been developed (in Appendix C) for estimation of composite conductivity. The method is based on mixtures of ellipsoidal particles of any shapes.

Simplified Composite Theory – Elasticity

It has been justified in Chap. 8 that a complete analysis of composites with arbitrary phase geometries can be made by the method developed in this book. It is recognized, however, that the great many geometrical parameters (up to 10) and stiffness coefficients needed for such analysis are by far not present in most normal practice.

The main purpose of this chapter is to show how the theory can be simplified to reflect more realistically the somewhat limited knowledge available in most practice on geometry and elasticity (Poisson's ratios especially).

A theory is presented, which meets the demands for simplifications. The theory is formulated as a simple operational summary of the general theory. It is presented in a self-contained way such that it can be read/applied without a deeper understanding of the general parts of this book.

Thus, this chapter can be read as an independent article on the analysis of composite materials. As indicated in the introductory "Overview" section to this book: "Readers, who are interested primarily in applications, may start at Chap. 10".

A number of comparative studies have been made between results obtained by various simplified versions of the theory and results obtained by the accurate version. It has been found that very acceptable results are obtained introducing the following basic simplifications:

- Both Poisson's ratios are 0.2 (in most practice Poisson's ratios varies in 0.1–0.3).
- Both shape functions (μ_P, μ_S) can be approximated by their shear versions. They are quantified by two shape factors, μ_P^0, μ_S^0 , and one critical concentration, for example c_S . They vary linearly¹ all the way in $c = 0 - 1$ such

¹ This assumption is made exclusively to facilitate calculations on the basis of a minimum of relevant geometrical information. According to Sect. 7.2 *any* shape function description can be used which complies with the conditions explained in Sect. 4.1.3.

that $\mu_P + \mu_S = a$ where the constant $0 \leq a \leq 1$ is the so-called geo-path factor $a = \mu_P^0 + \mu_S^0$.

Immediate consequences of these assumptions are the following modifications: Poisson's parameters become $\kappa_S = \gamma_S = 1$, Stiffness ratios become $N_k = N_g = n_k = n_g = n$, geo-functions become identical, $\theta_k = \theta_g = \theta$. Any internal stress component (σ_{Pij} and σ_{Sij}) relative to its external stress counterpart becomes predicted as σ_P/σ and σ_S/σ . Average normalized stiffness $k = g = e$ are predicted. For typographical reasons this triviality is not always expressed. Thus, whenever e is mentioned subsequently k and g may as well be thought of – or vice versa.

A consequence of introducing the simplified description of shape functions is that the other shape factors μ_P^1, μ_S^1 , and the other critical concentration appearing in the accurate analysis become dependent variables. For practice, however, this discrepancy can be counteracted for by simple averaging measures as explained in Sect. 10.1.3.

A further consequence is that the analysis now becomes based on shape factors as they are presented in Fig. 10.1, instead of factors which depend on Poisson ratios as shown in Figs. 7.10–7.12.

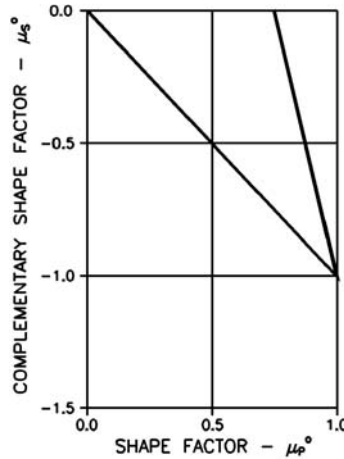


Fig. 10.1. Shape factor graph for simplified stiffness analysis

The subsequent presentation of the simplified theory and applications will follow the same disposition as used in the general theory: Description of geometry, quantification of geometry, preparation of analysis, and the analysis itself. The text is rather brief. As the “translation” of accurate analysis to simplified analysis is rather obvious, no further explanations are really necessary.

10.1 Basis of Analysis

The composites considered in this analysis are isotropic mixtures of two linear elastic components: phase P and phase S. The amount of phase P is quantified by the so-called volume concentration defined by $c = V_P/(V_P + V_S)$ where volume is denoted by V . The volume concentration of phase S then becomes $1 - c$.

The specific composite properties considered are stiffness and eigenstrain phenomenon (such as shrinkage and thermal expansion) as related to volume concentration, composite geometry, and phase properties: Young's moduli E_P and E_S with stiffness ratio $n = E_P/E_S$ and linear eigenstrains λ_P and λ_S . (Further notations used in the text are explained in the list of notations at the end of this book).

The strength of the composite analysis presented, relative to other prediction methods (with fixed, not variable types of composite geometries such as spheres and fibers in a matrix), is that global (standard) solutions are presented which apply for any composite geometry represented by a so-called geo-function, θ . Specific composites are considered by so-called shape functions, μ_P and μ_S , to introduce into the geo-function. Properties can be predicted where geometry can be respected as it really develops in natural or man-made composite materials.

10.1.1 Geometry

The shape functions just mentioned define composite geometry as shown in Fig. 10.2 with so-called shape factors (μ_P^0, μ_S^0) and critical concentrations, c_P and $c_S \leq c_P$: Shape factors tell about the shapes of phase components at dilute concentrations. Critical concentrations are concentrations where the composite geometry changes from one type to another type.

At fixed concentrations we operate with the following types² of composite geometries: DC means a discrete phase P in a continuous phase S. MM means a mixed phase P geometry in a mixed phase S geometry, while CD means a continuous phase P mixed with a discrete phase S. We notice that MM-geometries (if porous) are partly impregnable. In modern terminology this means that phase P percolation exists in composites with $c > c_S$. Percolation is complete for $c \geq c_P$. Porous materials have lost any coherence in this concentration area with no stiffness and strength left.

Composite geometries may change as the result of volume transformations associated with increasing phase P concentration. We will think of changes as they are stylized in Fig. 10.2: At increasing concentration, from $c = 0$,

² A phase with continuous geometry (C) is a phase in which the total composite can be traversed without crossing the other phase. This is not possible in a phase with discrete geometry (D). A mixed geometry (M) is a continuous geometry with some discrete elements.

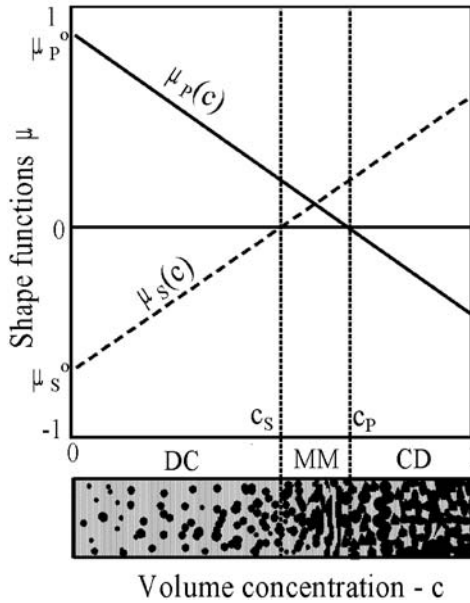


Fig. 10.2. Geometrical significance of shape functions. $(\mu_P, \mu_S) = (+, -)$ means discrete P in continuous S. $(\mu_P, \mu_S) = (+, +)$ means mixed P in mixed S. $(\mu_P, \mu_S) = (-, +)$ means continuous P with discrete S. *Black* and *white* signatures denote phase P and phase S respectively

discrete P elements agglomerate and change their shapes approaching a state at $c = c_S$ where they start forming continuous geometries. Phase P grows fully continuous between $c = c_S$ and $c = c_P$ such that the composite geometry is a mixture of a continuous phase P with discrete de-agglomerating phase S particles from the concentration of $c = c_P$.

In a complementary way the geometry history of phase S follows the history of phase P and vice versa. Formally the geometries just explained can be shifted along the concentration axis. A composite may develop from having a DC geometry at $c = 0$ to having a MM geometry at $c = 1$. Such composite geometries, with $c_P > 1$ and $0 < c_S < 1$, are named DC-MM geometries. Other composites may keep their DC type of geometry all the way up to $c = 1$ in which case the composite geometry is denoted as a DC-DC geometry, with both critical concentrations > 1 . The geometry outlined in Fig. 10.2 changes from DC to CD geometry which makes it a DC-CD geometry with both critical concentrations in $c = 0 - 1$.

Ideal geometries at $c = 0$ and at $c = 1$ of a DC-CD composite are illustrated in Figs. 10.3 and 10.4 respectively. We notice in this context that the composite theory developed is based on the concept that any isotropic composite geometry is a station on a geo-path going from the CSA_P geometry shown in Fig. 10.3 to the CSA_S geometry shown in Fig. 10.4. CSA is an

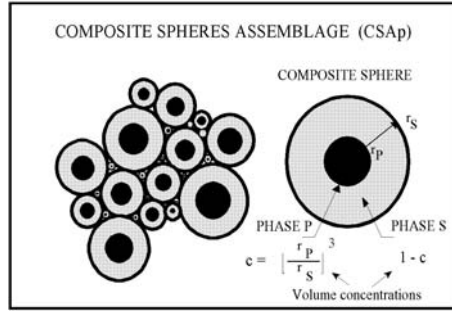


Fig. 10.3. Composite spherical assemblage with phase P particles, CSA_P

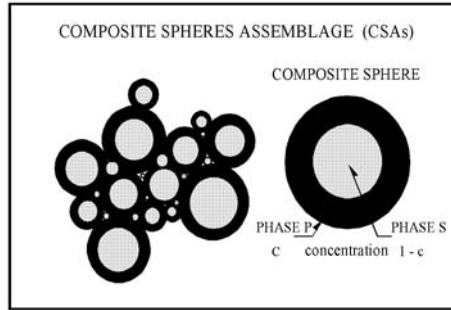


Fig. 10.4. Composite Spheres Assemblage with phase S particles (CSA_S)

abbreviation of Composite Spheres Assemblage introduced by Hashin in [4]. It is noticed that the four letter symbols for composite geometries are subsequently also used in the meaning, a “DC-CD type of composite” or just a “DC-CD composite”.

10.1.2 Quantification of Composite Geometry

The various types of geometries considered are listed in Fig. 10.5 which defines the following two composite classes considered in this chapter: *Particulate composites* are defined by the former row. They have a “particles in a matrix” geometry (DC) at small concentrations. *Lamella composites* are defined by the latter row. They have a mixed phase P geometry in a mixed phase S geometry (MM) at low concentrations. The phenomenon of percolation previously considered is noticed to appear in Fig. 10.5 in concentrations areas indicated by gray shadings ($c > c_S$).

Remarks: We emphasize that the terms “particulate composites” and “lamella composites” are “working” terms, which define composites by their geometries at low concentrations. The complete geometry classification according to Chap. 7 is decided by critical concentrations as shown in Table 10.1.

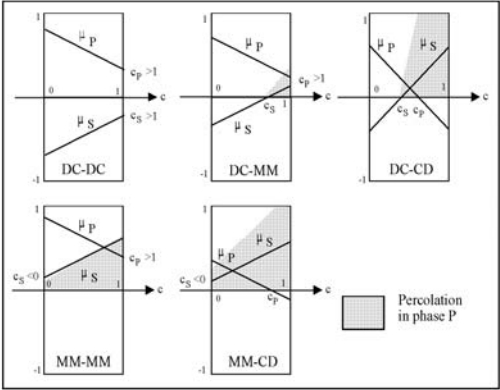


Fig. 10.5. Composite types versus critical concentrations. Former and latter two letters denote composite geometry at $c = 0$ and at $c = 1$ respectively

Table 10.1. Range of critical concentrations applying for various composites with linear shape functions, implying $c_P = -c_S\mu_P^0/\mu_S^0$

Type		Crit-con c_S	Examples
DC	DC	$c_S > 1$	Particulate composite (concrete, mortar). Extremely high quality of grading (approaching CSA _P composites). <i>Pore system:</i> Not impregnable. Finite stiffness at any porosity
	MM	$1 > c_S > -\mu_S^0/\mu_P^0$	Particulate composite (concrete, mortar) with particle interference at $c = c_S$. Increasing quality of grading is quantified by larger concentration c_S at first interference. <i>Pore system:</i> Only impregnable for porosities $c > c_S$. Finite stiffness at any porosity.
	CD	$-\mu_S^0/\mu_P^0 > c_S > 0$	Mixed powders (ceramics). <i>Pore system:</i> Only impregnable for porosities $c > c_S$. No stiffness for porosities $c > c_P$.
MM	MM	$-\mu_S^0/\mu_P^0 > c_S$	Mixed lamella/foils (“3D-plywood”). <i>Pore system:</i> Fully open at any porosity. Finite stiffness at any porosity.
	CD	$0 > c_S > -\mu_S^0/\mu_P^0$	Mixed lamella/foils (“3D-plywood”). <i>Pore system:</i> Fully open at any porosity. No stiffness for porosities $c > c_P$.

Particle Shapes – Aspect Ratio

Particle shapes are subsequently referred by their aspect ratios $A = \text{length}/\text{diameter}$ of particles. Spherical particles have $A = 1$. Long particles (fibers) have $A > 1$. Flat particles (discs) have $A < 1$.

Shape Factors and Geo-Paths

Shape functions μ_P and μ_S are related as illustrated in Fig. 10.6, which is a modified reproduction of Fig. 7.26 in this book. The geometries passed when the phase P concentration increases from $c = 0$ to $c = 1$ are indicated in this figure by the geo-path.

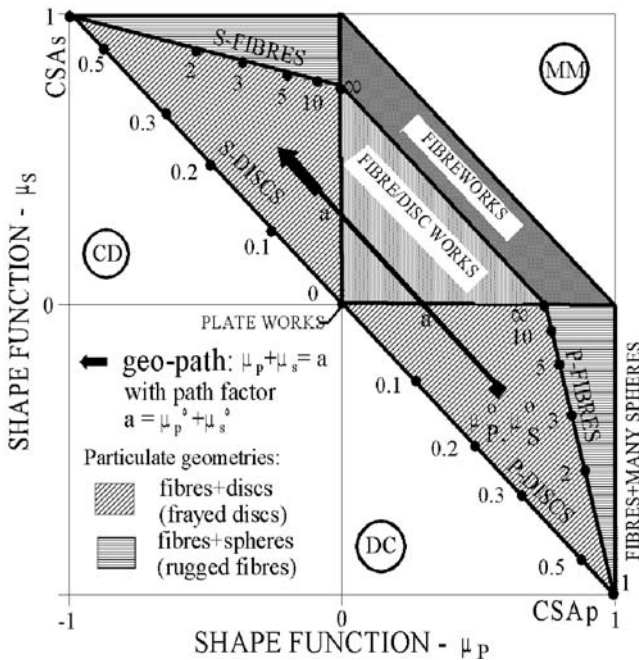


Fig. 10.6. Shape function graph with geo-path. Numbers indicate fiber aspect ratio A of particles. Fibreworks are agglomerating crumbled P and S fibers. Fiber/discworks are agglomerating crumbled P and S fibers and discs. Plateworks are crumbled discs (sheets, foils)

Shape factors can be calculated from Table 10.2, which represents a summary of the accurate shape factor determination in Sect. 7.1 – except that the shape factors for particulate composites with uni-shaped particles have been introduced by their “shear version” approximations (with $\nu_S = 0.2$) also presented in Sect. 7.1.

Table 10.2. Shape factors in simplified theory. Numbers in parenthesis indicate origins of expressions. The so-called geo-path factor is determined as $a = \mu_P^0 + \mu_S^0$. XX stands for DC, MM, CD, or CD

Particulate Composite (DC-XX)	
Uni-Shaped Particles	
$\mu_P^0 = \begin{cases} \frac{3A}{A^2 + A + 1}; & A \leq 1 \\ 3\frac{A^2 - A + 1}{4A^2 - 5A + 4}; & A > 1 \end{cases}; \mu_S^0 = - \begin{cases} \mu_P^0; & A \leq 1 \\ 4\mu_P^0 - 3; & A > 1 \end{cases} \quad (7.7 - 7.9)$	
Multi-Shaped Particles ³	
$\mu_P^0 = \langle m_0 \rangle; \quad \mu_S^0 = -\langle m_\infty \rangle \frac{1 - \langle m_0 \rangle}{1 - \langle m_\infty \rangle}$ <p>with $\langle m_0 \rangle = \left(\sum_{i=1}^{\infty} \frac{\alpha_i}{m_{0,i}} \right)^{-1}; \quad \langle m_\infty \rangle = \left(\sum_{i=1}^{\infty} \frac{\alpha_i}{m_{\infty,i}} \right)^{-1} \quad (7.12 + 7.11)$</p> <p>where α_i is volume fraction of joining aspect ratio A_i – and</p> $m_{0,i} = \begin{cases} \frac{3A_i}{A_i^2 + A_i + 1} & (A_i \leq 1) \\ 3\frac{A_i^2 - A_i + 1}{4A_i^2 - 5A_i + 4} & (A_i > 1) \end{cases}; \quad m_{\infty,i} = \frac{3A_i}{A_i^2 + A_i + 1} \text{ (any } A_i) \quad (7.8)$	
Lamella Composite (MM-XX)	
$\mu_P^i \approx \beta (1 - \gamma^i); \quad \mu_S^i \approx \beta \gamma^i \quad (i = 0, 1)$	

where β quantifies basic shapes agglomerating:

Long fibers and rugged fibers have $\beta = 3/4 - 1$
Discs-fiber mixture has $\beta \approx 0 - 3/4$
Discs and crumbled foils have $\beta \approx 0$ (7.16)

and γ^i quantifies degree of agglomeration:

from a DC geometry with $\gamma^0 = 0$
to a CD geometry with $\gamma^1 = 1$

Critical Concentrations

It is emphasized that the critical concentrations depend very much on the processing technique used to produce composites. We notice that particle size distribution is part of the processing. For particulate composites, for example, the critical concentration c_S can be thought of as the concentration at first interference of phase P particles. Improved quality of size distribution (smoothness and density) is considered by increasing c_S . At this concentration porous materials become very stiff when impregnated with a very stiff material. At the other critical concentration, $c = c_P$, the composite becomes a mixture of phase S elements completely wrapped in a matrix of phase P. As previously mentioned porous materials lose their stiffness and strength at c_P because phase P has become a continuous void system.

³ Approximate alternative to “Multi-shaped particles”:

$$\mu_P^0 \simeq \left(\sum_{i=1}^{\infty} \frac{\alpha_i}{\mu_{P,i}^0} \right)^{-1}; \quad \mu_S^0 \simeq \left(\sum_{i=1}^{\infty} \frac{\alpha_i}{\mu_{S,i}^0} \right)^{-1}$$

It is noticed that critical concentrations can be fictitious (outside $c = 0 - 1$). In such cases they do not, of course, have the immediate physical meanings just explained. Formally, however, we may keep the explanation given in order to describe in an easy way in which the rate of changing the composite geometry is influenced by the processing technique used. In such fictitious cases critical concentrations have to be estimated from experience, or detected from calibration experiments.

10.1.3 Preparation of Composite Analysis

The preparation of a composite analysis is as follows:

- Calculate shape factors (μ_P^0, μ_S^0) from Table 10.2. (Or for first estimate analysis: read directly from Fig. 10.6).
- Then decide the critical concentration c_S (or c_P) from knowing about mixing technology and observations made on geometrical formation.
- This information quantifies the composite geometry by the so-called shape functions expressed by (10.1).

We recall from the introductory section to this chapter: Shape functions are expressed by simple mathematical expressions (in order not to predict properties with an “accuracy” out of proportions to what is actually known about composite geometry). A consequence of such simplification is that the quantities of (μ_P^0, μ_S^0) and (c_S or c_P) chosen above must be adapted to each other such that the critical concentration not chosen is predicted realistically by (10.1). Figure 10.5 and Table 10.1 are useful when deciding on realistic shape functions for a practical composite analysis. An example of shape quantification is shown in Fig. 10.7.

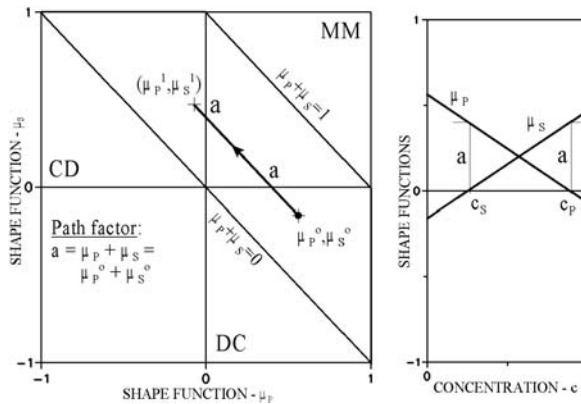


Fig. 10.7. Geo-path and shape functions for a DC-CD composite with multi shaped particles at $c = 0, 20\%(A = 0.1) + 80\%(A = 10)$ and a critical concentration of $c_S = 0.26$

- The last step of preparing a composite analysis with the global solutions (valid for any geometry) presented in Table 10.3 is to calculate the so-called geo-function expressed by (10.2).

$$\mu_S = \text{MIN} \left[\mu_S^0 \left(1 - \frac{c}{c_S} \right), 1 \right]; \quad \mu_P = \mu_P^0 \left(1 - \frac{c}{c_P} \right) \text{ with } c_P = -\frac{\mu_P^0}{\mu_S^0} c_S$$

(10.1)

and c_S estimated with guidance from Table 10.1 \Rightarrow

$$\text{Geo-path: } \mu_S = \begin{cases} a - \mu_P & \text{for } \mu_P > a - 1 \\ 1 & \text{for } \mu_P \leq a - 1 \end{cases} \text{ with path factor: } a = \mu_P^0 + \mu_S^0$$

$$\theta = \frac{1}{2} \left[\mu_P + n\mu_S + \sqrt{(\mu_P + n\mu_S)^2 + 4n(1 - \mu_P - \mu_S)} \right]; \quad n = \frac{E_P}{E_S} \quad (10.2)$$

10.2 Analysis

With composite geometry described by the geo-function presented in (10.2) a property analysis can now be made using the global predictions presented in Table 10.3 with symbols explained in the list of notations presented at the end of this book.

Table 10.3. Stiffness, stress, and eigenstrain/stress of composite material calculated by simplified method of analysis. (λ_P, λ_S) and (ρ_P, ρ_S) are eigenstrain (linear) and eigenstress (hydrostatic) of phase P and phase S respectively. K_S is bulk modulus of phase S

Stiffness	
$e = g = k = \frac{n + \theta[1 + c(n - 1)]}{n + \theta - c(n - 1)}$	
Stress Caused by External Load	
$\frac{\sigma_P}{\sigma} = \frac{n(1 + \theta)}{n + \theta[1 + c(n - 1)]}; \quad \frac{\sigma_S}{\sigma} = \frac{n + \theta}{n + \theta[1 + c(n - 1)]}$	
$\text{or } \frac{\sigma_P}{\sigma} = \frac{1/e - 1}{c(1/n - 1)}; \quad \frac{\sigma_S}{\sigma} = \frac{1/n - 1/e}{(1 - c)(1/n - 1)}$	
Eigenstrain	
$\lambda = \lambda_S + \Delta\lambda \frac{1/k - 1}{1/n - 1}; \quad (\Delta\lambda = \lambda_P - \lambda_S)$	
$\frac{\lambda}{\lambda_S} = \frac{1/n - 1/k}{1/n - 1}; \quad (\lambda_P = 0)$	
Eigenstress ($K_S \approx E_S/1.8$)	
$\rho_P = -3K_S\Delta\lambda \frac{c(1/n - 1) - (1/k - 1)}{c(1/n - 1)^2}; \quad \rho_S = -\frac{c}{1 - c}\rho_P$	

10.2.1 Bounds and Other Accurate Stiffness Expressions

It comes from [24, 43] and the present book that the above stiffness predictions are bounded between the exact solutions for the CSA composites illustrated in Figs. 10.3 and 10.4. This statement is expressed by the former expression in (10.3)

$$\frac{n+1+c(n-1)}{n+1-c(n-1)} \leq e \leq n \frac{2+c(n-1)}{2n-c(n-1)} \quad (n \geq 1)$$

(reverse < signs when $n < 1$)

(10.3)

$$\overset{\text{CSA}_P}{e(n, c)^* e(1/n, c)} = 1; \quad \overset{\text{Phase-symmetric}}{e(n, c)} = n^* e(1/n, 1 - c)$$

The stiffness bounds are obtained introducing $\theta \equiv 1$ and $\theta \equiv n$ respectively into the stiffness expression of Table 10.3. The bounds such determined are the same as can be obtained from the studies made by Hashin and Shtrikman in [3] on composite stiffness. The bounds are subsequently referred to by H/S.

The latter two relations in (10.3) are reproduced from [24]. They express some interesting relations between e , c , and n for CSA_P and phase-symmetric composites respectively. In the present context: TROC (approximately) and CROSS-composites.

10.2.2 Test of Theory

To test the accuracy of the simplified theory a composite analysis has been made on the TROC material and the phase symmetric CROSS material previously considered in Sects. 8.3.2 and 8.3.5 respectively with $v_P = v_S = 0.2$. The theory is applied with the geo-parameters presented in Figs. 10.8 and 10.9 (see Table 10.2). Solid lines in Figs. 10.10–10.13, show results obtained. Dots are FEM-data.

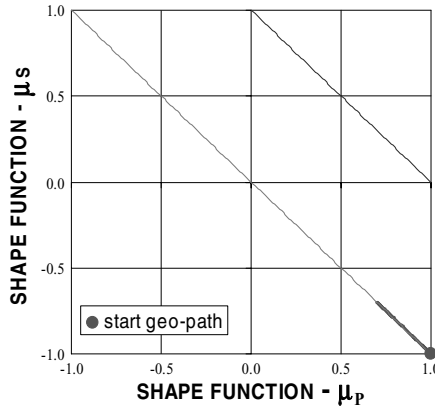


Fig. 10.8. TROC: DC-DC composite with $(\mu_P^0, \mu_S^0, c_S) = (1, -1, 3.33) \rightarrow (c_P = 3.33)$

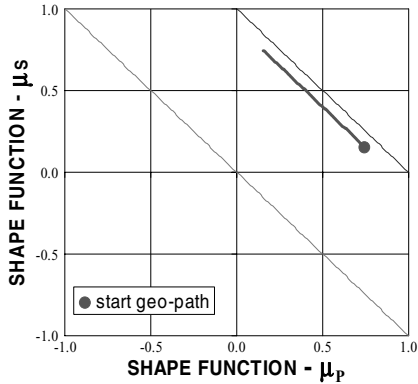


Fig. 10.9. CROSS: Phase-symmetric MM-MM: $(\beta, \gamma^0, \gamma^1) = (0.9, 17, 0.83) \rightarrow (\mu_P^0, \mu_S^0, c_S, c_P) = (0.75, 0.15, -0.25, 1.25)$

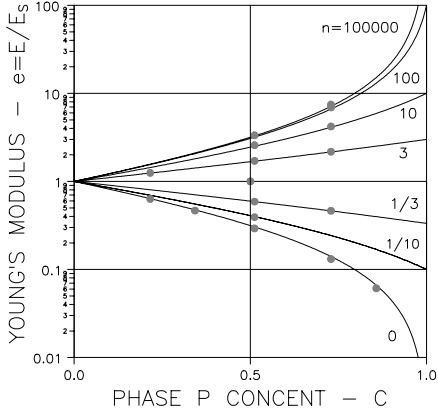


Fig. 10.10. TROC: Young's modulus predicted by simplified theory

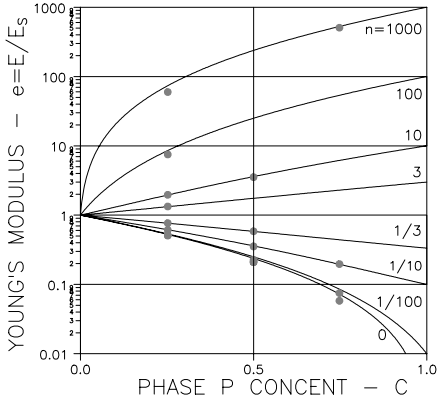


Fig. 10.11. CROSS: Young's modulus predicted by simplified theory

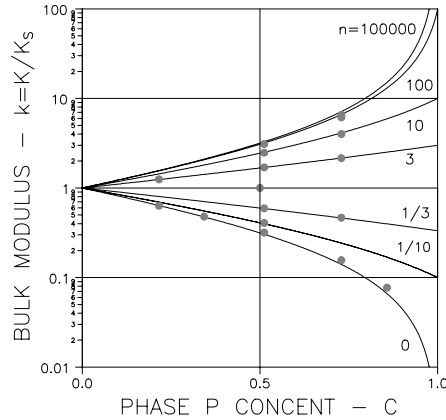


Fig. 10.12. TROC: Bulk modulus predicted by simplified theory

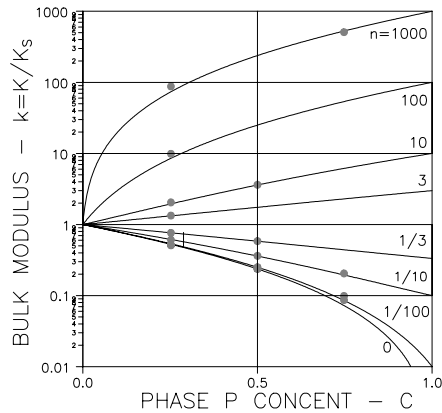


Fig. 10.13. CROSS: Bulk modulus predicted by simplified theory

Conclusion: It is observed that results predicted by the simplified theory are very close to the more accurately predicted results presented in Chap. 8. It seems then justified to continue the analysis of composite materials using the simplified theory. This statement is further justified in Sect. 10.4 where the theory is tested with respect to practical applicability.

10.3 Illustrative Examples

Theoretical examples are considered in this section, which illustrate how the simplified theory works in the analysis of various composite materials such as particulate composites, phase-symmetric composites and porous materials. Numerically, the analysis is made with Table 10.3 introducing geo-functions/shape functions from (10.2)/(10.1). Whenever possible, however,

full analytical solutions are presented in order to illustrate most clearly the basic influence of geometry on the behavior of composite materials. Practical examples are presented in Sect. 10.4 where the theory is tested against real experimental data.

10.3.1 Composites with Spherical Particles (CSA_P)

As previously mentioned a CSA_P composite has a geo-function of $\theta \equiv 1$ which makes it easy to perform a complete composite analysis with Table 10.3. The results are presented in Table 10.4. The additional solutions of the matrix stresses at spheres are developed in [56,57] from the Sokolnikoff stress solutions [52] of a hollow sphere subjected to internal pressure (equal to pressure in phase P). We re-call that the stiffness of a CSA_P composite represents the lower H/S bound solution for $n > 1$, and the lower H/S bound solution for $n < 1$. Some results of an eigenstrain/stress analysis are presented in Figs. 10.14 and 10.15.

Table 10.4. Composite analysis of CSA_P -material. In eigenstrain/stress analysis: (λ_P, λ_S) and (ρ_P, ρ_S) are eigenstrain (linear) and eigenstress (hydrostatic) of phase P and phase S respectively. $\sigma_{S,RAD}$ is radial phase S stress at sphere, $\sigma_{S,TAN}$ is tangential phase S stress at sphere

Problem	CSA_P -Solutions
Young's modulus	$e = \frac{E}{E_S} = \frac{A+n}{1+An}$ with $A = \frac{1-c}{1+c}$ and $n = \frac{E_P}{E_S}$
Internal stress caused by external stress σ	$\sigma_P = \sigma \frac{(1+A)n}{A+n}; \quad \sigma_S = \frac{\sigma - c\sigma_P}{1-c}$
Eigenstrain/stress caused by particle eigenstrain λ_P and matrix eigenstrain λ_S	$\lambda = \lambda_S + \Delta\lambda \frac{n(1-A)}{A+n}; \quad \Delta\lambda = \lambda_P - \lambda_S$ $\rho_P = -3K_P\Delta\lambda \frac{A}{A+n}; \quad \rho_S = -\frac{c}{1-c}\rho_P; \quad K_P = \frac{E_P}{1.8}$
Matrix-stress at spheres	$\sigma_{S,RAD} = \rho_P; \quad \sigma_{S,TAN} = -\frac{3-A}{4A}\rho_P$

10.3.2 Nearly CSA_P Composites

We look at particulate DC-DC composites with spherical particles (aspect ratio $A = 1$). According to the simplified composite theory, shape factors for such composites are $\mu_P^0 = -\mu_S^0 = 1$ with critical concentrations $c_P = c_S > 1$. A composite analysis with Table 10.3 proceeds with the following geo-function obtained by (10.1) and (10.2).

$$\theta = \frac{1}{2} \left[D + \sqrt{D^2 + 4n} \right] \quad \text{with } D = (1-n) \left(1 - \frac{c}{c_S} \right); \quad n = \frac{E_P}{E_S} \quad (10.4)$$

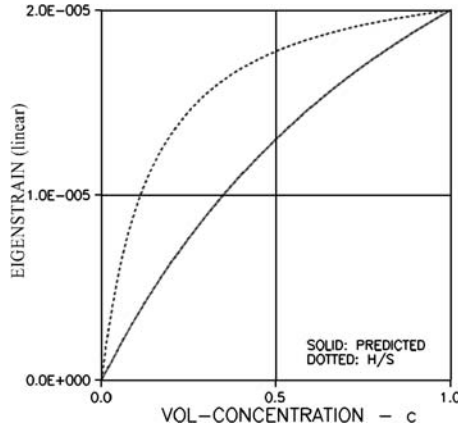


Fig. 10.14. Thermal eigenstrain/ $^{\circ}\text{C}$ of CSA_P composite $(E_P, E_S) = (15, 1)^* 10^2 \text{ MPa}$. $(\lambda_P, \lambda_S) = (2 \cdot 10^{-5}, 0)/^{\circ}\text{C}$

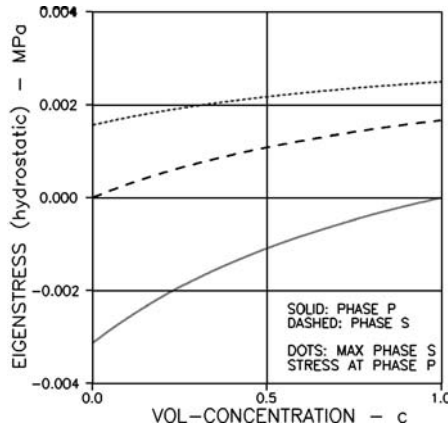


Fig. 10.15. Thermal eigenstress/ $^{\circ}\text{C}$ in CSA_P composite $(E_P, E_S) = (15, 1)^* 10^2 \text{ MPa}$. $(\lambda_P, \lambda_S) = (2 \cdot 10^{-5}, 0)/^{\circ}\text{C}$

Comment: As previously mentioned, the critical concentration c_S tells about quality of the phase P size distribution (smoothness and density). Increasing quality is associated with increasing c_S . CSA_P composites have an extremely high quality of size distribution, $c_S = \infty$. Some results from a composite analysis of a nearly CSA_P composite with a less ideal size P distribution ($c_S = 1$) are shown in Figs. 10.16 and 10.17.

10.3.3 Phase Symmetric Composites

Looking at composites which change geometry along a disc path with $\mu_P = -\mu_S$ (see Fig. 10.6) we get coinciding critical concentrations, $c_P = c_S = 0.5$,

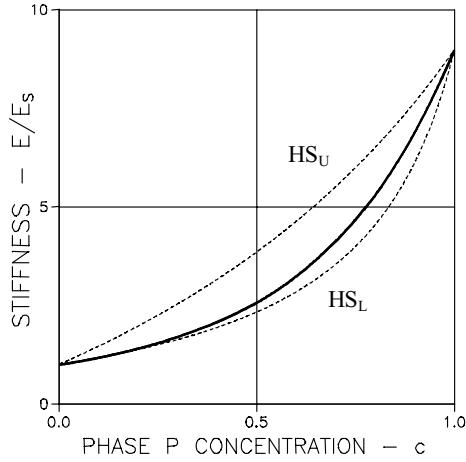


Fig. 10.16. Stiffness of a nearly CSA_P composite with $c_S = 1$ and $n = 9$

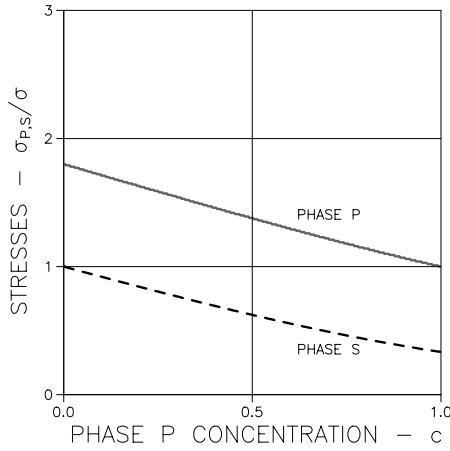


Fig. 10.17. Stresses in a nearly CSA_P composite with $c_S = 1$ and $n = 9$

from (10.1) which produces the geo-function presented in (10.5), forming the basis for the analysis of so-called phase-symmetric compacted powder composites (DC-CD) and phase-symmetric compacted lamella composites (MM-MM).

$$\theta = \frac{1}{2} \left[D + \sqrt{D^2 + 4n} \right]; \quad c_P = c_S = 0.5 \quad (10.5)$$

$$D = \mu_P^0 (1 - 2c)(1 - n)$$

Example 1: Compacted Spheres Composite

A special phase-symmetric composite is the one made with compacted spherical powders ($\mu_P^0 = 1$). The geo-function for this composite becomes as expressed by (10.6) by which the stiffness solution presented in (10.7) is predicted by Table 10.3. Stiffness and other results of a composite analysis with Table 10.3 are demonstrated in Figs. 10.18–10.21.

$$\theta = \frac{1}{2} \left[D + \sqrt{D^2 + 4n} \right]; \quad \text{Spheres: } c_S = c_P = 0.5 \quad (10.6)$$

$$D = (1 - n)(1 - 2c)$$

$$e = \frac{1}{2} \left[(1 - n)(1 - 2c) + \sqrt{(1 - n)^2(1 - 2c)^2 + 4n} \right] \quad (10.7)$$

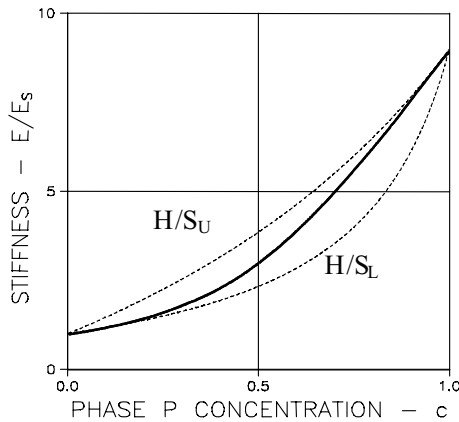


Fig. 10.18. Stiffness of spherical-powder composite with $n = 9$

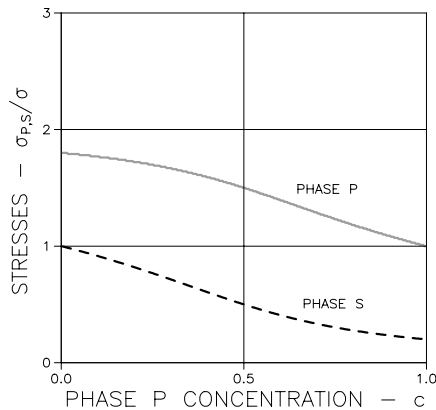


Fig. 10.19. Stresses in spherical-powder composite with $n = 9$

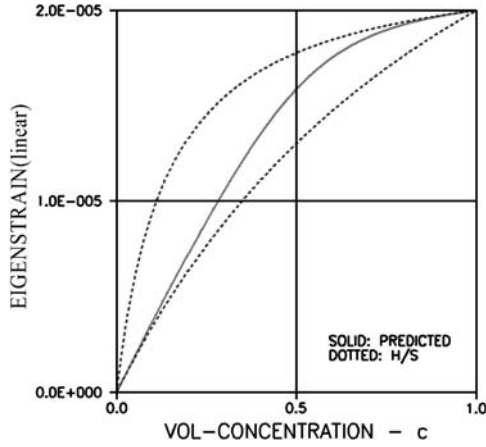


Fig. 10.20. Thermal eigenstrain/ $^{\circ}\text{C}$ of spherical powder composite. $(E_P, E_S) = (15, 1) * 10^2 \text{ MPa}$. $(\lambda_P, \lambda_S) = (2 * 10^{-5}, 0)/^{\circ}\text{C}$

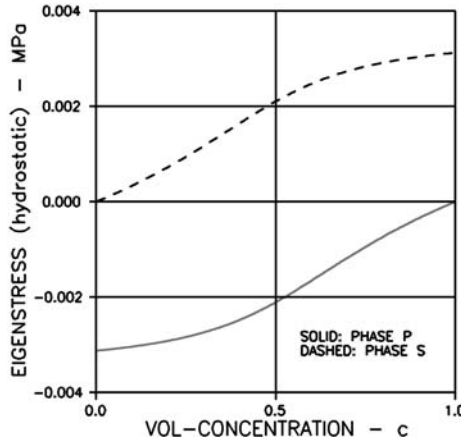


Fig. 10.21. Thermal eigenstress/ $^{\circ}\text{C}$ in spherical powder composite. $(E_P, E_S) = (15, 1) * 10^2 \text{ MPa}$. $(\lambda_P, \lambda_S) = (2 * 10^{-5}, 0)/^{\circ}\text{C}$

Remarks: It is observed that (10.7) is exactly the same expression as can be deduced from the analysis of Budiansky [13] on phase-symmetric composites made of compacted spheres. It is of some interest to notice that (10.7) relates to the simple P/H-bounds as illustrated in Fig. 10.22. It is also interesting to notice that (10.7) can be obtained implicitly from the general stiffness expression in Table 10.3 by introducing $\theta = e$.

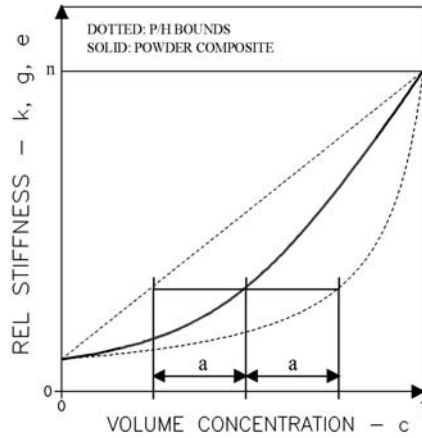


Fig. 10.22. Stiffness of spherical powder composite is “horizontal mean” of P/H bounds

Example 2: Compacted Lamella Composite

A compaction of a mixture of crumbled P-plates and S-plates with $\mu_P^0 = 0$ can be thought of as the plate counterpart to the compacted spheres composite just considered. A geo-function of $\theta = \sqrt{n}$ is obtained from (10.5) which is the same geo-function applying for the crumbled foils composite previously considered in Sect. 4.1.4. The composite stiffness obtained from Table 10.3 is presented in (10.8) with examples shown in Fig. 10.23. The results of a subsequent stress analysis are illustrated in Fig. 10.24.

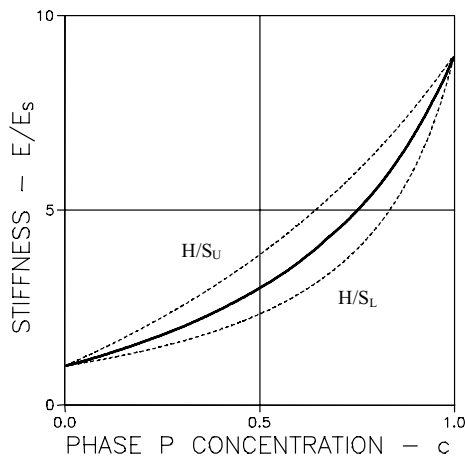


Fig. 10.23. Stiffness of crumbled foils composite with $n = 9$

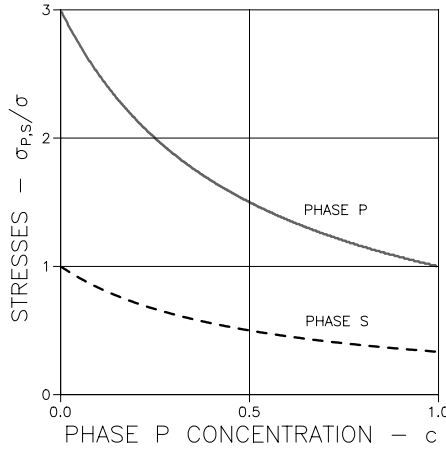


Fig. 10.24. Stresses in crumbled foils composite with $n = 9$

$$e = \frac{n + \sqrt{n}[1 + c(n - 1)]}{n + \sqrt{n} - c(n - 1)} ; \quad \text{crumbled foils } (\theta = \sqrt{n}) \quad (10.8)$$

10.3.4 Eigenstrain/Stress versus Geometry

The influence of phase geometry on composite shrinkage and stress is demonstrated in this section. We proceed using the simplified composite analysis as summarized in Table 10.3.

The TROC (DC-DC) and CROSS (CC-CC) composites previously defined in Figs. 10.8 and 10.9 are considered with geo-parameters, phase properties, and eigenstrains defined as follows:

$$\begin{aligned} \text{TROC} \quad & (\mu_P^0, \mu_S^0, c_S) = (1, -1, 3.33) \quad (c_P = 3.33) \\ \text{CROSS} \quad & (\beta, \gamma^0, \gamma^1) = (0.9, 0.17, 0.83) \\ & \rightarrow (\mu_P^0, \mu_S^0, c_S, c_P) = (0.75, 0.15, -0.25, 1.25) \\ \text{Phase S:} \quad & E_S = 1000 \text{ MPa, Shrinkage, } \lambda_S = -3\% \\ \text{Phase P:} \quad & E_P = 30000 \text{ MPa, Shrinkage, } \lambda_P = 0 \end{aligned}$$

The results of an eigenstrain/stress analysis are presented in Figs. 10.25–10.28.

10.3.5 Porous Materials

Porous materials are composites where one phase is an empty pore system. In the present context we consider phase P to be pores. Porosity and stiffness ratio are then given by c and $n = 0$ respectively from which the following stiffness expression is easily obtained by the simplified analysis with a geo-function of $\theta = \mu_P$. Stiffness is identical 0 whenever negative values are predicted.

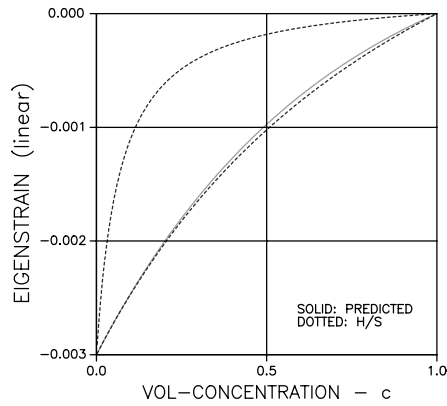


Fig. 10.25. Eigenstrain (shrinkage) of TROC composite with shrinking phase S

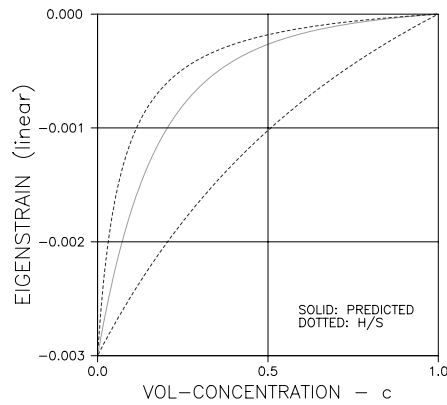


Fig. 10.26. Eigenstrain (shrinkage) of CROSS composite with shrinking phase S

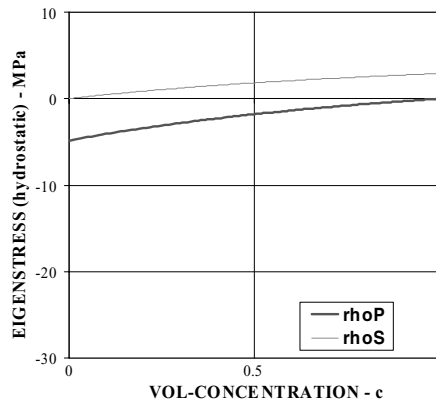


Fig. 10.27. Eigenstress in TROC composite with shrinking phase S

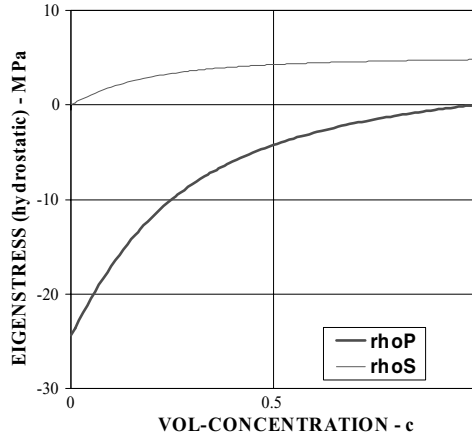


Fig. 10.28. Eigenstress in CROSS composite with shrinking phase S

$$e = \frac{1-c}{1+c/\theta_0} \quad \text{with} \quad \theta_0 = \begin{cases} \mu_P = \mu_P^0(1-c/c_P) & \text{when } c < c_P \\ 0 & \text{when } c > c_P \end{cases} \quad (10.9)$$

$$e \rightarrow 1 - \left(1 + \frac{1}{\mu_P^0}\right)c \quad \text{as } c \rightarrow 0$$

Examples of stiffness predictions by (10.9) are presented graphically in Figs. 10.29 and 10.30. An easy approximation of (10.9) is presented in (10.10) with $e \equiv 0$ for $c > c_P$. Qualitatively (10.10) applies at any $c_P < 1$. Quantitatively, however, it is best when c_P and μ_P^0 are related as indicated.

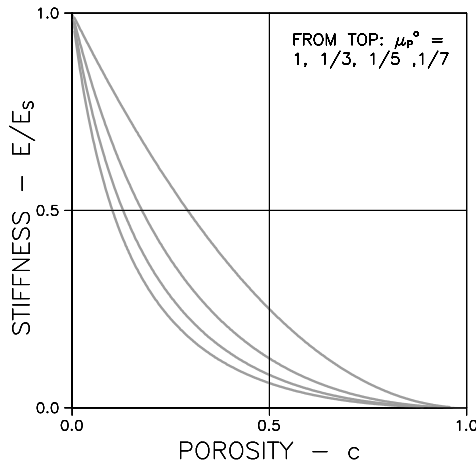


Fig. 10.29. Porous material with shape factors as indicated, and $c_P = 1$

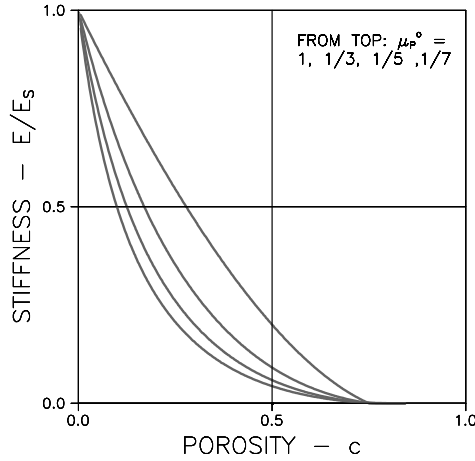


Fig. 10.30. Porous material with shape factors as indicated, and $c_P = 0.75$

$$e \approx \left(1 - \frac{c}{c_P}\right)^D \quad \text{with } D = c_P \left(1 + \frac{1}{\mu_P^0}\right) \quad \text{for } c_P \leq \begin{cases} 1 & \text{if } \mu_P^0 > 0.5 \\ \mu_P^0 & \text{if } \mu_P^0 < 0.5 \end{cases} \quad (10.10)$$

Remark: This equation tells us that a very simple porosity relation raised to a power, which reflects only the pore geometry, can predict stiffness of porous materials approximately. In general (with a fixed c_P) this power will increase with increasing complexity of the pore geometry (decreasing μ_P^0).

Theory versus Empirical Expressions

A variety of empirical stiffness-porosity expressions, critically reviewed by Fagerlund in [20], are presented in the literature on porous materials. It is of some interest to discuss briefly (10.9) and (10.10) in relation to the two expressions presented in (10.11) which are among the most frequently used to fit data obtained from tests on porous media – the former in [80, 81] and the latter in [82, 83] for example. F and H are constants to be determined experimentally.

$$\left. \begin{aligned} e &= (1 - c)^F \\ e &= \exp(-Hc) \end{aligned} \right) \rightarrow \begin{pmatrix} 1 - Fc \\ 1 - Hc \end{pmatrix} \quad \text{as } c \rightarrow 0 \quad (10.11)$$

Excellent fits are often observed by these expressions at low and moderately low porosities. At higher porosities, however, difficulties may be encountered. The former expression cannot be used when DC-CD and MM-CD composites are considered with $c_P < 1$. The latter expression always predicts a finite stiffness at $c = 1$. None of these disadvantages apply to (10.9) and (10.10).

Remark: Mathematically the expressions presented in (10.10) and (10.11) are of similar types. It is concluded that the factors F and H of the empirical expressions are related to composite geometry just as is the factor D in (10.10).

Deduction of Shape Parameters from Experiments

At low porosities both fit expressions in (10.11) and the results obtained by the present method in (10.9) and (10.10) approach identical stiffness quantities when (10.12) applies.

$$F = H = \frac{1}{\mu_P^0} + 1 \Rightarrow \mu_P^0 = \frac{1}{F - 1} = \frac{1}{H - 1} \quad (10.12)$$

Obviously this observation can be used to deduce shape factors from experimental data – or it can be used to give some geometrical explanation to the empirical factors F and H used in the literature. More general information, however, on the geometry and stiffness of porous materials can be retrieved from experimental data. We linearize (10.9) (with $e = E/E_S$) as shown in (10.13). Then μ_P^0 , c_P , and E_S are easily deduced by linear regression of the manipulated experimental data (X, Y) , optimizing the fit quality (r^2) with respect to c_P .

$$Y = Y_0 + \alpha X \quad \text{with} \quad X = \frac{c}{1 - c/c_P} \quad \text{and} \quad Y = \frac{1 - c}{E} \Rightarrow \quad (10.13)$$

$$E_S = 1/Y_0 ; \mu_P^0 = Y_0/\alpha \quad \text{from intersection } Y_0 \text{ and slope } \alpha$$

Remark: It is noticed that no other information on composite geometry than μ_P and c_P can be obtained directly from mechanical tests on porous materials. To get information on μ_S and c_S the pore system considered has to be impregnated – or supplementary studies on percolation and diffusivity have to be made.

Stiff Pore Systems

Stiff pore systems are composites where one phase (P) is extremely stiff relative to the other phase (S). The stiffness relation presented in (10.14) is easily obtained by the simplified analysis letting $n \rightarrow \infty$ and utilizing that the geo-function θ reduces as shown in Table 4.1. Infinite stiffness is predicted for $c \geq c_S$. A graphical representation of (10.14) is shown in Fig. 10.31. The composite considered is particulate with an aspect ratio of $A = 2$ and a critical concentration of $c_S = 0.6$. Equation (10.14) is also developed in [84, 85].

$$e = \frac{1 + \theta_\infty c}{1 - c} ; \theta_\infty = \begin{cases} \frac{\mu_P + \mu_S - 1}{\mu_S} & c < c_S \\ \infty & c > c_S \end{cases} \quad (10.14)$$

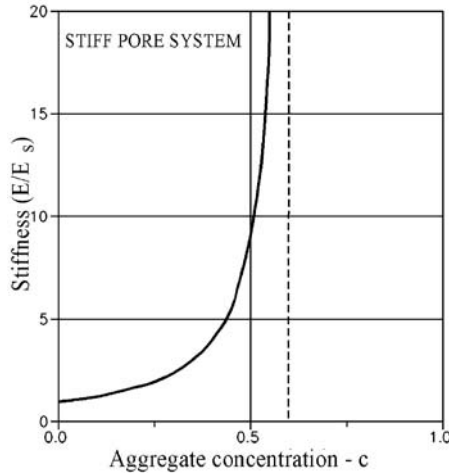


Fig. 10.31. Particulate composite with shape functions defined by particles of aspect ratios $A = 2$ and a critical concentration of $c_S = 0.6$

10.4 Theory and Experiments

A number of examples are presented in this section where experimentally obtained data for various mechanical composite properties are compared with data predicted by the simplified theory. Predictions of internal stresses are included whenever such information might be of interest.

Some times the analysis has to be slightly modified in order to consider special features, which apply to composites in practice. Examples are modifications with respect to interference phenomena, modifications with respect to incompletely impregnated pore systems, and modifications with respect to defective phase contacts. These topics are considered in the following section.

10.4.1 Some Irregular Geometries

Non-Flexible Geometry – Interference

We recall from Sect. 1.1.1 that flexible phase geometries primarily are considered in this book, which can adjust them selves (naturally, by compaction, or otherwise) to form a tight composite. When phase geometries are not flexible, air voids are inevitable at certain concentrations. For example: In a material reinforced by non-flexible phase P particles, voids will turn up at concentrations $c > c_{\text{PACK}}$. The latter concentration is the so-called packing concentration of particles (as packed in the composite) where a stable phase P structure is formed.

A number of theories (ex [86,87]) have been developed by which the packing concentration can be estimated. For uni-sized discs and fibers crude estimates can be made by (10.15), based on Fig. 10.32. In practice considerably

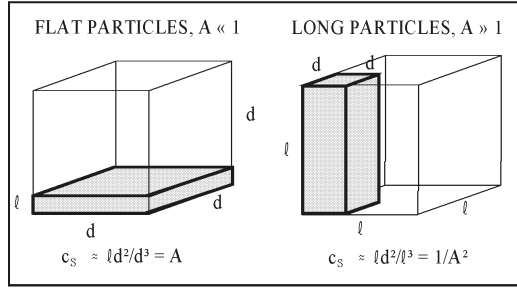


Fig. 10.32. Crude estimate of critical concentration, c_S , as related to aspect ratio

higher packing concentrations can be achieved by modern grading and vibration techniques.

$$c_{\text{PACK}} > 0.5 \begin{cases} 1/A^2; & A > 1 \\ A; & A < 1 \end{cases} \quad \text{rough estimate} \quad (10.15)$$

The amount of voids, $c_{\text{VOID}} = V_{\text{VOID}}/(V_S + V_{\text{VOID}})$, relative to the original phase S volume can be expressed as follows,

$$c_{\text{VOID}} = \begin{cases} \frac{c - c_{\text{PACK}}}{c(1 - c_{\text{PACK}})}; & c > c_{\text{PACK}} \\ 0; & c \leq c_{\text{PACK}} \end{cases} \quad (10.16)$$

There is some resemblance between c_{PACK} and the critical concentration c_S where phase P leaves the state of being 100% discrete. In the present context we may put $c_S \approx c_{\text{PACK}}$ assuming that the state of interference is considered to be a so-called stable interference where large areas of contact between neighboring particles are “glued” together by a very thin layer of a sufficiently strong phase S.

The analysis of composites with non-flexible phase P is not different from the analysis of composites hitherto considered when $c \leq c_S (= c_{\text{PACK}})$. When $c > c_{\text{PACK}}$ phase geometry is frozen to stay as it is at $c = c_{\text{PACK}}$ where the MM-geometry is just about to be encountered. The volume concentration of phase P (relative to phase S) can only increase by replacing some phase S material with voids. Obviously the stiffness of phase S now becomes that of a porous phase S. We introduce effective stiffness geometric properties as presented in (10.17) assuming that pores are spherical (other void shapes can easily be considered; to do so, however, is too speculative). We recall that composite geometry stays at the geometry defined at $c = c_{\text{PACK}}$. Then the analysis proceeds as explained in (10.18) following the general principles presented in this book. As a consequence of the frozen MM-geometry of the composite, stiffness approaches 0 as c approaches 1.

An example of a stiffness analysis of particulate composites with non-flexible multi-shaped particles is demonstrated in Figs. 10.33 and 10.34.

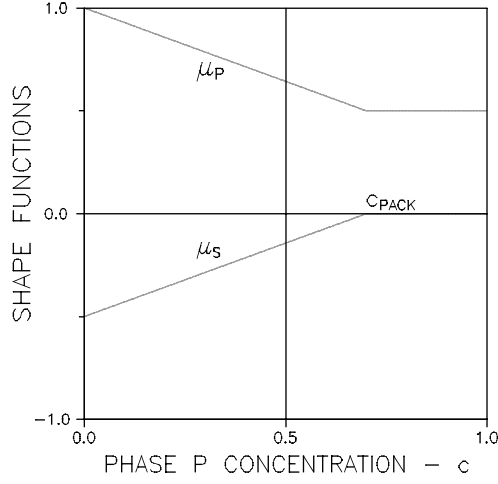


Fig. 10.33. Particulate composite with non-flexible particles. 10% short fibres ($A = 2.5$) + 90% spheres ($A = 1$) and $c_{\text{PACK}} = c_S = 0.7 \rightarrow (\mu_P^0, \mu_S^0) = (1, -0.5)$. $(E_S, E_P) = (25.75)$ MPa

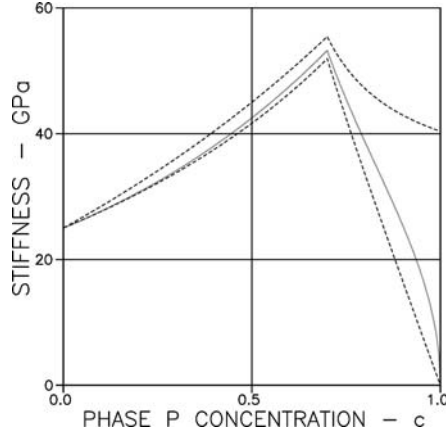


Fig. 10.34. Particulate composite with non-flexible particles as described in Fig. 10.33

$$\left. \begin{aligned} E_{S,\text{EFF}} &= E_S \frac{1 - c_{\text{VOID}}}{1 + c_{\text{VOID}}} ; \quad n_{\text{EFF}} = n \frac{1 + c_{\text{VOID}}}{1 - c_{\text{VOID}}} \\ \mu_{P,\text{EFF}} &\equiv \mu_P(c_{\text{PACK}}) ; \quad \mu_{S,\text{EFF}} \equiv \mu_S(c_{\text{PACK}}) \equiv 0 \\ \theta_{\text{EFF}} &= 0.5 \left[\mu_{P,\text{EFF}} + \sqrt{\mu_{P,\text{EFF}}^2 + 4n_{\text{EFF}}(1 - \mu_{P,\text{EFF}})} \right] \end{aligned} \right) \quad c > c_{\text{PACK}} \quad (10.17)$$

$$E = E_{S,\text{EFF}} \frac{n_{\text{EFF}} + \theta_{\text{EFF}}[1 + c_{\text{PACK}}(n_{\text{EFF}} - 1)]}{n_{\text{EFF}} + \theta_{\text{EFF}} - c_{\text{PACK}}(n_{\text{EFF}} - 1)} ; \quad c > c_{\text{PACK}} \quad (10.18)$$

In most practice the interference phenomenon is of theoretical interest mainly. For a number of reasons we do not want composites with self-inflicted voids. Much effort is made to produce particle size distributions such that voids can be avoided. In some special cases, however, where weight and heat insulation are principal design parameters such voids may be desirable. This feature is discussed in Sect. 10.4.5.

Incomplete Impregnation

If a composite is made by impregnation of a porous material, then the impregnant (phase P) may be porous itself for a number of reasons. Shrinkage of the impregnant, for example, may cause this phenomenon. In this case phase P appears as a porous material the effective stiffness property of which can be approximated as shown in (10.20) with void ratio and degree of impregnation defined in (10.19). Spherical void shapes are assumed. Other shapes can easily be considered. However, to assume void shapes others than spherical might be too speculative.

$$\begin{aligned} \beta &= \frac{\text{volume of impregnant}}{\text{pore volume}} && \text{is degree of impregnation} \\ c_{\text{VOID}} &= 1 - \beta && \text{is void ratio in impregnant} \end{aligned} \quad (10.19)$$

$$E_{P,\text{EFF}} \approx E_P \frac{1 - c_{\text{VOID}}}{1 + c_{\text{VOID}}} = E_P \frac{\beta}{2 - \beta} \Rightarrow n_{\text{EFF}} = n \frac{\beta}{2 - \beta} \quad (10.20)$$

Incomplete Phase Contact

For several reasons perfect contact between phases in a composite material may be destroyed. Impurities on aggregate, bleeding, early age volume changes, and particles interference in concrete, for example, may cause this problem. It is justified in Sect. 8.3.3 that missing phase contact in particulate composites with compact particles can be considered approximately in a stiffness analysis by replacing the stiffness ratio, n , with an effective stiffness ratio, n_{EFF} . In a slightly modified version the procedure is demonstrated in (10.21) determining the stiffness of a CSA_P composite with a degree of defective particle surface (S) defined as $\chi = S_{\text{INACTIVE}}/S$. Defective areas are considered with no voids associated.

$$e = \frac{A + n_{\text{EFF}}}{1 + A n_{\text{EFF}}} \quad \text{with} \quad \begin{cases} A = (1 - c)/(1 + c) \\ n_{\text{EFF}} = n(1 - \chi^a) \\ a = \max[1, 9/(5 + n)] \end{cases} \quad (10.21)$$

10.4.2 Various Porous Materials

Experimentally determined stiffness data of porous materials are compared in this section with data described by (10.9) in Sect. 10.3.5. Geo-parameters

(μ_P^0, c_P) and solid phase stiffness (E_S) have been deduced from the experimental stiffness data using the regression technique also explained in Sect. 10.3.5. In the following figures dots and lines present experimental data and theoretical data respectively.

Tile

Young's modulus of tile has been determined experimentally in [88] as shown by dots in Fig. 10.35. The theoretical stiffness presented is based on $E_S = 38000$ MPa, $\mu_P^0 = 0.9$, and $c_P = 0.53$.

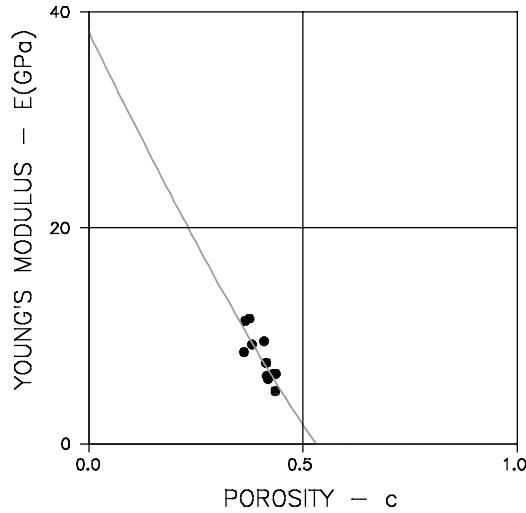


Fig. 10.35. Stiffness of tile: $(\mu_P^0, c_P) = (0.9, 0.53)$

Porous Magnesium Oxide

Experimental data on Young's modulus of porous magnesium oxide (MgO) were collected in [83] from six sources representing a variety of processing techniques. Porosities considered were $c < 30\%$. It was shown that all these data were fitted very well by the exponential expression presented in (10.11) with $H = 4.74$ and $E_S = 3.2 \cdot 10^5$ MPa. The data such described are digitalized as presented in Fig. 10.36 with dots. The theoretical data are based on the geometrical information $(\mu_P^0, c_P) = (0.24, 0.88)$. It is noticed that the shape factor obtained complies well with $\mu_P^0 \approx 0.26$ deduced by (10.12).

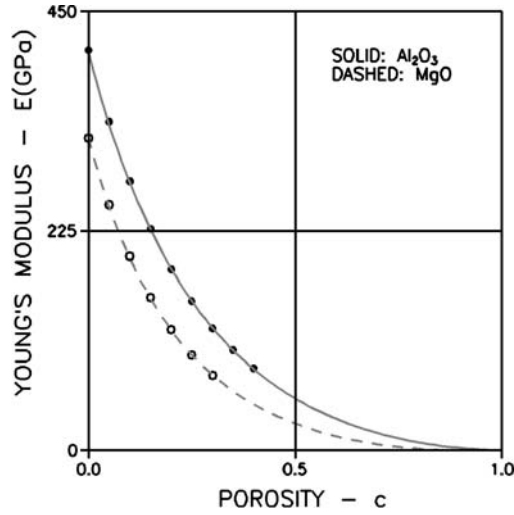


Fig. 10.36. Stiffness of porous materials made of polycrystalline oxides

Porous Aluminum Oxide

In a similar experimental analysis of the elasticity of porous aluminum oxide (Al_2O_3) it was shown in [89] that experimental data from 11 sources with porosities $c < 40\%$ were very well fitted by the exponential expression in (10.11) introducing $H = 3.95$ and $E_S = 4.1 \cdot 10^5$ MPa. The data such described are digitalized as presented in Fig. 10.36 with dots. The theoretical data are based on the geometrical information $(\mu_P^0, c_P) = (0.35, \approx 1)$. It is noticed that the shape factor obtained complies well with $\mu_P^0 \approx 0.34$ deduced by (10.12).

Hardened Cement Paste

The data presented in Fig. 10.37 illustrate the influence of porosity (evaporable water measurement) on elasticity of nearly fully hydrated hardened Portland cement paste (HCP). The experimental data presented in the figure are from [81, cement 15366]. They are related to two pore systems defined in [24]. *System I*: Solid phase (S) is made of cement gel solids, the pore phase is the total of cement gel pores and capillary pores. *System II*: Solid phase is cement gel; the pore phase is capillary pores. The theoretical data are based on the following information.

Composite:	System I: $(\mu_P^0, c_P) = (0.33, \approx 1)$
	System II: $(\mu_P^0, c_P) = (0.4, \approx 1)$
Phase S :	System I: $E_S = 80000$ MPa (gel solid)
	System II: $E_S = 32000$ MPa (gel including gel pores)

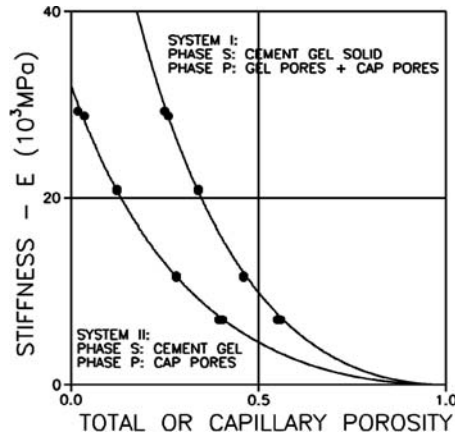


Fig. 10.37. Young's modulus of hardened Portland cement paste

Lime Mortar

An examination of lime mortars with porosities of approximately $c = 0.3$ was reported in [90]. Various material properties (such as stiffness, frost resistance, and capillary suction) were measured and related qualitatively to the microstructure of material tested. Different microscopic techniques were used to characterize the microstructure for homogeneity and coherence on a scale from $H = 1$ (bad) to $H = 5$ (high quality). The stiffness data are presented in Fig. 10.38.

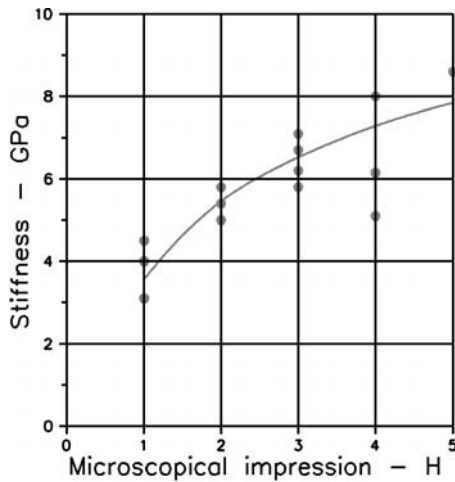


Fig. 10.38. Young's modulus of lime mortar as related to structure (microscopical impression H)

The idea was suggested by Nielsen [91,92] that the qualitative evaluation made in [90] can be quantified by (10.9) with $c_P = 1$ and shape factors $\mu_P^0 = H/5$ introduced. This means that high quality mortars are assumed to have spherical voids, while bad mortars have flat voids. Nielsen's description of structure versus stiffness made in this way with $E_S = 16$ GPa is illustrated in Fig. 10.38 reproduced from [91]. The ideas of Nielsen were evaluated positively in an image analysis [93] on planar sections made on some of the mortars considered in [90]. This analysis seems to indicate that it might be worthwhile pursuing the possibilities of using image analysis in quality control of porous materials.

Summary – Porous Materials

Stiffness data obtained from tests on porous materials have been shown in this section to be very well described by the theoretical (10.9). The geometrical information used indicate that the pore systems become finer and more complex (decreasing μ_P^0) as we go from tile ($\mu_P^0 = 0.9$), to HCP(cap-por) (0.4), to HCP(tot-por) and Al_2O_3 (0.33), to MgO (0.24). For comparison the results are compiled in (10.22). The lime mortar results are not presented in this equation because only one porosity was considered. At an average, however, one may expect that lime mortar behave approximately as HCP.

The expressions in (10.22) are ranked with respect to increasing powers of the stiffness descriptions. It is observed that this ranking is the same as ranking with respect to decreasing shape factors. This feature can be taken as an experimental justification of the theoretical statement made in Sect. 10.3.5 that stiffness of porous materials can be expressed by simple porosity relations raised to a power which increases with increasing complexity (away from spherical) of pore geometry.

$$\begin{array}{lll}
 e \approx (1 - 1.9c)^{1.12} & \text{Tile} & (\mu_P^0, c_P) = (0.9, 0.53) \\
 e \approx (1 - c)^{3.5} & \text{HCP(cap-pore)} & (\mu_P^0, c_P) = (0.4, 1) \\
 e \approx (1 - c)^{4.0} & \text{HCP(tot-pore), Al}_2\text{O}_3 & (\mu_P^0, c_P) = (0.33, 1) \\
 e \approx (1 - 1.14c)^{4.55} & \text{MgO} & (\mu_P^0, c_P) = (0.24, 0.88)
 \end{array} \quad (10.22)$$

It is interesting to note that the third expression in (10.22) is numerically identical to an empirical expression suggested in [94] to predict the elasticity of pore systems created by incomplete compaction of cement concrete. Thus, it seems that pores created by incomplete compaction of concretes have a geometry the complexity of which is similar to the geometry of the total pore system in HCP.

10.4.3 Sulphur Impregnated Cement/Silicate System

Figure 10.39 illustrates the influence of pores (measured by Helium comparison pycnometry) on the elasticity of autoclaved (“empty”) systems made of water and equal amounts of Portland cement and silica powders (SiO_2 , max

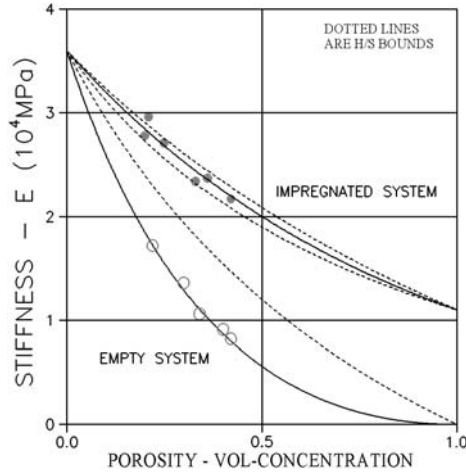


Fig. 10.39. Young's moduli of porous and sulphur impregnated autoclaved Portland cement/silicate systems

diameter 0.15 mm) – and such systems impregnated by sulphur. The experimental data are from [95] and [96] respectively. The theoretical data shown are predictions by the simplified composite theory with geo-parameters μ_P^0 , c_P , and solid phase stiffness E_S obtained by regression of experimental stiffness data from the empty system. The additional information on type of composite (phase symmetry) is estimated as no further geometrical information can be obtained from [95,96].

Composite: Phase-symmetric CC-CC with $(\mu_P^0, c_P) = (0.45, 1)$

Phase S: $E_S = 36000 \text{ MPa}$

Phase P: $E_P = 16000 \text{ MPa}, \beta = 0.82 (E_{P, \text{EFF}} = 11000 \text{ MPa})$

The stiffness of Sulphur is calculated from information presented in [97] for Young's moduli of polycrystalline sulphur. An inspection of the test results in [96] reveals that the degree of impregnation varies non-systematically between 0.75 and 0.87 with an average of $\beta = 0.82$ from which the effective stiffness of Sulphur is calculated by (10.20). (The incomplete impregnation was due to shrinkage of sulphur when solidifying).

Remarks: It is noticed that similar orders of magnitudes apply for the shape factor μ_P^0 and stiffness 1) for the pore system considered in this example and 2) for the HCP pore system II considered in Sect. 10.4.2, Fig. 10.37. This observation agrees with the expectation one might have that pores defined by Helium comparison pycnometry will not include gel pores. These pores are included in the “solid phase” of the system considered which has a stiffness of similar magnitude as cement gel in Fig. 10.37.

The assumed composite geometry (phase-symmetric CC-CC) of the system considered is justified implicitly by the excellent simultaneous agreement

between experimental data and theoretical data demonstrated in Fig. 10.39 for both empty and impregnated pore systems.

10.4.4 Salt Infected Bricks

The thermal expansion of salt infected (impregnated) bricks shown in Fig. 10.41 has been determined experimentally in [98] as related to porosity and weight amount of salt (NaCl). The theoretical data shown are based on the following information where β is degree of impregnation:

Composite: CC-CD with $(\mu_P^0, \mu_S^0, c_P) = (0.9, 0, 0.53)$, $(c_S = 0)$
 Phase S (Tile): $E_S = 38000 \text{ MPa}$, $\lambda_S = 6.0 \cdot 10^{-6} / ^\circ\text{C}$
 Phase P (Salt): $E_P = 20000 \text{ MPa}$, $\lambda_P = 3.8 \cdot 10^{-5} / ^\circ\text{C}$, $\beta = 0.15 - 0.25$

The thermal expansion coefficients (λ) of plain rock salt and plain tile were experimentally determined in [98]. The Young's modulus of salt is estimated from the literature [99]. The geometrical data (μ_P^0, c_P) and the Young's modulus for tile are reproduced from Sect. 10.4.2, Fig. 10.35. The additional information of a shape factor $\mu_S^0 = 0$ is estimated from knowing that the major part of pores in tile are continuous. We may think of a pearls on a string pore system with $\mu_S^0 = 0$. It is noticed that μ_S in Fig. 10.40 has been truncated to have $\max(\mu_S) = 1$ as required in (10.1). An inspection of the test results in [98] reveals that the degree of impregnation varies non-systematically as indicated with an average of $\beta = 0.20$ from which an effective stiffness $E_{P,\text{EFF}} = 2200 \text{ MPa}$ of the pore system can be calculated from (10.20).

Remark: The assumed geometry of tile as a CC-CD composite with shape functions described in Fig. 10.40 is implicitly justified by the excellent agreement between experimental data and theoretical data demonstrated in

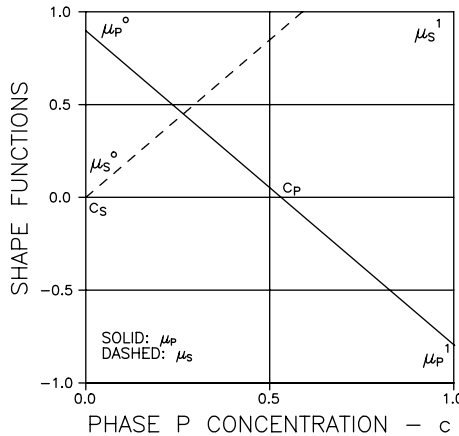


Fig. 10.40. Shape functions for tile: $(\mu_P^0, \mu_S^0, c_P) = (0.9, 0, 0)$

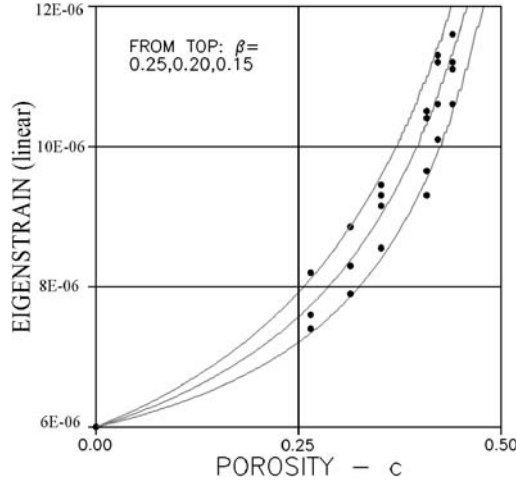


Fig. 10.41. Thermal eigenstrain ($^{\circ}\text{C}$) of salt infected tile

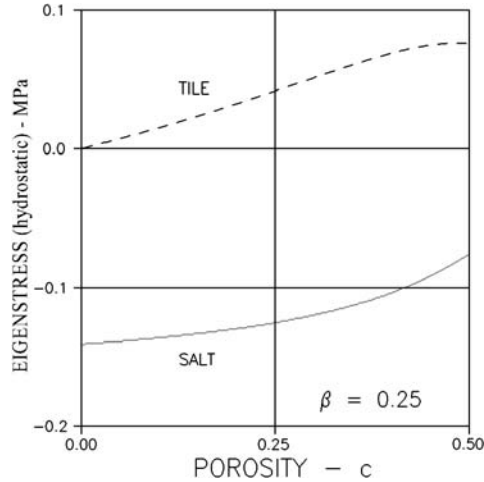


Fig. 10.42. Predicted thermal eigenstress ($^{\circ}\text{C}$) in salt infected brick

Fig. 10.41. The internal stress state calculated for a degree of impregnation, $\beta = 0.25$, is shown in Fig. 10.42.

10.4.5 Non-Flexible Particles in Particulate Composite

The experimental data shown in Fig. 10.43 are from tests reported in [100] on cement mortars made of cement paste mixed with compact, nearly uni-sized coarse quartz particles, which interfere at $c_{\text{PACK}} = 0.55$. It is assumed that the composite considered is basically a CSA_P material with $(\mu_P^0, \mu_S^0) = (1, -1)$.

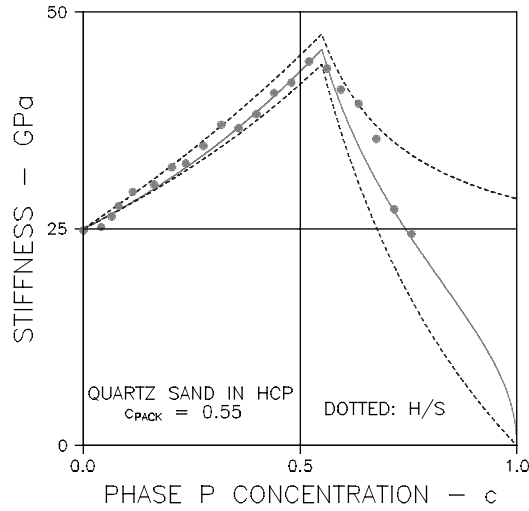


Fig. 10.43. Sand in HCP. $(E_P, E_S) = (75, 25)$ GPa. $(\mu_P^0, \mu_S^0) = (1, -1)$

The method of analysis used to predict stiffness (solid lines) is the one explained in Sect. 10.4.1 where particulate composites with non-flexible geometries are considered.

The experimental data shown in Fig. 10.44 are from [101] where the phenomenon of interference has been used deliberately (weight, economy, heat insulation) in design of lightweight concrete. The method of analysis used for

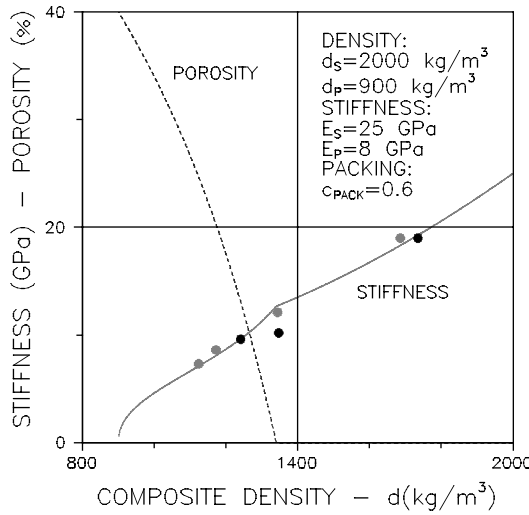


Fig. 10.44. Ligth clinker concrete. Material properties as indicated. $(\mu_P^0, \mu_S^0) = (1, -1)$

stiffness prediction (solid lines) is the same as used in the previous example. It is assumed that the concrete considered starts up at $c = 0$ being a CSA_P composite with $(\mu_P^0, \mu_S^0) = (1, -1)$. A packing concentration of $c_{\text{PACK}} = 0.6 (= c_S)$ is a realistic estimate for the packing of light clinker. Density of the composite is $d = c^*d_P + (1-c)^*d_S$. Porosity indicated in the figure is relative to composite volume, meaning porosity $= V_{\text{VOID}}/(V_S + V_P + V_{\text{VOID}}) = (c - c_{\text{PACK}})/c$.

10.4.6 Defective Phase Contact in Concrete

Hansen suggests in [102, 103] that stiffness of concrete (with stiffness ratio $n > 1$) can be predicted by the lower P/H bound as indicated by dots in Fig. 10.45. Hansen's suggestion is strongly justified by experimental data. Implicitly Hansen's observations seem to indicate that concrete is an anisotropically layered composite. Concrete, however, *is* a macroscopically isotropic composite similar to a CSA_P material (spheres in a continuous matrix). Stiffness should therefore be predicted close to the lower H/S-bound also indicated in Fig. 10.45.

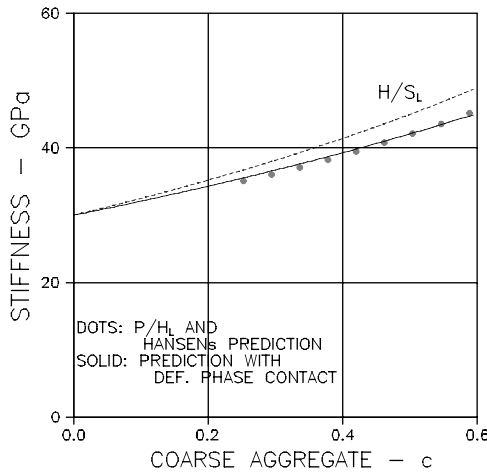


Fig. 10.45. Stiffness of concrete with defective contact between coarse aggregate and mortar

One might state that this discrepancy in observations can be explained as a consequence of defective phase contacts between aggregates and mortar. The theoretical data shown in Fig. 10.45 by a solid line, are calculated by (10.21) assuming that the concrete considered behaves as a CSA_P material with defective phase contacts. Further information used is:

Defective phase contact: $\chi = 20\%$
 Phase S (Mortar): $E_S = 30000 \text{ MPa}$
 Phase P (Coarse aggregate): $E_P = 70000 \text{ MPa}$

Stiffness such estimated are order of magnitudes usually met in concrete technology. The degree of defective phase contact assumed between coarse aggregate and mortar agrees with observations made by Nielsen in [104] on normal concrete.

It seems then justified by Fig. 10.45 that the “Hansen’s paradox” can very well be explained as the result of defective phase contacts.

A Strength Mechanism for Concrete

When stiffness reduction is known as a function of increasing defective bond areas then strength reduction can be estimated as follows using some ideas, suggested in [71] on the basis of the well-known “Compliance calibration equation”, see [105] for example. The ideas are subsequently demonstrated on a CSA_P composite subjected to a tensile stress σ . Defective bond areas are considered as a crack system expanding along the bond area. For such a crack system the energy involved in crack expansion can be expressed by the “Compliance calibration equation” formulated as shown in (10.23) with E (from (10.21)) and Γ denoting Young’s modulus and the so-called strain energy release rate respectively.

Equation (10.23) can be organized as shown in (10.24) performing the differentiation of E with respect to crack area. Strength (σ_{CR}) can then be predicted introducing a failure criterion, which tells that failure, will occur when Γ becomes critical ($\Gamma = \Gamma_{CR}$). Relative strength, $\sigma_{CR}/\sigma_{CR,REF}$, is given by the latter expression in (10.24) where Γ_{CR} has been eliminated introducing the reference strength ($\sigma_{CR,REF}$) at a reference degree of defective aggregate surface (χ_{REF}).

$$\Gamma \propto \sigma^2 \frac{d(1/E)}{dB} \text{ where } \begin{cases} \Gamma = \text{Strain energy release rate} \\ B = \frac{3\chi c}{R} = \text{Crack area per vol - unit} \\ R = \text{Radius of particle} \end{cases} \quad (10.23)$$

$$\frac{\Gamma E_s}{\sigma^2} \propto \frac{Rna\chi^{a-1}}{3c} \frac{1-A^2}{A+n_{EFF}^2} \Rightarrow \frac{\sigma_{CR}}{\sigma_{CR,REF}} = \frac{A+n_{EFF}}{A+n_{EFF,REF}} \left(\frac{\chi}{\chi_{REF}} \right)^{(1-a)/2} \quad (10.24)$$

An example is presented in Fig. 10.46 where (10.24) has been used to estimate which strength gain can be expected by reducing the defective bond areas on coarse aggregates in a concrete with $(c, n) = (0.5, 2.5)$ where c and n are volume concentration and stiffness ratio respectively of coarse aggregates.

It is emphasized that predicted strength must be truncated at a certain level determined by the theoretical (un-cracked) bond strength. It should also be noted that strength in the present context refers to bond failure. Other failure mechanisms may act simultaneously.

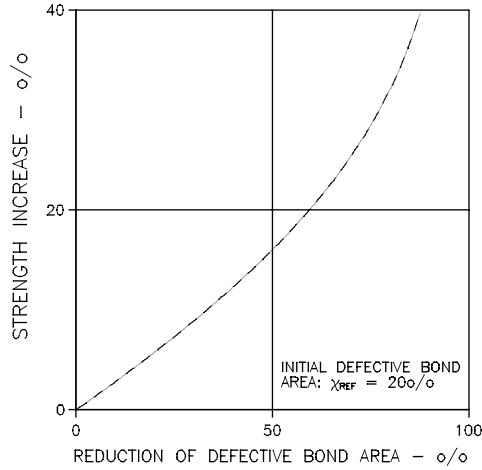


Fig. 10.46. Gain of concrete strength obtained by reducing defective bond areas on coarse aggregates

10.4.7 Hydrating Cement Paste and Concrete

The stiffness of a hardening cement paste (HCP) and concrete can be calculated from Table 10.5, which combines the composition models of these materials presented in Appendix E with the geometry of CSA_P composites. The concept of “basic paste” as well as the abbreviations in Table 10.5 are explained in the same appendix. W/C denotes water/cement ratio by weight. The exponent Q introduced to describe the stiffness of HCP with $W/C > 0.38$ considers empirically that the geometrical complexity of basic paste voids decreases with increasing degree of hydration.

Table 10.5. Stiffness of concrete and HCP. Volume parameters A_{VOID} and A_{CEM} are defined and quantified in Table E.1, Appendix E. Stiffness of basic paste and un-hydrated cement are denoted by E_{BAS} and $E_{CEM} = 55000$ MPa respectively

Concrete	
$E = E_{HCP} \frac{A + n}{1 + An}$ with $n = \frac{E_P}{E_{HCP}}$	
HCP	
$W/C > 0.38$	$E_{HCP} = E_{BAS} * A_{VOID}^Q$ with $Q = 7 - 5g(t)$
$W/C \leq 0.38$	$E_{HCP} = E_{BAS} * \frac{A_{CEM} + n_{BAS}}{1 + A_{CEM}n_{BAS}}$ with $n_{BAS} = \frac{E_{CEM}}{E_{BAS}} = \frac{1.7}{g(t)}$
Basic paste	$E_{BAS} = 32000 * g(t)$ MPa with degree of hydration $g(t) = \exp(-(\tau/t)^\beta)$

The quality of Table 10.5 to predict concrete stiffness is tested on results reported in [106] from tests on the age dependency of concrete stiffness. The concrete used and the stiffness data obtained in these tests are described/plotted in Fig. 10.48. The degree of hydration was very close to the one shown in Fig. 10.47, which is fitted from the experimental hydration data using the $g(t)$ -expression presented in Table 10.5.

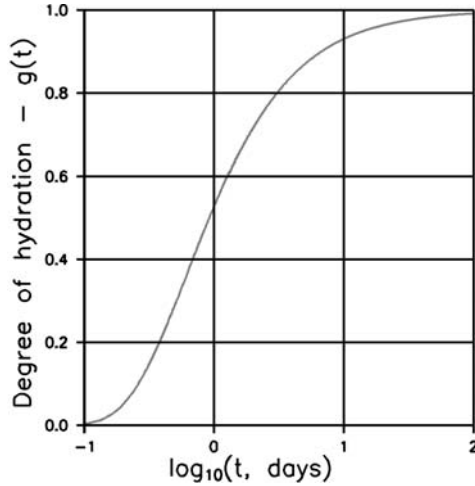


Fig. 10.47. Degree of hydration, $g(t)$ defined by $(\tau, \beta) = (0.625 \text{ days}, 0.95)$

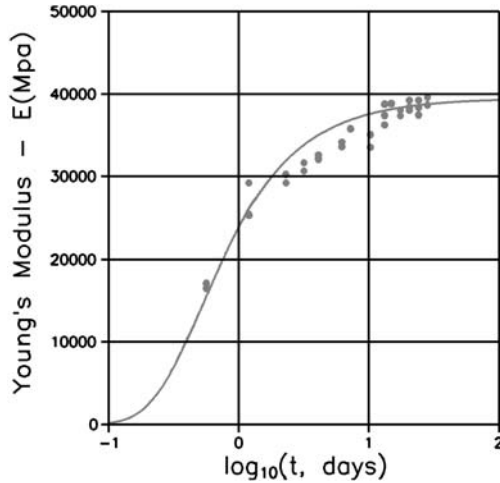


Fig. 10.48. Concrete with $(W/C, A/C) = (0.45, 5.21)$; $E_P = 50000 \text{ MPa}$, and degree of hydration from Fig. 10.47

The solid line in Fig. 10.48 is stiffness predicted by Table 10.5. The agreement between experimental data and theoretical data is observed to be reasonably good. Recently Bentz [107] has also studied the influence of hydration on the stiffness of HCP using a special computer simulation technique. Lokhorst and Breugel [108] studied the same phenomenon considering HCP as part of concrete, modeled as a layered composite.

Strength of HCP

An Anticipating Investigation: During shrinkage of concrete, tensile stresses develop in the cement paste phase. These stresses are subsequently predicted in Chap. 15. To evaluate how dangerous they are we will compare them with the tensile strength of HCP, which can be estimated to be one tenth of the compressive strength presented in (10.25). This expression is developed from a theory presented in [40, 109]: Compressive strength (S) as a function of age. Auxiliary expressions on porosity and hydration are presented in (10.26) and (10.27) reproduced from Appendix E. An illustrative example is presented in Fig. 10.49.

$$S = \begin{cases} 450(1 - c_{\text{TOT}})^B \text{ MPa} & \text{at } q > (W/C)/2 \\ 0 & \text{at } q < (W/C)/2 \end{cases} \quad \text{with } B = \frac{2.35}{[q(t) - 0.19]^{0.45}} \quad (10.25)$$

$$c_{\text{TOT}} = \begin{cases} \frac{100 W/C - 18q(t)}{100W/C + 32} & \text{when } W/C > 0.38 \\ \frac{100 W/C[1 - 0.47q(t)]}{100W/C + 32} & \text{when } W/C \leq 0.38 \end{cases} \quad \text{total HCP porosity} \quad (10.26)$$

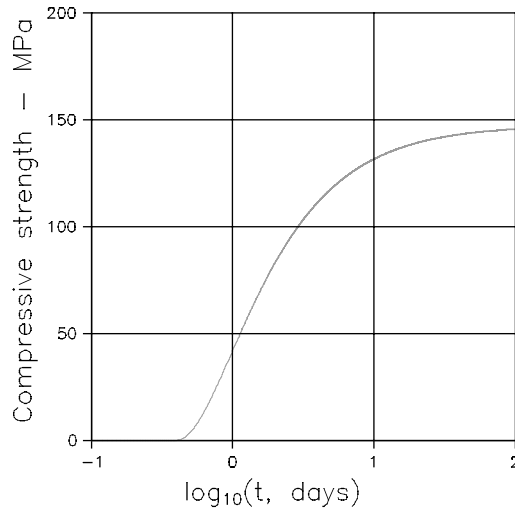


Fig. 10.49. Compressive strength of a HCP with $W/C = 0.45$ and degree of hydration from Fig. 10.47

$$q(t) = \begin{cases} g(t) & \text{when } W/C > 0.38 \\ \min \left(\frac{0.38}{W/C} g(t), 1 \right) & \text{when } W/C \leq 0.38 \end{cases} \quad \text{relative degree of hydration (10.27)}$$

10.5 Conclusion

The general composite analysis presented in Chap. 8 has been successfully simplified in this chapter to reflect realistically well the somewhat limited knowledge available in most practice on composite geometry. Standard stiffness-, stress-, and eigenstrain/stress solutions for various types of composites have been developed. Special attention has been given to the mechanical behaviour of porous materials.

The results of the simplified composite theory have been successfully compared with results obtained by FEM-analysis and experimental results elsewhere reported in the composite literature. Composites of different geometries have been considered such as hardened cement paste, salt infected tile materials, impregnated silicate systems, concrete, and cement mortars made with sand of discontinuous size grading. Stiffness was considered together with other composite properties such as thermal expansion and internal stresses. Also the effect of defective phase contact as well as interference between non-flexible particles on composite stiffness properties have been studied. Special topics considered are stiffness of porous materials relative to pore geometry.

All together it can be concluded that the simplified prediction method presented qualifies as an efficient tool in the analysis of various practical problems with respect to the mechanical behavior of composite materials. Combining this statement with the positive indications made on the many types of composite classes the theory can handle, it seems that the simplified composite theory presented is well qualified as the basic instrument in further studies of the behavior of composite materials. Examples, such as rheology and other physical properties are considered in subsequent chapters.

Further qualifications of the theory are demonstrated in subsequent chapters: It is shown in Chap. 12 that the theory can be used as a diagnostic “instrument” for evaluation of prediction methods with respect to reliability and underlying geometry. Methods such as experimentally, semi-theoretically, or theoretically (SCS) obtained are tested. It is demonstrated in Chap. 13 that the theory has potentials with respect to design of composites.

Simplified Composite Theory – Conductivity

The composite theory for conductivity in Chap. 9 is simplified in this chapter just as the theory of elastic composites in Chap. 8 has been simplified in Chap. 10. This means that the conductivity expressions from Chap. 9 can be used immediately as they are – with shape functions, however, simplified as described in Sect. 10.1.

The simplification procedure is demonstrated in the following example where the conductivity of porous materials is considered.

11.1 Illustrative Example

Equation (11.1), reproduced from (9.4), expresses the accurate conductivity of a porous material with shape function μ_P determined according to Chap. 7 with Poisson's ratios $\nu_P = \nu_S = 0$

$$q_0 = \frac{Q_0}{Q_S} = \frac{1 - c}{1 + c/\theta_0} \quad \text{with } \theta_0 = \begin{cases} 2\mu_P & \text{when } c < c_P \\ 0 & \text{when } c > c_P \end{cases} \quad \text{accurate solution (11.1)}$$

The simplified version of this expression becomes (11.2) because the simplified shape function, expressed according to Sect. 10.1 becomes (11.3) with shape factor μ_P^0 determined from Table 10.2.

$$q_0 = \frac{Q_0}{Q_S} = \begin{cases} \frac{1 - c}{1 + c/[2\mu_P^0(1 - c/c_P)]} & \text{when } c < c_P \\ 0 & \text{when } c \geq c_P \end{cases} \quad \text{simplified solution (11.2)}$$

$$\mu_P = \mu_P^0 (1 - c/c_P) \quad \text{simplified shape function} \quad (11.3)$$

Equation (11.2) can be used as follows to deduce the solid phase conductivity Q_S , the critical concentration c_P , and the shape factor μ_P^0 from experimental data, Q . The regression is made optimizing the fit quality (r^2) with respect to the critical concentration.

$$Y = Y_0 + \alpha X \text{ with } X = \frac{c}{1 - c/c_P} \text{ and } Y = \frac{1 - c}{Q} \Rightarrow$$

$$Q_S = \frac{1}{Y_0}; \quad \mu_P^0 = \frac{Y_0}{2\alpha} \quad \text{from intersection } (Y_0) \text{ and slope } (\alpha) \quad (11.4)$$

Ideally, c_P must agree with c_P determined by a linear regression of data from stiffness tests on the porous material considered, see (10.13).

11.1.1 On the Accuracy of Simplification

It is recognized that some accuracy is lost in a conductivity analysis using simple shape factors based on $\nu_P = \nu_S = 0.2$. However, subsequent examples and previous examples re-considered show that the loss of accuracy is not very significant. In the author's opinion the level of analytical accuracy in a simplified analysis corresponds rather well to the level of accuracy characterizing the determination of geometrical in-put data.

11.2 Applications

The practical applicability of the simplified conductivity analysis is demonstrated in this section. Properties looked at are thermal and electrical conductivities and chloride diffusivity. The analysis is straightforward as explained in the introductory text to this chapter. Bounds for properties predicted are calculated by (9.3).

11.2.1 Thermal Conductivity of Fire-Brick

The experimental data in Fig. 11.1 for firebricks are from [110]. A thermal conductivity of the solid $Q_S \approx 0.825 \text{ kcal/mh}^\circ\text{C}$, a shape factor $\mu_P^0 \approx 1$, and a critical concentration $c_P \approx 0.82$ have been deduced by regression of experimental data as explained in Sect. 11.1. With these geo-parameters the conductivity of porous bricks is predicted by (11.2). The results are shown with a solid line in Fig. 11.1.

11.2.2 Electrical Conductivity of Binary Metallic Mixtures

The experimental data shown in Fig. 11.2 are from tests [111] on the electrical conductivity of $\text{Cu}_2\text{Sb-Sb}$ systems with $n_Q = 0.27$. The solid line is conductivity theoretically predicted by the present theory with $(\mu_P^0, \mu_S^0, c_P) = (1, -1, 0.5)$, which defines a compacted phase-symmetric mixture of phase P and phase S spheres.

Landauer [47] showed that experimental data from a number of binary metallic mixtures were well fitted by the Böttcher/Landauer expression previously presented in Table 9.1. Some data, however, were not. An example is

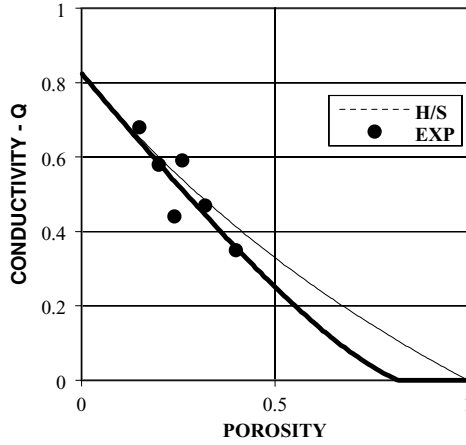


Fig. 11.1. Thermal conductivity of firebrick. Geometry: $(\mu_P^0, c_P) = (1, 0, 0.82)$

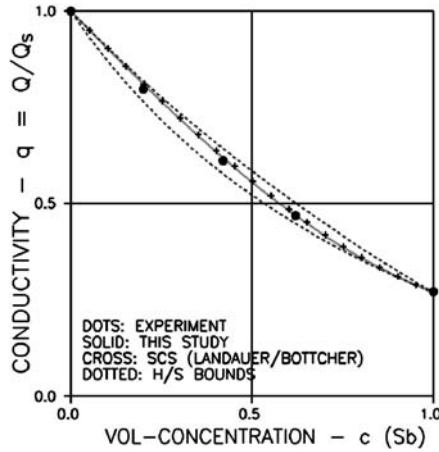


Fig. 11.2. Electrical conductivity of $\text{Cu}_2\text{Sb-Sb}$. DC-CD with $A = 1$ and $c_S = 0.5 \rightarrow (\mu_P^0, \mu_S^0, c_P, c_S) = (1, -1, 0.5, 0.5)$

shown in Fig. 11.3 with experimental data from [112] on $\text{Mg}_2\text{Pb-Pb}$ systems with $n_Q = 8.55$. The solid line represents data theoretically predicted by the present theory with $(\mu_P^0, \mu_S^0, c_P) = (-1, 1, 0.5)$.

Discussion

Conductivity for a number of binary metallic mixtures can be predicted on the basis of phase-symmetric DC-CD geometries created by compacted spheres – which also apply for the Budiansky's stiffness expression previously considered. It is noticed from Fig. 11.2 that the prediction qualities of the present theory and of the Böttcher/Landauer expression are very similar.

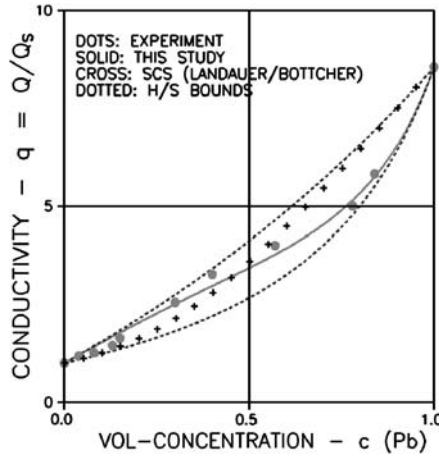


Fig. 11.3. Electrical conductivity of $\text{Mg}_2\text{Pb-Pb}$. Shape functions defined by $(\mu_P^0, \mu_S^0, c_P) = (-1, 1, 0.5)$

Apparently the geometries of the $\text{Cu}_2\text{Sb-Sb}$ and $\text{Mg}_2\text{Pb-Pb}$ systems considered in Fig. 11.2 and Fig. 11.3 respectively vary differently. Fig. 11.2 indicates that small amounts of Sb have spherical shapes such as in a CSA_P composite. Figure 11.3 indicates that small amounts of Pb have continuous shapes such as in a CSA_S composite $(\mu_P^0, \mu_S^0, c_P) = (-1, 1, 0.5)$. From a mechanical point of view the latter statement sounds somewhat strange. Apparently the electrical diffusion in a $\text{Mg}_2\text{Pb-Pb}$ system is a phenomenon which has its own way of using the mechanical composite structure. A first hypothesis to explain this feature might be that certain conductivity phenomena utilize the surfaces primarily of microstructures. A special future composite study is revealed by these remarks.

Incidentally, the discussion just made tells that the theory developed, theoretically, has no difficulty in handling the opposite geometrical trend $\text{CD} \rightarrow \text{DC}$ than what is implicitly assumed as default ($\text{DC} \rightarrow \text{CD}$) in this book, see Sect. 2.3.

11.2.3 Chloride Diffusion in Cement Paste System

Conductivity analyses is made on a cement paste system with the following phase properties and approximate geometry characteristics reproduced from Sect. 9.3.1.

The Chloride diffusion coefficients are $(Q_P, Q_S)/Q_P = (1, 0.00008)$ (with $Q_P = 2 \cdot 10^{-9} \text{ m}^2/\text{sec}$). The average aspect ratio of pores at low porosities is $A = 4$. The critical concentration is $c_S = 0.24$.

Based on these parameters a simplified conductivity analysis of the composite system considered can be made with shape functions and results

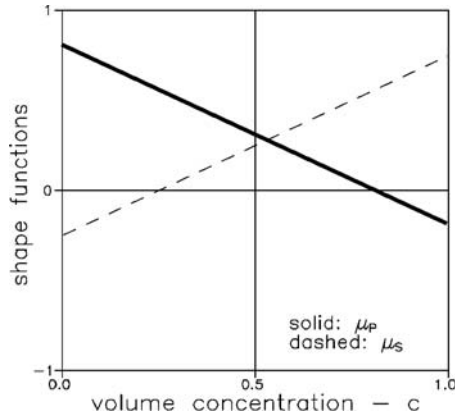


Fig. 11.4. Geometry of cement paste considered. c is cap-porosity

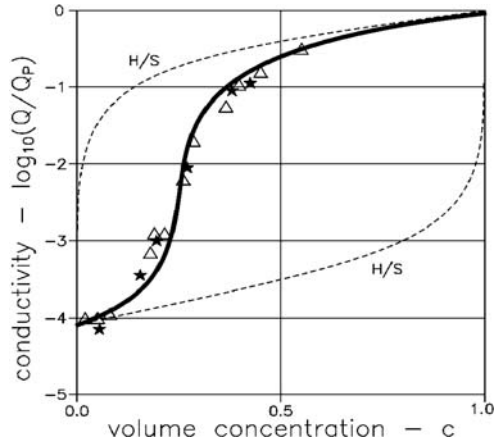


Fig. 11.5. Cement paste system considered: Chloride diffusivity as related to capillary porosity (c), present analysis

presented in Fig. 11.4 and in Fig. 11.5 respectively. The experimental data shown are reproduced from Sect. 9.3.1.

Remark: It is noticed that there are no significant differences between the results accurately predicted (Fig. 9.8) and those predicted by the present simplified theory.

Alternative Geometries

It is of some interest to compare the result just obtained with predictions based on more traditional concepts of materials geometry: The shape functions shown in Fig. 11.6 apply to the compacted spheres composite – also known as

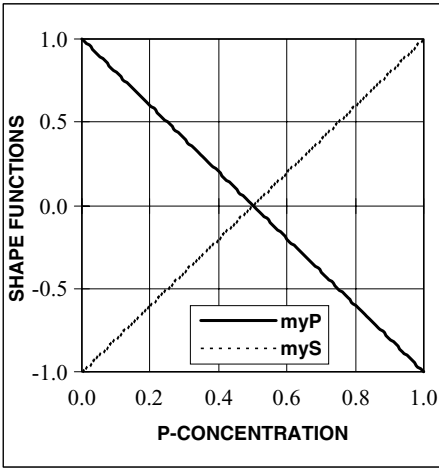


Fig. 11.6. Geometry for a compacted spheres system

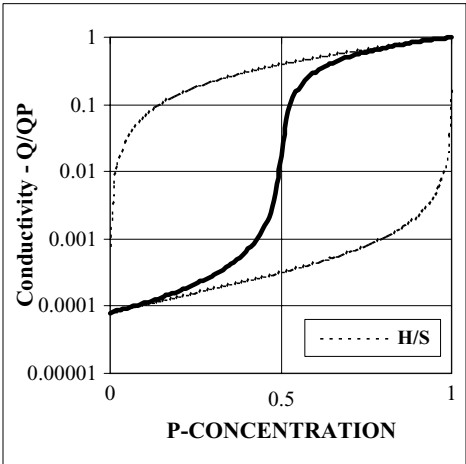


Fig. 11.7. Chloride diffusivity as related to capillary porosity in cement paste considered as a compacted spheres composite (The H/S bounds represent cement paste modeled as CSA_P and CSA_S composites respectively)

the *Budiansky model* ($A, c_S = 1, 0.5$). Predicted conductivities based on these shape functions are shown in Fig. 11.7. The H/S bounds also shown represent the materials conductivity if modeled as a CSA_P or a CSA_S composite respectively.

We notice from comparing Figs. 11.5 and 11.7 that the influence on conductivity of the geometries of the three alternative models considered is very different from the influence of the geometry defining the composite system originally considered in this example.

11.3 Conclusion

The general composite analysis presented in Chap. 9 has been successfully simplified in this chapter to reflect realistically well the somewhat limited knowledge available in most practice on composite geometry. Like the simplified theory for the elastic behavior of composites presented in Chap. 10 the results of the simplified conductivity analysis indicate that the theory has potentials 1) with respect to evaluation of prediction methods – and 2) with respect to design of composites. These features are discussed in subsequent Chaps. 12 and 13 respectively.

Diagnostic Aspects of Theory

The principles of the present theory to work with global descriptions (θ) of composite geometries have been successfully justified in previous chapters. Potentially these principles qualify the theory also to be used as a “diagnostic tool” in two areas of importance in modern composite theory:

- 1) Examination with respect to isotropy and geometry of empirical or semi-theoretical composite expressions. This subject is considered in this chapter.
- 2) Another area of importance is considered in the subsequent Chap. 13: Design of composite materials.

Not to exaggerate our knowledge to composite geometries, both analysis 1) and 2), will be performed on the basis of the simplified versions of the general theory, meaning Chaps. 10 and 11.

The composites hitherto considered in this book have geo-paths going from CSA_P to CSA_S geometries, which is the default path considered. The phase numbering P, S have been chosen consistent with this concept.

In this chapter where diagnostic aspects of the theory are considered we must be prepared to meet reversed geo-paths where composite geometries change along paths going from CSA_S geometries to CSA_P geometries, see Fig. 12.1. Theoretically, there are no difficulties in using the theory hitherto developed on composites with reversed geo-paths. Obviously some change of signs for shape functions must be introduced. And the critical concentrations will change their relative orders of magnitudes, meaning that the default $c_P \geq c_S$ becomes $c_P \leq c_S$.

A number of semi-empirical and semi-theoretical expressions are suggested in the literature for stiffness and conductivity prediction of composites. Very often these expressions are not well documented with respect to isotropy and consistency of underlying geometries. In other words:

- They are not guaranteed, not to violate the bounds of Hashin/Shtrikman’s, meaning that isotropy is not guaranteed.

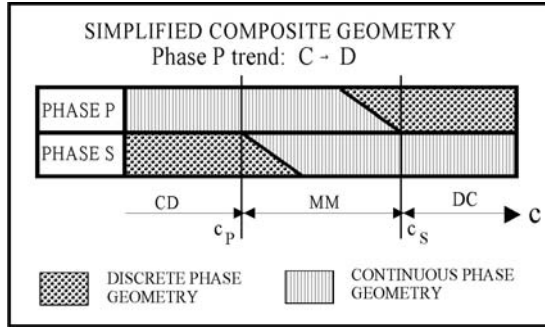


Fig. 12.1. Stylized illustration of a composite with reversed geo-path. Phase P geometry changes from C at $c = 0$ to D at $c = 1$

- They are not guarantied to have underlying geometries, which are invariable with respect to stiffness/conductivity ratios, n/n_Q .

Methods are developed in this chapter by which prediction methods can be checked with respect to isotropy and geometry. The frame of geometrical reference used is the concept of organic geometries used throughout this book. This means that geometries, successfully checked are those by which the present analysis¹ and the analysis being investigated will predict the same stiffness. Implicitly this statement means that each stiffness/conductivity expression that passes the checks can be taken as a justification of the composite analysis developed in this book.

We re-call that the composite geometries for SCS-solutions are self-defined and unknown, except at small phase P concentrations. To compare the present analysis with results from SCS-analysis it is of interest to know the underlying geometries.

Remarks: For SCS-expressions being tested, a special remark should be made: We re-call from the introduction to Chap. 7 that strict cylindrical particles (as used in a SCS-analysis) do not fully comply with the organic particles considered in this book, unless extreme stiffness ratios (n or $n_Q \rightarrow 0$, n or $n_Q \rightarrow \infty$) and/or aspect ratios $\approx 1/4 < A < \approx 4$ are considered.

Therefore, we cannot expect composite geometries to be fully independent of stiffness ratios unless the SCS-expressions considered are based on particles, which comply with these conditions. We can, however, expect that reliable composite *types* (DC-CD, MM-CD, ...) can be revealed – together with accurate shape factors, namely those applying to the particle shape used to establish the SCS-expression.

¹ It is important to notice that *any* shape function descriptions revealed are legitimate as long as they comply with the conditions explained in Sect. 4.1.3.

12.1 Stiffness

12.1.1 Examination of Stiffness Expressions

Isotropy Check

Stiffness expressions can be tested for consistency with respect to isotropy by the following expression,

$$\theta = \frac{[n - c(n-1)]e_{\text{EST}} - n}{1 + c(n-1) - e_{\text{EST}}} \text{ with } e_{\text{EST}} = e_{\text{EST}}(n); \text{ isotropy check} \quad (12.1)$$

which comes from Table 10.3 solving the stiffness expression (e) with respect to the geo-function (θ). The consistency considered requires that the geo-function obtained respects $n \leq \theta \leq 1$ when $n \leq 1$ and $n \geq \theta \geq 1$ when $n > 1$, see Fig. 4.2 simplified with $\kappa_P = \kappa_S = 1$.

Examples

Re-written versions of three of the more well-known semi-theoretical stiffness prediction methods are presented below. Hirsch [113]/Dougill [114] and Popovicz/Erdey [115] suggested that composite stiffness can be determined from the Paul/Hansen's lower bound e_L and Paul/Hansen's upper bound e_U (12.2) as shown in (12.3). The expression in (12.4) was suggested by Counto [116] and by Lokhorst & Breugel [108]. These three methods have recently been reviewed in [117] with respect to their quality to predict stiffness of fired clay-perlite composites. The theoretical expression added in (12.5) is deduced from the SCS-analysis of Budiansky [13] on a compacted spheres composite. The results of isotropy checks on these four expressions are presented in Figs. 12.2–12.6 where admissible θ -variations are indicated by shaded areas.

$$e_U = 1 + (n-1)c; \quad e_L = \frac{n}{n - (n-1)c} \quad (\text{Paul/Hansen}) \quad (12.2)$$

$$\begin{aligned} \frac{1}{e_{\text{EST}}} &= \frac{\alpha}{e_U} + \frac{1-\alpha}{e_L}; \quad (0 \leq \alpha \leq 1) \quad (\text{Hirsch/Dougill}) \\ e_{\text{EST}} &= \frac{1}{2}(e_U + e_L) \quad (\text{Popovics/Erdey}) \end{aligned} \quad (12.3)$$

$$\frac{1}{e_{\text{EST}}} = 1 - \sqrt{c} + \frac{\sqrt{c}}{1 + (n-1)\sqrt{c}} \quad (\text{Counto/Lokhorst - Breugel}) \quad (12.4)$$

$$e_{\text{EST}} = \frac{1}{2} \left[(1-n)(1-2c) + \sqrt{(1-n)^2(1-2c)^2 + 4n} \right] \quad (\text{Budiansky}) \quad (12.5)$$

It is obvious that only the Hirsch/Dougill expression with $\alpha = 0.5$, the Popovicz/Erdey expression, and the Budiansky expression qualify as reliable for stiffness prediction of isotropic composites. The expression suggested by

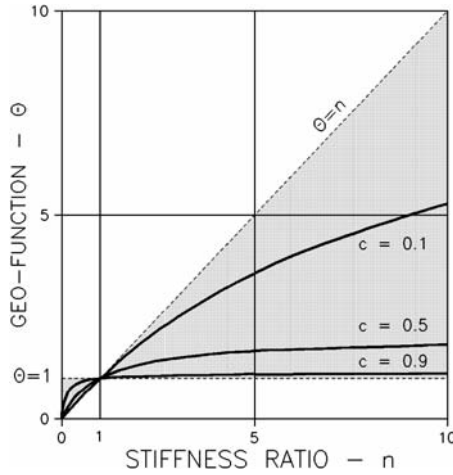


Fig. 12.2. Hirsch/Dougill with $a = 0.5$: Isotropy check (For other α the geo-functions fall outside the shaded area)

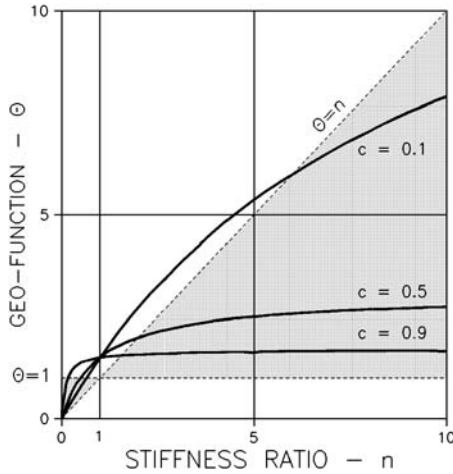


Fig. 12.3. Hirsch/Dougill with $a = 0.6$: Isotropy check

Counto and Lokhorst/Breugel is clearly influenced by some sort of anisotropic sub-modeling.

Remark: The review [117] of stiffness expressions previously referred to includes the Maxwell model [118] for particulate composite with spheres. This model applies for diffusion properties, not for stiffness. In the present isotropic check of composites the Maxwell model comes out with a geo-function of $\theta \equiv 2$ which is exactly the value expected for an expression predicting diffusion properties of composites considered by Maxwell, see Sect. 9.1.

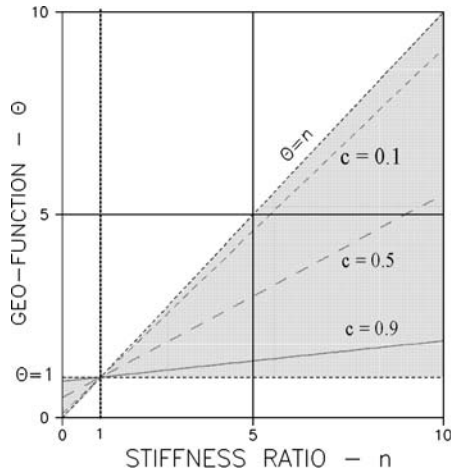


Fig. 12.4. Popovics/Erdey: Isotropy check

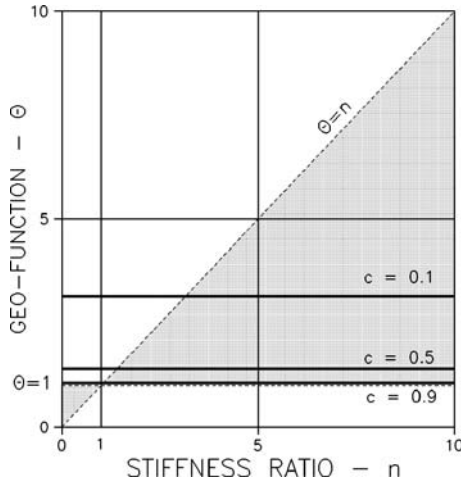


Fig. 12.5. Counto and Lokhorst-Breugel: Isotropy check

Geometry Check

Stiffness expressions can be checked as follows with respect to geometries. The geo-function applied in this book is examined in details as shown in (12.6). Specific shape functions (μ_P and μ_S) can be derived from this expression if geo-functions (θ_1, θ_2) are introduced as they are determined by (12.1) at two stiffness ratios (n_1, n_2). The results are presented in (12.7) from which the composite geometry can be evaluated.

As previously indicated, shape functions determined must show invariance with respect to stiffness ratios chosen if the stiffness expression investigated

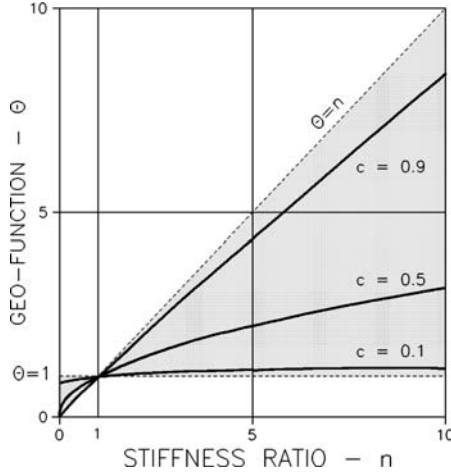


Fig. 12.6. Budiansky: Isotropy check

can be considered fully consistent with respect to geometry. For numerical reasons the well-known solutions $(\mu_P, \mu_S) \equiv (1, -1)$ for the CSA_P composite with $\theta \equiv 1$ – and $(\mu_P, \mu_S) \equiv (-1, 1)$ for the CSA_S composite with $\theta \equiv n$ cannot be predicted by (12.7).

$$\theta = \frac{1}{2} \left[\mu_P + n\mu_S + \sqrt{(\mu_P + n\mu_S)^2 + 4n(1 - \mu_P - \mu_S)} \right] \text{ is a root in}$$

$$\theta^2 - \theta(\mu_P + n\mu_S) - n(1 - \mu_P - \mu_S) = 0 \text{ which relate } \mu_P \text{ and } \mu_S \text{ by} \quad (12.6)$$

$$\mu_S = \frac{n(1 - \mu_P) - \theta(\theta - \mu_P)}{n(1 - \theta)} \quad \text{or} \quad \mu_P = \frac{n(1 - \mu_S) - \theta(\theta - n\mu_S)}{n - \theta}$$

$$\mu_P = \frac{n_1 n_2 (\theta_2 - \theta_1) + \theta_1^2 n_2 (1 - \theta_2) - \theta_2^2 n_1 (1 - \theta_1)}{n_1 n_2 (\theta_2 - \theta_1) + \theta_1 n_2 (1 - \theta_2) - \theta_2 n_1 (1 - \theta_1)} ; \quad \text{geometry check} \quad (12.7)$$

$$\mu_S = \frac{n_1 (1 - \mu_P) - \theta_1 (\theta_1 - \mu_P)}{n_1 (1 - \theta_1)}$$

Examples

The following checks are the results of running (12.7) with various combinations of stiffness ratios. The geometry check of the Budiansky's expression presented in Fig. 12.7 shows that the composite considered by this expression is a phase-symmetric DC-CD composite changing its geometry along a disc path – with P spheres in a continuous phase S at $c = 0$ to discrete phase S spheres in a continuous phase P at $c = 1$.

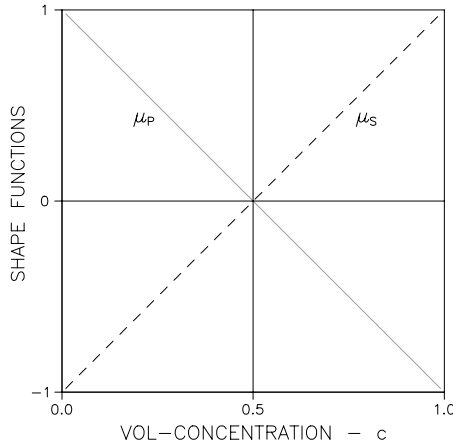


Fig. 12.7. Budiansky: Geometry check

The geometry check of the Popovics/Erdey expression presented in Fig. 12.8 shows that the composite considered by this expression is a phase-symmetric MM-MM composite changing its geometry along the path of PS-frameworks – with continuous phase S fibers in a continuous phase P at $c = 0$ to continuous phase P fibers in a continuous phase S at $c = 1$. Apparently the Popovics/Erdey expression applies to composites with geometries developing along a path which points in the opposite direction as the default direction chosen in this book, see introduction to this chapter.

A geometry check of the Hirsch/Dougill expression shows a strong n -dependency on shape functions, (the results of a geometry check become completely un-reasonable). The following examples illustrated in Figs. 12.9 and

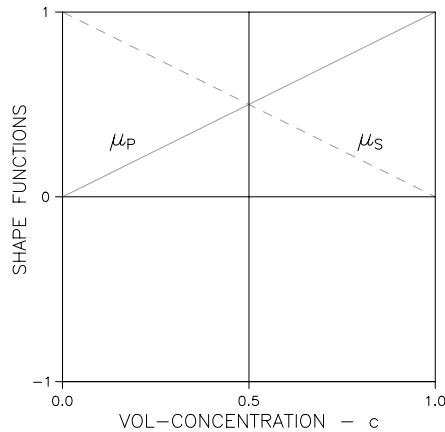


Fig. 12.8. Popovics/Erdey: Geometry check

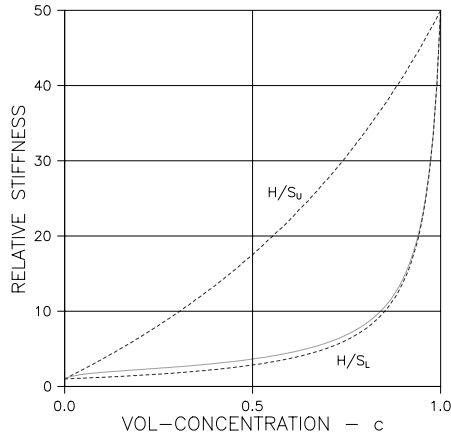


Fig. 12.9. Hirsch/Dougill stiffness prediction with stiffness ratio, $n = 50$

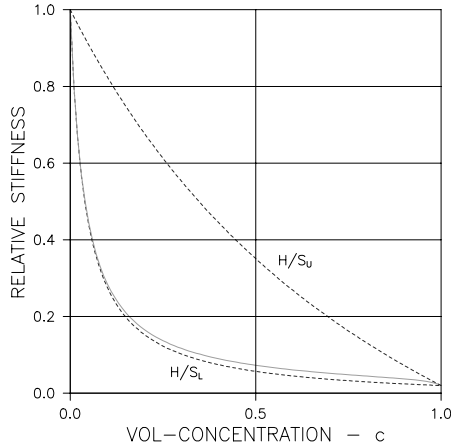


Fig. 12.10. Hirsch/Dougill stiffness prediction with stiffness ratio, $n = 0.02$

12.10 demonstrate the influence on stiffness of the stiffness ratio: At $n = 50$ the Hirsch/Dougill model corresponds to a nearly CSA_P composite. At $n = 1/50$ the model corresponds to the “opposite” of this material, namely a nearly CSA_S composite. It is obvious that such geometrical modeling is no good.

Summary

The stiffness estimates considered in this section are checked with the results summarized in Table 12.1.

Table 12.1. Summary of check results for stiffness estimates considered. Good results and less good results are denoted by “+” and “−” respectively. Reversed geo-path is denoted by “rev”

Method → ↓ Check	Hirsch/Dougill ($\alpha = 0.5$)	Popovics/Erdey	Counto/Lokhurst/ Breugel	Budiansky
Isotropy	+	+	−	+
Geometry	−	+ (rev)	−	+

12.2 Conductivity

Composite conductivity expressions can be examined with respect to isotropy and geometry just as stiffness expressions have been examined in Sect. 12.1. The analogy between stiffness and conductivity is considered such that (12.1), (12.6), and (12.7) become (12.8), (12.9), and (12.10).

The symbols appearing have the meanings explained in Chap. 9 (and Chap. 11). Subscripts 1 and 2 indicate properties determined with two conductivity ratios, n_{Q1} and n_{Q2} respectively.

$$\theta_Q = \frac{[n_Q - c(n_Q - 1)]q_{\text{EST}} - n_Q}{1 + c(n_Q - 1) - q_{\text{EST}}} \quad \text{with } q_{\text{EST}} = q_{\text{EST}}(n_Q); \text{ isotropy check} \quad (12.8)$$

$$\theta_Q = \mu_P + n_Q \mu_S + \sqrt{(\mu_P + n_Q \mu_S)^2 + 4n_Q(1 - \mu_P - \mu_S)} \quad \text{is a root in} \\ \theta_Q^2 - 2\theta(\mu_P + n_Q \mu_S) - 4n_Q(1 - \mu_P - \mu_S) = 0 \text{ relating } \mu_P \text{ and } \mu_S \text{ by} \quad (12.9)$$

$$\mu_S = \frac{4n_Q(1 - \mu_P) - \theta_Q(\theta_Q - 2\mu_P)}{2n_Q(2 - \theta_Q)} \quad ; \quad \mu_P = \frac{4n_Q(1 - \mu_S) - \theta_Q(\theta_Q - 2n_Q \mu_S)}{2(2n_Q - \theta_Q)}$$

$$\mu_P = \frac{4n_{Q1}n_{Q2}(\theta_{Q2} - \theta_{Q1}) + \theta_{Q1}^2 n_{Q2}(2 - \theta_{Q2}) - \theta_{Q2}^2 n_{Q1}(2 - \theta_{Q1})}{4n_{Q1}n_{Q2}(\theta_{Q2} - \theta_{Q1}) + 2\theta_{Q1}n_{Q2}(2 - \theta_{Q2}) - 2\theta_{Q2}n_{Q1}(2 - \theta_{Q1})} \quad (12.10)$$

$$\mu_S = \frac{4n_{Q1}(1 - \mu_P) - \theta_{Q1}(\theta_{Q1} - 2\mu_P)}{2n_{Q1}(2 - \theta_{Q1})} \quad ; \quad \text{geometry check}$$

Equations (12.8) and (12.10) will be used in the following section to reveal the underlying “hidden” geometries in the SCS-expressions presented in Table 9.1.

12.2.1 Examination of SCS-Expressions

Spheres: Böttcher/Landauer

The results of a geo-analysis of the Böttcher/Landauer’s SCS-solution in Table 9.1 are shown in Figs. 12.11 and 12.12. They define a phase-symmetric DC-CD composite geometry with $(\mu_P^0, \mu_S^0) = (1, -0.5)$ and $c_P = 2/3$. With Figs. 7.14 and 10.6 the geometry can be estimated to be the result of compacting powders made of very rugged fibers (many spheres mixed with a few fibers).

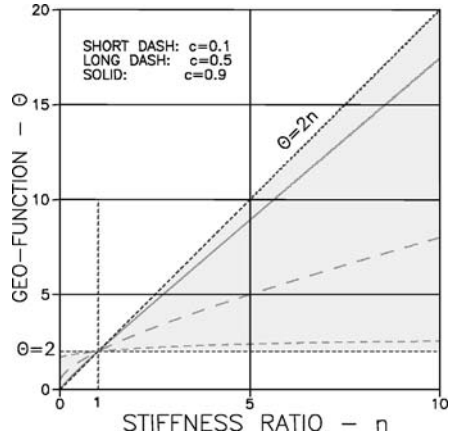


Fig. 12.11. Böttcher/Landauer: Isotropy check

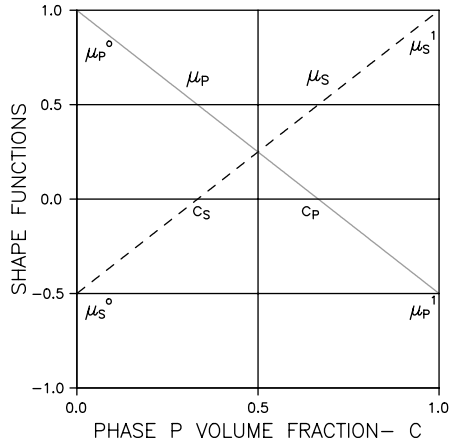


Fig. 12.12. Böttcher/Landauer: Geometry check

Long Fibers: Beek

The results of a geo-analysis of the Beek's SCS-solution in Table 9.1 are shown in Figs. 12.13 and 12.14. We re-call from the introduction to this chapter that we cannot expect a fully consistent geometry revealed from this SCS-solution ($A > 4$), unless stiffness ratios are extreme ($n_Q \rightarrow 0$ or $\rightarrow \infty$). The *type* of composite, however, is consistently revealed by (12.8) and (12.10) for various stiffness ratios to be a MM-CD composite with $(\mu_P^0, \mu_S^0) = (0.75, 0.25)$, $(\mu_P^1, \mu_S^1) = (-0.5, 1)$, and $c_P = 0.6$. The shape functions in Fig. 12.14 are determined with $(n_{Q1}, n_{Q2}) = (10^{-10}, 10^{10})$, simulating extreme stiffness ratios.

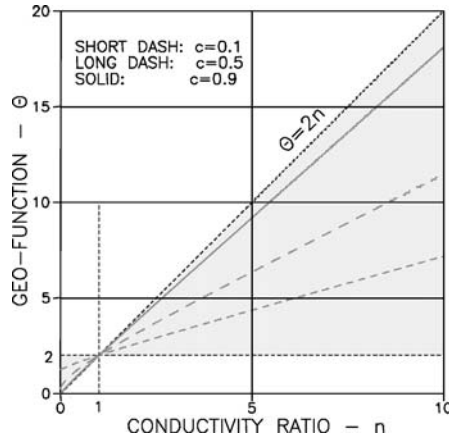


Fig. 12.13. Beek: Isotropy check

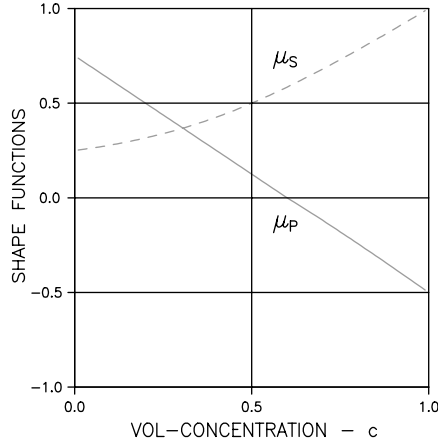


Fig. 12.14. Beek: Geometry check

From Fig. 10.6 the geometry can be estimated at $c = 0$ to be agglomerating P-fiberworks, changing to end at $c = 1$ as a mixture of S-fibers and S-spheres in a continuous phase P. The phase S geometry changes to be fully discrete at $c = 0.6$.

Thin Discs: Bruggeman

Obviously, see (9.3), a CSA_S geometry is the underlying composite geometry in the SCS-analysis of Bruggeman, which is based on strict discs with $A \ll 1$. This geometry-observation agrees with numerical SCS results obtained in Appendix C on both stiffness and conductivity of particulate composites with

thin discs. It also agrees with conclusions made in analytical studies on particulate composites (e.g. [14]) with thin discs.

In the context of the geometrical concept applied in this book thin discs act, by agglomeration, as phase P envelopes for phase S particles (CSA_S). From the opposite geometry (CSA_P) the geometry changes through the crumbled foils geometry previously explained in this book (e.g. Sects. 4.1.4 and 8.1.2), defining the “half way” phase P geometry between the geometry of a CSA_P and the geometry of a CSA_S .

The conductivity expression for crumbled foils has already been presented in (9.8). Experimental justifications for this expression have been presented in [76].

Summary

The SCS-estimates of conductivity presented in Table 9.1 are checked with the results summarized in Table 12.2. All estimates are evaluated positively with respect to both isotropy and stability of underlying composite geometries. All estimates are included as special “cases” of the theory presented in this book.

Table 12.2. Summary of check results for conductivity SCS-estimates considered in Table 9.1. Excellent results are marked +. A positive check on type of geometry is denoted (+)

Method → ↓ Check	Böttcher/Landauer (Spheres)	Beek (Long fibers)	Bruggeman (Thin discs)
Isotropy	+	+	+
Geometry	+	(+)	+

A special remark should be made to the Beek analysis of long fiber composites: Because the particle aspect ratio is very high ($A = \infty$) no fully consistent geometry can be found, as expected from the introduction to this chapter. The *type* of geometry, however, is fully consistent (also as expected).

12.3 Discussion

A quality check has been run on a number of stiffness and conductivity prediction methods for composite. As can be seen from Tables 12.1 and 12.2 most methods have been positively evaluated. As previously stated, each positive evaluation can be taken as a justification of the composite analysis developed in this book.

It is important to notice that *any* shape function description revealed is legitimate. The description does not need to follow a simplified straight-line representation. An example is the Beek expression for the conductivity of

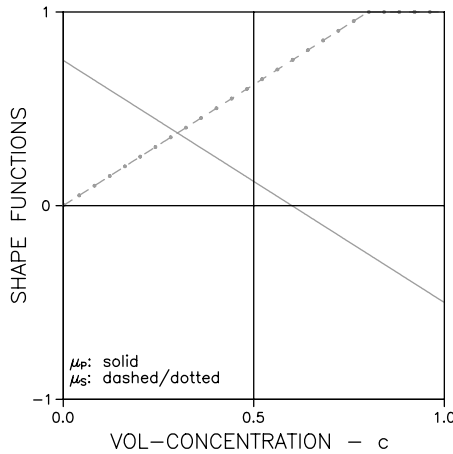


Fig. 12.15. Long fibers: Shape functions assumed for simplified conductivity analysis: $(A, c_P) = (1000, 0.6)$

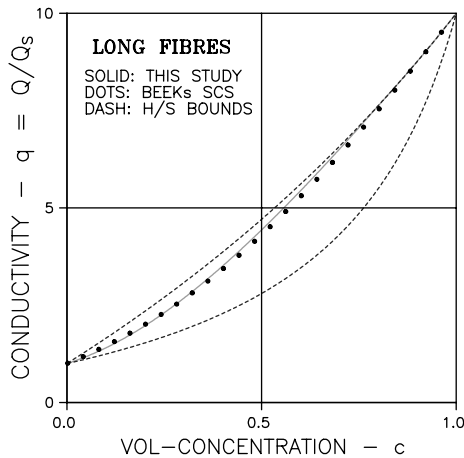


Fig. 12.16. Long fibers: Simplified conductivity analysis with shape functions from Fig. 12.15. Dots are results from Beek's expression. $n_Q = 10$

composites with long fibers, for which the shape functions shown in Fig. 12.14 is revealed. With these functions introduced the simplified conductivity theory in Chap. 11 will predict results, very similar² to such predicted by the Beek expression.

It is demonstrated in Figs. 12.15 and 12.16 that the simplified conductivity with simple shape function (linear) can predict results, which are extremely close to the Beek results.

² For extreme (high and low) n_Q the results become identical.

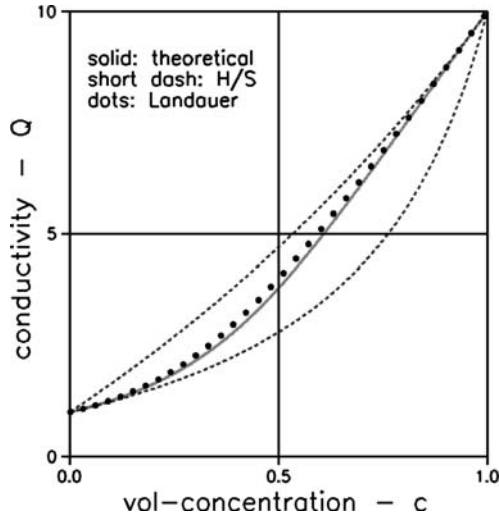


Fig. 12.17. Landauer's results predicted by the simplified conductivity theory with Budiansky shape functions. $(\mu_P^0, \mu_S^0, c_S) = (1, -1, 0.5)$ and $A = 1$

Although the Böttcher/Landauer estimate on conductivity and the Budiansky's estimate on stiffness are both based on a spherical particle, they do not reveal exactly the same composite geometry. The reason for this discrepancy is due to the feature previously mentioned that the geometry of SCS solutions is self-defined. Furthermore, a conductivity analysis is basically a bulk modulus analysis released from the restraints of a simultaneous shear modulus analysis.

Whatever shape functions (Landauer/Böttcher or Budiansky) are chosen, there will be no significant difference between predictions made with the Böttcher/Landauer expression and such made with the conductivity theory presented in this book using the "Budiansky geometry", see Fig. 12.17.

Aspects of Materials Design

The quality of the present theory to work with global descriptions (θ) of composite geometries, qualifies it to be used in design of composite materials, which is to predict geometry types which associate with prescribed composite properties.

We will explore this statement performing an inverse analysis of the composite expressions previously presented. Keeping our source materials defined as Phase P and Phase S, such analysis can be made by the following expressions, (13.1) and (13.2), applying for any geo-path.

Not to exaggerate our knowledge to composite geometries, however, the subsequent analysis will be performed on the basis of the simplified versions of the general theory, meaning Chaps. 10 and 11.

13.1 Geometries versus Properties

The first relations who tie geometry in general and mechanical/physical composite properties (e/q) together are (13.1) and (13.2) reproduced from (12.1) + (12.6) and (12.8) + (12.9) respectively.

$$\begin{aligned} \theta &= \frac{[n - c(n-1)]e - n}{1 + c(n-1) - e} && \text{Elasticity} \\ \mu_S &= \frac{n(1 - \mu_P) - \theta(\theta - \mu_P)}{n(1 - \theta)} ; \quad \mu_P = \frac{n(1 - \mu_S) - \theta(\theta - n\mu_S)}{n - \theta} \end{aligned} \quad (13.1)$$

$$\begin{aligned} \theta_Q &= \frac{[n_Q - c(n_Q-1)]q - n_Q}{1 + c(n_Q-1) - q} && \text{Conductivity} \\ \mu_S &= \frac{4n_Q(1 - \mu_P) - \theta_Q(\theta_Q - 2\mu_P)}{2n_Q(2 - \theta_Q)} ; \\ \mu_P &= \frac{4n_Q(1 - \mu_S) - \theta_Q(\theta_Q - 2n_Q\mu_S)}{2(2n_Q - \theta_Q)} \end{aligned} \quad (13.2)$$

13.2 Design

Theoretically, any geo-path ($\mu_S = f(\mu_P)$) are revealed by (13.1) and (13.2), which will “produce” prescribed composite properties. In order to simplify matters, however, we assume simple geo-paths, $\mu_P + \mu_S = a$, as previously defined in Sect. 10.1.3.

With a prescribed Young’s modulus of E^* , or conductivity Q^* , at a volume concentration of c^* the shape function values (μ_P^* , μ_S^*) associated with that concentration can now be determined as follows.

$$\begin{aligned} \theta^* &= \frac{[n - c^*(n - 1)]e^* - n}{1 + c^*(n - 1) - e^*} \Rightarrow & \text{Elasticity} \\ \mu_S^* &= \frac{n(1 - a) + \theta^*(a - \theta^*)}{\theta^*(1 - n)} : \quad \mu_P^* = a - \mu_S^* \end{aligned} \quad (13.3)$$

$$\begin{aligned} \theta_Q^* &= \frac{[n_Q - c^*(n_Q - 1)]q^* - n_Q}{1 + c^*(n_Q - 1) - q^*} \Rightarrow & \text{Conductivity} \\ \mu_S^* &= \frac{4n_Q(1 - a) + \theta_Q^*(2a - \theta_Q^*)}{2\theta_Q^*(1 - n_Q)} : \quad \mu_P^* = a - \mu_S^* \end{aligned} \quad (13.4)$$

With two prescribed Young’s moduli, E_1^* and E_2^* , or conductivities, Q_1^* and Q_2^* , at volume concentrations, c_1^* and c_2^* respectively the complete geo-path (covering any c of the composite material) can be determined utilizing that the final shape functions (μ_P , μ_S) vary linearly with volume concentrations as explained in Chap. 10. In other words, we extra/interpolate linearly between (μ_P^{*1} , μ_S^{*1}) and (μ_P^{*2} , μ_S^{*2}) as they are determined by (13.3) and (13.4).

We will demonstrate this procedure in the following two examples – recognizing that *prescribed properties must not, of course, violate the H/S-bounds presented by (10.3) and (9.3).*

Remark: It is noticed that (13.3) and (13.4) can also be used to construct more general geo-paths than the one presently considered with a constant path factor. The equations may be used with a path factor (a) that depends on concentration (c^*).

13.3 Illustrative Examples

13.3.1 Stiffness

The above analysis with a constant path factor is used to determine composite geometries that will “produce” prescribed Young’s moduli from known source materials. The results obtained are compared with predictions made with methods well known from the composite theory (Budiandsky [13], Hashin [3]).

Sources: $(E_P, E_S) = (0, 32000)$ MPa (Phase P are pores)

Chosen geo-path factor: $a = 0.5$.

Prescribed Young's moduli: $(E_1^*, E_2^*) = (12500, 5000)$ MPa at $(c_1^*, c_2^*) = (0.3, 0.5)$.

Results of analysis: Fig. 13.1 with $\mu_P^0, \mu_S^0 \approx 0.6, -0.1$ and $c_P, c_S \approx 0.8, 0.14$. Figs. 13.2 and 13.3.

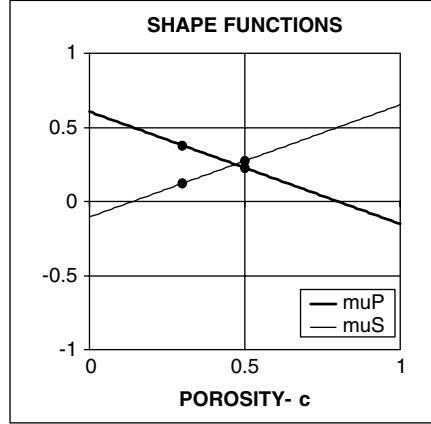


Fig. 13.1. Shape functions of a porous material designed with a geo-path factor of 0.5 that will “produce”, prescribed stiffness

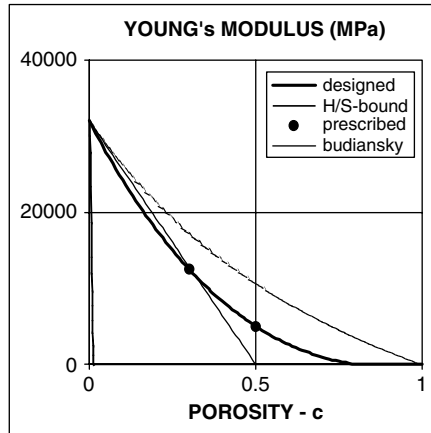


Fig. 13.2. Stiffness of a porous material designed with a geo-path factor of 0.5 that will “produce” prescribed stiffness

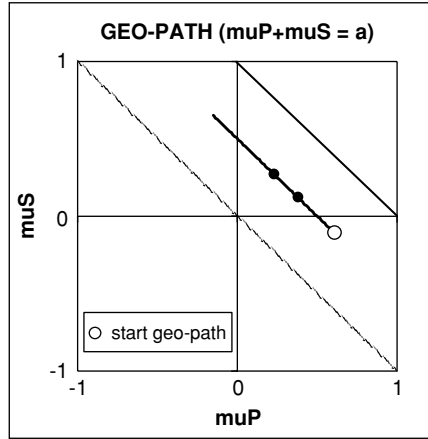


Fig. 13.3. Geo-path in present stiffness analysis

Evaluation of Geometry

The shape functions presented in Fig. 13.1 are easily transformed to the geo-path graph shown in Fig. 13.3. The prescribed stiffness data are properties of a composite produced with geometries described placing Fig. 13.3 on top of the master path graph in Fig. 10.6.

It can be checked by Table 10.2 that the resulting shape factors (μ_P^0, μ_S^0) can be obtained by mixing 55% voids of aspect ratios $A \approx 20$ with 45% voids of aspect ratios $A \approx 0.2$.

The mixing (void size distribution) should be such that the resulting critical concentrations (c_P, c_S) are obtained.

13.3.2 Conductivity

A similar analysis is used to determine composite geometries which will “produce” prescribed conductivities from known source materials. The results obtained are compared with predictions made with methods well known from the composite theory (Böttcher [119], Hashin [73]).

Sources: $(Q_P, Q_S)/Q_P = (1, 0.00008)$ with $Q_P = 2 * 10^{-9} \text{ m}^2/\text{sec}$ (Phase P are water saturated pores).

Chosen geo-path factor: $a = 0.5$.

Prescribed conductivities: $(Q_1^*, Q_2^*)/Q_P = (0.02, 0.32)$ at $(c_1^*, c_2^*) = (0.29, 0.55)$.

Results of analysis: Fig. 13.4 with $\mu_P^0, \mu_S^0 \approx 0.8, -0.3$ and $c_P, c_S \approx 0.72, 0.26$. Figs. 13.5 and 13.6.

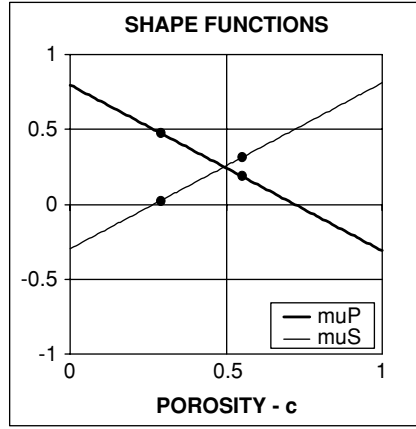


Fig. 13.4. Shape functions of a water-saturated porous material designed with a geo-path factor of 0.5, which will “produce”, prescribed conductivities

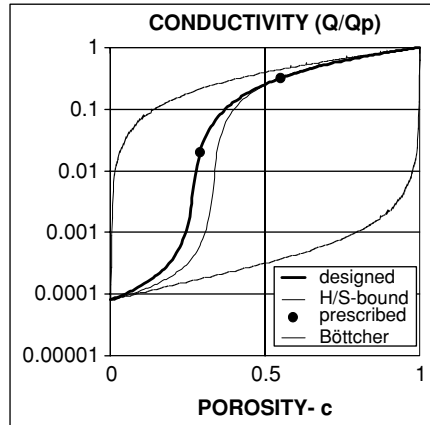


Fig. 13.5. Conductivity of a water-saturated porous material designed with a geo-path factor of 0.5, which will “produce” prescribed conductivities

Evaluation of Geometry

The shape functions presented in Fig. 13.4 are easily transformed to the geo-path graph shown in Fig. 13.6. The prescribed conductivity data are properties of a composite produced with geometries described placing Fig. 13.6 on top of the master path graph in Fig. 10.6.

It can be checked by Table 10.2 that the resulting shape factors (μ_P^0 , μ_S^0) can be obtained by mixing 98% voids of aspect ratios $A \approx 3.6$ with 2% voids of aspect ratios $A \approx 0.16$.

The mixing (void size distribution) should be such that the resulting critical concentrations (c_P , c_S) are obtained.

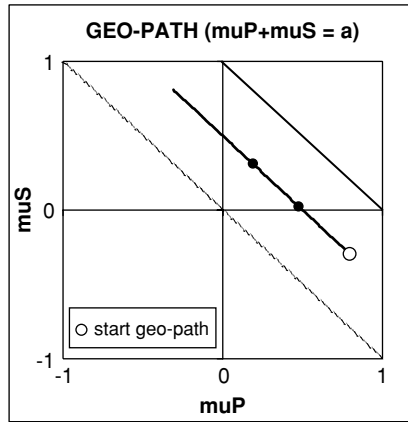


Fig. 13.6. Geo-path in present conductivity analysis

13.4 Discussion

A method has been presented in this chapter which applies for design of composites with simple geo-paths, $\mu_S + \mu_P = a$. Such geo-paths have previously been shown to apply well in property predictions for a number of composites produced with traditional technologies: Particles mixed into a continuous matrix, compaction of powders, production of porous materials, impregnation of porous materials, three dimensional “Plywood” composites, and particulate composites with self-inflicted pores such as light clinker concrete.

An interesting aspect of the composite theory presented is that it offers the possibility to explore in general, how geo-paths should look to obtain prescribed material properties. This feature may act as a challenge to traditional technologies: Can we do better by new, not yet known, technologies? In order to answer this question we have to open new research projects such as the following:

- FEM tests on a number of standard composites must be made – from which shape function values can be deduced at various concentrations – in principles as reported in this book and in [24] for various particulate composites and so-called grid composites (CC).
- Parallel technology studies must be made on, how to produce such standard composites in practice.

Viscoelasticity

Any relation previously developed on geometry, stiffness, stress, strain, and eigenstress/strain are further developed in Chap. 15 also to apply when composites are considered with linear viscoelastic components. The analytical basics for doing so are certain powerful analogies, which exist between the theory of viscoelasticity and the theory of elasticity. To keep this book self-contained with respect to viscoelastic analysis, including analogies, it has been found appropriate to summarize very briefly the theory of viscoelasticity as it has been adapted by the author in (e.g. [59, 120, 121]) for the analysis of viscoelastic composites.

Viscoelastic materials are considered which comply with the elastic materials considered in Chap. 10, meaning that bulk creep and shear creep develops proportionally with Poisson's ratios keeping the orders of magnitudes ≈ 0.2 . Theoretically it is not difficult to perform a more general analysis [122, 123]. The mathematics, however, will increase to a level, which cannot be justified by our present knowledge on the rheological properties of most materials, especially when composite geometrical aspects are also considered as they are in Chap. 15. The relevance of assuming an approximately constant Poisson's ratio in concrete analysis has been further discussed in [124].

Unless otherwise indicated viscoelastic materials are considered with constant material properties meaning, for example, that Young's modulus does not change with time. Most materials behave in this way. One very important group of materials, however, does not. Portland cement paste and related materials are so-called aging viscoelastic materials with properties, which change considerably, especially at young ages ($< \approx 3$ weeks). At more mature ages hardened cement paste (HCP) and concrete can be considered by easy approximate methods presented in this chapter together with methods developed for the analysis of non-aging viscoelastic materials. These methods suffice for most practice. At early age loading, however, cement paste and concrete have to be considered by the more complex theory of aging viscoelasticity presented by the author in [120, 124, 125].

14.1 Stress-Strain Relations

The stress-strain relation of a viscoelastic material can be expressed in three different ways as shown in (14.1), see [126] for example. The integral expressions relate strain and stress through the creep function, $C(t)$ defined in Fig. 14.1, or the relaxation function, $R(t)$, defined in Fig. 14.2. The creep function and the relaxation function are related as shown in (14.2).

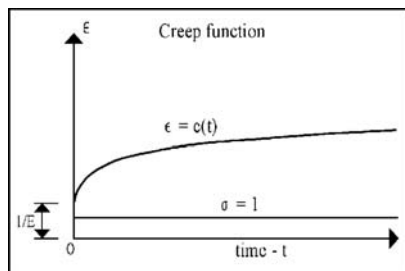


Fig. 14.1. Creep function is strain of material subjected to a constant stress of magnitude 1 at $t = 0$

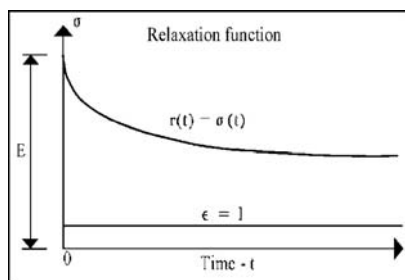


Fig. 14.2. Relaxation function is stress in material subjected to a constant strain of magnitude 1 applied at $t = 0$

$$\begin{aligned}
 \sum_{k=0}^N p_k \frac{d^k \sigma}{dt^k} &= \sum_{k=0}^N q_k \frac{d^k \varepsilon}{dt^k} && \text{differential representation} \\
 \varepsilon &= \int_{t=-\infty}^t C(t-\theta) \frac{d\sigma}{d\theta} d\theta && \text{creep integral representation} \\
 \sigma &= \int_{t=-\infty}^t R(t-\theta) \frac{d\varepsilon}{d\theta} d\theta && \text{relaxation integral representation}
 \end{aligned} \tag{14.1}$$

$$\int_{t=-\infty}^t C(t-\theta) \frac{dR(\theta)}{d\theta} d\theta = \int_{t=-\infty}^t R(t-\theta) \frac{dC(\theta)}{d\theta} d\theta \equiv 1 \quad (14.2)$$

14.1.1 Analogy Young's Modulus

Very compact and efficient versions of the stress-strain relations for viscoelastic materials can be obtained by Laplace transformation of (14.1), see [126, 127]. This feature has been used by the author in [121] to introduce the concept of “analogy Young’s modulus” into the theory of viscoelasticity: Laplace transformed stress and Laplace transformed strain are related by the viscoelastic “Hooke’s law” presented in (14.3) where the analogy Young’s modulus E^A relates to Laplace transformed creep- and relaxation functions as presented in (14.4).

The advantage of introducing the analogy Young’s modulus is that statements or expressions subsequently presented can be given a very rational and short formulation, especially when viscoelastic composites are considered.

$$\bar{\varepsilon} = \frac{\bar{\sigma}}{E^A} \quad \text{“Hooke’s law” with laplace transformed stress and strain} \quad (14.3)$$

$$E^A = E^A(s) = \frac{\sum_{k=0}^N q_k s^k}{\sum_{k=0}^N p_k s^k} = \frac{1}{s\bar{C}(s)} = s\bar{R}(s) \quad \text{Analogy Young’s modulus} \quad (14.4)$$

Laplace Transformation: In Laplace transformation the image function, over lined $\bar{f}(s)$, and the object function $f(t)$ are related as shown in (14.5). The symbols L and L^{-1} mean Laplace transformed and inversion of Laplace transformed respectively. The complex variable is denoted by s . α and β are real numbers. The imaginary unit is denoted by i .

$$\begin{aligned} \bar{f}(s) &= L\{f(t)\} = \int_{0-}^{\infty} f(t) e^{-st} dt \\ f(t) &= L^{-1}\{\bar{f}(s)\} = \frac{1}{2\pi i} \lim_{\beta \rightarrow \infty} \int_{\alpha-i\beta}^{\alpha+i\beta} \bar{f}(s) e^{st} ds \end{aligned} \quad (14.5)$$

Information on Laplace transformation, Laplace transformed, and their inverse can be found in a number of mathematical handbooks, for example [128–130]. Numerical methods are found in [131–133]. Some general properties of Laplace transforms and some special Laplace transforms are shown in Table 14.1.

Elastic-Viscoelastic Analogy (e-v-Analogy)

A number of analogies have been presented (e.g. [127, 134, 135]) which formulate the relationship between *quasi-static* stress analysis of viscoelastic structures and similar stress analysis of elastic counterpart structures. The

Table 14.1. Some general properties of Laplace transforms and some special Laplace transforms. Gamma function $\Gamma(a+1) = \text{faculty } a(a!)$

Object – $f(t)$	Image – $\bar{f}(s)$	Object – $f(t)$	Image – $\bar{f}(s)$
$c^*g(t)$	$c^*\bar{g}(s)$	$H(t)$ (Heaviside)	$\frac{1}{s}$
$g(t) + h(t)$	$\bar{g}(s) + \bar{h}(s)$	$\delta(t) = \frac{dH(t)}{dt}$ (Dirac)	1
$g(t)^* \exp(c^*t)$	$\bar{g}(s - c)$	$t^n (n \geq 0)$	$\frac{\Gamma(n+1)}{s^{n+1}} = \frac{n!}{s^{n+1}}$
$g(t/c)$	$c^*\bar{g}(cs)$	e^{-ct}	$\frac{1}{s+c}$
$g(t - \tau)$	$e^{-\tau s} * \bar{g}(s)$	$t^n e^{-ct}$	$\frac{n!}{(s+c)^{n+1}}$
$\int_0^t g(\tau)^* h(t - \tau) d\tau$	$\bar{g}(s)^* \bar{h}(s)$	$\cos(\omega t)$	$\frac{s}{s^2 + \omega^2}$
$\int_0^t g(\tau) d\tau$	$\bar{g}(s)/s$	$\sin(\omega t)$	$\frac{\omega}{s^2 + \omega^2}$
$\frac{d^n g(t)}{dt^n}; g(t < 0) \equiv 0$	$s^n \bar{g}(s)$	$\frac{1}{c}(1 - e^{-ct})$	$\frac{1}{s(s+c)}$
$f(0) = \lim_{s \rightarrow \infty} [s^* \bar{f}(s)]; f(\infty) = \lim_{s \rightarrow 0} [s^* \bar{f}(s)]$		$\frac{1}{c} \left[t - \frac{1}{c}(1 - e^{-ct}) \right]$	$\frac{1}{s^2(s+c)}$
		$\frac{e^{-at} - e^{-bt}}{b - a}$	$\frac{1}{(s+a)(s+b)}$

basic version of these analogies (elastic-viscoelastic analogies, e-v-analogies) can be expressed as follows: Viscoelastic solutions are obtained from their corresponding elastic solutions replacing flexibility ($1/E$) or stiffness (E) in these solutions with the corresponding viscoelastic integral operators expressed in (14.6).

$$\frac{1}{E} \Rightarrow \int_{-\infty}^t C(t - \theta) \frac{d[\]}{d\theta} d\theta; \quad E \Rightarrow \int_{-\infty}^t R(t - \theta) \frac{d[\]}{d\theta} d\theta \quad (14.6)$$

The author's version of the e-v-analogy is the following formulated and applied in [120, 121]:

The Laplace transformed solution to a linear-viscoelastic structural problem is obtained from the corresponding linear-elastic solution by replacing Young's modulus with the analogy Young's modulus presented in (14.4) – and time dependent terms, such as load/stress and displacement/strain, with their respective Laplace transformed quantities.

Unless otherwise indicated this (quasi-static) version of the e-v-analogy is always used in the following sections of this book. Formally the e-v-analogy works as outlined in (14.7) where Δ_{VISC} is the solution to a viscoelastic

problem in the analysis of a viscoelastic body. Time dependent actions are symbolized by $P = P(t)$. Usually the inversion of the second expression in (14.7) must be made by handbook tables or by numerical means as previously referred to.

$$\left. \begin{aligned} \Delta_{\text{ELAS}}(t) &= F[E, P(t)] \\ \overline{\Delta}_{\text{VISC}}(s) &= F[E^A(s), \overline{P}(s)] \\ \Delta_{\text{VISC}}(t) &= L^{-1}\{\overline{\Delta}_{\text{VISC}}(s)\} \end{aligned} \right) \text{E-v-analogy} \quad (14.7)$$

14.1.2 Vibrations

We re-call that the analogy just considered applies strictly only for quasi-static analysis with any forces of inertia neglected. A general analogy, however, can be established which considers such forces also (dynamic problems). Keeping the concept of analogy Young's modulus in mind it can be concluded from [136, 137] that:

The Laplace transformed solution to a viscoelastic structural problem is obtained by Laplace transforming its elastic counterpart solution, and replace Young's modulus with its analogy Young's modulus.

Obviously the quasi-static e-v-analogy previously considered is included in this general analogy. Usually the Laplace transforms obtained are rather complicated. Numerical inversion procedures have to be used. One special dynamic problem, however, can be solved in a more easy way. As shall subsequently be seen the important harmonic vibration problem can be solved analytically introducing the so-called complex Young's modulus.

Complex Young's Modulus

The special stress-strain relation presented in (14.8) applies to viscoelastic materials subjected to harmonic stress $\sigma_H = \sigma_0 e^{i\omega t}$ where σ_0 is stress amplitude, ω is angular frequency¹, and i is complex unity. The so-called complex Young's modulus E_C is related to the analogy Young's modulus as shown in (14.9). The stress-strain relation is graphically presented in Figs. 14.3 and 14.4 with complex Young's modulus in algebraic notation as explained in (14.10).

$$\begin{aligned} \varepsilon_H &= \frac{\sigma_H}{E_C} \quad \text{with harmonic stress/strain} \quad \left(\begin{aligned} \sigma_H &= \sigma_0 \exp(i\omega t) \\ \varepsilon_H &= \varepsilon_0 \exp(i(\omega t - \delta)) \end{aligned} \right) \\ \varepsilon_0 &= \frac{\sigma_0}{|E_C|} \quad \text{is strain amplitude and } \delta \text{ is loss angle} \end{aligned} \quad (14.8)$$

$$E_C = E_C(\omega) = E^A(i\omega) \quad \text{Complex Young's modulus} \quad (14.9)$$

¹ Angular frequency $\omega = 2\pi/T$ where T is cyclic time. It relates to traditional frequency, f (cycles/time unit) by $\omega = 2\pi f$. If time unit is second then f is in Hz.

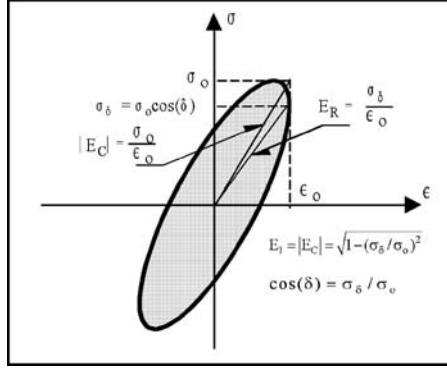


Fig. 14.3. Stress-strain test of viscoelastic material subjected to harmonic vibration

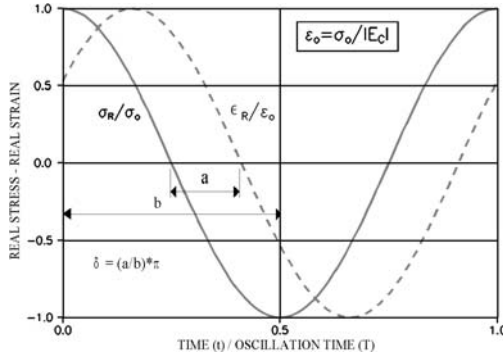


Fig. 14.4. Oscillation time $T \rightarrow$ frequency $f = 1/T$, (angular frequency $\omega = 2\pi f$)

$$\begin{aligned}
 E_C &= E_R + iE_I && E_R, E_I \text{ are real, and imaginary Youngs moduli} \\
 |E_C| &= \sqrt{E_R^2 + E_I^2} && \text{is absolute stiffness} \\
 \tan(\delta) &= E_I/E_R && \text{is loss tangent}
 \end{aligned}
 \tag{14.10}$$

Equations (14.8) and (14.9) are easily verified by the first expression in (14.1) introducing stress and strain from (14.8) and then comparing the results obtained with (14.4). An example of complex Young's modulus determined by (14.9) is presented in Sect. 14.3.

Creep functions and relaxation functions are related to the complex Young's modulus by (14.11) adapted from [138–140]. An example of creep and relaxation determined by the complex Young's modulus are presented in the subsequent Sect. 14.3.

$$\begin{aligned}
R(t) &= E - \frac{2}{\pi} \int_0^{\infty} E_I(\omega) \frac{1 - \cos(\omega t)}{\omega} d\omega \quad (E \text{ is } R \text{ at very high } \omega) \\
C(t) &= \frac{1}{E} + \frac{2}{\pi} \int_0^{\infty} J_I(\omega) \frac{1 - \cos(\omega t)}{\omega} d\omega; \quad \left(J_I = \frac{E_I}{|E_C|^2} \right)
\end{aligned} \tag{14.11}$$

Remark: We re-call that one of the functions considered in (14.11) (usually the relaxation function) can be determined from the other one (creep function) by (14.2).

Vibration Analogy

From [136,137] can be concluded that the general e-v-analogy previously presented can be continued as follows when harmonic vibration problems specifically are considered (keeping in mind the concept of analogy Young's modulus):

The analysis of a viscoelastic structure with sine (or cosine) varying load can be made by the theory of elasticity with Young's modulus replaced by its viscoelastic counterpart, namely the complex Young's modulus expressed by $E_C = E^A(i\omega)$ from (14.4).

Formally the analogy works as outlined in (14.12) where the vibration deflection Δ of a viscoelastic body is considered subjected to the harmonically varying load P_H .

$$\begin{aligned}
\Delta_{H,EL} &= F[E, P_H] \\
\Delta_{H,VISC} &= F[E_C, P_H]
\end{aligned} \quad \text{Vibration-analogy} \tag{14.12}$$

Experimental Vibration Analysis


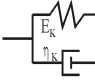

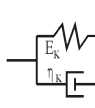


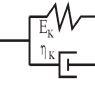
The vibration analogy has been used by the author in [141–144] to develop a method by which the complex Young's modulus of a material can be determined experimentally by modern vibration analysis equipment like the Brüel & Kjær type 3550 apparatus [145]. Equation (14.11) subsequently determines creep and relaxation. This new experimental method of determining materials viscoelasticity is a promising supplement [146] to the more traditional ways of material testing by direct measurements of creep and relaxation, see Figs. 14.1 and 14.2.

14.2 Models of Viscoelastic Materials

A complete analogy exists between viscoelastic stress-strain relations and force-deflection relations for mechanical systems composed of springs (Hooke elements) and dash-pots (Newton elements). For practical convenience we

subdivide viscoelastic materials into two groups: Simple viscoelastic materials, and less simple viscoelastic materials. The former group can be modeled as shown in Table 14.2 with up to 4 basic elements (Hooke, Newton). More than 4 basic elements are needed to model the latter group of materials.

Table 14.2. Simple models of viscoelastic materials. Hooke and Newton are the basic models. Reproduced from [121]

MODELS		MATERIAL PARAMETERS
 HOOKE	 THOMSON	$\tau = \frac{\eta}{E} ; \tau_K = \frac{\eta_K}{E_K}$ <i>Relaxation times</i>
 NEWTON	 LETHERSICH	
 MAXWELL	 KELVIN	$\alpha = \frac{E}{E_K} ; m_T = 1 + \alpha ; m_L = \frac{1}{1 + \eta/\eta_K}$
 BURGERS		$m_{B1} = \frac{1}{2} \left(1 + \alpha + \frac{\tau_K}{\tau} \pm \sqrt{\left(1 + \alpha + \frac{\tau_K}{\tau} \right)^2 - 4 \frac{\tau_K}{\tau}} \right)$
		<i>Control</i> : $m_{B1} m_{B2} = \frac{\tau_K}{\tau} ; m_{B1} + m_{B2} = 1 + \alpha + \frac{\tau_K}{\tau}$

14.2.1 Simple Models

Closed analytical expressions for stress-strain relations, analogy Young’s moduli, creep- and relaxation functions apply for simple viscoelastic materials. They are summarized in Tables 14.3 and 14.4 reproduced from [121]. Complex stiffness of the simple material models is easily obtained by replacing s with $i\omega$ as explained in (14.9).

The so-called Burgers model is the most general of the simple models of a viscoelastic material. All basic strain modes observed in practice are considered: Elastic strain (Hooke), delayed elastic strain (Kelvin), and flow strain (Newton). The latter two strain components are also named reversible creep and irreversible creep respectively. The Burgers model can model the viscoelasticity of a number of building materials.

14.2.2 Less Simple Models

It can be shown that general mechanical models for viscoelastic materials can be established in two ways. One general model is a Maxwell model connected in series with a chain of several Kelvin models in series. The other general model is a Hooke model connected in parallel with a chain of several Maxwell models in parallel. Both these models are discussed in further details in Appendix D.

Table 14.3. Simple viscoelastic models: Stress-strain relations and analogy Young's moduli. Abbreviations from Table 14.2. Reproduced from [121]

Model	Stress-Strain Relation	E^A (Analogy-E)
Hooke	$\sigma = E\varepsilon$	E
Newton	$\sigma = \eta \frac{d\varepsilon}{dt}$	ηs
Maxwell	$\frac{d\sigma}{dt} + \frac{\sigma}{\tau} = E \frac{d\varepsilon}{dt}$	$E \frac{s}{s + 1/\tau}$
Kelvin	$\sigma = E_K \left(\tau_K \frac{d\varepsilon}{dt} + \varepsilon \right)$	$E_K \tau_K (s + 1/\tau_K)$
Thomson	$\tau_K \frac{d\sigma}{dt} + m_T \sigma = E \left(\tau_K \frac{d\varepsilon}{dt} + \varepsilon \right)$	$E \frac{s + 1/\tau_K}{s + m_T/\tau_K}$
Lethersich	$\tau_K \frac{d\sigma}{dt} + m_L \sigma = m_L \eta \left(\tau_K \frac{d^2\varepsilon}{dt^2} + \frac{d\varepsilon}{dt} \right)$	$m_L \eta \frac{s(s + 1/\tau_K)}{s + m_L/\tau_K}$
Burgers	$\tau_K^2 \frac{d^2\sigma}{dt^2} + (m_{B1} + m_{B2})\tau_K \frac{d\sigma}{dt} + m_{B1}m_{B2}\sigma = E \left(\tau_K^2 \frac{d^2\varepsilon}{dt^2} + \tau_K \frac{d\varepsilon}{dt} \right)$	$E \frac{s(s + 1/\tau_K)}{(s + m_{B1}/\tau_K)(s + m_{B2}/\tau_K)}$

Table 14.4. Simple viscoelastic models: Creep functions and relaxation functions. Abbreviations from Table 14.2. Reproduced from [121]

Model	Creep Function	Relaxation Function
Hooke	$1/E$	E
Newton	t/η	$\eta\delta(t)$; Diracs delta function $\delta(t)$
Maxwell	$\frac{1}{E} \left(1 + \frac{t}{\tau} \right)$	$E \exp \left(-\frac{t}{\tau} \right)$
Kelvin	$\frac{1}{E_K} \left(1 - \exp \left(-\frac{t}{\tau_K} \right) \right)$	$E_K (1 + \tau_K \delta(t))$
Thomson	$\frac{1}{E} \left(1 + \alpha \left[1 - \exp \left(-\frac{t}{\tau_K} \right) \right] \right)$	$E \left(1 - \frac{\alpha}{1 + \alpha} \left[1 - \exp \left(-m_T \frac{t}{\tau_K} \right) \right] \right)$
Lethersich	$\frac{t}{\eta} + \frac{1}{E_K} \left(1 - \exp \left(-\frac{t}{\tau_K} \right) \right)$	$m_L \eta \left(\delta(t) + \frac{1 + m_L}{\tau_K} \exp \left(-m_L \frac{t}{\tau_K} \right) \right)$
Burgers	$\frac{1}{E} \left(1 + \frac{t}{\tau} + \alpha \left[1 - \exp \left(-\frac{t}{\tau_K} \right) \right] \right)$	$\frac{E}{m_{B1} - m_{B2}} \left[(m_{B1} - 1) \exp \left(-m_{B1} \frac{t}{\tau_K} \right) - (m_{B2} - 1) \exp \left(-m_{B2} \frac{t}{\tau_K} \right) \right]$

Power Law Model (Wood, Polymers, Ceramics)

A very special and important “less simple model” is the so-called Power Law model presented in Table 14.5. This model cannot be composed by a finite number of elementary mechanisms. An infinite number of elements have to be used.

The Power Law model is the result of a complete analysis made in [140] of an expression, $C(t) = (1 + at^b)/E$ with constants a and b , which has very often been used successfully in the literature (e.g. [147]) to fit experimental data

from creep tests on a variety of building materials such as wood, polymers, and ceramic materials. Physically the fit expression is very unfortunate (one material constant “ a ” has the dimension of time raised to minus the other material constant “ b ”).

Re-formulated, however, as it is in Table 14.5 the expression becomes viscoelastically sound, characterizing the materials rheology by independent material properties, namely the relaxation time τ (or creep doubling time ($C(\tau) = 2C(0)$), and the dimensionless creep power, b .

Table 14.5. Power law creep. $Z(x) = \Gamma(1 + b)(x/\tau)^b$ where Γ means gamma function. Reproduced from [140]. τ is relaxation time. b is creep power

Power Law Creep	
Creep Function $C(t)$	Relaxation Function $R(t)$
$\frac{1}{E} \left(1 + \left(\frac{t}{\tau} \right)^b \right)$	$E \sum_{k=0}^{\infty} \frac{(-Z(t))^k}{\Gamma(1 + kb)} \approx \frac{1}{C(t)} \text{ if } b < \frac{1}{3}$
Analogy Young's Modulus $E^A(s)$	
$E \frac{(\tau s)^b}{\Gamma(1 + b) + (\tau s)^b}$	

The Power Law model is a very efficient tool in viscoelastic stress-strain analysis. A number of material problems for a number of different materials can be solved in one approach, by developing standard solutions (“master solutions”) from which solutions for specific materials can be picked introducing specific material parameters, τ and b .

Remark: The efficiency of the Power Law model in viscoelastic stress-strain analysis of materials can be generalized to include the influence of curing conditions with respect to moisture and temperature: The relaxation time is the obvious materials parameter to be influenced by climatic conditions. For wood, for example, τ is known to be very sensitive to moisture content [148]. This observation has been utilized in [148–150] to produce “master graphs” from which fatigue-life of wood can be predicted as a function of moisture content.

Complex stiffness of a material with Power-law creep is obtained by replacing s with $i\omega$ in $E^A(s)$ as explained in (14.9). The results are presented in (14.13) and (14.14) reproduced from [140]. The Power law creep model

degenerates with $b = 1$ to the so-called Maxwell model defined in Table 14.2. The complex stiffness quantities become very simple as demonstrated in (14.15).

$$|E_C| = \frac{E}{\sqrt{1 + Y^2 + 2Y \cos(b\pi/2)}} ; \quad \tan \delta = \frac{Y \sin(b\pi/2)}{1 + Y \cos(b\pi/2)}$$

$$\text{with } Y = \frac{\Gamma(1+b)}{(\tau\omega)^b} = \frac{b!}{(\tau\omega)^b} = \frac{\tan(\delta)}{\sin(b\pi/2) - \tan(\delta) \cos(b\pi/2)} \quad (14.13)$$

$$E_R = E \frac{1 + Y \cos(b\pi/2)}{1 + Y^2 + 2Y \cos(b\pi/2)} ; \quad E_I = E \frac{Y \sin(b\pi/2)}{1 + Y^2 + 2Y \cos(b\pi/2)}$$

$$|E_C| \rightarrow \begin{cases} E & \text{if } \omega \rightarrow \infty \\ 0 & \text{if } \omega \rightarrow 0 \end{cases} ; \quad \tan(\delta) \rightarrow \begin{cases} 0 & \text{if } \omega \rightarrow \infty \\ \tan(b\pi/2) & \text{if } \omega \rightarrow 0 \end{cases} \quad (14.14)$$

$$|E_C| = E \frac{\tau\omega}{\sqrt{1 + (\tau\omega)^2}} = E \cos(\delta) ; \quad \tan(\delta) = \frac{1}{\tau\omega} ; \quad (\text{Maxwell}) \quad (14.15)$$

Time Modified Models – Aging Viscosity

Some viscoelastic materials like Portland cement paste and concrete are so-called aging viscoelastic materials [120] with time dependent material properties meaning that the creep functions, relaxation functions, and the material parameters p and q in (14.1) become dependent of time. Some aging materials, however, can be analyzed by the theory of non-aging materials hitherto considered if we assume that the “spring constants” (E) in the mechanical models are constants (in practice almost constants) and that viscosities (η) change in the same way with age. Then the aging phenomenon can be removed by introducing a modified time as subsequently demonstrated in (14.16) and (14.17) on a Maxwell material with age dependent viscosity or time dependent relaxation time.

The modified time, defined by $\tau(t)d\phi/dt = 1$, is presented in (14.18).

$$\begin{aligned} \text{Aging Maxwell:} \quad & \frac{d\sigma}{dt} + \frac{\sigma}{\tau(t)} = E \frac{d\varepsilon}{dt} \Rightarrow \\ \text{differentiation through } \phi : \quad & \frac{d\sigma}{d\phi} \frac{d\phi}{dt} + \frac{\sigma}{\tau(t)} = E \frac{d\varepsilon}{d\phi} \frac{d\phi}{dt} \Rightarrow \\ & \frac{d\sigma}{d\phi} + \frac{\sigma}{\tau(t)d\phi/dt} = E \frac{d\varepsilon}{d\phi} \Rightarrow \end{aligned} \quad (14.16)$$

$$\left. \begin{array}{l} \text{Maxwell with modified} \\ \text{time } \phi \text{ and } “\tau” = 1 \end{array} \right\} \quad \frac{d\sigma}{d\phi} + \sigma = E \frac{d\varepsilon}{d\phi} \quad (14.17)$$

$$\phi = \phi(t) = \int_{t_0}^{t+t_0} \frac{1}{\tau(\theta)} d\theta \quad \text{with } \begin{cases} \text{time } t \text{ measured from} \\ \text{age at first loading } t_0 \end{cases} \quad \text{modified time} \quad (14.18)$$

Thus, a Maxwell material with aging viscosity can be considered as a non-aging Maxwell material when time t is replaced with modified time ϕ (also named “creep parameter”), and relaxation time τ is replaced with modified relaxation time $\tau = 1$. Then from Table 14.4 creep functions and relaxation functions become as presented in the first row of Table 14.6.

Remarks: The e-v-analogy applies for time-modified models if stress and strain are formulated in modified time before Laplace transformation. The vibration analogy, however, does not apply. The analogy becomes meaningless introducing “harmonic” variations in stress and strain with time in modified time.

Hardened Cement Paste (HCP)

Based on the classical papers of Dischinger’s [151, 152] on creep of concrete the modified time concept was suggested by the author in [120, 153] and subsequently further developed and generalized in a number of papers [121, 154–156, 161] on the rheology of hardened Portland cement paste and Portland cement based materials. The concept was introduced into international concrete codes in [157].

For hardened HCP, cured at $(T, RH) \approx (20^\circ\text{C}, 60\%)$, the creep parameter can be estimated by the expression presented in Table 14.6, which is developed from (14.18) assuming a relaxation time (or viscosity) which develops proportional with time. The expressions presented in Table 14.6 are consistent with general rheological observations made in [120, 124, 125] on cement paste and concrete.

Table 14.6. Creep of hardened cement paste at t days after loading at the age of t_0 days. Creep factor is denoted by ϕ^*

Mature HCP (age >3 weeks)	
Creep Function	Relaxation Function
$C(t)_{\text{HCP}} = \frac{1}{E_{\text{HCP}}} (1 + \phi).$	$R(t)_{\text{HCP}} = E_{\text{HCP}} \exp(-\phi)$
Stiffness (MPa)	Creep Parameter (t in days)
$E_{\text{HCP}}(\text{Table 10.5}, g(t) \equiv 1)$	$\phi = \phi^* \log_E \left(\frac{t + t_0}{t_0} \right); \phi^* \approx \begin{cases} 1.4 & ; W/C \geq 0.4 \\ 3.5W/C & ; W/C < 0.4 \end{cases}$

The creep parameter for hardened HCP is independent of $W/C > 0.4$ – basically because the relative viscosity of a viscoelastic material is not influenced by voids [84, 85, 121].

A composite analysis of concrete will subsequently be demonstrated in Chap. 15 where concrete is modeled as aggregates mixed into a matrix of

Table 14.7. Drying shrinkage of hardened cement paste. Shrinkage factor is denoted by k

Drying Shrinkage of HCP at RH ≈ 0.6
$\lambda = k^* \phi$ with $k \approx -0.5\%$

cement paste. In this context, it is of great interest to evaluate the influence of cement paste shrinkage on the shrinkage of concrete. For this purpose shrinkage of cement paste can be estimated by Table 14.7, adopting an idea from [161].

Remark: When early age cement pastes are considered where stiffness and viscosity properties change very much with age, the concept of time modified Maxwell behavior is not applicable. More refined models have to be used such as referred to in Sect. 15.2.4.

14.3 Summary, Analysis, and Approximate Analysis

A number of material models have been demonstrated in this chapter, some of which are of immediate relevance for the analysis of viscoelastic materials often met in practice. Examples are cement- and wood based materials, asphalt, and polymers.

Various tools have been presented which can be used to predict the stress-strain behavior of viscoelastic materials subjected to static or dynamic loads. Methods are presented which relate material properties (creep function, relaxation function, and complex elastic moduli) of relevance for such analysis. An illustrative example of property conversion between complex elastic moduli and creep/relaxation functions are demonstrated in Figs. 14.5 and 14.6.

The material considered is a Burgers material with $E = 30000$ MPa, $\alpha = 1$, and $(\tau, \tau_K) = (1000, 10)$ days. The complex Young's modulus is determined from the analogy Young's modulus presented in Table 14.3 replacing the argument s with $i\omega$ as previously explained in (14.9). The creep/relaxation results, shown with dots in Fig. 14.6, are subsequently determined with (14.11). (A computer with complex number facilities is needed for these transactions).

The creep function and relaxation function presented in Fig. 14.6 with a solid line are exact as determined directly from Table 14.4. The two data sets agree very positively (as they should) which tells about the quality of (14.11) to act as a materials property "converter".

Remark: The latter observation is emphasized: With modern technology, the data in Fig. 14.5 could have been detected experimentally, meaning that (14.11) opens a new way of property determination for viscoelastic materials, see Sect. 14.1.2.

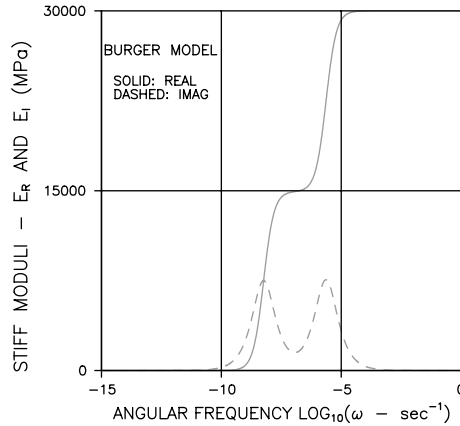


Fig. 14.5. Complex stiffness of Burgers: $E = 30000$ MPa, $\alpha = 1$, and $(\tau, \tau_K) = (1000, 10)$ days

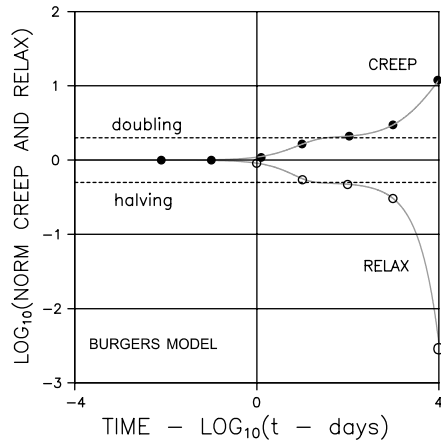


Fig. 14.6. Creep and relaxation calculated from “experimental” complex Young’s modulus in Fig. 14.5

14.3.1 Approximate Analysis

The well known “effective modulus method” (E^{EFF} -method) (e.g. [158, 159]) presented in (14.19) for quasi-static stress-strain analysis of viscoelastic materials is a crude approximation of the accurate stress-strain analysis considered in this chapter. The advantage in practice of the E^{EFF} -method is that it is very convenient to use for first stress-strain estimates. It is emphasized, however, that the method when used un-reflected (as it commonly is) may lead to results which are completely wrong. This discrepancy was recognized already in [158]. An obvious false prediction is that ε becomes 0 whenever σ drops to 0. Obviously the method cannot be used in vibration analysis.

$$\varepsilon(t) \approx \frac{\sigma(t)}{E^{\text{EFF}}} \quad \text{with} \quad E^{\text{EFF}} = \frac{1}{C(t)} = \frac{E}{1 + \phi} \quad \underline{E^{\text{EFF}}\text{-method}} \quad (14.19)$$

where $\phi = \phi(t) = EC(t) - 1$ is the so-called creep parameter

A general description of the “accuracy” of the E^{EFF} -method is impossible. It will depend on both type of materials viscosity and type of problem to be solved. However, for the type of problems (analysis of material properties) considered in this book we “risk” to state the following simple quality assessment of the E^{EFF} -method. The statement is based on results obtained from running a number of evaluation calculations on Burgers, Thomson, Maxwell, and Power-Law viscoelastic materials – and on the author’s work on creep of concrete in [160, 161].

Reasonable estimates can be obtained by the E^{EFF} -method when stress varies monotonically, restricted as outlined in (14.20). The better estimates are obtained when the materials considered have creep functions (C) and relaxations functions (R) which are, approximately, each others reciprocals, meaning $R^*C > \text{approx } 0.9$.

When $R^*C < 0.9$ the E^{EFF} -method can still be used (with stress restricted as just explained). Creep parameters $\phi < 4$, however, are required. Obviously the E^{EFF} -method cannot in general be used to predict a relaxation function. It might be necessary to determine this function numerically from the creep function using the basic (14.2).

Similar “rules” will apply when modified E^{EFF} -methods are used as these are formulated in (e.g. [162, 163]).

$$\sigma_0(1 + \phi)^{-1} < \sigma < \sigma_0(1 + \phi) \quad \sigma_0 = \sigma(t = 0) \quad (14.20)$$

or $\sigma = k\phi$ where k is a constant

The E^{EFF} -method applies almost accurately when Power-Law materials are considered with $b < 0.3$. As previously observed the creep function and the relaxation function for such materials are each other’s reciprocals.

Approximate Inversion Method

The effective Young’s modulus can be related to the analogy Young’s modulus E^A by the following deductions using (14.4) and the “left section, lower row expression” of Table 14.1.

$$\bar{C}(s) = \frac{1}{sE^A(s)} \Rightarrow C(\infty) = \lim_{s \rightarrow 0} \frac{1}{E^A(s)} \quad \text{and} \quad C(0) = \lim_{s \rightarrow \infty} \frac{1}{E^A(s)} \quad (\text{accurate})$$

$$\text{estimate } C(t) \approx \frac{1}{E^A(\gamma/t)}; \quad \underline{E^{\text{EFF}} = \frac{1}{C(t)} \approx E^A(\gamma/t)} \quad (\text{approximate}) \quad (14.21)$$

where γ is a so-called inversion parameter for which the order of magnitude can be estimated to be $0.5 < \gamma < 1$ with minimum and maximum applying to “only reversible creep” and “only viscous creep” respectively.

Remark: It can easily be shown that (14.21) is a special result of using the following approximate inversion rule developed from Table 14.1,

$$\begin{aligned} \bar{F}(s) \text{ is image function of } F(t); \text{ then} \\ \underline{F(t) \approx G(\gamma/t) \quad \text{where } G(s) = s\bar{F}(s) \quad (\text{approx inversion rule})} \end{aligned} \quad (14.22)$$

which can be used directly to develop approximate real solutions from their Laplace transformed counterparts. This procedure (*approximate inversion method*) is demonstrated in the following expression for stress in a Thomson material subjected to a constant strain, $\varepsilon = 1$ (Laplace transformed strain, $1/s$).

$$\bar{\sigma} = \bar{\varepsilon}^* E^A = \frac{1}{s} E \frac{s + 1/\tau_K}{s + m_T/\tau_K} \Rightarrow \sigma(t) \approx E \frac{1 + t/\gamma/\tau_K}{1 + m_T t/\gamma/\tau_K} \quad (14.23)$$

The results of a stress analysis of a Thomson material using the E^{EFF} -method and the approximate inversion method respectively are compared in Fig. 14.7.

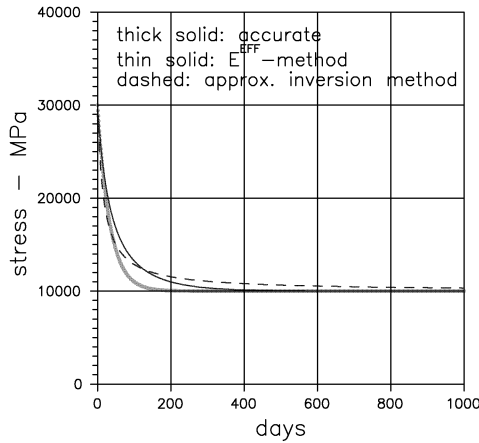


Fig. 14.7. Thomson model loaded with constant strain $\varepsilon = 1$. $E = 30000$ MPa, $\alpha = 2$, $\tau_K = 100$ days. Approximate inversion with $\gamma = 0.5$

Remark: In this book the approximate inversion method is considered mainly as an interesting curiosum. Approximate analyses are always made with the original E^{EFF} -method (14.19) unless otherwise indicated.

Viscoelastic Composites

Creep functions, relaxation functions, internal stresses, and eigenstress/strain phenomenon of composite materials with various geometrical configurations are predicted in this chapter from known viscoelastic properties of the constituent phases.

Basically the composites considered in this chapter are the same as those defined in Chap. 10: Viscoelastic composite components are considered with constant Poisson's ratios of the order of magnitudes ≈ 0.2 . The composite geometry can be sufficiently well described using the simple shape function descriptions defined in Chap. 10. There are no theoretical problems in generalizing a viscoelastic analysis to more general composites with respect to Poisson's ratios and shape functions. The mathematics, however, will increase to a level, which cannot be justified by our present knowledge on geometries and rheological properties of composite phases.

In principles the analytical methods used in this chapter are the same as have been developed previously by the author [120,121] in studies on the rheological behavior of prestressed concrete and on the viscoelasticity of concrete as a function of aggregate content – and in [164] in a study of stiffness and damping of impregnated materials.

In most examples presented the theory is illustrated using composite components, which exhibit Power Law creep. The principles, however, are kept general such that composites can be considered with components of any viscoelastic observance. The reason for choosing Power law creep as “default viscoelastic behavior” in examples is that many viscoelastic materials in practice can be well approximated in this way – and that analytical results obtained can be presented very explicitly. These features have previously been discussed in Sect. 14.2.2.

15.1 Composite Analysis

15.1.1 Accurate Analysis

The theoretical basis of the analysis presented in this chapter is the finding of Hashin's [165, 166] that the complex stiffness (E_C) of a composite made of viscoelastic phases (P, S) can be determined by the elastic counterpart composite stiffness (E), replacing phase stiffness (E_P, E_S) with their respective complex counterparts (E_{PC}, E_{SC}).

Keeping in mind the significance of the analogy Young's modulus previously introduced in Sect. 14.1.1, and re-calling the vibration analogy from Sect. 14.1.2, Hashin's observation means that the analogy Young's modulus of a composite material (E^A) can be obtained from the elastic counterpart stiffness solution (E), replacing phase stiffness (E_P, E_S) with their respective analogy Young's moduli (E_P^A, E_S^A).

Having established the basic rheological property (E^A) of the composite material we may proceed just as explained in Chap. 14 with the composite material considered as a homogeneous viscoelastic material. A further conclusion which can be made from [165, 166] and the concept presented in this book of an analogy Young's modulus, is that composite stress/strain solutions can be established from Laplace transforming the elastic counterpart solutions (Table 10.3) and replacing (E_P, E_S) with (E_P^A, E_S^A). A summary of results such obtained from an analysis of composite materials is presented in Tables 15.1 and 15.2. Analogy Young's moduli (E_P^A, E_S^A) for various homogeneous materials are presented in Sect. 14.2.

Remarks: The procedure presented in Table 15.1 of determining the creep and relaxation functions for a composite material from the complex stiffness is very efficient using computers with the capability of handling complex numbers. It is obvious how the experimental vibration analysis explained in Sect. 14.1.2 can be used also in the research on composite geometry versus viscoelasticity of composite materials.

With respect to the determination of creep- and relaxation functions we re-call that only one of these functions are needed to predict the other one by the basic (14.2).

In general the determination of internal stress and eigenstrain-stress as expressed in Table 15.2 calls for numerical Laplace-inversions. Alternatively, approximate solutions can be found as explained in the following section.

15.1.2 Approximate Analysis

A very simple approximate quasi-static analysis of viscoelastic composites can be obtained from the elastic counterpart analysis explained in (15.1),

$$F \approx F_{\text{ELAST}}(P, E_P^{\text{EFF}}, E_S^{\text{EFF}}) \text{ where } F_{\text{ELAST}} = F_{\text{ELAST}}(P, E_P, E_S) \quad (15.1)$$

Table 15.1. Complex Young's modulus, creep, and relaxation of composite material determined from Young's modulus of such material. Examples are composites made of components exhibiting Power law viscoelasticity. $[]_P$ and $[]_S$ mean that E, b , and τ in $[]$ are subscripted as indicated

Young's Modulus \Rightarrow Analogy Young's Modulus	
$E = E(E_P, E_S) \Rightarrow E^A = E^A(s) = E(E_P^A, E_S^A)$	
Example	$E_P^A = \left[E \frac{(\tau s)^b}{\Gamma(1+b) + (\tau s)^b} \right]_P$; $E_S^A = \left[E \frac{(\tau s)^b}{\Gamma(1+b) + (\tau s)^b} \right]_S$
Analogy Young's Modulus \Rightarrow Complex Young's Modulus	
$E^A = E^A(s) = E(E_P^A, E_S^A) \Rightarrow E_C = E^A(i\omega) = E(E_{PC}, E_{SC}) = E_R(\omega) + iE_I(\omega)$	
Example	$E_{PC} = \left[E \frac{(i\tau\omega)^b}{\Gamma(1+b) + (i\tau\omega)^b} \right]_P$; $E_{SC} = \left[E \frac{(i\tau\omega)^b}{\Gamma(1+b) + (i\tau\omega)^b} \right]_S$
Complex Young's Modulus \Rightarrow Relaxation and Creep	
$R(t) = E - \frac{2}{\pi} \int_0^\infty E_I(\omega) \frac{1 - \cos(\omega t)}{\omega} d\omega$ $C(t) = \frac{1}{E} + \frac{2}{\pi} \int_0^\infty J_I(\omega) \frac{1 - \cos(\omega t)}{\omega} d\omega; \left(J_I = \frac{E_I}{ E_C ^2} \right)$	
Or Analogy Young's Modulus \Rightarrow Relaxation and Creep	
$C(t) = L^{-1} \left[\frac{1}{sE^A} \right]; R(t) = L^{-1} \left[\frac{E^A}{s} \right]$	

Table 15.2. Internal stress from external load on, and eigenstrain/stress in composite material determined from analogy Young's modulus of such material

Internal Stress from Ext-Load ($e^A = E^A/E_S^A$; $n^A = E_P^A/E_S^A$)	
$\sigma_P(t) = \frac{1}{c} L^{-1} \left[\bar{\sigma} \frac{1/e^A - 1}{1/n^A - 1} \right]; \sigma_S(t) = \frac{\sigma(t) - c\sigma_P(t)}{1 - c}$	
Eigenstrain/Stress ($K_S^A \approx E_S^A/1.8$)	
$\lambda(t) = L^{-1} \left(\bar{\lambda}_S + \bar{\Delta}\lambda \frac{1/e^A - 1}{1/n^A - 1} \right)$ with $\bar{\Delta}\lambda = \bar{\lambda}_P - \bar{\lambda}_S$	
$\rho_P(t) = -L^{-1} \left(3\bar{\Delta}\lambda K_S^A \frac{c(1/n^A - 1) - (1/e^A - 1)}{c(1/n^A - 1)^2} \right); \rho_S(t) = -\frac{c}{1 - c} \rho_P(t)$	

where F_{ELAST} and F are the elastic and viscoelastic solutions respectively to the problem considered. E_P^{EFF} and E_S^{EFF} are the effective Young's moduli explained in Sect. 14.3.1. Load (stress or strain) is denoted by P . In another formulation the method was first suggested by Ross [158] as an easy way of estimating the stress distribution in a composite structure made of concrete and steel. An example of applying (15.1) in a composite analysis is explained in (15.2). The elastic composite stiffness, E , is converted to the creep function of the counterpart viscoelastic composite.

$$C(t) \approx \frac{1}{E^{\text{EFF}}} \text{ with } E^{\text{EFF}} = E(E_P^{\text{EFF}}, E_S^{\text{EFF}}) \text{ where } E = E(E_P, E_S) \quad (15.2)$$

Remark: The quality of composite solutions obtained by the “composite E^{EFF} -method” depends on the quality of E_P^{EFF} and E_S^{EFF} considered in Sect. 14.3.1. The load restrictions explained in this section must hold for each phase also on a “composite level”. The author’s (tentative) experience with respect to the quality of E^{EFF} -estimates is the following:

Estimates of “reasonable accuracy” can be obtained for the material properties, creep functions, creep stresses, eigenstress/strain properties. To get a similar level of accuracy for “estimated” relaxation functions, it might be necessary to determine this function numerically from the creep function using the basic (14.2).

In general, estimates of reasonably high accuracy can be expected in any analysis when composites are considered where both components have Power Law viscoelasticity with $b < 1/3$.

These statements are based on testing the composite E^{EFF} -method on composites such as Maxwell materials mixed with elastic spheres, mixtures of two materials exhibiting Power Law creep, and layered composites made of two Maxwell materials.

Approximate Inversion Method

It is tempting (see Sect. 14.3.1) to use this method when problem solutions are formulated by their Laplace transformed as they are in Tables 15.1 and 15.2: Multiply the Laplace transformed solution with s and then replace s with γ/t . The inversion parameter γ , however, has to be estimated as some composite average of inversion parameters applying to phases P and S. In the author’s opinion this feature disqualifies, in practice, the approximate inversion method to be better than the plain E^{EFF} -method. In any case, more research has to be made on this matter.

15.2 Applications

Some examples are presented in this section, which illustrate how the analysis of viscoelastic composites just explained in Sect. 15.1 works on various

composites. We emphasize that the accurate method of analysis is always used – unless otherwise indicated.

15.2.1 Porous Materials and Stiff Pore Systems

It is of some interest to know how does a very soft phase P ($n = 0$) and very stiff phase P ($n = \infty$) modify the rheology of a composite. The question is immediately answered as presented in (15.3) developed from (10.9), (10.14), and (14.4).

$$\begin{aligned} \frac{R_0(t)}{R_S(t)} = \frac{C_S(t)}{C_0(t)} = \frac{1-c}{1+c/\theta_0} ; \quad \theta_0 = \begin{cases} \mu_P & c \leq c_P \\ 0 & c > c_P \end{cases} \\ \frac{R_\infty(t)}{R_S(t)} = \frac{C_S(t)}{C_\infty(t)} = \frac{1+\theta_\infty c}{1-c} ; \quad \theta_\infty = \begin{cases} \frac{\mu_P + \mu_S - 1}{\mu_S} & c < c_S \\ \infty & c > c_S \end{cases} \end{aligned} \quad (15.3)$$

This expression tells that composite creep- and relaxation functions are proportional with the corresponding function of the matrix material (phase S). Examples of this statement are the following:

Fresh concrete and asphalt concrete can be modeled as a mixture of stiff particles in a Newton material with viscosity, η_S . According to (15.3) the mixture can also be modeled as a Newton material. The viscosity η_∞ is proportional with the viscosity of the Newton material in the same way as the stiffness of a stiff pore system relates to the stiffness of its matrix, see Sect. 10.3.5 with Fig. 10.31.

Equation (15.3) has been used by the author in [84] to predict the rheological behavior of fluids mixed with voids or with very stiff particles. The latter application is of special interest when modern self-compacting concretes (SCC) are considered [85].

15.2.2 Particulate Composite

A CSA_P composite is considered with viscoelastic components. The questions are, how does this composite creep, relax, and how do stresses develop internally when the composite is loaded externally or by eigenstrains.

The questions asked are solved as explained in Sect. 15.1: The elastic solutions are presented in Chap. 10, Tables 10.3 and 10.4. The Laplace transformed “viscoelastic” answers to the problems formulated are determined from these solutions replacing the stiffness moduli (E, n) with their viscoelastic counterparts (E^A, n^A) and load with the Laplace transformed load. The final solutions are determined by Laplace inversion.

The analysis is exemplified in (15.4) looking at the phase P stress in a CSA_P composite subjected to an external load. The abbreviations used (and others for further viscoelastic analysis of CSA composites) are explained in (15.5).

$$\sigma_P = \sigma \frac{(1+A)n}{A+n} \quad \text{elastic particle stress} \Rightarrow \quad (15.4)$$

$$\overline{\sigma_P} = \overline{\sigma} \frac{(1+A)n^A}{A+n^A} \Rightarrow \sigma_P(t) = L^{-1} \left(\overline{\sigma} \frac{(1+A)n^A}{A+n^A} \right)$$

$$\left. \begin{aligned} e &= \frac{A+n}{1+An} ; & E &= E_S \frac{A+n}{1+An} ; & n &= \frac{E_P}{E_S} \\ e^A &= \frac{A+n^A}{1+An^A} ; & E^A &= E_S^A \frac{A+n^A}{1+An^A} ; & n^A &= \frac{E_P^A}{E_S^A} \end{aligned} \right) \text{CSA}_P \text{ with } A = \frac{1-c}{1+c} \quad (15.5)$$

Maxwell-Hooke CSA_P-Composite

It is now assumed that the particle phase (P) is elastic and the matrix phase (S) is viscoelastic like a Maxwell material. The analysis proceeds as just explained with material specific analogy stiffness properties and appropriate abbreviations presented in Table 15.3, and with Laplace transformation/inversion used as described in Table 14.1. The final sets of answers to the questions asked are summarized in Table 15.4.

15.2.3 Mature Cement Concrete

It has previously been discussed, that concrete (and cement paste) can be considered non-aging introducing the authors concept of modified time, see Sect. 14.2.2. This means that the results of Table 15.4 apply for concrete when the Maxwell relaxation time, τ , is replaced with “1”, and time in general, t , is replaced with the modified time, ϕ .

The results obtained are presented in Table 15.5. The expressions presented in Table 15.6 are of special interest when normal concretes and porous “concretes” are considered.

We emphasize that phase S properties in general (including E_S and ϕ) are the HCP properties presented in Table 14.6.

Table 15.3. Auxiliary quantities for viscoelastic analysis of CSA_P-material with a Maxwell matrix (phase S) and elastic particles (phase P). The abbreviations, E (composite Young’s modulus) and A are explained in (15.5)

Maxwell-Hooke CSA _P -material	
Phase properties	$\left. \begin{aligned} E_S^A &= E_S \frac{s}{s+1/\tau} \text{ Maxwell} \\ E_P^A &= E_P \text{ Hooke} \end{aligned} \right) ; \quad n^A = n \frac{s+1/\tau}{s}$
Abbreviations appropriate in viscoelastic analysis	$Q_1 = \frac{n}{A+n} ; \quad Q_2 = \frac{An}{1+An}$
Analogy Young’s modulus	$e^A = e \frac{s+Q_1/\tau}{s+Q_2/\tau} ; \quad E^A = E \frac{s}{s+1/\tau} \frac{s+Q_1/\tau}{s+Q_2/\tau}$

Table 15.4. Viscoelastic composite analysis of CSA_P-material. In eigenstrain/stress analysis: λ is composite eigenstrain (linear). (λ_P , λ_S) and (ρ_P , ρ_S) are eigenstrain (linear) and eigenstress (hydrostatic) of phase P and phase S respectively. $\sigma_{S,RAD}$ and $\sigma_{S,TAN}$ are radial and tangential phase S stress respectively at a sphere. Bulk modulus $K_{S,P} \approx E_{S,P}/1.8$. The abbreviations, A , E (composite Young's modulus), e , Q_1 , and Q_2 , are explained in Table 15.3

Problem	Viscoelastic CSA _P -Solutions
Creep function	$C(t) = \frac{1}{E} \left[1 + Ae^{\frac{t}{\tau}} + \frac{A(1-Ae)}{n} (1 - \exp(-Q_1 \frac{t}{\tau})) \right]$
Relaxation function	$R(t) = E \left[\frac{A}{e} \exp\left(-\frac{t}{\tau}\right) + \frac{n(1-A^2)}{A+n} \exp\left(-Q_2 \frac{t}{\tau}\right) \right]$
Internal stress caused by constant external load σ	$\sigma_P = \sigma \frac{n(1+A)}{A+n} \left[1 + \frac{A}{n} (1 - \exp(-Q_1 \frac{t}{\tau})) \right]$ $\sigma_S = \frac{\sigma - c\sigma_P}{1-c}$
Eigenstrain/stress caused by matrix (linear) eigenstrain $\lambda_S = kt$	$\lambda = kA \left[t + \frac{1-A}{n} \tau (1 - \exp(-Q_1 \frac{t}{\tau})) \right]$ $\rho_P = 3kK_S A \tau (1 - \exp(-Q_1 \frac{t}{\tau}))$; $\rho_S = -\frac{c}{1-c} \rho_P$
Max-matrix stress at spheres	$\sigma_{S,RAD} = \rho_P$; $\sigma_{S,TAN} = -\frac{3-A}{4A} \rho_P$
Matrix stress at spheres from const $\Delta\lambda = \lambda_P - \lambda_S$	$\sigma_{S,RAD} = -3K_P \Delta\lambda \frac{A}{A+n} \exp(-Q_1 \frac{t}{\tau})$; $\sigma_{S,TAN} = -\frac{3-A}{4A} \sigma_{S,RAD}$

Table 15.5. Viscoelastic composite analysis of concrete. Abbreviations are explained in Table 15.3

Problem	Concrete Solutions
Creep function	$C(t) = \frac{1}{E} \left[1 + Ae\phi_S + \frac{A(1-Ae)}{n} (1 - \exp(-Q_1\phi_S)) \right]$
Relaxation function	$R(t) = E \left[\frac{A}{e} \exp(-\phi_S) + \frac{n(1-A^2)}{A+n} \exp(-Q_2\phi_S) \right]$
Internal stress caused by constant external load σ	$\sigma_P = \sigma \frac{n(1+A)}{A+n} \left[1 + \frac{A}{n} (1 - \exp(-Q_1\phi_S)) \right]$ $\sigma_S = \frac{\sigma - c\sigma_P}{1-c}$
Eigenstrain/stress caused by matrix (linear) eigenstrain $\lambda_S = k\phi_S$	$\lambda = kA \left[\phi_S + \frac{1-A}{n} (1 - \exp(-Q_1\phi_S)) \right]$ $\rho_P = 3kK_S A (1 - \exp(-Q_1\phi_S))$; $\rho_S = -\frac{c}{1-c} \rho_P$
Max-matrix stress at spheres	$\sigma_{S,RAD} = \rho_P$; $\sigma_{S,TAN} = -\frac{3-A}{4A} \rho_P$
Matrix stress at spheres from const $\Delta\lambda = \lambda_P - \lambda_S$	$\sigma_{S,RAD} = -3K_P \Delta\lambda \frac{A}{A+n} \exp(-Q_1\phi_S)$; $\sigma_{S,TAN} = -\frac{3-A}{4A} \sigma_{S,RAD}$

Table 15.6. Special solutions for concrete with hard aggregates or with very soft aggregates (voids)

Problem	Special Concrete Solutions
Creep function	$C(t) = \frac{1}{E} (1 + \phi)$ with $\phi = \begin{cases} A \frac{E}{E_S} \phi_S & \text{when } n > 2 \\ \phi_S & \text{when } n = 0 \end{cases}$
Eigenstrain caused by matrix eigenstrain λ_S	$\lambda = \begin{cases} \approx A^* \lambda_S & \text{when } n > 2 \\ = \lambda_S & \text{when } n = 0 \end{cases}$

The normal concrete results in Table 15.6 comply reasonably well (orders of magnitudes) with the following observations:

- Creep strain of concrete relative to creep strain of cement paste varies with $(1 - c)^B$ with B increasing from 1.7 to 2.1 with time under load [167].
- Shrinkage of concrete relative to shrinkage of cement paste varies with $(1 - c)^B$ with $B \approx 1.7$ [168], with $B \approx 1.4$ [169], and with $B \approx 1.2$ –1.7 [170].

Examples

Two examples are now presented on how the results in Table 15.5 can be used in practice to predict creep, relaxation, and eigenstrain/stress in concrete. The concrete considered has a water/cement ratio of $W/C = 0.4$ and a total aggregate/cement ratio of $A/C = 4.33$ from which a volume concentration of $c = 0.7$ is obtained from Table E1 in Appendix E. The aggregate stiffness is $E_P = 55000$ MPa. The rheological cement paste properties used in the analysis are predicted from Table 14.6 with an estimated creep factor of $\phi^* = 1.4$.

Example 1. The concrete is loaded at the age of $t_0 = 28$ days. The creep function and the relaxation function predicted from Table 15.5 are illustrated in Figs. 15.1 and 15.2.

Example 2. The concrete is exposed to drying from the age of $t_0 = 28$ days. The drying is anticipated to cause a HCP shrinkage corresponding to a shrinkage factor of $k = -0.0005$ (see Table 14.7). With this information, the concrete eigenstrain and internal stresses shown in Figs. 15.3 and 15.4 are predicted by Table 15.5. The dotted data presented in Figs. 15.3 and 15.4 are from an experimental study by Nielsen [104] on the influence of shrinkage on aggregate stress in concrete. The concrete (LL3) used by Nielsen is exactly as previously defined in this section.

Nielsen's study in [104]: Strain gauges were attached to an artificial steel “stone” constructed to simulate very precisely the stiffness properties of the other coarse aggregates. The data shown in Figs. 15.3 and 15.4 are typical discrete averages. The experiments, however, were continuously monitored in

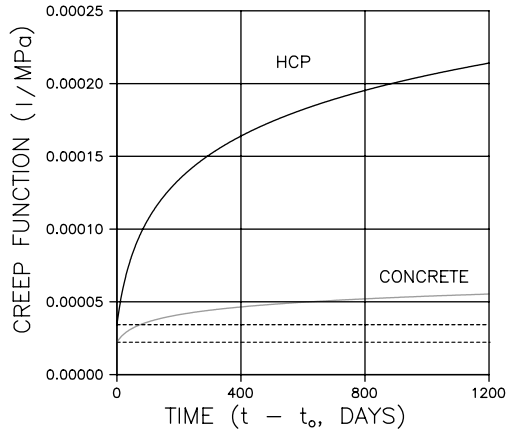


Fig. 15.1. Creep function of concrete considered. $t_0 = 28$ days

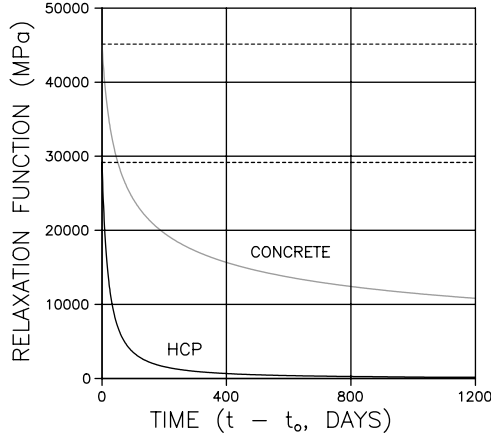


Fig. 15.2. Relaxation function of concrete considered. $t_0 = 28$ days

age periods 0–60, 200–260, and 860–915 days. A single set of data was monitored at the end of the experiment at 1060 days. Unfortunately no rheological information on cement paste and concrete are reported in [104]. There is also no information on shrinkage of paste. The *simultaneous* agreements, however, between experimental and theoretical strain/stress data observed in Figs. 15.3 and 15.4 indicate that the creep and shrinkage behavior of the concrete used by Nielsen are well simulated by the creep- and shrinkage factors assumed.

Remark: It is noticed from Fig. 15.4 that the max HCP stress is threateningly close to the tensile strength of HCP estimated to be one tenth of the compressive strength predicted by (10.25).

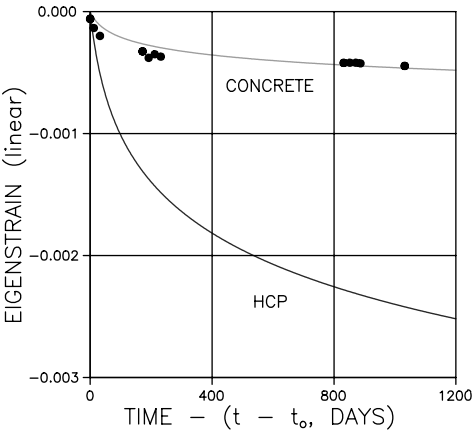


Fig. 15.3. Eigenstrain in concrete considered in example 2. Drying at RH = 60% from the age of $t_0 = 28$ days

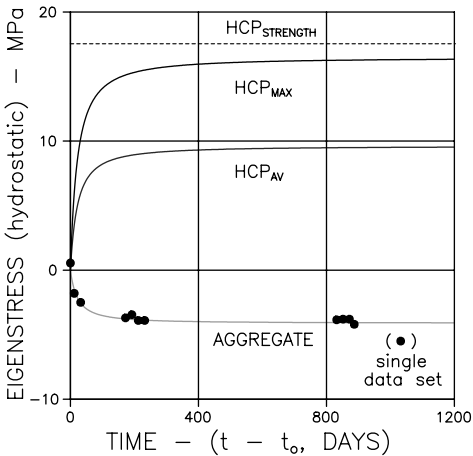


Fig. 15.4. Eigenstress of concrete considered in example 2. Drying at RH = 60% from the age of $t_0 = 28$ days

A Strength Mechanism for Concrete

The elastic stress at a sphere (phase P) in an infinite continuum (phase S) can be developed from Goodier [45] as presented by the former expression in (15.6). Load at infinity (S) and stresses of interest are defined in Fig. 15.5 together with coordinates. The corresponding stresses in a CSA_P-composite with many spheres are predicted by the SCS method previously explained (E_S is replaced with E and n with $E_P/E = n/e$). The results are presented in the second expression of (15.6).

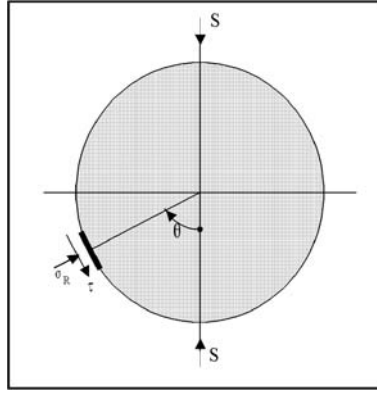


Fig. 15.5. The sphere of Goodier's

$$\begin{aligned}
 \sigma_R &= S(1 + \cos(2\theta)) \frac{n}{1+n}; \quad \tau = S \sin(2\theta) \frac{n}{1+n} \quad (\text{single sphere}) \\
 \sigma_R &= S(1 + \cos(2\theta)) \frac{n}{e+n}; \quad \tau = S \sin(2\theta) \frac{n}{e+n} \quad (\text{SCS solution}) \\
 \text{where } e &= e(c, n) = \frac{A+n}{1+An}, \quad A = \frac{1-c}{1+c} \quad \text{and } n = \frac{E_P}{E_S}
 \end{aligned} \tag{15.6}$$

The elastic composite strength expression presented in (15.8) can be predicted from the composite stresses if we assume that the so-called Coulomb's failure condition expressed in (15.7) applies in bond areas between phases.

$$\tau = C + \sigma_R \tan(\lambda); \quad \left(\begin{array}{l} C \text{ is cohesion in bond area} \\ \lambda \text{ is friction angle in bond area} \end{array} \right) \tag{15.7}$$

$$S_{CR} = \frac{C \cos(\lambda)}{1 - \sin(\lambda)} \frac{n+e}{n} \quad \text{at} \quad \theta = \frac{1}{2} \arctan \left(-\frac{1}{\tan(\lambda)} \right) + \frac{\pi}{2} \tag{15.8}$$

The strength of concrete can be found approximately as shown in (15.9) using the simple E^{EFF} -method with $n = E_P/E_{\text{HCP}}$.

$$S_{CR} = \frac{C \cos(\lambda)}{1 - \sin(\lambda)} \frac{n_{\text{EFF}} + e_{\text{EFF}}}{n_{\text{EFF}}} \quad \text{with} \quad \left(\begin{array}{l} n_{\text{EFF}} = n(1 + \phi_{\text{HCP}}) \\ e_{\text{EFF}} = e(c, n_{\text{EFF}}) \end{array} \right) \tag{15.9}$$

Some results of strength prediction by (15.9) are presented in Fig. 15.6. A concrete is considered made with $W/C = 0.4$ and a total aggregate concentration of $c = 0.7$. The aggregate stiffness is $E_P = 70000$ MPa. Age at loading is $t_0 = 28$ days. A creep factor of $\phi^* = 1.4$ is assumed (Table 14.6). Bond failure is controlled by Coulomb parameters $C = 30$ MPa and $\lambda = 30^\circ$ (producing $\theta = 60^\circ$).

It is noticed that the concrete considered has a threshold strength of approximately 70%. Sustained loads lower than this threshold strength will never cause failure. Rüschi made a similar conclusion in his classical experimental work on creep-rupture in concrete [171, 172].

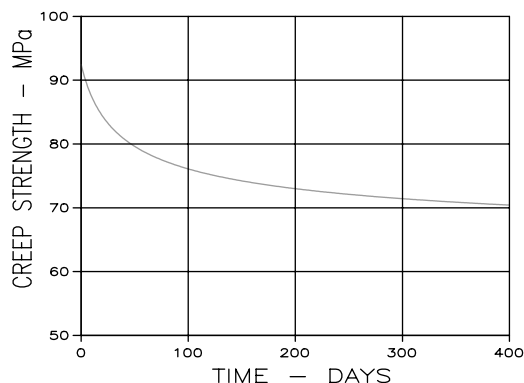


Fig. 15.6. Creep strength of concrete. Bond shear failure between coarse aggregate and mortar

15.2.4 Young Concrete

It is recalled that the creep parameter presented in Table 14.6 for cement pastes applies for ages $> \approx 3$ weeks. This time limit of validity applies of course also for the concrete results presented in Sect. 15.2.3.

When Young's modulus of the material considered changes significantly with time the method of introducing modified time cannot be used. More refined models have to be used which reflect the general effect of aging on all sub-elements in the materials stress-strain relation, for example on any materials parameter p and q appearing in the differential viscoelastic description presented in (14.1). A general constitutive model of this kind has recently been developed by the author in [124] which applies for concretes (including HCP) of any composition (water/cement and aggregate/cement ratios), any curing conditions, and for any age of loading greater than about half a day.

The results of a general composite analysis of concrete (creep, relaxation, and eigenstrain/eigenstress/prestress phenomenon) are not presented in this book. They can, however, be studied in [173, 174]. Quite recently [125] the general theory has been adapted for fast FEM analysis of concrete structures.

15.2.5 Influence of Geometry on Viscoelastic Composite Behavior

Particulate Composite versus Grid Reinforced Composite

Two viscoelastic composites are considered. They are identical except for geometry. One composite is a particle reinforced material like cement concrete. The other composite is a regular framework reinforced material like the CROSS-material previously defined. The geometries are quantified as follows,

Composite A: DC-DC (*TROC*) with $(\mu_P^0, \mu_S^0, c_P) = (1, -1, 3.33), c = 0.5$

Composite B: CC-CC (*CROSS*) with $(\mu_P^0, \mu_S^0, c_P) = (0.75, 0.15, 1.25), c = 0.5$

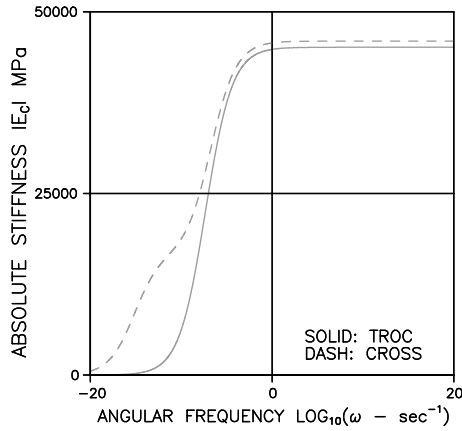


Fig. 15.7. Influence of phase geometry on absolute stiffness of composites described in the text. Accurate analysis

Both phases are Power Law viscoelastic with the following parameters,

Phase S: $E_S = 30000$ MPa, $\tau_S = 15$ days, $b = 0.3$

Phase P: $E_P = 70000$ MPa, $\tau_P = 10^{10}$ days, $b = 0.3$

The complex stiffness of the composites just defined is calculated as shown in Table 15.1. The resulting absolute stiffness and loss-angle (see (14.10)) are shown in Figs. 15.7 and 15.8. Quantities at the very high and at the very low frequencies are of rather academic interest. In the present context, however, they are needed in order to get a complete picture of the phenomena considered.

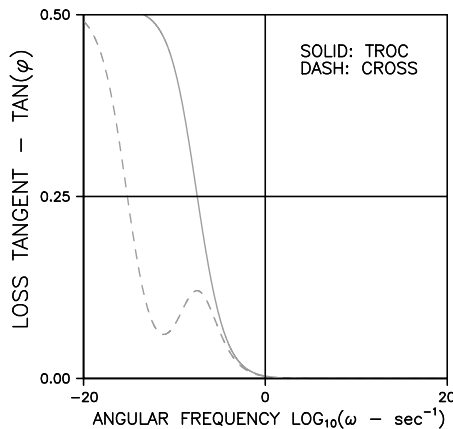


Fig. 15.8. Influence of phase geometry on loss-tangents of composites described in the text. Accurate analysis

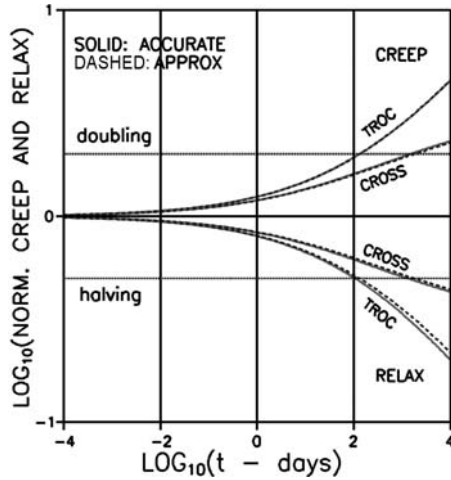


Fig. 15.9. Influence of phase geometry on creep and relaxation for composites defined in text

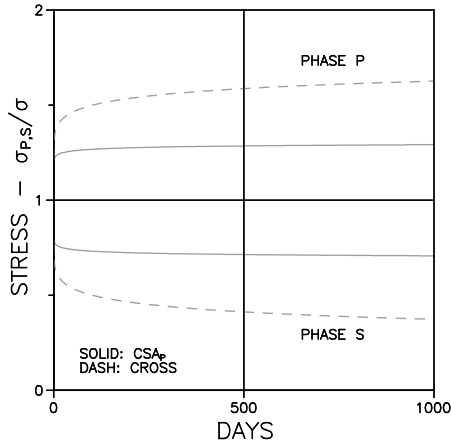


Fig. 15.10. Influence of phase geometry on internal creep stresses in composites described in text

Creep and relaxation of the composite are calculated as shown in Table 15.1 from the composite complex Young's moduli just determined in Figs. 15.7 and 15.8. Solid lines in Fig. 15.9 present the results. The results shown by dotted lines are calculated by the approximate E^{EFF} -method explained in Sect. 15.1.2 with elastic solutions from Table 10.3. As expected from Sect. 15.1.2, accurate data and approximate data almost coincide because both creep powers involved are $b < \approx 0.3$.

When the two composites considered are subjected to a constant external load, internal stresses develop as shown in Fig. 15.10. The stress state has

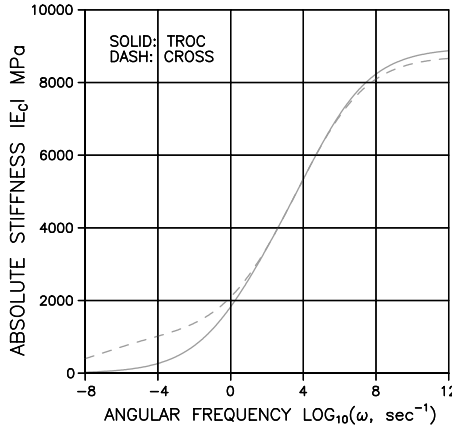


Fig. 15.11. $(E_P, E_S) = (5000, 15000)$ MPa. $(\tau_P, \tau_S) = (100, 10^{-10})$ days. $b_P = b_S = 1/4$. $c = 0.5$

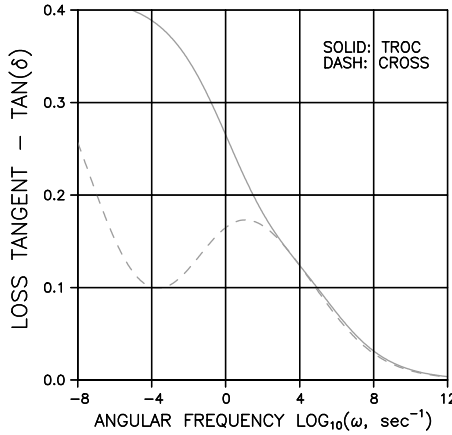


Fig. 15.12. $(E_P, E_S) = (5000, 15000)$ MPa. $(\tau_P, \tau_S) = (100, 10^{-10})$ days. $b_P = b_S = 1/4$. $c = 0.5$

been determined using the approximate method. As both $b < \approx 0.3$ we may expect stresses to be fairly well predicted in this way.

Other examples on composite viscoelastic behavior as influenced by TROC and CROSS-geometries are illustrated in Figs. 15.11 and 15.12. Again, the two composites considered only differ by their internal geometries.

Two Particulate Composites with Different Particle Shapes

Two particulate composites like asphalt concretes are considered with the following geometrical properties and Power Law viscoelastic phase properties.

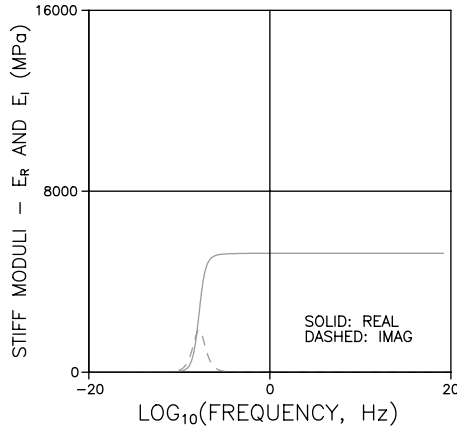


Fig. 15.13. Complex Young's modulus of asphalt concrete with spherical aggregates

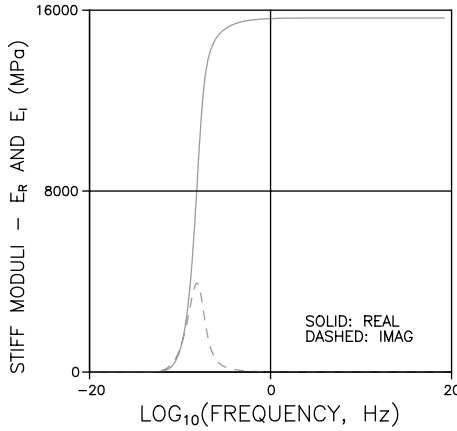


Fig. 15.14. Complex Young's modulus of asphalt concrete with very thin disc shaped aggregates

Composite A: DC-DC (spheres) with $(\mu_P^0, \mu_S^0, c_P) = (1, -1, \infty)$, $c = 0.7$
 Composite B: DC-DC (discs, $A = 0.0035$) with $(\mu_P^0, \mu_S^0, c_P) = (0.01, -0.01, \infty)$,
 $c = 0.7$
 Phase S: $E_S = 1000$ MPa, $\tau_S = 100$ days, $b = 0.8$
 Phase P: $E_P = 70000$ MPa, $\tau_P = 10^4$ days, $b = 0.25$

The complex stiffness of the composites just defined is calculated as suggested in Table 15.1. The resulting real stiffness and imaginary stiffness are presented in Figs. 15.13 and 15.14.

Subsequently the creep and relaxation functions of the composites are calculated. Table 15.1 is used again, now with the composite complex Young's moduli just determined as in-pu t data. The results are presented with solid

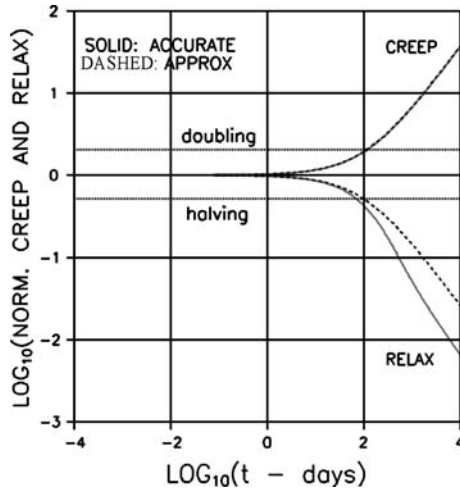


Fig. 15.15. Asphalt concrete with spherical aggregates

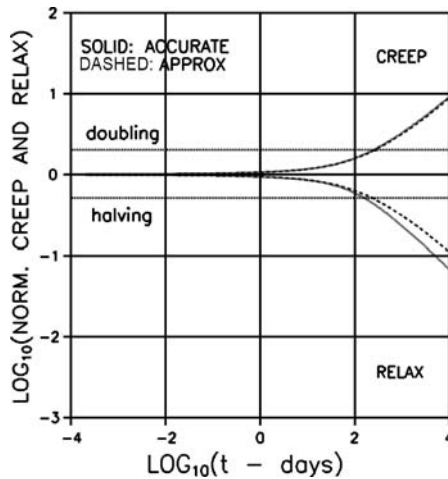


Fig. 15.16. Asphalt concrete with very thin disc shaped aggregates

lines in Figs. 15.15 and 15.16. The results shown by dotted lines are calculated by the approximate E^{EFF} -method explained in Sect. 15.1.2 with elastic solutions presented in Table 10.3. As expected, these results cannot in general be considered very reliable as both creep powers b involved are not $< 1/3$.

15.2.6 Monomer Impregnated HCP and Porous Glass

Experiments on monomer-impregnated HCP and porous glass are reported by Hastrup in [175]. Specific properties considered are composite viscoelasticity

versus degree of impregnation (β = volume of impregnant/accessible pore volume). The results of Hastrup's are shown in Figs. 15.17–15.20.

Detailed Materials Description

A more detailed description of the materials used is the following: The impregnant is in situ polymerized methylmethacrylate monomer. The porous glass considered is porous fused silica glass¹ (porosity $c = 33\%$, accessible for both water and impregnant). The HCP considered is made with $W/C = 0.4$ (degree of hydration ≈ 0.75 , porosity is $c = 36\%$ and $c = 30\%$ accessible for water and impregnant respectively).

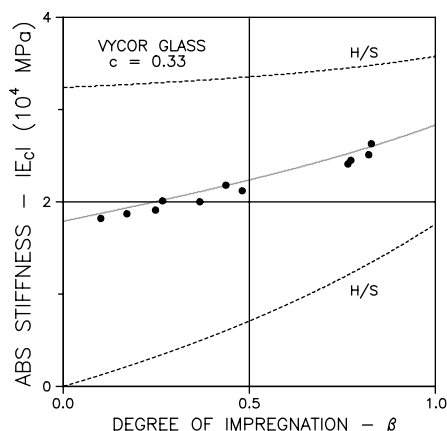


Fig. 15.17. Absolute Young's modulus of impregnated porous glass

The material properties presented below are from [175] except for the HCP data with respect to porosity and Young's modulus of the solid phase (E_S). These data are reproduced from a composite analysis made in [164] of the original HCP data respecting that porosity must relate to voids accessible for the impregnant.

Glass: $E_S = 64300$ MPa, loss $\tan(\delta_S) = 0.06\%$

HCP (solid): $E_S = 57000$ MPa, loss $\tan(\delta_S) = 0.27\%$

Monomer: $E_P = 4700$ MPa, loss $\tan(\delta_P) = 6.16\%$

The geo-parameters (μ_P^0, c_P) are determined from the "porous data" using the regression method explained in Sect. 10.3.5. Open (impregnable) pore systems are assumed with $\mu_S^0 = 0$.

Porous glass: CC-CC with $(\mu_P^0, \mu_S^0, c_P) = (0.35, 0, 1), c = 0.33$

HCP: CC-CC with $(\mu_P^0, \mu_S^0, c_P) = (0.50, 0, 1), c = 0.30$

¹ Vycor, Corning Glass Works, Corning, NY

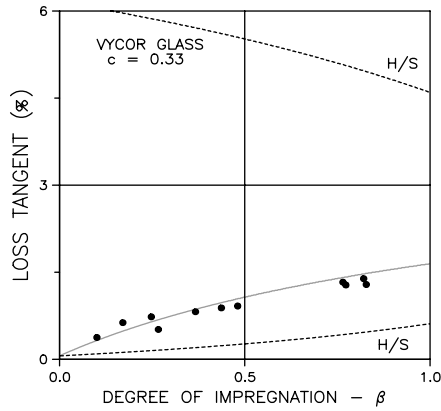


Fig. 15.18. Loss tangent of impregnated porous glass

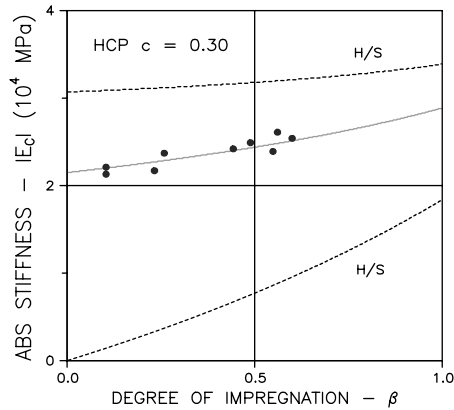


Fig. 15.19. Absolute Young's modulus of impregnated Hardened cement paste

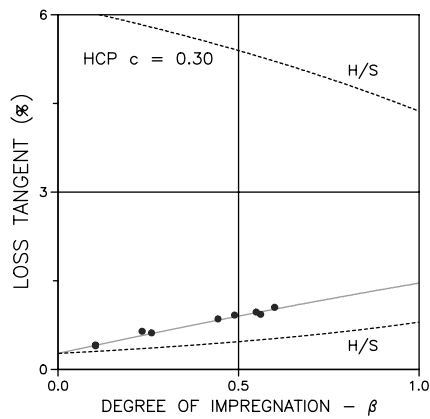


Fig. 15.20. Loss tangent of impregnated Hardened Portland cement paste

Composite Analysis

It is now demonstrated that the results of Hastrup's can be explained by the theories developed in this book – more specifically by the “Complex Young's modulus” expression in Table 15.1.

First, however, we have to re-organize Hastrup's stiffness and loss data for phases P and S in a way he does not present them, namely by their complex stiffness moduli, E_{PC} and E_{SC} . We do so by anticipating that both phases are Power law viscoelastic² – and then re-writing (14.13) to obtain (15.10) with Power law creep powers (b) to be determined by calibration with experimental data (it is worthwhile noticing that relaxation times (τ) do not appear in (15.10)). The degree of impregnation, β , is considered in (15.10) by the efficiency factor $\beta/(2 - \beta)$ reproduced from Sect. 10.4.1.

$$\begin{aligned}
 E_{PC} &= E_P \frac{1 + Y_P \cos(b_P \pi/2) + i Y_P \sin(b_P \pi/2)}{1 + Y_P^2 + 2 Y_P \cos(b_P \pi/2)} \frac{\beta}{2 - \beta} \\
 E_{SC} &= E_S \frac{1 + Y_S \cos(b_S \pi/2) + i Y_S \sin(b_S \pi/2)}{1 + Y_S^2 + 2 Y_S \cos(b_S \pi/2)} \quad \text{with} \\
 Y_P &= \frac{\tan \delta_P}{\sin(b_P \pi/2) - \cos(b_P \pi/2) \tan \delta_P} \quad \text{and} \\
 Y_S &= \frac{\tan \delta_S}{\sin(b_S \pi/2) - \cos(b_S \pi/2) \tan \delta_S}
 \end{aligned} \tag{15.10}$$

Results and Discussion

The solid lines shown in Figs. 15.17–15.20 are data predicted by $E_C = E(E_{PC}, E_{SC})$ as explained in Table 15.1 (with absolute stiffness and loss tangent calculated by (14.10)). A very satisfactory agreement is demonstrated between experiments and the theory developed in this book. This means that the assumption of phase P and phase S behaving as Power Law viscoelastic materials is justified. For both matrix phases (S) the calibrated creep power is $b_S = 0.25$. The calibrated creep power, $b_P = 1$, indicates that the impregnant behaves like a Maxwell material.

15.2.7 Damping of Wood

A study on the damping properties of wood has been reported by the author in [176]. One purpose of this study was to explain the “curious” damping results from bending vibration experiments on Hoop Pine, reported by Pentoney [177] and shown by dashed lines³ in Fig. 15.21. It is shown in [176] that Pentoney's data can only be explained by modifying our concept of wood from being a homogeneous material to being a composite material.

² The relevance of this assumption is justified when looking at the final, overall results of the analysis.

³ Right graph: Average of 6 domestic woods. Left upper graph: Compression wood. Left lower graph: Normal wood.

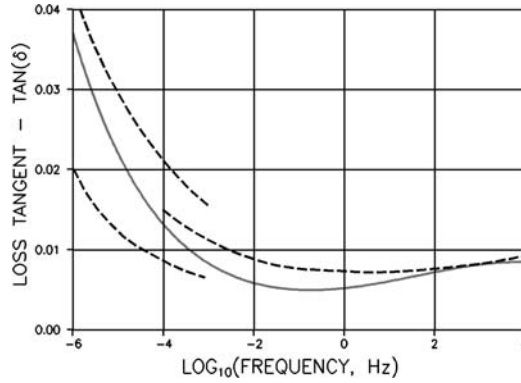


Fig. 15.21. Damping of Hoop Pine wood in bending parallel to grain

The following very plausible materials model was suggested in [176]: Wood is a composite made of very long parallel fibers (P) in an isotropic matrix (S, Lignin mainly). Both components exhibit simple Power-law viscoelastic behavior. The theoretical results shown in Fig. 15.21 with a solid line are obtained by the theory presented in this book with $c = 0.9$, $(E_P, E_S) = (16000, 16000)$ MPa, $(b_P, b_S) = (0.25, 0.2)$, and $(\tau_P, \tau_S) = (10^4, 10^{-10})$ days. A geo-function of $\theta \equiv \infty$ is applied as suggested in Sect. 5.3.3 for equal-strain analysis of plane-isotropic composites.

The damping of wood is normally determined from assuming that this material is homogeneous with a Power Law creep function as it is measured in static tests ($f < \text{approx } 0.005$ Hz). With such information, a loss behavior can be calculated as shown in Fig. 15.22, see [140].

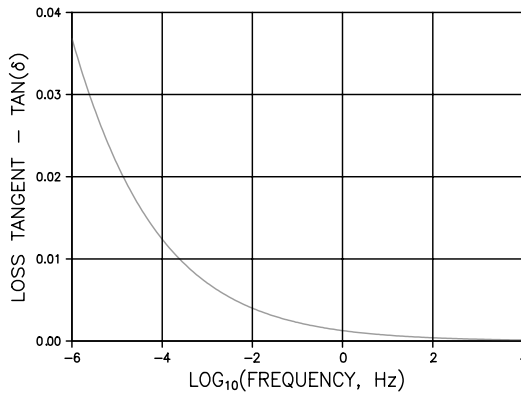


Fig. 15.22. Damping of “normal” wood in bending parallel to grain. $(E, \tau, b) = (16000 \text{ MPa}, 10^4 \text{ days}, 0.25)$

Conclusion

It can be concluded from Figs. 15.21 and 15.22 that the normal concept of wood being a homogeneous material holds for most engineering practice. For high frequency loadings, however, we must accept wood to be a composite material.

The example considered demonstrates how vibration experiments may change the traditional modeling of a material from being a homogeneous material to being a micro-composite. In this context we re-call from Sects. 14.1.2 and 15.1.1 the great potentials offered by modern experimental vibration analysis.

15.3 Discussion

It has been demonstrated in this chapter how the influence of geometry on the behavior of viscoelastic composites can be determined by relatively simple mathematical means. The power of Table 15.1 to predict composite creep and relaxation from known elastic composite behavior should be emphasized.

The significance of knowing the complex stiffness of a composite is of special interest in this context. Complex stiffness can be determined theoretically by knowing the geometry of the composite considered – or it can be determined experimentally (without knowing the geometry, as shown by the author in [141]). This means that further research on geometry versus composite behavior can benefit very much from refining the experimental and mathematical techniques used in modern experimental vibration analysis [143].

Final Remarks

We re-call from the introductory chapter, “Overview”: The subject dealt with in this book is the mechanical and physical behavior of composites as influenced by composite geometry. This subject has a high priority in the general study of composite materials. A better understanding of the behavior of natural composites, improvement of such materials, and design of new materials with prescribed properties are just three examples in modern materials research where more knowledge on geometry versus materials property is absolutely necessary.

The author’s contribution to the research on composite geometry versus composite properties has been presented in this book. The theory developed is tested/justified against a number of numerical data obtained from experiments and finite element analysis within areas such as elastic-, viscoelastic-, and conductivity behavior of composites, including associated internal strain/stress states. The theory has also been tested against exact composite solutions known from the literature.

Methods¹ are presented by which the properties of composite materials can be predicted from knowing the mechanical/physical properties and geometries of the constituent composite elements.

Basically, the theory presented is the joint result of the following three-step analysis (1–3). The additional steps (4–5) are “spin-off” results while the latter step (6) is an auxiliary composite analysis.

1. Various composite geometries are classified – and shape functions are developed to quantify these geometries.
2. Global solutions (master solutions) to property problems are developed which are valid for any composite geometry.

¹ For most practice these methods are formulated to become the basis of an efficient software package “COM-APPL”, which can be downloaded from <http://www.mat-mek.dk>.

3. Local solutions are presented, combining global solutions with specific shape functions.
4. A “test method” is presented with respect to quality control of prediction methods suggested in the field of composite materials. Methods especially examined are the so-called SCS-methods (Self Consistent Scheme).
5. A materials design procedure is suggested by which prescribed material properties can be related to composite geometry.
6. To test some basic influence of particle shapes on the stiffness and conductivity of particulate composites a generalized SCS-analysis has been developed (in Appendix C). It works with mixtures of ellipsoidal particles of arbitrary shapes.

A

Elasticity

A.1 Isotropy

Stiffness of an isotropic elastic material is defined by the bulk modulus K and the shear modulus G . Young's modulus E , and the Poisson's ratio (ν) together with two v -parameters (κ and γ) are related to K and G as follows.

$$\begin{aligned} E &= \frac{9KG}{3K+G} ; \quad \nu = \frac{3K-2G}{2(3K+G)} \\ G &= \frac{E}{2(1+\nu)} ; \quad K = \frac{E}{3(1-2\nu)} \\ \kappa &= \frac{2(1-2\nu)}{1+\nu} ; \quad \gamma = \frac{7-5\nu}{2(4-5\nu)} \end{aligned} \tag{A.1}$$

A.1.1 Composite Aspects

In composite theory it is very often appropriate to relate composite elastic moduli (K, G, E, ν) to elastic moduli (K_S, G_S, E_S, ν_S) of an isotropic reference material S . Dimensionless versions of E and ν are then presented as follows with $k = K/K_S$, $g = G/G_S$, and $e = E/E_S$

$$e = \frac{3kg}{2(1+\nu_S)k + (1-2\nu_S)g} ; \quad \nu = \frac{(1+\nu_S)k - (1-2\nu_S)g}{2(1+\nu_S)k + (1-2\nu_S)g} \tag{A.2}$$

A.1.2 Stress-Strain

The stress tensor σ_{ij} and the strain tensor ε_{ij} are related as follows (e.g. [52]) when an isotropic elastic material is considered with stiffness properties from (A.1).

$$\varepsilon_{ij} = \frac{1+\nu}{E} \left(\sigma_{ij} - \delta_{ij} \frac{\nu}{1+\nu} \sigma_{kk} \right) \quad i, j = 1, 2, 3$$

$$\sigma_{ij} = \frac{E}{1+\nu} \left(\varepsilon_{ij} + \delta_{ij} \frac{\nu}{1-2\nu} \varepsilon_{kk} \right) \quad (\text{A.3})$$

with Kroneckers delta $\delta_{ij} = \begin{cases} 1 & \text{if } i = j \\ 0 & \text{if } i \neq j \end{cases}$

Volumetric stress and strain are denoted by $\sigma_{kk} = \sigma_{11} + \sigma_{22} + \sigma_{33}$ and $\varepsilon_{kk} = \varepsilon_{11} + \varepsilon_{22} + \varepsilon_{33}$ respectively. The stress strain relation can also be written as follows in two expressions – one relating volumetric strain to volumetric stress – and another one relating deviatoric strain (e_{ij}) to deviatoric stress (s_{ij}).

$$\varepsilon_{kk} = \frac{\sigma_{kk}}{3K} \quad \text{with} \quad \begin{cases} \varepsilon_{kk} = \varepsilon_{11} + \varepsilon_{22} + \varepsilon_{33} & \text{volumetric strain} \\ \sigma_{kk} = \sigma_{11} + \sigma_{22} + \sigma_{33} & \text{volumetric stress} \end{cases} \quad (\text{A.4})$$

$$e_{ij} = \frac{s_{ij}}{2G} \quad \text{with} \quad \begin{cases} e_{ij} = \varepsilon_{ij} - \delta_{ij} \varepsilon_{kk}/3 & \text{deviatoric strain} \\ s_{ij} = \sigma_{ij} - \delta_{ij} \sigma_{kk}/3 & \text{deviatoric stress} \end{cases}$$

A.2 Cubic Elasticity

In intermediate, but important, sections of this book cubically elastic materials are referred to. It is therefore of relevance to define such materials – and to discuss how their elastic parameters relate to isotropic materials.

Stiffness of a cubic elastic material is defined by the cubic bulk modulus K_C , the cubic shear modulus G_C , and the cubic Young's modulus E_C or the cubic Poisson's ratio ν_C . The constitutive equation of a cubical elastic material can be expressed as shown in (A.5) using the coordinate system defined in Fig. A.1 with stress-strain planes coinciding with planes of elastic symmetry (and materials symmetry).

A FEM-analysis has been made in [70] on some cubic material models. The stiffness parameters for these materials were determined performing the two “FEM-experiments” outlined in (A.6) and (A.7). The cubic Young's modulus, the cubic Poisson's ratio, and the cubic bulk modulus are obtained from the “axial experiment” explained in (A.6). The cubic shear modulus is obtained from the “shear experiment” explained in (A.7).

$$\begin{bmatrix} \varepsilon_x \\ \varepsilon_y \\ \varepsilon_z \\ \varepsilon_{xy} \\ \varepsilon_{xz} \\ \varepsilon_{yz} \end{bmatrix} = \begin{bmatrix} 1/E_C & -\nu_C/E_C & -\nu_C/E_C & 0 & 0 & 0 \\ -\nu_C/E_C & 1/E_C & -\nu_C/E_C & 0 & 0 & 0 \\ -\nu_C/E_C & -\nu_C/E_C & 1/E_C & 0 & 0 & 0 \\ 0 & 0 & 0 & 1/2G_C & 0 & 0 \\ 0 & 0 & 0 & 0 & 1/2G_C & 0 \\ 0 & 0 & 0 & 0 & 0 & 1/2G_C \end{bmatrix} * \begin{bmatrix} \sigma_x \\ \sigma_y \\ \sigma_z \\ \sigma_{xy} \\ \sigma_{xz} \\ \sigma_{yz} \end{bmatrix} \quad (\text{A.5})$$

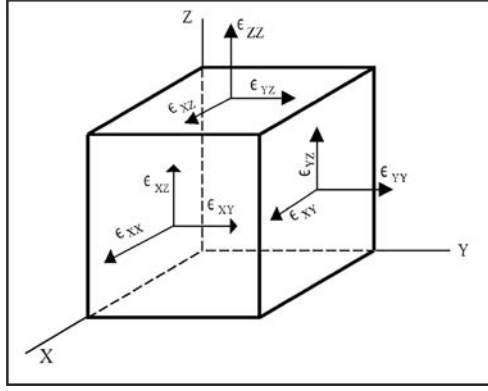


Fig. A.1. Coordinate system used in FEM-analysis

Conditions : $\varepsilon_x = \varepsilon_y = \varepsilon_{xy} = \varepsilon_{xz} = \varepsilon_{yz} = 0$

Load \Rightarrow response : $\varepsilon_Z \Rightarrow \sigma_X (= \sigma_Y)$

$$\text{Results : } E_C = \frac{\sigma_z^2 - 2\sigma_x^2 + \sigma_x\sigma_z}{\varepsilon_z(\sigma_x + \sigma_z)} ; \quad \nu_C = \frac{\sigma_x}{\sigma_x + \sigma_z} \Rightarrow \quad (\text{A.6})$$

$$K_C = \frac{E_C}{3(1 - 2\nu_C)}$$

Conditions : $\varepsilon_x = \varepsilon_y = \varepsilon_z = \varepsilon_{xz} = \varepsilon_{yz} = 0$

Load \Rightarrow response : $\varepsilon_{XY} \Rightarrow \sigma_{XY}$

$$\text{Result : } G_C = \frac{\sigma_{xy}}{2\varepsilon_{xy}} \quad (\text{A.7})$$

A.2.1 Poly-Cubic Elasticity

Isotropic mixtures of parts from a cubic material behave elastically, just as an isotropic mixture of cubic crystals. Equation (A.8) expresses the exact bulk modulus for such mixtures [178].

$$K = K_C = \frac{E_C}{3(1 - 2\nu_C)} \quad (\text{A.8})$$

No corresponding exact poly-cubic shear modulus solution has yet been found. However, it has been shown [179] that the true value is bounded between two solutions derived in [180,181]. Some re-writing of these boundary values imply

$$\left(\frac{1}{G_C} + \frac{2}{5} \left(\frac{2(1 + \nu_C)}{E_C} - \frac{1}{G_C} \right) \right)^{-1} \leq G \leq G_C + \frac{2}{5} \left(\frac{E_C}{2(1 + \nu_C)} - G_C \right) \quad (\text{A.9})$$

The lower bound [181] is based on an assumption, which is tantamount to assuming that the state of stress is identical from crystal to crystal. Correspondingly the upper bound [180] assumes identical states of strain. If the

crystals were isotropic then (A.9) predicts $G = G_C$. Improved bounds for polycrystals have been given by Hashin and Shtrikman [182]. For the present work, however, the bounds in (A.9) suffice. The upper and lower bounds are sufficiently close to justify simple mean value approximations.

A.2.2 Composite Aspects

When isotropic mixtures of cubic composite elements are considered it is very often appropriate to relate composite cubic elastic moduli (K_C, G_C, E_C, ν_C) to the elastic moduli (K_S, G_S, E_S, ν_S) of an isotropic reference material S . Normalized versions of (A.8) and (A.9) with respect to phase S are presented as follows with relative coefficients of cubical elasticity $k_C = K_C/K_S$, $g_C = G_C/G_S$, and $e_C = E_C/E_S$,

$$k = k_C = e_C \frac{1 - 2\nu_S}{1 - 2\nu_C} \Rightarrow \nu_C = \frac{1}{2} \left(1 - \frac{e_C}{k_C} (1 - 2\nu_S) \right)$$

$$\left[\frac{1}{g_C} + \frac{2}{5} \left(\frac{1 + \nu_C}{1 + \nu_S} \frac{1}{e_C} - \frac{1}{g_C} \right) \right]^{-1} \leq g \leq g_C + \frac{2}{5} \left(\frac{1 + \nu_S}{1 + \nu_C} e_C - g_C \right) \quad (\text{A.10})$$

which can also be expressed as follows with ν_C introduced

$$\frac{1}{g} \leq \frac{3}{5g_C} + \frac{1}{5(1 + \nu_S)} \left(\frac{3}{e_C} - \frac{1 - 2\nu_S}{k_C} \right)$$

$$g \leq \frac{3g_C}{5} + \frac{4(1 + \nu_S)}{5} \left(\frac{3}{e_C} - \frac{1 - 2\nu_S}{k_C} \right)^{-1} \quad (\text{A.11})$$

B

Dilute Particulate Composites

The main purpose of this appendix is to show how average particle stresses in an isotropic dilute particulate composite can be evaluated numerically. The particles are cylindrical with lengths l and cross-sections $d \times d$ (aspect ratios $A = l/d$). The isotropic composite is thought to be an isotropic mixture of parts from a cubic composite with similar particles, see Fig. B.1.

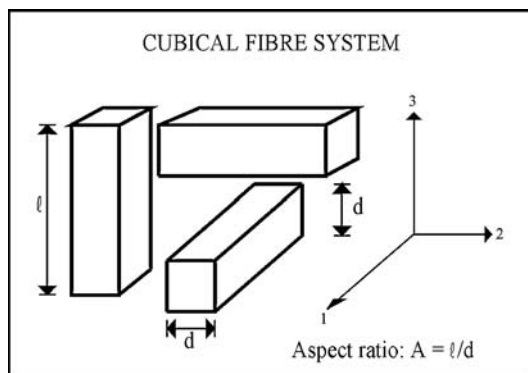


Fig. B.1. Isotropic fiber composite is an isotropic mixture of parts from this cubic model

It is emphasized that whenever cubic behavior is considered the stress coordinate system referred to is the system defined in Fig. B.2 where coordinate planes coincide with planes of elastic symmetry.

B.1 Cubic Stiffness, Shape Parameters, and Stress

The composite stiffness expressions presented in Sect. 3.1 can be written as follows applying for the dilute cubic composite just described in Fig. B.1.

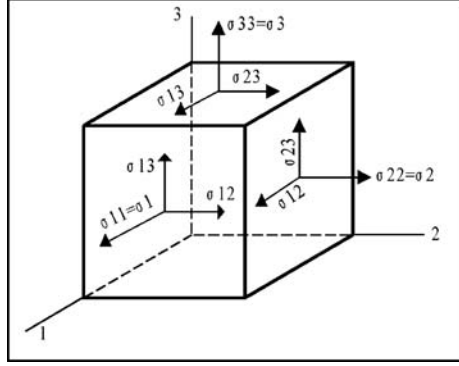


Fig. B.2. Coordinate system with coordinate planes coinciding with planes of elastic symmetry

$$\begin{aligned}
 \frac{1}{k^C} &= 1 + \left(1 + \frac{1}{p_k^C}\right) c \quad \text{with} \quad \frac{1}{p_k^C} = \frac{1 - n_k}{n_k} \frac{\sigma_{Pkk}^{0C}}{\sigma_{kk}} - 1 \\
 \frac{1}{g^C} &= 1 + \left(1 + \frac{1}{p_g^C}\right) c \quad \text{with} \quad \frac{1}{p_g^C} = \frac{1 - n_g}{n_g} \frac{s_{Pij}^{0C}}{s_{ij}} - 1 \\
 \frac{1}{e^C} &= 1 + \left(1 + \frac{1}{p_e^C}\right) c \quad \text{with} \quad \frac{1}{p_e^C} = \frac{1 - n}{n} \frac{S_{Pii}^{0C}}{\sigma_{ii}} - 1 \quad \text{with} \quad (B.1) \\
 S_{Pii}^{0C} &= \frac{1 + \nu_P - n(1 + \nu_S)}{1 - n} \sigma_{Pii}^{0C} - \frac{\nu_P - n\nu_S}{1 - n} \sigma_{Pkk}^{0C}; \quad \text{and} \\
 n &= \frac{E_P}{E_S} \quad (ii = 11, 22, 33)
 \end{aligned}$$

Cubical stiffness are denoted by $k^C = K^C/K_S$, $g^C = G^C/G_S$, and $e^C = E^C/E_S$ with superscript C denoting cubical behavior. Cubical shape coefficients are defined by p^C which can be determined numerically if the appropriate stress components are known.

B.1.1 Particle Stress

For the cubic composite defined in Fig. B.1 we can determine these stresses in the following way: The particles are thought of as orthogonal “triple” particles with very large distances between single particles. The average particle stresses for these triple particles can be determined by means of (B.2) after having solved the stress problems described in Figs. B.3, B.4, and B.5 by the Eshelby’s classical analysis [183] of the stress field at an ellipsoidal particle in an infinite homogeneous matrix.

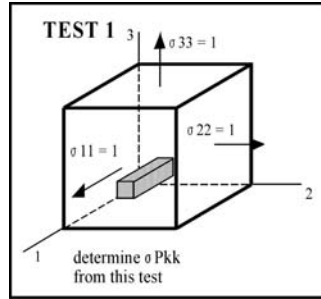


Fig. B.3. Stress analysis for cubic bulk behavior

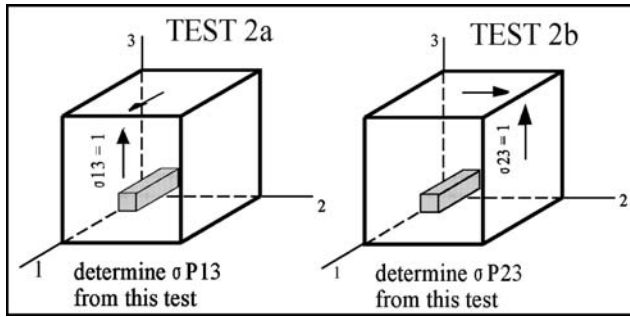


Fig. B.4. Stress analysis for cubic shear behavior

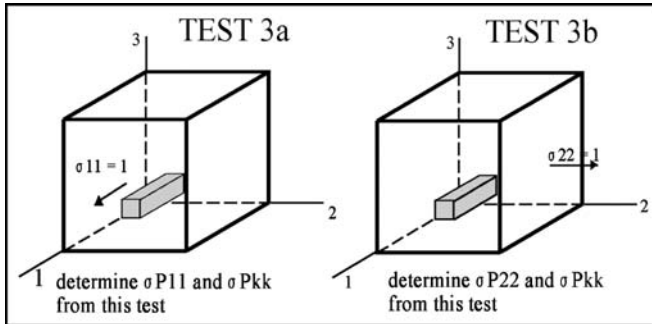


Fig. B.5. Stress analysis for cubic uni-axial behavior

Remark: The computer program developed by the author to translate the basic theoretical results of Eshelby to numerical quantities has kindly been crosschecked by Henrik Stang [184] using an algorithm developed for his own work on composite materials [14].

$$\begin{aligned}
\frac{\sigma_{Pkk}^{0C}}{\sigma_{kk}} &= \frac{\sigma_{Pkk}^0}{\sigma_{kk}} && \text{from TEST I (bulk)} \\
\frac{s_{Pij}^{0C}}{s_{ij}} &= \frac{1}{3} \left(2 \frac{\sigma_{P13}^0}{\sigma_{13}} + \sigma_P \frac{\sigma_{P23}^0}{\sigma_{23}} \right) && \text{from TEST II (shear)} \\
\frac{S_{Pii}^{0C}}{\sigma_{ii}} &= \frac{1}{3} \left(\frac{S_{P11}^0}{\sigma_{11}} + 2 \frac{S_{P22}^0}{\sigma_{22}} \right) && \text{from TEST III (Young) } (ii = 11, 22, 33)
\end{aligned} \tag{B.2}$$

Now, cubic stiffness can be determined by (B.1) calculating the cubic shape coefficients, p_k^C , p_g^C , and p_e^C as indicated with stress components calculated from (B.2).

B.1.2 Isotropic Stiffness, Shape Coefficients, and Stress

The isotropic counterpart to (B.1) is

$$\frac{1}{k} = 1 + \left(1 + \frac{1}{p_k} \right) c; \quad \frac{1}{g} = 1 + \left(1 + \frac{1}{p_g} \right) c \tag{B.3}$$

where the isotropic shape coefficients, p_k and p_g , are related to their cubic counterparts presented in (B.4). This expression is obtained from the poly-cubic (isotropic) stiffness bound solutions presented in (A.10) and (A.11) (Appendix A) introducing cubic stiffness from (B.1) and observing that the g -bounds for dilute poly-cubic materials coincide. This observation means that (B.4) and (B.3) are exact.

$$\frac{1}{p_k} = \frac{1}{p_k^C}; \quad \frac{1}{p_g} = \frac{3}{5p_g^C} + \frac{1}{5(1 + \nu_S)} \left(\frac{3}{p_e^C} - \frac{1 - 2\nu_S}{p_k^C} \right) \tag{B.4}$$

B.1.3 Particle Stress

By means of (3.8) accurate particle stresses in isotropic dilute composites can now be derived from (B.3) as shown in (B.5).

$$\begin{aligned}
\frac{\sigma_{Pkk}^0}{\sigma_{kk}} &= \left(1 + \frac{1}{p_k} \right) \frac{n_k}{1 - n_k} = f_k(E_P, E_S, \nu_P, \nu_S) \\
\frac{s_{Pij}^0}{s_{ij}} &= \left(1 + \frac{1}{p_g} \right) \frac{n_g}{1 - n_g} = f_g(E_P, E_S, \nu_P, \nu_S)
\end{aligned} \tag{B.5}$$

Remark: We emphasize that the stress functions, f , in (B.5) and anywhere in this book implicitly also carry the argument A (aspect ratio) – including the stress functions of Goodier's in (3.9) where $A = 1$ (sphere).

C

SCS-Analysis

C.1 Stiffness

As previously mentioned in Chap. 3, exact composite stiffness can be predicted by (3.6) if exact stress solutions are known (at any concentration c) for one of the constituent phases. Stiffness estimates, however, can be made on considerably less stress information using the so-called Self Consistency Scheme (SCS) introduced in Sect. 3.3: The stress of a phase P element at any concentration in a composite can be estimated from the low concentration stress solution ($c = 0$) for phase P replacing the properties of phase S in that solution with the isotropic properties of the composite. This statement is formalized in (C.1) with stress functions, f_k and f_g . In the present study these functions, are as determined numerically for ellipsoidal particles in (B.5).

$$\begin{array}{cc}
 \text{Single particle } c \gg 1 & \text{SCS - estimates: } c \text{ in general} \\
 \left. \begin{array}{l} \frac{\sigma_{Pkk}^0}{\sigma_{kk}} = f_k = f_k(E_P, E_S, \nu_P, \nu_S) \\ \frac{s_{Pij}^0}{s_{ij}} = f_g = f_g(E_P, E_S, \nu_P, \nu_S) \end{array} \right\} \Rightarrow \left(\begin{array}{l} \frac{\sigma_{Pkk}}{\sigma_{kk}} = f_k(E_P, E, \nu_P, \nu) \\ \frac{s_{Pij}}{s_{ij}} = f_g(E_P, E, \nu_P, \nu) \end{array} \right) \quad (C.1)
 \end{array}$$

With known stress functions, composite stiffness is now predicted implicitly by (3.6) introducing the SCS-estimates of phase P stresses. The results of this procedure are summarized in (C.2). The two stiffness expressions are coupled by the third expression shown, relating stiffness to Poisson's ratio. Relations between elastic moduli are reproduced from (A.1) in Appendix A.

$$\begin{aligned}
 Y_k &= \frac{K_P}{K} - \frac{K_P}{K_S} + c \left(\frac{K_P}{K_S} - 1 \right) f_k(E_P, E, \nu_P, \nu) = 0; \quad E = 3K(1 - 2\nu) \\
 Y_g &= \frac{G_P}{G} - \frac{G_P}{G_S} + c \left(\frac{G_P}{G_S} - 1 \right) f_g(E_P, E, \nu_P, \nu) = 0; \quad E = 2G(1 + \nu) \quad (C.2) \\
 \nu &= \frac{3K - 2G}{2(3K + G)}
 \end{aligned}$$

As previously mentioned in Chap. 3 the SCS method was first applied for stiffness prediction of particulate composites with spherical particles [13]. The solution could be given an analytical form because of the very simple Goodier/Dewey stress functions presented in (3.9). In the SCS-analysis presently considered various particle shapes can be considered because shape dependent stress functions are introduced from Appendix B.

In general (C.2) has to be solved numerically. With known f_k and f_g functions calculation starts at $c \approx 0$ with an estimate of the composite Poisson's ratio $\nu \approx \nu_S$. Then K and G are determined by the former two expressions in (C.2) (letting K and G grow between their limits, $K_S - K_P$ and $G_S - G_P$, respectively). Then a new Poisson's ratio is calculated from K and G , and the analysis is repeated with a better estimate of the Poisson's ratio. Calculation stops when a satisfactory agreement is obtained between estimated and calculated Poisson's ratios. Then the analysis proceeds with next volume concentration c .

It is obvious that SCS-solutions are accurate at low phase P concentrations if f_k and f_g are accurately known. The approximate nature, however, of stiffness estimates by SCS at higher phase P concentrations must be emphasized. The geometry considered in this region is somewhat self-defining. This feature is clearly observed from the subsequent section where results from a SCS-analysis are compared with experimental results.

C.1.1 Spherical Particles

It has previously been indicated that the present analysis, (C.2), reduces to become the Budiansky's analysis [13] when particulate composites with spherical particles are considered. For this particular the expressions decouple when $\nu_P = \nu_S = 0.2$, meaning that the following results can be calculated immediately.

$$e = k = g = 0.5 \left[D + \sqrt{D^2 + 4n} \right] ; \quad (\nu \equiv 0.2)$$

$$\text{with } D = (1 - n)(1 - 2c) ; \quad (n = n_k = n_g) \quad (\text{C.3})$$

Equation (C.3) (Fig. C.1) predicts zero stiffness of porous materials ($n = 0$) and infinite stiffness of stiff pore systems ($n = \infty$) for $c > 0.5$. Obviously the geometrical model of the composite considered is that of a phase symmetric DC-CD powder composite with agglomerating spherical phase P elements which create a fully continuous phase P at $c = 0.5$ dissolving phase S into discrete elements which approach spherical particles at $c = 1$. The concentration area of geometry transition is extremely narrow. Thus both critical concentrations c_P and c_S are 0.5.

The experimental stiffness shown in Fig. C.1 is from tests on porous sintered aluminum reported in [22]. Obviously the pore geometry of the material used in these tests does not comply with the pore system "described" by the Budiansky analysis. No better predictions, however, can be obtained by

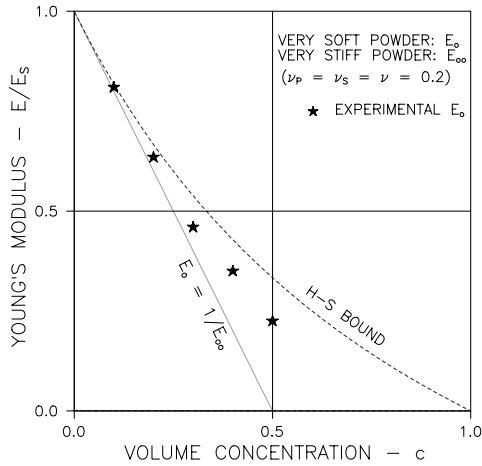


Fig. C.1. Composite with very soft and very stiff spherical powders

the SCS-method. This feature is demonstrated in the following section where the SCS-analysis is applied to particulate composites with particles of non-spherical shapes: Any shape different from spherical causes predicted stiffness of porous materials to be lower than the Budiansky solution.

C.1.2 Various Particle Shapes and Cracks

A number of results using the present SCS-analysis on materials reinforced with particles of various shapes are presented in Figs. C.2–C.5: Fibers of aspect ratios (particle length/diameter) $A > 1$, spheres with $A = 1$, and discs and plates with $A < 1$. The H/S bounds referred to are calculated from the general expressions presented in Chap. 5.

It is noticed from Figs. C.2 and C.3 that any deviation from spherical shapes of particles will increase composite stiffness from that predicted by the Budiansky solution (spheres, $A = 1$) when $n > 1$. Any deviation from spherical shapes will decrease composite stiffness from that predicted by the Budiansky solution when $n < 1$. The most efficient influence on stiffness of particle shape is observed when particles are plates and discs ($A < 1$).

It is, at the same time observed that stiffness of a composite made with very thin discs ($A \ll 1$) approaches the H/S upper bound when $n > 1$, and the H/S lower bound when $n < 1$. These observations agree with statements made in analytical studies on particulate materials (ex [14]) made with very thin discs.

Cracks: The stiffness of cracked materials can also be considered by the SCS-method presented. The results coincide perfectly with results obtained in Sect. 8.2.1 from the general composite theory developed in this book – and also with results otherwise determined in the composite literature.

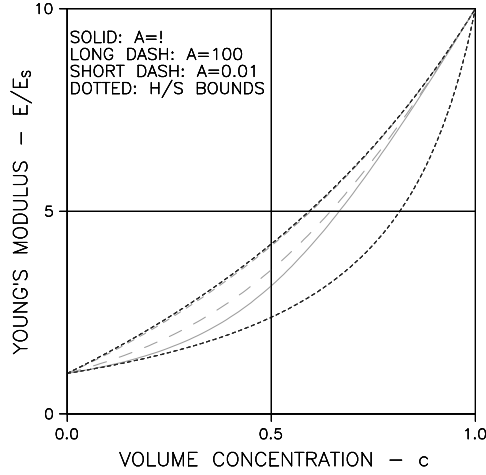


Fig. C.2. Composites with discs ($A = 0.01$), compacts ($A = 1$), and fibers ($A = 100$). $(E_P, E_S) = (10, 1)$, $(v_P = v_S = 0.2)$

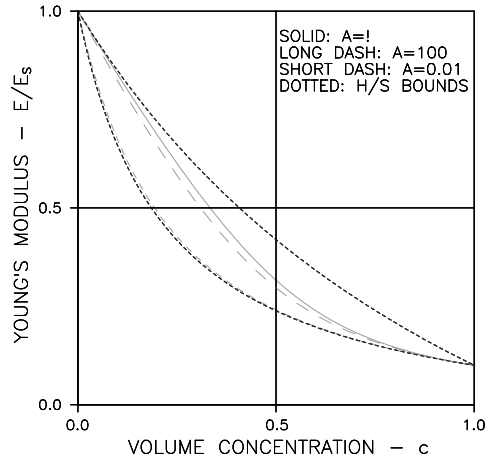


Fig. C.3. Composites with discs ($A = 0.01$), compacts ($A = 1$), and fibers ($A = 100$). $(E_P, E_S) = (0.1, 1)$, $v_P = v_S = 0.2$

C.1.3 Multi-Shaped Particles

When particulate composites are considered with multi-shaped particles (C.1) and (C.2) are used with averaged stress functions expressed as follows, see (7.10) in Sect. 7.1.1. An example of stiffness prediction for such materials is presented in Fig. C.5.

$$\langle f_k \rangle = \sum_{i=1}^{\infty} \alpha_i f_{k,i} ; \quad \langle f_g \rangle = \sum_{i=1}^{\infty} \alpha_i f_{g,i} ; \quad \sum_{i=1}^{\infty} \alpha_i = 1 \quad (\text{C.4})$$

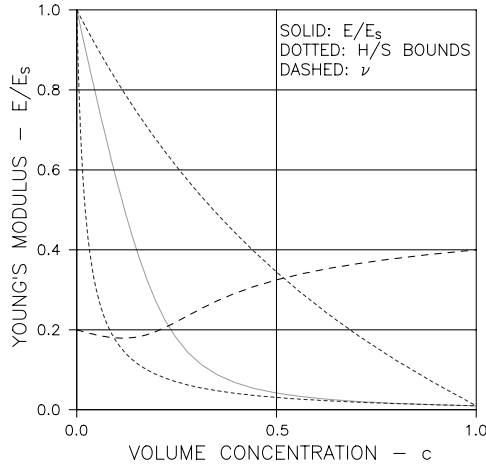


Fig. C.4. Composite with plate particles ($A = 0.1$), $(E_P, E_S) = (0.01, 1)$, $(\nu_P, \nu_S) = (0.4, 0.2)$

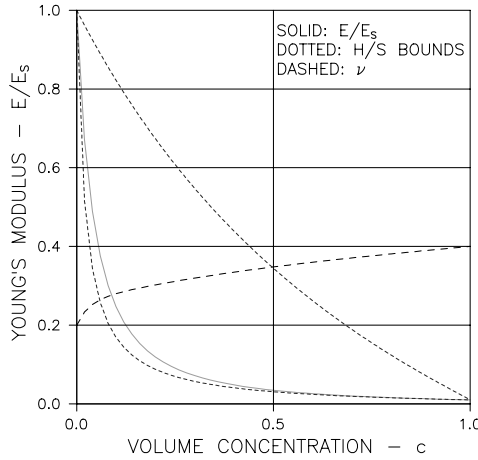


Fig. C.5. Composite as in Fig. C.4. Plate particles, however is a mixture of 50% $A = 0.1 + 50\% A = 0.001$

C.2 Other Physical Properties

Other physical properties (conductivities) such as thermal and electrical conductivities, diffusion coefficients, dielectric constants, and magnetic permeabilities can be determined from stiffness analysis by an analogy explained in Chap. 9. In the present SCS context this analogy can be formulated from (C.2) as shown in (C.5) where $Q_S, Q_P = n_Q Q_S$, and Q are the physical properties of phase S, phase P, and composite respectively. Ratio of conductivity is introduced as $n_Q = Q_P/Q_S$.

$$Y = \frac{Q_P}{Q} - \frac{Q_P}{Q_S} + c \left(\frac{Q_P}{Q_S} - 1 \right) f_k(3Q_P, 3Q, 0, 0) = 0 \quad (\text{C.5})$$

The point of departure in developing (C.5) from the analogy just mentioned is the former expression in (C.1) with $f_k = f_k(E_P, E_S, v_P, v_S) = f_k(3Q_P, 3Q_S, 0, 0)$ with $(Q_P, Q_S) = (K_P, K_S)$ and $(v_P, v_S) = (0, 0)$.

In principles, the conductivity (C.5) can be solved numerically just as the stiffness (C.2) was solved.

C.2.1 Spherical Particles

When particulate composites with spherical particles are considered, (C.5) can be used with the exact Goodier/Dewey stress functions f_k and f_g presented in (3.9). Then the following conductivity expression can be developed immediately,

$$q = \frac{1}{4} \left[B + \sqrt{B^2 + 8n_Q} \right] \quad \text{with} \quad B = 2 - 3c - n_Q(1 - 3c) \quad (\text{C.6})$$

which was first developed by Böttcher and Landauer in their analysis [47, 48] of spherical powder composites.

C.2.2 Particles of Various Shapes and Cracks

Some examples are presented in Figs. C.6–C.8 on composite conductivity determined by (C.5). The bounds shown are calculated by (9.3).

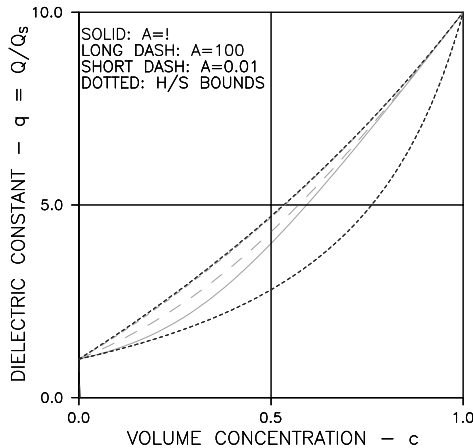


Fig. C.6. Conductivity of particulate composite with particles of various aspect ratios, $(Q_P, Q_S) = (10, 1)$

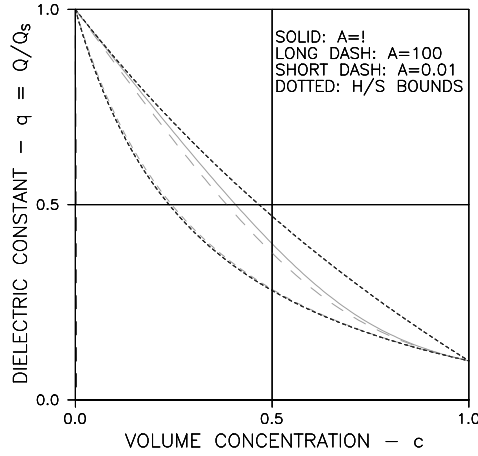


Fig. C.7. Conductivity of particulate composite with particles of various aspect ratios, $(Q_P, Q_S) = (0.1, 1)$

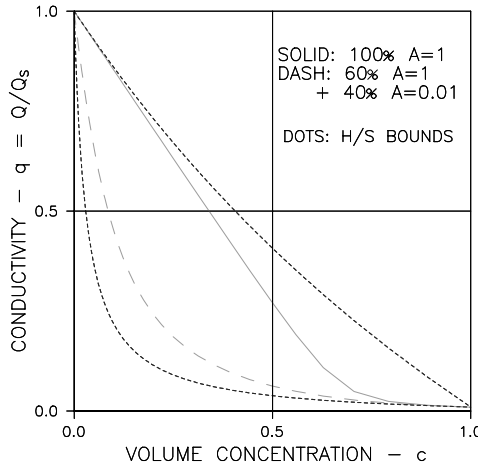


Fig. C.8. Conductivity of a composite: (1) with spheres and (2) with a mixture of spheres and discs. $(Q_P, Q_S) = (0.01, 1)$

Similar comments can be made on composite conductivities determined by SCS-analysis as were previously made on composite stiffness determined by SCS: For conductivity ratios, $n_Q > 1$, it is noticed from Fig. C.6 that any deviation from spherical shapes of particles in a particulate composite will increase composite conductivity relative to that determined for spherical particles. For conductivity ratios, $n_Q < 1$, it is noticed from Fig. C.7 that any deviation from spherical shapes will decrease composite conductivity from that determined for spherical particles.

In general, the most efficient influence on composite conductivity of particle shape is observed when particles are plates and discs ($A < 1$).

Figures C.6 and C.7 also indicate that the conductivity of a composite made with very thin discs ($A \ll 1$) approaches the H/S upper bound when $n_Q = Q_P/Q_S > 1$, and the H/S lower bound when $n_Q < 1$.

Cracks: The conductivity of cracked materials can also be considered by the SCS-method presented. The results coincide perfectly with results obtained in Sect. 9.2.3 from the general composite theory developed in this book – and also with results otherwise determined in the composite literature.

C.2.3 Multi-Shaped Particles

When particulate composites are considered with multi-shaped particles (C.5) is used with an averaged “stress function” just as in a stiffness analysis. An example is shown in Fig. C.8.

D

General Viscoelastic Models

It can be shown (e.g. [138]) that general mechanical models for viscoelastic materials can be established in two ways as illustrated in Table D.1. One general model is a Maxwell model connected in series with a chain of several Kelvin models in series. E denotes momentary stiffness, E_{REL} denotes delayed stiffness and τ denotes relaxation time. The number of Kelvin elements (N) can be finite with creep functions consequently described as shown in (D.1) – or it can be infinite in which case creep functions can be expressed as shown in Table D.1 with continuously distributed Kelvin relaxation times considered by the so-called retardation spectrum, $L = L(\tau)$.

The other general model is a Hooke model connected in parallel with a chain of several Maxwell models in parallel. E denotes momentary stiffness, E_{REL} denotes relaxed (final) stiffness and τ denotes relaxation time. The number of Maxwell elements (N) can be finite with relaxation functions consequently described as shown in (D.1) – or it can be infinite in which case relaxation functions can be expressed as shown in Table D.1 with continuously distributed Maxwell relaxation times considered by the so-called relaxation spectrum, $H = H(\tau)$.

$$\begin{aligned} C(t) &= \frac{1}{E} + \frac{t}{\eta} + \sum_{n=1}^N \frac{1}{E_n} \left(1 - \exp\left(-\frac{t}{\tau_n}\right) \right) ; \quad \text{Kelvin chain} \\ R(t) &= E_{\text{REL}} + \sum_{n=1}^N E_n \exp\left(-\frac{t}{\tau_n}\right) ; \quad \text{Maxwell chain} \end{aligned} \tag{D.1}$$

Remark: It is emphasized that the two spectra are not independent. They relate to each other as indicated by the two alternate expressions in Table D.1 for the analogy Young's modulus. It is also emphasized that the results in (D.1) can be predicted from Table D.1 with discrete rheological spectra (retardation, relaxation). Most often the analysis of complex viscoelastic materials can only be made numerically. In this context should be mentioned that useful

Table D.1. Complex viscoelastic models with spectra and analogy Young’s moduli. Reproduced from [185]

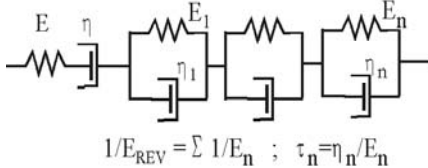
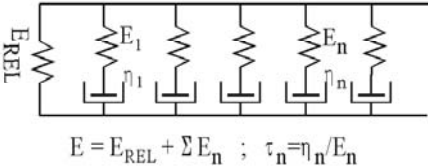
KELVIN CHAIN		MAXWELL CHAIN	
			
$1/E_{REV} = \sum 1/E_n \quad ; \quad \tau_n = \eta_n/E_n$		$E = E_{REL} + \sum E_n \quad ; \quad \tau_n = \eta_n/E_n$	
Retardation Spectrum $L(\tau)$		Relaxation Spectrum $H(\tau)$	
$L(\tau)$ with $\int_0^\infty \frac{L(\tau)}{\tau} d\tau = \frac{1}{E_{REV}}$		$H(\tau)$ with $\int_0^\infty \frac{H(\tau)}{\tau} d\tau = E - E_{REL}$	
Creep Function $C(t)$		Relaxation Function $R(t)$	
$\frac{1}{E} + \frac{t}{\eta} + \int_0^\infty \frac{L(\tau)}{\tau} \left(1 - \exp\left(-\frac{t}{\tau}\right)\right) d\tau$		$E_{REL} + \int_0^\infty \frac{H(\tau)}{\tau} \exp\left(-\frac{t}{\tau}\right) d\tau$	
Analogy Young's Modulus $E^A(s)$			
$\left[\frac{1}{E} + \frac{1}{\eta s} + \int_0^\infty \frac{L(\tau)}{\tau(1+\tau s)} d\tau\right]^{-1} =$		$= E_{REL} + \int_0^\infty \frac{sH(\tau)}{1+\tau s} d\tau$	

Table D.2. Power law creep. $Z(x) = \Gamma(1+b)(x/\tau)^b$ where Γ means gamma function. Reproduced from [140]

Power Law Creep	
Retardation Spectrum $L(\tau)$	Relaxation Spectrum $H(\tau)$
$\frac{Z(\tau) \sin(b\pi)}{\pi E}$	$\frac{E}{\pi} \frac{Z(\tau) \sin(b\pi)}{1 + Z(\tau)^2 + 2Z(\tau) \cos(b\pi)}$

information on couplings between rheological characteristics of materials can be found in [138, 140, 186, 187] for example.

The *Power Law model* introduced in Sect. 14.2.2 is a model, which can only be explained by a composition of an infinite number of elementary mechanical elements. The spectra associated are presented in Table D.2 reproduced from [140].

E

HCP and Concrete

E.1 Volume Models

At various occasions HCP and concrete are studied in this book. The volumetric models used for these materials are presented in Table E.1 that is based on the basic paste concept developed by the author in [154]. Water/cement and aggregate/cement ratios (by weights) are denoted by W/C and A/C respectively. Basic paste is that volume part of a hardening cement paste which will hydrate 100% transforming to cement gel, including gel pores.

Table E.1. Composition of concrete and HCP as related to $A/C, W/C$, and basic paste. Any volume concentration is relative to total volume of components considered. Vol-parameter is $A_i = (1 - c_i)/(1 + c_i)$ with $i = \text{cem, void}$

Concrete		
is HCP mixed with aggregates of volume concentration c	$c = \frac{38A/C}{100W/C + 38A/C + 32}$	$A = \frac{1 - c}{1 + c}$
Hardening Cement Paste (HCP)		
with $W/C > 0.38$ is basic paste mixed with voids of vol-concentration c_{VOID}	$c_{\text{VOID}} = \frac{100W/C - 38}{100W/C + 32}$	$A_{\text{VOID}} = \frac{35}{100W/C - 3}$
with $W/C \leq 0.38$ is basic paste mixed with cem-grains of vol-concentration c_{CEM}	$c_{\text{CEM}} = \frac{32 - 84W/C}{100W/C + 32}$	$A_{\text{CEM}} = \frac{23W/C}{8 + 2W/C}$

Basic paste has a constant volume. Its stiffness, however, is time dependent with $E_{\text{BAS}} = 3.2e4 * g(t)$ MPa where $g(t)$ is the absolute degree of hydration (amount of cement hydrated at time t , relative to total amount of cement).

Cement grains (subscript cem in Table E.1), which will never hydrate act as particles in basic paste. Water, which will never be used in the hydration process acts as voids (subscript void in Table E.1) in basic paste.

Densities assumed in Table E.1 are 3.1 gr/cm³ and 2.6 gr/cm³ for cement and aggregates respectively. Hydration products (gel, including gel pores) occupy a volume, 2.2 greater than the bulk volume of the cement involved in the hydration process. These specifications are consistent with the hydration studies of Powers and Brownyard [188,189].

The major advantage of using the concept of basic paste in concrete analysis is that a simple two-phase model can always model hardening cement paste.

E.2 Porosity of Hardening Cement Paste

Also the porosities of hardening cement paste are of interest in this book. The porosity expressions presented in Table E.2 are reproduced from [78] where they have been determined on the basis of the principles developed by Powers and Brownyard in [188,189] previously referred to.

The time dependent change of porosities is controlled by the absolute degree of hydration, $g(t)$ previously referred to. The description of $g(t)$ presented in Table E.2 is suggested by Freiesleben in [190] with characteristic hydration parameters τ and β . The relative degree of hydration $q(t)$ is amount of cement hydrated relative to the amount of cement which can be hydrated in capillary space available. The two hydration degrees are related as shown in the Table E.2. Porosities predicted by Table E.2 are presented in Figs. E.1–E.3.

Table E.2. Total porosity c_{TOT} and capillary porosity c_{CAP} in hardening cement paste. Absolute degree of hydration and relative degree of hydration are denoted by $g(t)$ and $q(t)$ respectively

W/C	c_{TOT}	c_{CAP}	$q(t)$
>0.38	$\frac{100W/C - 18q(t)}{100W/C + 32}$	$\frac{100W/C - 38q(t)}{100W/C + 32}$	$g(t)$
≤ 0.38	$\frac{100W/C[1 - 0.47q(t)]}{100W/C + 32}$	$\frac{100W/C[1 - q(t)]}{100W/C + 32}$	$\min \left[\frac{0.38}{W/C} g(t), 1 \right]$
HCP coheres only if $q \geq \max(0.5W/C, 0.19)$			
$g(t) = \exp[-(\tau/t)^\beta]$ absolute degree of hydration			

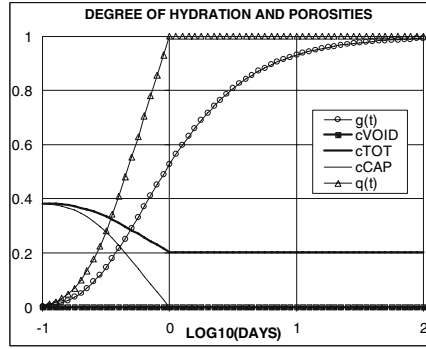


Fig. E.1. $W/C = 0.2$. $\tau = 0.625$ days. $\beta = 0.95$

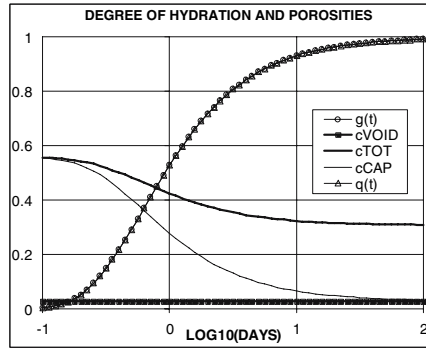


Fig. E.2. $W/C = 0.4$. $\tau = 0.625$ days. $\beta = 0.95$, $g(t)$ and $q(t)$ coincide

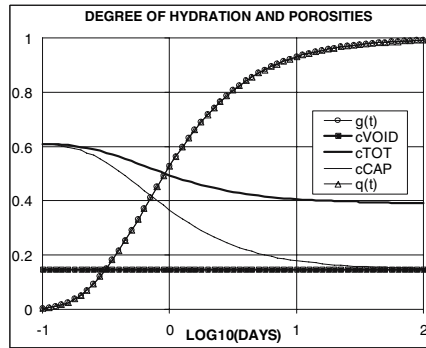


Fig. E.3. $W/C = 0.5$. $\tau = 0.625$ days. $\beta = 0.95$, $g(t)$ and $q(t)$ coincide

Notations

The notations most frequently used in this book are listed below. A few symbols have been allowed to have two meanings – only, however, where the proper meaning is obvious from the text associated. The list does not include local symbols used only in intermediate results.

	Sub/superscripts
P, S	Phase P and phase S respectively
no sub/superscript	Composite material
k, g	Bulk- and deviatoric behavior respectively
$(\text{sub})_0$	Porous material (or state of reference)
$(\text{sup})^0$	Dilute solution
∞	Very stiff inclusions
EFF	Effective quantity
EST	Estimated quantity
	Volume
V	Phase volumes
$c = V_P/(V_S + V_P)$	Volume concentration of phase P
$1 - c$	Volume concentration of phase S
$A = (1 - c)/(1 + c)$	Volume parameter
c_{PACK}	Void ratio in a packed pile of particles
	Geometry
c_P, c_S	Critical concentrations
$c_{\text{SYM}} = (c_P + c_S)/2$	Symmetry concentration
μ^0, μ^1	Shape factors
μ	Shape function
θ	Geometry function
A	Fiber aspect ratio (length/diameter)
β	Pore saturation of impregnated phase P
p	Density (number per volume unit) of voids or cracks

E	Elasticity Young's modulus
K	Bulk modulus
G	Shear modulus
ν	Poisson's ratio
$\kappa = 2(1 - 2\nu)/(1 + \nu)$	Bulk Poisson factor
$\gamma = (7 - 5\nu)/(4 - 5\nu)/2$	Shear Poisson factor
$n = E_P/E_S$	Stiffness ratio – relative stiffness Young stiffness ratio
$n_k = K_P/K_S$	Bulk stiffness ratio
$n_g = G_P/G_S$	Shear stiffness ratio
$N_k = n_k \kappa_P / \kappa_S = n_g$	Modified bulk stiffness ratio
$N_g = n_g \gamma_P / \gamma_S$	Modified shear stiffness ratio
$e = E/E_S$	Relative stiffness of composite Relative Young's modulus of composite
$k = K/K_S$	Relative bulk modulus of composite
$g = G/G_S$	Relative shear modulus of composite
Q	Conductivity Conductivity
$q = Q/Q_S$	Relative conductivity of composite
$n_Q = Q_P/Q_S$	Conductivity ratio
t	Viscoelasticity time
T	Oscillation (cyclic) time
ω	$= 2\pi/T$, angular frequency
f	$= \omega/(2\pi)$, traditional frequency, cycles/time unit
$C(t)$	Creep function
$R(t)$	Relaxation function
τ	Relaxation time
b	Creep power in Power-Law creep
ϕ, ϕ^*	Creep parameter and creep factor respectively for HCP and concrete
E_C	Complex Young's modulus
E_R	Real Young's modulus
E_I	Imaginary Young's modulus
δ	Loss angle
$\tan(\delta) = E_I/E_R$	Loss tangent
σ_{ij}	Stress/strain General stress ($i = 1, 2, 3, j = 1, 2, 3$)
σ_{kk}	Volumetric stress ($\sigma_{11} + \sigma_{22} + \sigma_{33}$)
$\sigma_{kk}/3$	Hydraulic pressure/tension
s_{ij}	Deviatoric stress

ε_{ij}	General strain
ε_{kk}	Volumetric strain
e_{ij}	Deviatoric strain
	Eigenstrain/stress
λ	Eigenstrain (linear)
ρ	Eigenstress (hydrostatic)
	Abbreviations
CSA	Composites spheres assemblage
CSA_P/CSA_S	CSA with phase P/phase S as kernel
TROC	Special particulate composite
CROSS	Special grid composite
H/S	Hashin-Shtrikman's stiffness/conductivity bounds
P/H	Paul-Hansen's stiffness bounds
W/C	Water/cement ratio by weight
HCP	Hardened cement paste

References

1. Paul, B.: "Prediction of elastic constants of multi-phase materials". Trans. of the Metallurgical Soc. of AIME, 218(1960), 36–41.
2. Hansen, T.C.: "Creep of concrete: A discussion of some fundamental problems". Bulletin no. 33(1958), Svenska Forskningsinstitutet för Cement och Betong, Tekniska Högskolan, Stockholm".
3. Hashin, Z. and Shtrikman, S.: "Variational approach to the theory of elastic behavior of multi-phase materials". J. Mech. Solids, 11(1963), 127–140.
4. Hashin, Z.: "Elastic moduli of heterogeneous materials". J. Appl. Mech., 29(1962), 143–150.
5. Hill, R.: "Elastic properties of reinforced solids: Some theoretical principles". J. Mech. Phys. Solids, 11(1963), 357–372.
6. Christoffersen, J.: "Elastic and elastic-plastic composites – a new approach, DCAMM Rep. 61(1973) (Danish Centre for Applied Mathematics and Mechanics, Tech. Univ. Denmark, Copenhagen.
7. Levin, V.M.: "Determination of effective elastic moduli of composite materials", Sov. Phys. – Dokl., 20(1975), 147.
8. G.P. Sendeckyj (ed): "Mechanics of composite materials", Vol. II in "Composite materials" (edited by Broutman, L.J. and R.H. Krock), Academic Press, New York, 1974.
9. Chow, T.S.: "The effect of particle shape on the mechanical properties of filled polymers" (review), Journ. Materials Science, Vol. 15(1980), pp. 1873–1888.
10. Halpin, J.C. and N.J. Pagano. 1970. Stiffness and Expansion Estimates for oriented and random fibrous composites. AFML-TR-69-341.
11. Mori, T. and Tanaka, K.: "Average stress in matrix and average energy of materials with misfitting inclusions", Acta Metallica, 21(1973), 571–574.
12. Benveniste, Y.: "A new approach to the application of Mori-Tanaka's theory in composite materials", Mechanics Mater., 6(1987), 147–157.
13. Budiansky, B.: "On the elastic moduli of some heterogeneous materials". J. Mech. Phys. Solids, 13(1965), 223–227.
14. Stang, Henrik: "En kompositmaterialteori og dens anvendelse til beskrivelse af træpåvirkede cementkompositter" (in danish, "A composite theory and its application to cement based composites subjected to tension"), Thesis, Institute of Structural Mechanics, Tech. Univ. Denmark, 1984.

15. Reiter, T., Dvorak, G.J., and Tvergaard, V.: "Micromechanical models for graded composite materials", *J. of the Mechanics and Physics of Solids*, 45(1997), 1281–1302.
16. Reiter, T. and Dvorak, G.J.: "Micromechanical models for graded composite materials: II. Thermomechanical loading", *J. of the Mechanics and Physics of Solids*, 46(1998), 1655–1673.
17. Hale, D.K.: "The physical properties of composite materials" (review paper), *Journ. Mat. Sc.* Vol. 11(1976), pp. 2105–2141.
18. Torquato, S.: "Effective stiffness tensor of composite media: I. Exact series expansions", *J. Mech. Phys. Solids*, 45(1997), 1421–1448.
19. *Idem*: "Effective stiffness tensor of composite media: II, Application to isotropic dispersions", *J. Mech. Phys. Solids*, 46(1998), 1411–1440.
20. Fagerlund, G.: "Samband mellan porositet och materials mekaniske egenskaper" (in swedish, "Relations between porosity and mechanical properties of materials"), *Div. Build. Technology, Tech. Univ. Lund, Sweden*, 1971.
21. Hasselman, D.P.H.: "Relation between effects of porosity on strength and on Young's modulus of elasticity of polycrystalline materials", *J. Am. Ceram. Soc.*, 46(1963), 564–565.
22. Coble, R.L. and Kingery, W.D.: "Effect of porosity on physical properties of sintered alumina", *J. Am. Ceram. Soc.*, 39(1956), 377–385.
23. Nielsen, L. Fuglsang: "Strength and Stiffness of Porous Materials", *Journ. Am. Ceramic Soc.*, 73(1990), 2684–89.
24. *Idem*: "Elastic Properties of Two-Phase Materials", *Materials Science and Engineering*, 52(1982), 39–62.
25. Milton, G.W.: "Composites: A myriad of Microstructure Independent Relations", pp. 443–459 in *Proc. (eds. T. Tatsumi, E. Watanabe, T. Kambe) of the XIXth Int. Congr. of Theoretical and Applied Mechanics, Kyoto, Japan, 25–31 August 1996, published by Elsevier 1997*.
26. Sigmund, O.: "Materials with prescribed constitutive parameters: An inverse homogenization problem" *Int. J. Solids Structures* 31(1994), 2313–2229.
27. *Idem*: "Tailoring materials with prescribed elastic properties", *Mechanics of Materials* 20(1995), 304–368.
28. Milton, G.W. and Cherkaev, A.V.: "Which elasticity tensors are realizable", *J. of Engineering Materials and Technology*, 117(1995), 483–493.
29. Agarwal, B.D., Panizza, G.A., and Broutman, L.J.: "Micromechanics analysis of porous and filled ceramic composites", *Journ. Am. Ceramic Soc.*, 54(1971), 620–624.
30. Adams, D.F.: Section D: "Solution techniques" in "Elastoplastic behavior of composites", pp. 169–208 in "Mechanics of Composite Materials", Vol. II in "Composite materials" (edited by Broutman, L.J. and R.H. Krock), Academic Press, New York 1974.
31. Zaitsev, Y.B.: "Crack propagation in a composite material", in "Fracture Mechanics of Concrete", (ed. F.H. Wittmann), Elsevier 1983.
32. Zaitsev, Y.W. and F.H. Wittmann: "Simulation of crack propagation and failure of concrete", *Mater. and Struct.* 14(1981), 357–365.
33. Tvergaard, V.: "Fibre debonding and breakage in a whisker-reinforced metal", *Mat. Sc. & Eng.*, A190(1995), 215–222.
34. Bentz, D.: "Three-Dimensional Computer Simulation of Portland Cement Hydration and Microstructure Development", *J. Am. Ceram. Soc.*, 80(1997), 3–21.

35. Garboczi, E.J.: "Finite Element and Finite Difference Programs for Computing the Linear Electric and Elastic Properties of Digital Images of Random Materials", Report NISTIR 6269(1998), National Institute of Standards and Technology (NIST), Gaithersburg, Maryland 20899, USA.
36. Bentz, D.P., Garboczi, E.J., Jennings, H.M., and Quenard, D.A.: "Multi-Scale Digital-Image-Based Modelling of Cement-Based Materials", MRS Proceedings, *ibid* (1995), 33–42.
37. Bendsoe, M.P.: "Methods for the optimization of structural topology, shape and material", Springer Verlag, Berlin, 1995, p. 271.
38. Jacobsen, J.B., Olhoff, N., and Rønholt, E: "Generalized shape optimization of three-dimensional structures using materials with optimum microstructure", *Mechanics of Materials*, 28(1998), 207–225.
39. Pedersen, P.: "On sensitivity analysis and optimal design of specially orthotropic laminates", *Eng. Opt.*, 11(1987), 305–316.
40. Nielsen, L. Fuglsang: "On strength of porous material—simple systems and densified systems", *Materials and Structures*, 31(1998), 651–661.
41. Hammerslev, J.M. in *Proc. Cambridge Phil. Soc.*, 53(1957), 642.
42. Stauffer, D. and Aharony, A.: "Introduction to percolation theory", 2nd ed., Taylor and Francis, London, 1992.
43. Nielsen, L. Fuglsang: "Stiffness and other physical properties of composites as related to phase geometry and connectivity – Part I: Methods of analysis", 3rd Symposium on Building Physics in the Nordic Countries, Copenhagen, Sept. 13.–15. 1993. Proceedings Vol. 2 (Bjarne Saxhof, editor) Thermal Insulation Laboratory, Technical University Denmark, 1993, pp. 725–734.
44. Bentz, D.P.: Modelling cement microstructure: "Pixels, particles, and property prediction", *Materials and Structures*, Vol. 32(1999), 187–195.
45. Goodier, J.N.: "Concentration of Stress around Spherical and Cylindrical Inclusions and Flaws", *J. Appl. Mech.*, 55(1933), 39.
46. Dewey, J.M.: "The elastic constants of materials loaded with non-rigid fillers", *J. Appl. Phys.*, 18(1947), 578.
47. Landauer, R.: "The electric resistance of binary metallic mixtures", *J. Appl. Phys.* 23(1952), 779.
48. Böttcher, C.J.F.: "The dielectric constant of crystalline powders", *Rec. Trav. Pays-Bas*, 64(1945), 47.
49. Bruggeman, D.A.G.: "The calculation of various physical constants of heterogeneous substances, I: The dielectric constants and conductivities of mixtures composed of isotropic substances", *Ann. Phys. Lpz.*, 24(1935), 636.
50. Van Beek, L.K.H.: "Progress in dielectrics", Vol. 7, 69–114, Heywood, London, 1967.
51. Christensen, R.M. and Lo, K.H.: "Solutions for the effective shear properties in three phase sphere and cylinder models", *J. Mech. Phys. Solids*, 27(1979), 315.
52. Sokolnikoff, J.S.: "Mathematical theory of elasticity", McGraw-Hill, New York, 2nd edn., 1956.
53. Eshelby, J.D.: "The determination of the elastic field of an ellipsoidal inclusion, and related problems", *Proc. R. Soc. London, Ser. A*, 241(1957), 376–396.
54. Grabovsky, Y., Milton, G.W.: "Exact relations for composites: Towards a complete solution", *Documenta Mathematica, Extra Volume ICM III(1998)*, 623–632.

55. Grabovsky, Y., Milton, G.W., and Sage, D.S.: "Exact relations for effective tensors of composites: Necessary conditions and sufficient conditions", Report November (1998), Department of Mathematics, University of Utah, Salt Lake City, USA.
56. Nielsen, L. Fuglsang: "Shrinkage, Swelling, and Stiffness of Composites – Strain and Stress caused by Hygro-thermal action and Solidification or Freezing of Liquid Impregnant", Bygningssstatistiske Meddelelser, 62(1991), 47–78.
57. *Idem*: "Mechanics of composite material subjected to eigenstress – With special reference to frost resistance of porous brittle material", Danish Building Research Institute, SBI-Bulletin 96(1993).
58. *Idem*: "Drying of wood, Part I: Stresses caused by drying", "... Part II: Damage free drying", Bygningssstatistiske Meddelelser, 57(1986), p. 73–115.
59. *Idem*: "Interne Spannungen sowie Schwind- und Temperaturdeformationen des Betons", Cement and Concrete Research, 4(1974), 31–44.
60. Pickett, G.: "Effect of aggregate on shrinkage of concrete", Journ. Am. Concrete Inst., 52(1956), 581.
61. Hansen, T.C. and Nielsen, K.E.C.: "Effect of aggregate properties on concrete shrinkage", Journ. Am. Concrete Inst., 62(1965), 783.
62. Xi, Yunping and Jennings, H.M.: "Shrinkage of cement paste and concrete modelled by a multiscale effective homogeneous theory", Materials and Structures, 30(1997), 329–339.
63. Sendekyi, G.P.: "Elastic behavior of composites", pp. 46–83 in "Mechanics of Composite Materials", Vol. II in "Composite materials" (edited by Broutman, L.J. and R.H. Krock), Academic Press, New York 1974.
64. Nielsen, L. Fuglsang: "Pore size distribution and shrinkage of porous materials", Report 316(1994), Building Materials Lab., Techn. University of Denmark.
65. Bentz, P.B.: "Modelling drying shrinkage in reconstructed porous materials: Application to porous Vycor glass", Modelling Simul. Mater. Sci. Eng. 6(1998), 211–236.
66. Nielsen, L. Fuglsang: "Rheology of some fluid extreme composites – such as fresh self-compacting concrete", Nordic Concrete Research, 2(2001), 83–93.
67. Geiker, M.R., Brandl, M., Thrane, L. Nyholm, and Nielsen, L. Fuglsang: "Effect of coarse aggregate fraction and shape on the rheological properties of self-compacting concrete". Cement, Concrete, and Aggregates, Vol. 24, No. 1, June 2002.
68. Budiansky, B. and R.J. O'Connell: "Elastic moduli of a cracked solid", Int. J. Solids Struct., 12(1976), 81–97.
69. Davis, W.E.A.: "The dielectric constants of axially isotropic composite materials", J. Phys. D. 7(1974), 1016–1029.
70. Nielsen, L. Fuglsang: "Finite Element Analysis of two basic Composites", Documentation report R-089(2004), Dept. of Civ. Eng., Technical University of Denmark.
71. *Idem*: "On the Effect of Defective Phase Contact on the Mechanical Behavior of Particulate Composites like Concrete", Cement and Concrete Research, 12(1982), 685.
72. Hashin, Z.: "Assessment of Self Consistent Scheme approximation: Conductivity of particulate composites", J. Compos. Mater. Vol. 2(1968), 284.

73. Hashin, Z. and Shtrikman, S.: "A variational approach to the theory of the effective magnetic permeability of multiphase materials", J. Appl. Phys. 33(1962), 3125.
74. Bentz, D.P., Jensen, O.M., Coats, A.M., and Glasser, F.P.: "Influence of Silica Fume on diffusivity in cement-based Materials. Part I: Experimental and computer modelling studies on cement pastes", Submitted to Cement and Concrete Research 1999.
75. Delagrave, A., Marchand, J., and Pigeon, M.: "Influence of microstructure on the tritiated water diffusivity of mortars", Adv. Cem. Based Materials, 7(1998), 60–65.
76. Mejlhede Jensen, O.: Chloride ingress in cement paste and mortar measured by Electron Probe Micro Analysis", Report R51(1999), Dept. Struct. Eng. and Materials, Tech. Univ. Denmark.
77. Mills, R. and Lobo, V.M.M.: "Self-diffusion in electrolyte solutions", Elsevier, Amsterdam, (1989), 317.
78. Nielsen, L. Fuglsang: "Strength developments in hardened cement paste—Examination of some empirical equations", Materials and Structures, 26(1993), 255–260.
79. Christensen, B.: "Microstructural studies of hydrating portland cement-based materials using impedance spectroscopy", Ph.D. thesis, Northwestern University (1993).
80. Powers, T. C.: "Fundamental aspects of the shrinkage of concrete" (in german), Die Bauwirtschaft, 15(1961), 344–49.
81. Helmuth, R.A. and D.H. Turk: "Elastic moduli of hardened Portland cement and Tricalcium silicate pastes: Effects of porosity", pp. 135–144 in Symposium on structure of Portland cement and concrete. Highw. Res. Bd., Spec. Rept., No. 90, 1966.
82. Murray et al: "The hot pressing of ceramics", in W.D. Kingery: Ceramic Fabrication Processes, J. Wiley & Sons, New York, 1958.
83. Spriggs, R. M., Brissette, L. A., and Vasilos, T.: "Effect of porosity on elastic and shear moduli of polycrystalline magnesium oxide". J. Am. Ceram. Soc., 45(1962), 400.
84. Nielsen, L. Fuglsang: "Rheology of extreme composites", In "Papers in Structural Engineering and Materials – A Centenary Celebration", 179–187, Dept. of Struct. and Materials, Tech. Univ. Denmark, 2000.
85. *Idem*: "Rheology of some extreme liquid composites – such as fresh self-compacting concretes". Nordic Concrete Research, 2(2001), no. 7.
86. Wu, T.T.: "The effect of inclusion shape on the elastic moduli of a two-phase material", Int. J. Solids Structures, 2(1966), 1.
87. Ollivier, J.P. and Massat, M.: Permeability and microstructure of concrete: A review of modeling", Cem. and Concr. Res., 22(1992), 503–514.
88. Hansen, E. dePlace and Schmidt, L.: "Sammenhæng mellem porøsitet og elasticitetsmodul, samt porøsitet og styrke for teglsten", (in danish, Stiffness and strength of bricks as related to porosity), A students report in Material mechanics (Course 6110), Spring 1988, Build. Mat. Lab., Techn. Univ. Denmark.
89. Knudsen, F.P.: "Effect of porosity on Young's modulus of Alumina", J. Am. Ceram. Soc., 45(1962), 94–95.
90. Konow, Thorborg von: "Restaurering och reparation med puts- och murbruk" (in swedish: Restoration and repair with lime mortars), dr. thesis, Åbo Akademi University Press, Åbo, Finland, 1997.

91. Nielsen, Anders: "Porous materials – structure and properties", in "Selected research studies from Scandinavia", pp. 94–103, Report TVBM-3078(1997), Lund Institute of Technology, Div. Building Materials, Lund, Sweden.
92. *Idem*: "Ny viden om kalk og kalkmørtler" (in danish: New knowledge on lime and lime mortars), MAT-NYT 2(1998), Danish Society of Materials Testing and Research, Copenhagen, Denmark.
93. Madsen, D.H., Jeppesen, M.J., and Weidemann, H.C.: "Porestørrelsesfordeling i kalkmørtel" (in danish: Pore size distribution in lime mortar). A students report, course 59409, spring 1998, Dept. Struct. Eng. and Materials, (supervisors: Nielsen. A. and Nielsen, L.F.).
94. Hansen, T.C.: "Influence of aggregate and voids on modulus of elasticity of concrete, cement mortar, and cement paste", Proc. Am. Concr. Inst., 62(1965), 193–216.
95. J.J. Beaudoin and R.F. Feldman: "A study of mechanical properties of autoclaved Calcium silicate systems", Cem. Concr. Res., 5(1975), 103–118.
96. R.F. Feldman and J.J. Beaudoin: Studies of composites made by impregnation of porous bodies. I. Sulphur impregnant in Portland cement systems", Cem. Concr. Res., 7(1977), 19–30.
97. Clark, S.P.: "Handbook og physical constants", rev. ed; Memoir 97, The geological Society of America, Inc., New York, 1966.
98. Larsen, E.S. and Nielsen, C.B.: "Decay of bricks due to salt". Materials and Structures, 23(1990), 16–25.
99. Ashby, M.F.: "Materials data", Cambridge Univ. Eng. Dept., 1981.
100. Ishai, O.: "Influence of sand concentration on deformations of mortar beams under low stresses", ACI Journ., Proceedings 58(1961), 611–622.
101. Palmus, L.: "Letklinkerbetons mekaniske egenskaber" (in danish, Mechanical properties of light clinker concrete), M.Sc. thesis, Spring 1996, Dept. Struct. Engineering and Materials, Tech. Univ. Denmark.
102. Hansen, T.C.: "Creep and stress relaxation of concrete", Proc. 31(1960), Swedish Cement and Concrete Res. Ins., Tech. Univ. of Stockholm, Sweden.
103. *Idem*: "Influence of aggregate and voids on modulus of elasticity of concrete, cement, and cement paste", J. Am. Concr. Inst., Proc. 62(1965), 193.
104. Nielsen, K.E.C.: "Aggregate stresses in concrete", Thesis, Proc. 41(1971), Swedish Cement and Concrete Res. Inst., Tech. Univ. Stockholm, Sweden.
105. Tada, H., Paris, P.C., and Irwin, G.C.: "The Stress Analysis of Cracks Handbook", Del Research Corp., Hellertown, Pa, 1973.
106. Spange, H. and Pedersen, E.S.: "Early age properties of selected concrete", in "High Performance Concrete – The Contractors Technology, HETEK", Report 59(1997), Ministry of Transport, Road Directorate, Denmark.
107. Bentz, D.P.: Modeling cement microstructure: Pixels, particles, and property prediction", Materials and Structures, Vol. 32(1999), 187–195.
108. Lokhorst, S.J. and van Breugel, K.: "Simulation of the effect of geometrical changes of the microstructure on the deformational behavior of hardening concrete", Cement and Concrete Res., Vol. 27(1997), 1465–1479.
109. Nielsen, L. Fuglsang: "Strength developments in hardened cement paste – Examination of some empirical equations", Materials and Structures, 26(1993), 255–260.
110. Corson, P.B.: "Correlation functions for predicting properties of heterogeneous materials, IV: Effective thermal conductivity of two-phase solids", J. Appl. Phys. (USA) 45(1974), 3180.

111. Stephens, E. and Evans, E.J.: "The Hall effect and other properties of copper-antimony series of alloys", *Phil. Mag.* 7(1929), 161.
112. Stephanow, N.J.: "Electrical conductivity of alloys", *Z. anorg. u. allgem. Chem.* 78(1912), 1.
113. Hirsch, T.J.: "Modulus of elasticity of concrete affected by elastic moduli of cement paste matrix and aggregate", *Proc. Am. Concrete Inst.*, 59(1962), 427.
114. Dougill, J.W.: "Modulus of elasticity of concrete affected by elastic moduli of cement paste matrix and aggregate, Discussion of paper by T.J. Hirsch", *Proc. Am. Concrete Inst.*, 59(1962), 1363.
115. Popovics, S. and Erdey, M.: "Estimation of the modulus of elasticity of concrete-like composite materials", *Mat. and Struct.* 3(16)(1970), 253–260.
116. Counto, U.J.: "The effect of the elastic modulus of the aggregate on the elastic modulus, creep, and creep recovery of concrete", *Mag. Concrete Res.*, 16(1964), 129.
117. Tanacan, L. and Ersoy, H.Y.: "Mechanical properties of fired clay-perlite as composite material", *Journ. Materials in Civil Engineering*, February 2000, 55–59.
118. Maxwell, J.C.: *Treatise on electricity and magnetism*, 1(1873), 365.
119. Böttcher, C.J.F.: "The dielectric constant of crystalline powders", *Rec. Trav. Pays-Bas*, 64(1945), 47.
120. Nielsen, L. Fuglsang: "Effects of Creep in Uncracked Composite Structures of Steel and Concrete", *Bygningssstatistiske Meddelelser*, 38(1967), 65.
121. *Idem*: "Rheologiske Egenskaber for isotrope linear-viskoelastiske Kompositmaterialer", *Cement and Concrete Research*, 3(1973), 751–766.
122. *Idem*: "New Methods in Practical creep Analysis of Concrete", *Seventh Int. Congr. on Rheology*, Gothenburg, Sweden 1976. *Proc. Chalmers Univ. of Technology*, Gothenburg (1976), 98.
123. *Idem*: "Creep of Concrete under a Multi-Axial State of Stress", *Fifth Int. Congr. on Rheology*, Kyoto, Japan 1968, *Proc. Vol. II*, 527, University of Tokyo Press 1970.
124. *Idem*: "Composite analysis of concrete – Creep, relaxation, and eigenstrain/stress", in "High Performance Concrete – The Contractors Technology, HETEK", Report 112(1997), Ministry of Transport, Road Directorate, Denmark.
125. *Idem*: "Time-dependent behavior of concrete – a basic algorithm for FEM-analysis", *Bygningssstatistiske Meddelelser*, 70(1999).
126. Flügge, W.: "Viscoelasticity", *Blaisdell Publ. Comp.*, London 1967.
127. Lee, E.H.: "Stress analysis in viscoelastic bodies". *Quarterly of Appl. Mathematics*, 13(1955), 183.
128. Carslaw, H.S. and J.C. Jaeger: "Operational methods in applied mathematics". Dower, New York, 1963.
129. Erdelyi, A. (ed): "Tables of integral transforms, Bateman Manuscript Project, Vol. 1, McGraw-Hill, New York, 1954.
130. Murray, R.S.: *Mathematical handbook*, *Schaum's Outline Series*, McGraw-Hill, Inc., New York, 1968 (31th printing 1993).
131. Bellman, R.E., R.E. Kalaba, and J. Lockett: "Numerical Inversion of the laplace transforms" *Am. Elsevier Publ. Comp.*, New York, 1966.
132. Garbow, B.S., Giunta, G., Lyness, J.N., and Murli, A.: "Software for the implementation of Weierstrass's method for the inverse Laplace transformation problem", *ACM Trans. Math. Soft.*, 14(1988), 163–170.

133. *Idem*: "Algorithm 662. A Fortran software package for the numerical inversion of the Laplace transform based on Week's method", ACM Trans. Math. Soft., 14(1988), 171–176.
134. McHenry, D.: "A new aspect of creep in concrete and its application to design", ASTM Proc., 43(1943), pp. 1069–1084.
135. Alfrey, T.: "Non-Homogeneous Stresses in Viscoelastic Media". Qu. Appl. Math. 2(1944), 113.
136. Nowacki, W.: "Dynamics of elastic systems", Chapman & Hall Ltd, London 1963.
137. Ditlevsen, O.: "Stiffness replacement principle in linear visco-elastic structures", personally communicated research note, Dept. Struct. Eng. and Mat., Tech. Univ. Denmark, 16.05.1996.
138. Nowick, A.S., and Berry, B.S.: "Anelastic relaxation in crystalline solids", Academic Press, New York, 1972.
139. Schwarzl, F.R.: "Numerical calculation of stress relaxation modulus from dynamic data for linear viscoelastic materials", Rheologica Acta, 14(1975), pp. 581–590.
140. Nielsen, L. Fuglsang: "Power Law Creep as Related to Relaxation, Elasticity, Damping, Rheological Spectra and Creep Recovery – With Special Reference to Wood", Conference of Int. Union of Forestry Research Organizations (IUFRO), Xalapa, Mexico, December 1984. Proc., Build. Mat. Lab., Techn. Univ. Denmark 1985, 181–204.
141. *Idem*: "Material properties determined by vibration analysis", Materialenyt 1(1995), 4–46, Danish Society for Materials Testing and Research (DSM).
142. *Idem*: "Improved method for complex modulus estimation", Application Note, 1996, Brüel & Kjær A/S, Denmark, (co-authors, N.J. Wismer and S. Gade).
143. *Idem*: "Further developments in material properties determined by vibration analysis" (co-authors, L.V. Andreasen and M. Seifert), Materialenyt, 3(1996), Danish Society for Materials Testing and Research (DSM).
144. *Idem*: "An improved method for estimating the dynamic properties of materials", Sound & Vibration, Instrumentation reference issue, February 2000, 20–24, (co-authors, N.J. Wismer and S. Gade).
145. Døssing, O.: "Structural testing, Part I: Mechanical mobility measurement and Structural testing" and "Part II: Modal analysis and simulation", Brüel & Kjær, Nærum, Denmark, 1988.
146. Andreasen, L. and Seifert, M.: "Materialeprøvning med Svingningsudstyr", M.Sc. thesis, Build. Mat. Lab., Tec. Univ. Denmark, 1995.
147. Nielsen, A.: "Rheology of building materials", thesis, Statens Institut för Byggnadsforskning, Stockholm, Document D6(1972).
148. Nielsen, L. Fuglsang: "Lifetime and residual strength of wood subjected to static and variable load", Holz als Roh- u. Werkstoff, 58(2000), 81–90 and 141–152.
149. *Idem*: "On the influence of crack closure on strength estimates of wood", Holz als Roh- u. Werkstoff, 62(2004), 81–87.
150. *Idem*: "On the influence of moisture and load variations on the mechanical behavior of wood", Contribution to the COST-Action E24 workshop on "Reliability based design of timber structures" held in Ljubljana, Slovenia, October 7–8, 2004.

151. Dischinger, F.: "Untersuchungen über die Knicksicherheit, die elastische Verformung und das Kriechen des Betons bei Bogenbrücken", *Bauingenieur* 1937, 487–520, 539–552, 595–621.
152. *Idem*: "Elastische und plastische Verformungen der Eisenbetontragwerke und insbesondere der Bogenbrücken", *Bauingenieur* 1939, 53–63, 286–294, 426–437, 563–572.
153. Nielsen, L. Fuglsang: "Kriechen und Relaxations des Betons", *Beton- und Stahlbetonbau*, 11(1970), 272–275.
154. *Idem*: "On the Prediction of Rheological Parameters for Concrete", Nordic Conference on Deformations in Concrete Structures, Copenhagen, march 1980. Proc. DIALOG 1/80(1980), 81, Danish Engineering Academy, Dept. Civ. Eng., Lyngby, Denmark.
155. *Idem*: "On the Prediction of Creep Functions for Concrete", in "Fundamental Research on Creep and Shrinkage of Concrete" (ed. F. Wittmann), Martinus Nijhoff Publishers, The Hague 1982, 279–289.
156. *Idem*: "On the applicability of modified Dischinger equations", *Cement & Concrete Res.*, 7(1977), 159–160.
157. CEB-FIP: "Model code for concrete structures", Comité Euro-International du Béton, Paris, 1978.
158. Ross, A.D.: "Creep of concrete under variable stress". *ACI journ.*, Proc. 54(1958), 739–758.
159. Illston, J.M., Dinwoodie, J.M., and Smith, A.A.: "Concrete, Timber, and Metals – the nature and behavior of structural materials", Van Nostrand Reinhold Company, New York, 1979. (Chapter 10 on "Response of Concrete to Stress").
160. Nielsen, L. Fuglsang: "Constitutive equations for concrete", *Bygningsstatistiske Meddelelser*, 45(1974), 65.
161. *Idem*: "The improved Dischinger method as related to other methods and practical applicability", pp. 169–191 in "Design for Creep and Shrinkage in Concrete Structures", Special Publication SP-76(1982), American Concrete Institute.
162. Trost, H.: "Auswirkungen des Superpositionsprinzips auf Kriech- und Relaxationsprobleme bei Beton und Spannbeton", *Beton- und Stahlbetonbau* 62(1962), 230–238, 261–269.
163. Bazant, Z.P.: "Prediction of Concrete Creep Effects using Age-Adjusted Effective Modulus Method", *ACI-Journal*, 69(1972), 212–217.
164. Nielsen, L. Fuglsang: "Elasticity and Damping of Porous Materials and Impregnated Materials", *Journ. Am. Ceramic Soc.*, 67(1984), 93–98.
165. Hashin, Z.: "Viscoelastic behavior of heterogeneous media", *J. Appl. Mech.* (Transaction of the ASME), 1965, 630–636.
166. *Idem*: "Complex moduli of viscoelastic composites", *Int. J. Solids Struct.*, 6(1970), 539–52 and 6(1970), 797–807.
167. Neville, A.M.: "Creep of concrete as a function of its cement paste content", *Mag. Concr. Res.*, 16(1964), 21.
168. Pickett, G.: "Effect of aggregate on shrinkage of concrete and a hypothesis concerning shrinkage", *Proc. Am. Concrete Inst.*, 52(1956), 581.
169. Markestad, A. and Maage, M.: "Building Materials, Vol. II", (norwegian, Bygningsmateriallære II), textbook, TAPIR, Trondheim, Norway, 1978.
170. L'Hermite, R.G.: "Volume changes of concrete", *Chemistry of Cement*, 4th Int. Symp., Washington, 1960, p. 659.
171. Rüsch, H.: "Physikalische Fragen der Betonprüfung". *Zement-Kalk-Gips* 12 (1954), 27–39.

172. *Idem*: "Researches towards a general flexural theory for structural concrete, Proceedings of the ACI, 1957, 1.
173. Nielsen, L. Fuglsang: "ComCon (version 1.0) – Software for Composite analysis of concrete (Creep, relaxation, eigenstrain/stress, loss of prestress): Underlying theory and documentation", Report I-21, Dept. Struct. Eng. and Materials, Tech. Univ. Denmark, 1999.
174. Mullit, Paw: "ComCon (version 1.0) – Software for Composite analysis of concrete (Creep, relaxation, eigenstrain/stress, loss of prestress): User Manual", Report I-22, Dept. Struct. Eng. and Materials, Tech. Univ. Denmark, 1999.
175. Hastrup, K.: "Polymerimpregnering af porøse materialer" (in danish, Polymer impregnation of porous materials), Thesis, Build. Mat. Lab., Tech. Univ. Denmark, Tech. Report 42(1976).
176. Nielsen, L. Fuglsang: "Power-Law creep of wood – composite and dynamic aspects", Conference of Int. Union of Forestry Research Organizations (IUFRO), Bordeaux – France, 17.–21. August, 1992. Proc., Build. Mat. Lab., Tech. Univ. Denmark, 1993, pp. 25–33.
177. Pentoney, R.E.: "Time-dependent mechanical properties of wood", Int. conf. on "The mechanical behavior of wood", held at the Univ. of California, Berkeley, California, USA, Aug. 27 – Sept. 1, 1962. Proc. (ed. A.P. Schniewind), University Extension, Univ. of California. Northern Area, USA 1963.
178. Nowick, A.S., and Berry, B.S.: "Anelastic relaxation in crystalline solids", Academic Press, New York, 1972.
179. Hill, R.: "Elastic behaviour of crystalline aggregate", Proc. Phys. Soc. (London), A65(1952), nr 389, 349.
180. Voigt, W.: "Lehrbuch der Krystallphysik", Teubner, Leipzig, 1910 (reprinted, Teubner, Stuttgart, 1966).
181. Reuss, A.: "Berechnung der fließgrenze von Mischkristallen auf Grund der Plastizitätsbedingung für Einkristalle", Ztschr. f. angew. Math. u. Mech., 9(1929), 49.
182. Hashin, Z. and Shtrikman, S.: "A variational approach to the theory of the elastic behavior of polycrystals", Mech. Phys. Solids, 10(1962), 343.
183. Eshelby, J.D.: "The determination of the elastic field of an ellipsoidal inclusion, and related problems", Proc. R. Soc. London, Ser. A, 241(1957), 376–396.
184. Stang, Henrik: Personal communication, Dept. Struct. Eng. and Mat., Tech. Univ., Denmark, April 1997.
185. Nielsen, L. Fuglsang: "Materiale mekanik II – Rheologi, Brud, Kompositmaterialer og Levetid", (in danish, Material mechanics II – Rheology, Damage, Composites, and Fatigue), Textbook (TR-189), Build. Mat. Lab., Techn. Univ. Denmark, 1988.
186. Leaderman, H.: "Viscoelastic phenomena in amorphous high polymeric systems", Chap. 1 in Eirich, F. (ed): "Rheology", Vol. II, Academic Press Inc., New York, 1958.
187. Schwarzl, F.R.: "Numerical calculation of stress relaxation modulus from dynamic data for linear viscoelastic materials", Rheologica Acta, 14(1975), pp. 581–590.
188. Powers, T.C.: "Physical properties of cement paste", Proc. Fourth Int. Symp. on the Chemistry of Cement, Washington, D.C., 1960, US Dept. of Commerce, National Bureau of Standards, Book 2(1962), no. 43.

189. Powers, T.C. and T.L. Brownyard: "Studies of the physical properties of hardened cement paste", ACI Journ., Proc. 41(1946-47), 101, 249, 469, 549, 669, 845, 865, 933, 971, (Chicago, Portland Cement Ass., Res. Dept. Bulletin 22(1948)).
190. Hansen, P. Freiesleben: "Hærdeteknologi-1, Portland cement" og "Hærdeteknologi-2, Dekrementmetoden", Bkf-centralen, 1978.